Multiscale Study of Behaviour of Alkali-Activated Fly Ash-Slag Paste at Elevated Temperatures

WENLIN TU

Department of Civil, Environmental and Geomatic Engineering

University College London

This thesis is submitted for the degree of

Doctor of Philosophy in Civil Engineering

I would like to dedicate this thesis to my loving parents.

Declaration

I, Wenlin Tu confirm that the work presented in my thesis is my own. Where information has been derived from other sources, I confirm that this has been indicated in the thesis.

WENLIN TU

15/05/2024

Abstract

Alkali-activated materials (AAM) are studied as a novel sustainable binder to substitute Portland cement in concrete. They can possibly reduce up to 80% CO_2 emissions by consuming wastes and industrial by-products, which are rich in aluminosilicate, such as fly ash, slag and metakaolin. Compared with alkali-activated fly ash and alkali-activated slag, alkali-activated fly ash-slag (AAFS) exhibits an excellent balance between engineering properties and practical fabricability. However, the behaviour of AAFS paste at elevated temperatures remains unclear in terms of high temperature performance, which impedes its potential application as future high-temperature/fire-resistant construction materials. To date, the microstructural evolution and micromechanical properties of AAFS paste at elevated temperatures have not been extensively explored from a multiscale viewpoint. Also, the in-depth investigation on the microstructure-property relationships in AAFS is still lacking. Hence, it is vital to gain a comprehensive understanding of AAFS paste and explore the inherent damage mechanisms at elevated temperatures.

To tackle this challenge, for the first time, this thesis presents a systematic study on the behaviour of AAFS paste at 20 to 800 °C in terms of multiscale microstructural characterisation, micromechanical, thermal and mechanical properties. A series of advanced characterisation techniques including nuclear magnetic resonance (NMR), X-ray diffraction (XRD) and Fourier transform infrared spectroscopy (FTIR) are undertaken to characterise the nanostructures and phase assemblage of AAFS paste after exposure to 20, 105, 200, 400, 600 and 800 °C. Meanwhile, the microstructural characteristics of AAFS paste in terms of morphology changes, crack development and pore structure evolution are monitored using backscattered electron microscopy (BSEM), mercury intrusion porosimetry (MIP) and X-ray microcomputed tomography (XCT). Thermal and mechanical properties are determined from thermogravimetric analysis (TGA), thermal deformation, compressive and flexural strength tests.

Based on the findings above, the multiscale microstructural characteristics of AAFS paste are discussed in three different levels: (1) Level 0: solid gel particles (N-A-S-H, C-A-S-H and N-C-A-S-H), (2) Level I gel matrix (solid gel particles and gel pores), and (3) Level II paste (unreacted particles, reaction products and pores). The nanostructure of solid gel particles in AAFS paste is significantly altered as temperatures rise beyond 200 °C, resulting in the

decomposition of C-A-S-H gels and domination of N-A-S-H gels at 800 °C. At Level I, the gel matrix in AAFS paste experiences refinement at up to 200 °C, followed by a continuous drop in gel porosity to around 5% when reaching 600 °C. After 800 °C, new crystalline phases in terms of nepheline and gehlenite are observed, taking up around 26.3% and 21.5% of the crystalline phases by volume. At the paste level, results indicate that the compressive strength of AAFS paste rises by 77.5% at 200 °C, followed by a mitigation from 200 to 600 °C and a regain at 800 °C. Different phases in AAFS paste including unreacted particles, reaction products and pores take up 30%, 67.7% and 2.31% at ambient temperature, and 4.95%, 84.8% and 10.3% after exposure to 800 °C, respectively. The decomposition of binder gels occurs while gel pores are filled at elevated temperatures up to 800 °C, along with the crack development, whereas micro-cracks are healed by melting and viscous sintering.

Therefore, the relationships between microstructural evolution and mechanical properties of AAFS paste at elevated temperatures are explored and discussed in depth to gain insights into the underlying degradation mechanisms. These damage mechanisms are summarised at three temperature ranges including Stage 1 (20-200 °C): further geopolymerisation and pore pressure build-up, Stage 2: (200-600 °C) thermal gradient and phase decomposition, and Stage 3 (600-800 °C): recrystallisation and viscous sintering.

To sum up, this thesis significantly advances the understanding of AAFS paste at elevated temperatures and relevant damage mechanisms, offering crucial insights for its application as sustainable, high-temperature resistant materials in buildings and other infrastructures.

Impact statement

This PhD thesis represents a significant advancement in the field of sustainable cement-free construction materials, particularly in the development and understanding of alkali-activated concrete (AAC) at elevated temperatures. For the first time, a systematic and comprehensive experimental investigation of the multiscale microstructural characteristics, thermal, micromechanical, and mechanical properties of alkali-activated fly ash-slag (AAFS) paste is conducted, which provides crucial insights into the high-temperature-induced damage mechanisms and their implications for the structural integrity and durability of AAFS.

From the academic perspective, this thesis provides fundamental understandings of the behaviour of AAFS pastes at elevated temperatures, detailing how changes at the nano-scale can impact overall material properties and damage evolution. This contributes to the broader field of sustainable material science, particularly in understanding the performance of such environmentally-friendly construction material under extreme conditions. By demonstrating the potential of AAFS to withstand high temperatures while maintaining structural integrity through self-healing properties and sintering effects, this thesis promotes the further development of high-temperature resistant cementitious materials and potential damage mitigation strategies.

From the industrial perspective, this thesis widens the future use of AAFS, which can help reduce the carbon footprint of the construction industry by offering an alternative to traditional cement-based materials, aligning with global sustainability goals. Furthermore, the multiscale characterisation of AAFS paste at various temperatures provides a foundation for its application in heat-intensive environments such as fire-resistant barriers, nuclear plants, and infrastructure exposed to high thermal gradients. With the systematic investigation of AAFS at elevated temperatures, this thesis can help to establish industry standards and policies on the use of this material in construction, particularly in terms of specifications for high-temperature performance and durability.

From environmental, social and economic perspectives, the work in this thesis provides the guidance for safer, more resilient building practices and materials that are better suited to challenging operating conditions with the use of recycled materials.

Acknowledgements

I would like to express my sincerest appreciation to my supervisor, Dr Mingzhong Zhang. Knowing him for more than eight years, he has been patiently and continuously offering guidance and assistance. I would not be able to complete this journey without his constant support. Many thanks to my secondary supervisor, Dr Yukun Hu, for his help on my research and career development.

I am deeply indebted to Dr Guohao Fang from Shenzhen University for his support on my experimental work and continuous help on my career development. I would like to thank Prof Biqin Dong, Guanqi Wei, Ruixi Li, Guohong Wang and Changzhi Jiang for their strong support with my experiments in China. In addition, my deep appreciation should also go to Dr Sadjad Naderi for his guidance and suggestion. The financial support provided by UCL Overseas Research Scholarship and Graduate Research Scholarship is gratefully acknowledged.

I am grateful to Professor Marios Soutsos and Professor Beatrice Baudet for their roles as examiners during my PhD viva. Their insightful feedback and rigorous evaluation significantly contributed to the refinement of my thesis.

I want to say special thanks to Xiaowen Zhu, Shengqian Ruan, Yansong Wang, Mian Xie, Dr Qianyu Luo, Choi Lin Chan, Yiwei Xuan, Rong Tian and Dr Hui Zhong, who came to UCL to pursue the PhD degree together, for their continuous help and encouragement throughout these years, and for all the delightful moments we shared. Starting my PhD journey during pandemic was very tough. I would like to acknowledge the countless spiritual support from my friends, Linxuan Zou, Rachel Zhu, Annie Zhou, Kimi Xie, Zihan Liao and Mengyuan Xia. Most importantly, I want to thank Jay Lin, who always cares for me and stands by my side from the first day of my PhD journey. His presence and encouragement provide me with strength and love through every challenge I faced along the way.

Lastly, I would like to express my sincerest appreciation to my mom and dad, who have been my unwavering pillars of support throughout the many years of my higher education journey in the UK. I am forever thankful for their endless love and the sacrifices they have made, allowing me to pursue my dreams.

UCL Research Paper Declaration Form

referencing the doctoral candidate's own published work(s)

Please use this form to declare if parts of your thesis are already available in another format, e.g. if data, text, or figures:

- *have been uploaded to a preprint server*
- *are in submission to a peer-reviewed publication*
- *have been published in a peer-reviewed publication, e.g. journal, textbook.*

This form should be completed as many times as necessary. For instance, if you have seven thesis chapters, two of which containing material that has already been published, you would complete this form twice.

1. **For a research manuscript that has already been published** (if not yet published, please skip to section 2)

   a) **What is the title of the manuscript?**

   Behaviour of alkali-activated concrete at elevated temperatures: a critical review

   b) **Please include a link to or doi for the work**

   https://doi.org/10.1016/j.cemconcomp.2023.104961

   c) **Where was the work published?**

   Cement and Concrete Composites

   d) **Who published the work?** (e.g. OUP)

   Elsevier

   e) **When was the work published?**

   2023

   f) **List the manuscript's authors in the order they appear on the publication**

   Wenlin Tu, Mingzhong Zhang

   g) **Was the work peer reviewed?**

   Yes

   h) **Have you retained the copyright?**

   Yes

   i) **Was an earlier form of the manuscript uploaded to a preprint server?** (e.g. medRxiv). If 'Yes', please give a link or doi)

   No

   If 'No', please seek permission from the relevant publisher and check the box next to the below statement:

   ☐

   *I acknowledge permission of the publisher named under **1d** to include in this thesis portions of the publication named as included in **1c**.*

2. **For a research manuscript prepared for publication but that has not yet been published** (if already published, please skip to section 3)

a) **What is the current title of the manuscript?**

N/A

b) **Has the manuscript been uploaded to a preprint server?** (e.g. medRxiv; if 'Yes', please give a link or doi)

N/A

c) **Where is the work intended to be published?** (e.g. journal names)

N/A

d) **List the manuscript's authors in the intended authorship order**

N/A

e) **Stage of publication** (e.g. in submission)

N/A

3. **For multi-authored work, please give a statement of contribution covering all authors** (if single-author, please skip to section 4)

   Wenlin Tu has the following contributions: Conceptualisation, Methodology, Investigation, Data curation, Visualisation, Writing – Original draft. **Mingzhong Zhang** has the following contributions: Conceptualisation, Funding acquisition, Project administration, Supervision, Writing – review & editing.

4. **In which chapter(s) of your thesis can this material be found?**

   Chapter 2

5. **e-Signatures confirming that the information above is accurate** (this form should be co-signed by the supervisor/ senior author unless this is not appropriate, e.g. if the paper was a single-author work)

   Candidate

   Wenlin Tu

   Date:

   14/05/2024

   Supervisor/ Senior Author (where appropriate)

   Mingzhong Zhang

   Date

   14/05/2024

UCL Research Paper Declaration Form

referencing the doctoral candidate's own published work(s)

Please use this form to declare if parts of your thesis are already available in another format, e.g. if data, text, or figures:

- *have been uploaded to a preprint server*
- *are in submission to a peer-reviewed publication*
- *have been published in a peer-reviewed publication, e.g. journal, textbook.*

This form should be completed as many times as necessary. For instance, if you have seven thesis chapters, two of which containing material that has already been published, you would complete this form twice.

1. **For a research manuscript that has already been published** (if not yet published, please skip to section 2)

   a) **What is the title of the manuscript?**

   Multiscale study of microstructural evolution in alkali-activated fly ash-slag paste at elevated temperatures

   b) **Please include a link to or doi for the work**

   https://doi.org/10.1016/j.cemconcomp.2023.105258

   c) **Where was the work published?**

   Cement and Concrete Composites

   d) **Who published the work?** (e.g. OUP)

   Elsevier

   e) **When was the work published?**

   2023

   f) **List the manuscript's authors in the order they appear on the publication**

   Wenlin Tu, Guohao Fang, Biqin Dong, Mingzhong Zhang

   g) **Was the work peer reviewed?**

   Yes

   h) **Have you retained the copyright?**

   Yes

   i) **Was an earlier form of the manuscript uploaded to a preprint server?** (e.g. medRxiv). If 'Yes', please give a link or doi)

   No

   If 'No', please seek permission from the relevant publisher and check the box next to the below statement:

   ☐

   *I acknowledge permission of the publisher named under **1d** to include in this thesis portions of the publication named as included in **1c**.*

2. **For a research manuscript prepared for publication but that has not yet been published** (if already published, please skip to section 3)

a) **What is the current title of the manuscript?**

N/A

b) **Has the manuscript been uploaded to a preprint server?** (e.g. medRxiv; if 'Yes', please give a link or doi)

N/A

c) **Where is the work intended to be published?** (e.g. journal names)

N/A

d) **List the manuscript's authors in the intended authorship order**

N/A

e) **Stage of publication** (e.g. in submission)

N/A

3. **For multi-authored work, please give a statement of contribution covering all authors** (if single-author, please skip to section 4)
   Wenlin Tu has the following contributions: Conceptualisation, Methodology, Investigation, Data curation, Visualisation, Writing – Original draft. **Guohao Fang** has the following contributions: Methodology, Funding acquisition, Project administration. **Biqin Dong** has the following contributions: Methodology, Funding acquisition, Project administration. **Mingzhong Zhang** has the following contributions: Conceptualisation, Funding acquisition, Project administration, Supervision, Writing – review & editing.

4. **In which chapter(s) of your thesis can this material be found?**

   Chapter 3 and 5

5. **e-Signatures confirming that the information above is accurate** (this form should be co-signed by the supervisor/ senior author unless this is not appropriate, e.g. if the paper was a single-author work)

   Candidate

   Wenlin Tu

   Date:

   14/05/2024

   Supervisor/ Senior Author (where appropriate)

   Mingzhong Zhang

   Date

   14/05/2024

UCL Research Paper Declaration Form

referencing the doctoral candidate's own published work(s)

Please use this form to declare if parts of your thesis are already available in another format, e.g. if data, text, or figures:

- *have been uploaded to a preprint server*
- *are in submission to a peer-reviewed publication*
- *have been published in a peer-reviewed publication, e.g. journal, textbook.*

This form should be completed as many times as necessary. For instance, if you have seven thesis chapters, two of which containing material that has already been published, you would complete this form twice.

1. **For a research manuscript that has already been published** (if not yet published, please skip to section 2)

   a) **What is the title of the manuscript?**

   Behaviour of alkali-activated fly ash-slag paste at elevated temperatures: An experimental study

   b) **Please include a link to or doi for the work**

   https://doi.org/10.1016/j.cemconcomp.2024.105438

   c) **Where was the work published?**

   Cement and Concrete Composites

   d) **Who published the work?** (e.g. OUP)

   Elsevier

   e) **When was the work published?**

   2024

   f) **List the manuscript's authors in the order they appear on the publication**

   Wenlin Tu, Guohao Fang, Biqin Dong, Mingzhong Zhang

   g) **Was the work peer reviewed?**

   Yes

   h) **Have you retained the copyright?**

   Yes

   i) **Was an earlier form of the manuscript uploaded to a preprint server?** (e.g. medRxiv). If 'Yes', please give a link or doi)

   No

   If 'No', please seek permission from the relevant publisher and check the box next to the below statement:

   ☐

   *I acknowledge permission of the publisher named under **1d** to include in this thesis portions of the publication named as included in **1c**.*

2. **For a research manuscript prepared for publication but that has not yet been published** (if already published, please skip to section 3)

a) **What is the current title of the manuscript?**

N/A

b) **Has the manuscript been uploaded to a preprint server?** (e.g. medRxiv; if 'Yes', please give a link or doi)

N/A

c) **Where is the work intended to be published?** (e.g. journal names)

N/A

d) **List the manuscript's authors in the intended authorship order**

N/A

e) **Stage of publication** (e.g. in submission)

N/A

3. **For multi-authored work, please give a statement of contribution covering all authors** (if single-author, please skip to section 4)

Wenlin Tu has the following contributions: Conceptualisation, Methodology, Investigation, Data curation, Visualisation, Writing – Original draft. **Guohao Fang** has the following contributions: Methodology, Funding acquisition, Project administration. **Biqin Dong** has the following contributions: Methodology, Funding acquisition, Project administration. **Mingzhong Zhang** has the following contributions: Conceptualisation, Funding acquisition, Project administration, Supervision, Writing – review & editing.

4. **In which chapter(s) of your thesis can this material be found?**

Chapter 3, 4 and 5

5. **e-Signatures confirming that the information above is accurate** (this form should be co-signed by the supervisor/ senior author unless this is not appropriate, e.g. if the paper was a single-author work)

Candidate

Wenlin Tu

Date:

14/05/2024

Supervisor/ Senior Author (where appropriate)

Mingzhong Zhang

Date

14/05/2024

UCL Research Paper Declaration Form

referencing the doctoral candidate's own published work(s)

Please use this form to declare if parts of your thesis are already available in another format, e.g. if data, text, or figures:

- *have been uploaded to a preprint server*
- *are in submission to a peer-reviewed publication*
- *have been published in a peer-reviewed publication, e.g. journal, textbook.*

This form should be completed as many times as necessary. For instance, if you have seven thesis chapters, two of which containing material that has already been published, you would complete this form twice.

1. **For a research manuscript that has already been published** (if not yet published, please skip to section 2)

   a) **What is the title of the manuscript?**

   Multiscale microstructure and micromechanical properties of alkali-activated concrete: A critical review

   b) **Please include a link to or doi for the work**

   https://doi.org/10.1016/j.cemconcomp.2024.105664

   c) **Where was the work published?**

   Cement and Concrete Composites

   d) **Who published the work?** (e.g. OUP)

   Elsevier

   e) **When was the work published?**

   2024

   f) **List the manuscript's authors in the order they appear on the publication**

   Wenlin Tu, Mingzhong Zhang

   g) **Was the work peer reviewed?**

   Yes

   h) **Have you retained the copyright?**

   Yes

   i) **Was an earlier form of the manuscript uploaded to a preprint server?** (e.g. medRxiv). If 'Yes', please give a link or doi)

   No

   If 'No', please seek permission from the relevant publisher and check the box next to the below statement:

   ☐

   *I acknowledge permission of the publisher named under **1d** to include in this thesis portions of the publication named as included in **1c**.*

2. **For a research manuscript prepared for publication but that has not yet been published** (if already published, please skip to section 3)

a) **What is the current title of the manuscript?**

N/A

b) **Has the manuscript been uploaded to a preprint server?** (e.g. medRxiv; if 'Yes', please give a link or doi)

N/A

c) **Where is the work intended to be published?** (e.g. journal names)

N/A

d) **List the manuscript's authors in the intended authorship order**

N/A

e) **Stage of publication** (e.g. in submission)

N/A

3. **For multi-authored work, please give a statement of contribution covering all authors** (if single-author, please skip to section 4)

   Wenlin Tu has the following contributions: Conceptualisation, Methodology, Investigation, Data curation, Visualisation, Writing – Original draft. **Mingzhong Zhang** has the following contributions: Conceptualisation, Funding acquisition, Project administration, Supervision, Writing – review & editing.

4. **In which chapter(s) of your thesis can this material be found?**

   Chapter 2

5. **e-Signatures confirming that the information above is accurate** (this form should be co-signed by the supervisor/ senior author unless this is not appropriate, e.g. if the paper was a single-author work)

   Candidate

   Wenlin Tu

   Date:

   16/09/2024

   Supervisor/ Senior Author (where appropriate)

   Mingzhong Zhang

   Date

   16/09/2024

UCL Research Paper Declaration Form

referencing the doctoral candidate's own published work(s)

Please use this form to declare if parts of your thesis are already available in another format, e.g. if data, text, or figures:

- *have been uploaded to a preprint server*
- *are in submission to a peer-reviewed publication*
- *have been published in a peer-reviewed publication, e.g. journal, textbook.*

This form should be completed as many times as necessary. For instance, if you have seven thesis chapters, two of which containing material that has already been published, you would complete this form twice.

1. **For a research manuscript that has already been published** (if not yet published, please skip to section 2)

   a) **What is the title of the manuscript?**

   Micromechanical analysis of alkali-activated fly ash-slag paste subjected to elevated temperatures

   b) **Please include a link to or doi for the work**

   https://doi.org/10.1016/j.cemconcomp.2024.105735

   c) **Where was the work published?**

   Cement and Concrete Composites

   d) **Who published the work?** (e.g. OUP)

   Elsevier

   e) **When was the work published?**

   2024

   f) **List the manuscript's authors in the order they appear on the publication**

   Wenlin Tu, Guohao Fang, Biqin Dong, Mingzhong Zhang

   g) **Was the work peer reviewed?**

   Yes

   h) **Have you retained the copyright?**

   Yes

   i) **Was an earlier form of the manuscript uploaded to a preprint server?** (e.g. medRxiv). If 'Yes', please give a link or doi)

   No

   If 'No', please seek permission from the relevant publisher and check the box next to the below statement:

   ☐

   *I acknowledge permission of the publisher named under **1d** to include in this thesis portions of the publication named as included in **1c**.*

2. **For a research manuscript prepared for publication but that has not yet been published** (if already published, please skip to section 3)

a) **What is the current title of the manuscript?**

N/A

b) **Has the manuscript been uploaded to a preprint server?** (e.g. medRxiv; if 'Yes', please give a link or doi)

N/A

c) **Where is the work intended to be published?** (e.g. journal names)

N/A

d) **List the manuscript's authors in the intended authorship order**

N/A

e) **Stage of publication** (e.g. in submission)

N/A

3. **For multi-authored work, please give a statement of contribution covering all authors** (if single-author, please skip to section 4)
Wenlin Tu has the following contributions: Conceptualisation, Methodology, Investigation, Data curation, Visualisation, Writing – Original draft. **Guohao Fang** has the following contributions: Methodology, Funding acquisition, Project administration. **Biqin Dong** has the following contributions: Methodology, Funding acquisition, Project administration. **Mingzhong Zhang** has the following contributions: Conceptualisation, Funding acquisition, Project administration, Supervision, Writing – review & editing.

4. **In which chapter(s) of your thesis can this material be found?**

   Chapter 4 and 5

5. **e-Signatures confirming that the information above is accurate** (this form should be co-signed by the supervisor/ senior author unless this is not appropriate, e.g. if the paper was a single-author work)

   Candidate

   Wenlin Tu

   Date:

   16/09/2024

   Supervisor/ Senior Author (where appropriate)

   Mingzhong Zhang

   Date

   16/09/2024

Contents

List of Figures

List of Tables

Abbreviations

AAM	Alkali-activated materials
AAC	Alkali-activated concrete
AAF	Alkali-activated fly ash
AAFS	Alkali-activated fly ash-slag
AAMK	Alkali-activated metakaolin
AAS	Alkali-activated slag
AFM	Atomic force microscopy
AL	Alkaline activator
BSEM	Backscattered scanning electron microscopy
C-A-S-H	Calcium-alumina-silicate-hydrate
DTG	Derivative thermogravimetry
GGBS	Ground granulated blast-furnace slag
ITZ	Interfacial transition zone
N-A-S-H	Sodium-alumina-silicate-hydrate
P	Precursor
PP	Polypropylene
PCC	Portland cement concrete
SH	Sodium hydroxide
SP	Superplasticiser
SS	Sodium silicate

EDS	Energy dispersive spectrometry
FTIR	Fourier transform infrared spectroscopy
MIP	Mercury intrusion porosimetry
NMR	Nuclear magnetic resonance
QXRD	Rietveld-based quantitative X-ray diffraction
TEM	Transmission electron microscopy
TGA	Thermogravimetric analysis
XRD	X-ray diffraction
XRF	X-ray fluorescence spectrometry
XCT	X-ray microcomputed tomography

Chapter 1 Introduction

1.1 Research background

Portland cement concrete (PCC) is the most commonly used construction material, which may inevitably experience damage and durability loss under severe conditions, such as high humidity, chemical attacks and abrupt temperature change [1]. Among those, high temperature exposure is one of the extreme scenarios that can cause serious risks or even catastrophes if any large-scale concrete structure collapses [2-5]. As a promising alternative to PCC, alkali-activated concrete (AAC) is a sustainable cement-free construction material produced through alkaline activation of aluminosilicates such as fly ash and ground granulated blast-furnace slag, which can possess superior thermal stability and high-temperature resistance with 60-80% less CO_2 emissions compared to PCC products [6-12]. The application of AAC as a substitute for PCC can not only help to boost sustainability of construction materials, but also reduce the amount of industrial wastes [13-16]. Moreover, AAC exhibits better mechanical performance and stable structure integrity at elevated temperatures of up to 800-900 °C in comparison with PCC [17, 18]. Hence, the application of AAC in high temperature scenarios has been increasingly explored, such as fire protective coatings, tunnels, thermal insulators and thermal energy storage concrete [19-22].

Nevertheless, AAC would also experience significant damage when exposed to high temperatures due to different mechanisms including thermal incompatibility, pore pressure build-up and phase transformation [23-25]. Thermal incompatibility is induced by the difference in thermal expansion coefficient of different constituents of AAC. For instance, aggregates tend to expand while AAC matrix experiences shrinkage when exposed to elevated temperatures, leading to crack initiation and propagation [24, 26, 27]. Pore pressure build-up results from the moisture transport from the heated surface to the cooler region in AAC matrix subjected to high temperatures. The accumulation of condensed water vapour in the non-

deformable pore structure of AAC would thereby cause damage and crack development [4, 28, 29]. Furthermore, the phase transformation and rearrangement of crystalline structure in AAC at elevated temperatures would lead to strength gain and loss, depending on the thermal stability [30-33]. Therefore, to promote the broader application of AAC in civil infrastructure, it is vital to systematically investigate the behaviour of AAC at elevated temperatures.

The commonly studied AAC can be classified into two categories: (1) single-precursor system such as alkali-activated fly ash (AAF), alkali-activated metakaolin (AAMK) and alkali-activated slag (AAS), and (2) blended precursor system such as alkali-activated fly ash-slag (AAFS) and alkali-activated slag-metakaolin. Among them, AAF exhibits superior mechanical performance after exposure to 800 °C [34-36], attributed to the porous matrix structure with internal-connected channels, which prevents the vapour pressure accumulation at high temperatures [23-25]. AAMK tends to form a more compact and denser internal structure with less pore evolution at elevated temperatures, resulting in a more serious pore pressure-induced damage compared to AAF [35, 37]. Due to the additional hydrated phases formed because of the high calcium content of slag, AAS suffers from a significant strength reduction as the decomposition of $CaCO_3$ can take place at around 756 °C [10, 25, 38]. Thus, AAF is considered as a good choice for high temperature scenarios. However, the in-situ application of AAF is extensively impeded since the activation of fly ash requires heat curing of 60-85 °C to gain acceptable early strength [39, 40]. Hence, a blended system (i.e. AAFS) cured at ambient temperature is introduced, as the incorporation of slag can enhance the degree of alkaline activation of fly ash at ambient temperature [34, 41, 42].

Regarding microstructural characteristics, only few studies have attempted to explore the phase transformation and physical changes of AAFS at elevated temperatures. AAFS paste is considered as a multiphase heterogeneous composite material, consisting of unreacted fly ash and slag particles, reaction products and pores [39]. Hence, the microstructural features of AAFS can be characterised at three different levels: Level 0 denotes the nanostructure of solid gel particles that are the elementary components of crystalline and amorphous phases in AAFS [39, 43-45]. The addition of a calcium source leads to the coexistence of sodium-alumina-silicate-hydrate (N-A-S-H) and calcium-alumina-silicate-hydrate (C-A-S-H) gels, with partial replacement of sodium from N-A-S-H gel to form the hybrid sodium-calcium-alumina-silicate-hydrate (N-C-A-S-H) gel that has a higher degree of cross-linking [22, 46-48]. These three

types of reaction products dominate the AAFS paste, which take up more than 90% of the binder weight [48]. Level I corresponds to the chemical composition of the AAFS gel matrix, which is agglomerated by the solid gel particles and gel pores. Level II stands for AAFS paste at micro-scale, composed of gel matrix, unreacted fly ash and slag particles and pores. To date, the microstructural characteristics of AAFS at elevated temperatures have never been thoroughly understood and systematically investigated. Furthermore, the existing studies on microstructural characteristics of AAFS were mainly focused on ambient temperature, while the damage evolution in AAFS at elevated temperatures has not been explored from a multiscale and three-dimensional (3D) point of view.

On the other hand, some attempts have been made to study the behaviour of AAFS subjected to elevated temperatures by assessing thermal and mechanical properties under different temperature levels ranging from 20 to 800 °C, [22, 32, 49-51]. At 20-400 °C, pore pressure build-up is considered as the dominant factor that leads to damage in AAFS [4, 52]. Meanwhile, further geopolymerisation takes place, which contributes to strength gains along with the development of binder gels [5, 53-55]. After 400 °C, the residual compressive strength of AAFS is enhanced by approximately 0-25% of the original strength [2]. From 400 to 600 °C, a noticeable decline of retained strength in AAFS can be found, due to the dehydration and decomposition of calcite [34, 56]. The retained strength of AAFS after 600 °C exposure can be reduced to less than 30% of that at ambient temperature [57]. When the exposure temperature reaches 800 °C, phase transformation and viscous sintering are the factors that influence the mechanical performance of AAFS [58-60]. Viscous sintering can enhance the mechanical performance, which is associated with the collapse of nano-pores and flow of aluminosilicates, improving the interparticle bonding [2, 55, 61]. This effect can result in the densification of AAFS matrix with the increase of gel-to-space ratio and self-healing of microcracks [62]. Thus, the residual strength of AAFS after 800 °C heating was found to rise by up to 10% in comparison with that after exposure to 600 °C [2]. At 1000 °C, about 10% of the original strength remains in AAFS, implying the loss of mechanical integrity in AAFS when the temperature exceeds 800 °C [2, 59]. However, the micromechanical properties of different solid phases in AAFS paste before and after high temperature exposure have never been studied, while aforementioned properties have not been linked to each other to explore the underlying damage mechanisms at different temperature levels. Therefore, to gain a comprehensive

understanding of the behaviour of AAFS paste at elevated temperatures, the following aspects remain insufficiently explored:

- Fundamental insights of the multiscale microstructural characteristics of AAFS paste from solid gel particle to paste at up to 800 °C.
- Three-dimensional (3D) visualisation of damage evolution in AAFS paste at elevated temperatures.
- Behaviour of AAFS paste at elevated temperatures with special focus on micromechanical properties and microstructure-mechanical property relationships.
- Inherent damage mechanisms of AAFS paste elevated temperatures.

1.2 Research aim and objectives

The overall aim of this research is to conduct a systematic study into the behaviour of AAFS paste at elevated temperatures in terms of multiscale microstructural characteristics and thermal and mechanical properties, and study the inherent damage mechanisms associated with high-temperature exposure. The findings of this research offer a comprehensive understanding of the high-temperature-induced damage evolution in AAFS paste, thereby contributing to the advancement of this sustainable material and enhancing its potential for engineering applications in heat-resistant contexts. To achieve this aim, the specific objectives of this study are outlined as follows:

- To explore the multiscale microstructural characteristics of AAFS paste at elevated temperatures including nanostructure, chemical compositions and microstructural features in terms of morphology changes, crack development and pore structure characteristics from solid gel particle to gel matrix and paste.
- To investigate the damage evolution in AAFS paste at 20 ºC and elevated temperatures including 105, 200, 400, 600 and 800 ºC, and to visualise the evolution of pore structure in 3D.
- To study the behaviour of AAFS paste at elevated temperatures regarding thermal, micromechanical and mechanical properties, and explore the microstructure-mechanical

property relationships to thoroughly understand the mechanical performance of this material.

- To evaluate the inherent damage mechanisms of AAFS paste at different temperatures based on the experimental results, thereby provide insights into the development of future damage mitigation strategies.

1.3 Research strategy

To accomplish the aforementioned objectives, the strategies implemented are given as follows:

- The multiscale microstructural features of AAFS paste at elevated temperatures are characterised at different length scales with a series of advanced characterisation techniques: Level 0 (1-10 nm): solid gel particle, Level I (10 nm - 1 μm): gel matrix and Level II (1 μm - 100 μm): paste. Level 0 refers to the nanostructure of AAFS solid gel particle, which is explored via nuclear magnetic resonance (NMR). At Level I, the chemical compositions of AAFS gel matrix regarding crystalline phases and amorphous phases are determined by X-ray diffraction (XRD) and Fourier transform infrared spectroscopy (FTIR), respectively. At Level II, the microstructure of AAFS paste is studied by means of backscattered scanning electron microscopy-energy dispersive spectrometry (BSEM-EDS) and mercury intrusion porosimetry (MIP).
- The damage evolution of AAFS paste is investigated by 3D scanning using X-ray microcomputed tomography (XCT). The XCT results are analysed by image analysing software Avizo to visualise the evolution of internal structure in the paste matrix.
- A series of tests including atomic force microscopy (AFM), thermogravimetric analysis (TGA), dilatometry, nanoindentation, compressive strength and three-point bending tests are performed to investigate the behaviour of AAFS paste, thereby exploring the microstructure-mechanical property relationships as the temperature increases.
- Based on the experimental results obtained above, the inherent damage mechanisms of AAFS paste are proposed and discussed based on different temperature ranges including: Stage 1: 20-200 ºC, Stage 2: 200-600 ºC and Stage 3: 600-800 ºC.

1.4 Thesis outline

This thesis consists of the following six chapters as seen in Figure 1.1.

Chapter 1 offers a general introduction to this research, outlining the background, aim and objectives, and overarching research strategy.

Chapter 2 delivers a critical review on the multiscale microstructural characteristics and micromechanical properties of AAC at ambient temperature. It also discusses the behaviour of AAC at elevated temperatures, focusing on changes in microstructure, thermal and mechanical properties. Additionally, this chapter summarises the existing damage mechanisms associated with AAC and discusses various approaches for their mitigation.

Chapter 3 presents a systematic experimental study on the multiscale microstructural characteristics of AAFS paste at 20-800 ºC from a multiscale perspective. This includes an in-depth analysis across three distinct levels: Level 0: solid gel particle, Level I: gel matrix and Level II: paste. The microstructural evolution of AAFS paste is thoroughly investigated, covering aspects of nanostructure arrangement, crystalline phase characterisation, amorphous phase identification, solid phase assemblage and pore structure analysis.

Chapter 4 details an experimental study that investigates the behaviour of AAFS paste across a temperature range from 20 to 800 ºC, concentrating on physical, thermal, micromechanical and mechanical properties. Furthermore, this chapter discusses and elaborates the underlying microstructure-micromechanical property relationships in AAFS paste after high temperature exposure.

Chapter 5 establishes the damage mechanisms of AAFS paste at elevated temperatures based on the experimental results. The temperature is categorised into three different stages: Stage 1: 20-200 ºC, Stage 2: 200-600 ºC and Stage 3: 600-800 ºC.

Chapter 6 gives a summary of the main contributions and conclusions drawn from this research. The limitations encountered during this research and recommendations for future research are also provided in this chapter.

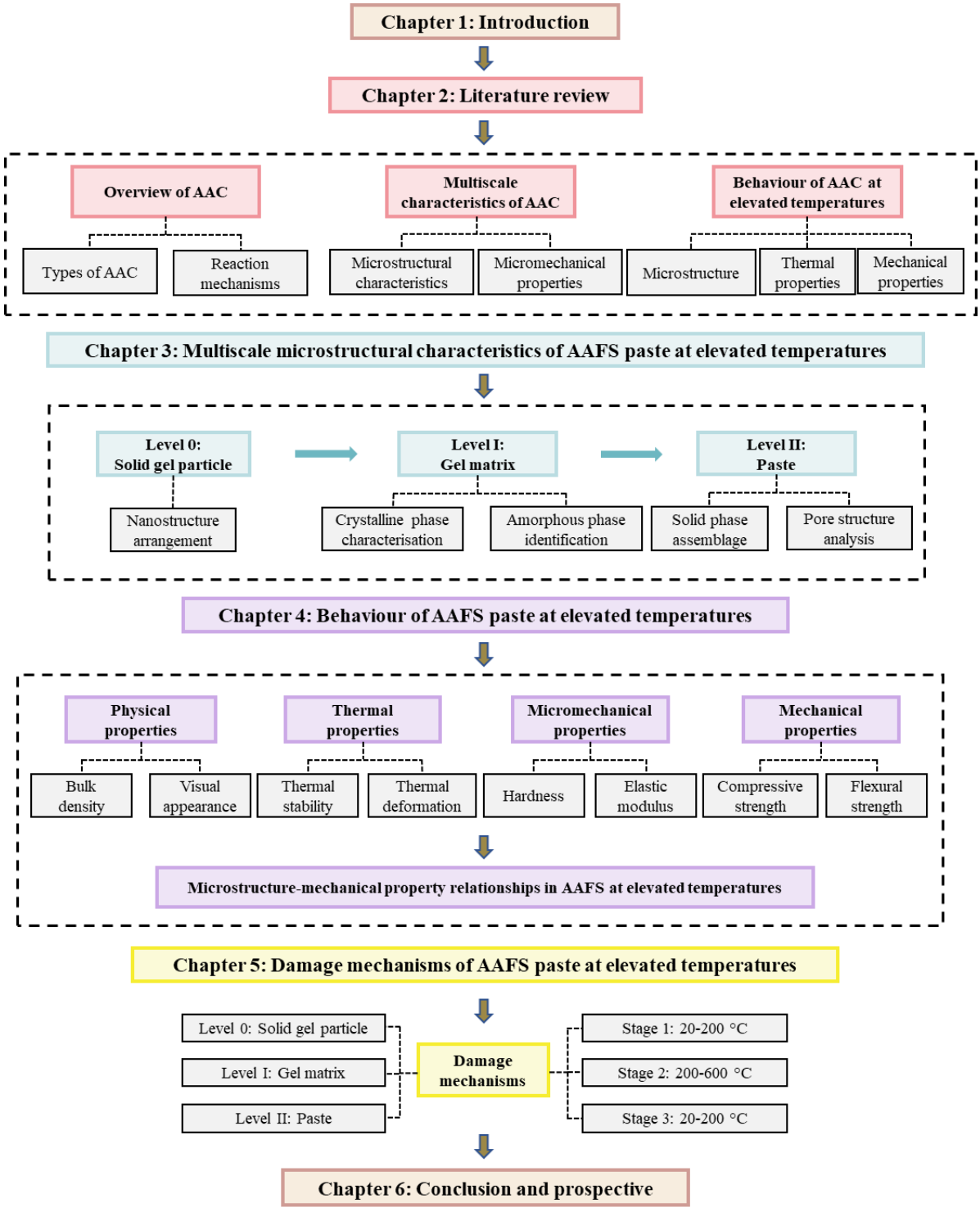

Figure 1.1. Outline of this thesis.

Chapter 2 Literature Review

2.1 Introduction

This chapter presents a critical review on the behaviour of AAC at both ambient and elevated temperatures. Initially, the types of AAC and their chemical reactions are briefly introduced to explain the constituents and reaction mechanisms involved. Afterwards, the chapter explores the multiscale microstructural characteristics and micromechanical properties of AAC at ambient temperature, discussing these aspects across multiple length scales. Furthermore, the behaviour of AAC at elevated temperatures is reviewed comprehensively, focusing particularly on microstructural evolution as well as thermal and mechanical properties, with an emphasis on damage mechanisms and mitigation approaches. The chapter concludes by identifying existing research gap and limitations in this field. Part of this chapter has been presented in the following manuscripts:

W. Tu, M. Zhang, Behaviour of alkali-activated concrete at elevated temperatures: A critical review, *Cement and Concrete Composites*, 138 (2023) 104961.

W. Tu, M. Zhang, Multiscale microstructure and micromechanical properties of alkali-activated concrete: A critical review. *Cement and Concrete Composites*, 152 (2024) 105664.

2.2 Classification and chemical reactions of alkali-activated concrete (AAC)

AAC can be categorised based on different types of source materials utilised. In this section, the classification of AAC is introduced, based on systems using single and blended precursors. The corresponding reaction mechanisms of AAC are also discussed.

2.2.1 Constituents

As a promising alternative material to PCC, AAC has been demonstrated to achieve excellent mechanical properties and durability with environmental benefits [12, 63-65]. In particular, the use of AAC can significantly contribute to reduction of CO_2 emissions and carbon footprint while improving pollution levels and energy consumption compared to PCC [66-69]. AAC consists of precursor, alkaline activator, aggregate and superplasticiser (SP). A variety of aluminosilicate materials can be used as precursors in AAC, such as fly ash (i.e. a by-product of coal-fired power stations), slag (i.e. a by-product of steel manufacturing), metakaolin, bottom ash and silica fume. The most commonly used precursors in AAC include fly ash, slag, metakaolin and their blends, which produce different types of AAC using alkaline solutions like sodium hydroxide (SH), sodium silicate (SS), potassium hydroxide (KOH) and potassium silicates (K_2SiO_3) [70-73]. In general, the classification of AAC can be based on single precursor system and blended precursor system. In single precursor system, alkali-activated fly ash (AAF) and alkali-activated metakaolin (AAMK) are considered as low-calcium AAC [73-76]. After dissolution of precursors and condensation reaction, alkaline aluminosilicate hydrates in a network structure are formed [77, 78]. Alkali-activated slag (AAS) is regarded as high-calcium AAC, which undergoes the activation process with substitution of aluminium by silicate to form binder gels [79, 80]. At ambient temperature, AAS exhibits excellent early-age mechanical performance, while AAF requires heat curing at around 60-90 °C for 24 h to achieve acceptable early-age comparative strength [81, 82]. However, AAF shows more superior fresh properties and suffers much less from strength reduction than AAS after exposure to elevated temperatures of up to 800 °C [12, 23-25]. Herein, the alkali-activated fly ash-slag (AAFS) has been introduced in blended precursor system, which can achieve desirable fresh and mechanical properties at ambient curing temperature [39].

2.2.2 Reaction mechanisms

Single precursor system

The identification of reaction products in AAC and relevant reaction mechanisms are mainly dependent on the calcium content in the system, which can determine the dominant types of

gels within the matrix. The main reaction product in AAF and AAMK is an aluminosilicate-type gel, whereas calcium (alumino) silicate hydrate-type gel dominates the structure of AAS [64, 83]. The conceptual scheme for alkaline activation in the single precursor system is illustrated in Figure 2.1. In general, the reaction process in both AAF and AAS can be divided into four steps: (a) dissolution, (b) rearrangement, (c) gel nucleation, and (d) solidification, hardening and strength development [64]. The reaction starts with the generation of a colloidal solution of fine particles by the activation of alkaline solutions, followed by a combination into a continuous solid gel phase. Firstly, the dissolution of alumina and silica in precursors takes place under an alkaline environment composed of sodium/potassium hydroxides and silicates. The activation process disrupts the integrity of Si-O-Si and Al-O-Al bonds in fly ash, as well as Ca-O and Si-O-Si bonds in slag [84]. In consequence, different types of dissolved species are formed.

Afterwards, the formation of silica and alumino-silica dimers takes place, followed by trimers, tetramers and so on [46, 84, 85]. As the dissolution progresses, the rearrangement and exchange among dissolved species occur inside the structure, where the reaction of aluminium is more rapid than silicon at early stage of reaction due to a weaker bond in Al-O compared to Si-O [86]. Then, gel nucleation starts to take place with two main reaction products precipitated, consisting of cross-linked and disordered structures. In the low-calcium system with AAF, the sodium-alumina-silicate-hydrate (N-A-S-H) gels are formed, which tend to be Al-rich during early reaction process with an increase in the silicon concentration as time goes by. As for the high-calcium system with AAS, the calcium-alumina-silicate-hydrate (C-A-S-H) gels are the main reaction products [64, 84].

Blend precursor system

In terms of blend precursor system with AAFS, many studies have reported the possibility of chemical interactions within the precursors as the reaction goes on [84]. This indicates that the development of N-A-S-H and C-A-S-H gels is not independent with structural and compositional changes during the reaction process [87, 88]. Within AAFS, a proportion of Ca^{2+} are released during the dissolution of slag particles, which can potentially substitute Na^{+} or be incorporated into N-A-S-H gels to form N-C-A-S-H gels, as shown in Figure 2.1. The local co-

existences and phase transformation among N-A-S-H, C-A-S-H and N-C-A-S-H gels were suggested in AAFS, owing to a heterogeneous chemical distribution in the matrix [48, 84].

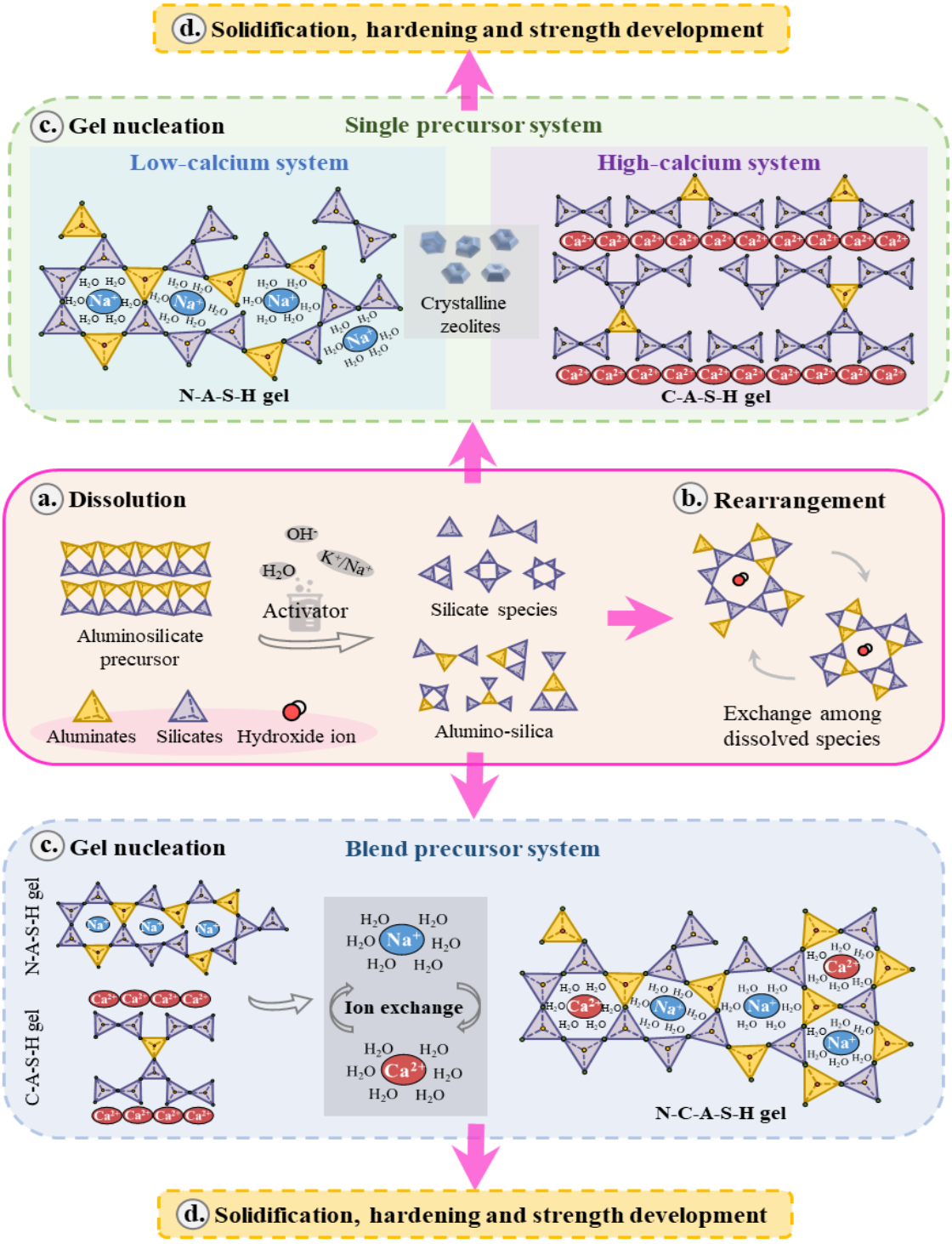

Figure 2.1. Schematic diagram of AAC reaction mechanisms (adapted from [64, 86, 90-92]).

The interaction mechanisms between the activation of different precursors have been proposed in different aspects. Firstly, the microstructural characteristics of reaction products can be modified after the inclusion of blend precursors. Compared with plain AAS, a change in lattice parameters of C-A-S-H gels is noticed after only a slight addition of fly ash [48]. On the other hand, the deceleration or acceleration on certain crystalline phases is revealed. The increase of slag addition can either depress or trigger the precipitation of zeolite-type phases, since the local formation of N-C-A-S-H from N-A-S-H gels enhances the degree of heterogeneity in amorphous phases that impedes zeolite crystallisation [48]. A further inclusion of calcium from slag can lead to phase transformation from N-C-A-S-H to C-A-S-H gels, which possibly replace alkali by its superior affinity to silicon [88, 89]. Furthermore, the spatial heterogeneity can be a crucial factor, depending on the binder ratio, dissolution kinetics of unreacted particles and local aqueous environments [48].

2.3 Multiscale microstructural characteristics of AAC

Based on the mentioned reaction mechanisms and main reaction products in AAF, AAS and AAFS, their microstructural characteristics are systematically reviewed at multiple length scales in this section, spanning from nano-scale to macro-scale. Due to the complex heterogeneous structure of AAC, four different levels are introduced in Figure 2.2 covering:

- **Level 0** (1-10 nm): solid gel particle (N-A-S-H, C-A-S-H and N-C-A-S-H)
- **Level I** (10 nm - 1 μm): gel matrix (solid gel particles + gel pores)
- **Level II** (1 μm - 100 μm): paste (unreacted particles + reaction products + pores)
- **Level III** (> 100 μm): mortar and concrete.

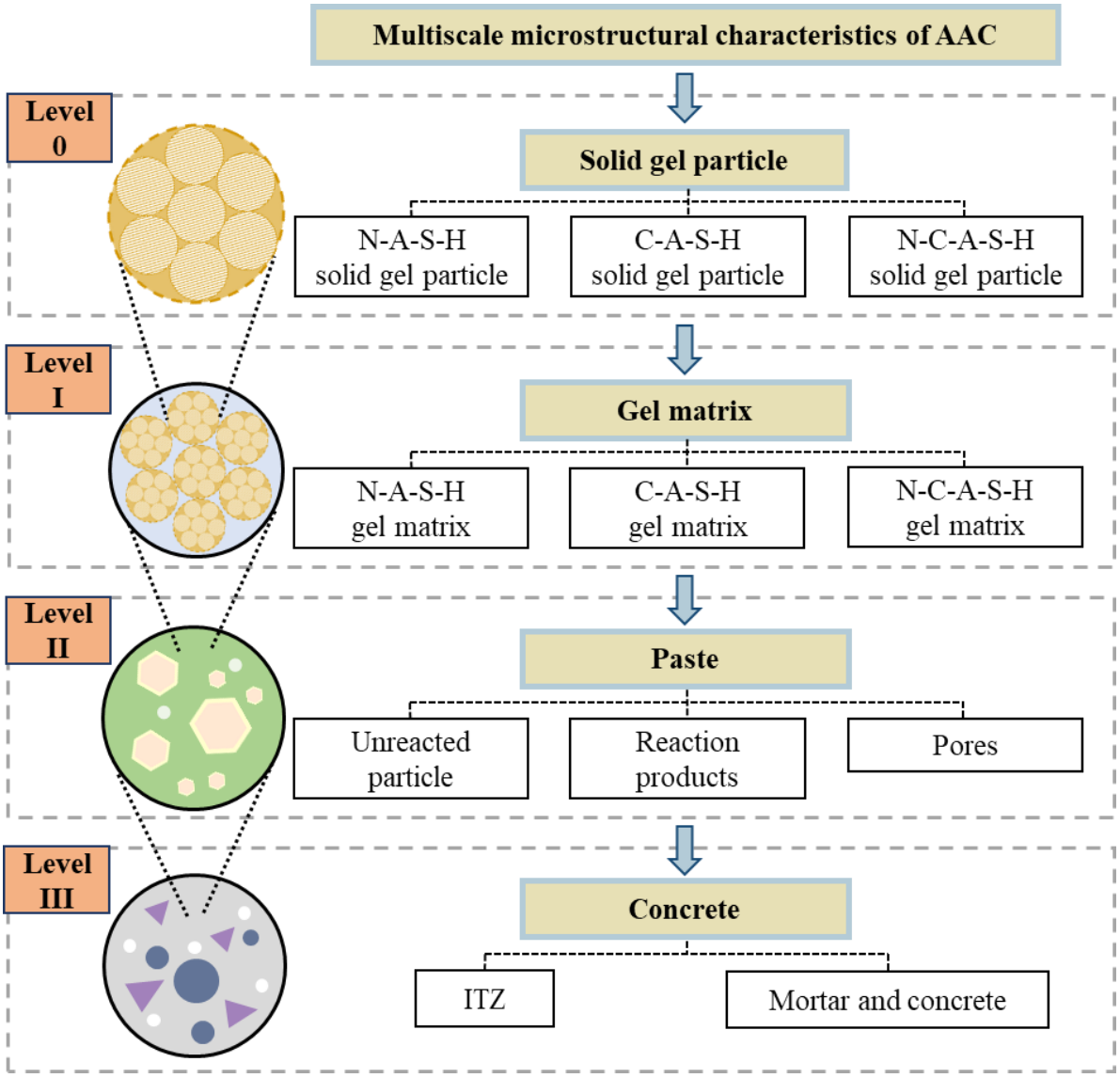

Figure 2.2. Multiscale microstructural characteristics of AAC.

2.3.1 Level 0: Solid gel particle

Level 0 delineates the nanoscale level, referring to the fundamental solid gel particle that serves as elementary component within the binder gel matrix [48, 84, 93]. The nanoscopic characterisation of three main types of solid gel particles (N-A-S-H, C-A-S-H and N-C-A-S-H) will be reviewed in this section with respect to microstructure and micromechanical properties.

N-A-S-H solid gel particle

As the dominant reaction products in AAF and AAMK, N-A-S-H gels have highly cross-linked structures with SiO_4 and AlO_4 tetrahedra connected by shared O atoms, as illustrated in Figure 2.3(a) [83]. The cross-links among chains provide sufficient cavities for the accommodation of alkali cations (Na^+), mitigating the charge deficiency resulting from the substitution of silica (Si^{4+}) with aluminium (Al^{3+}). N-A-S-H gels consist of a significant amount of Q^4(mAl) sites, which present in 3D networks with a silicon tetrahedron connecting to other three tetrahedrons. At the start of activation process, the formation of N-A-S-H gels is initiated by an Al-rich phase, where Si tetrahedra becomes coordinated with Al tetrahedra to form structures like Q^4(4Al) [84]. This preference for cross-linking Al atoms over Si atoms predominates at this moment. As the curing time increases, the structure would change from Al-rich N-A-S-H with Si/Al ratio of around 1 to Si-rich N-A-S-H with a roughly doubled Si/Al ratio [94, 95]. The generation of Si-rich N-A-S-H gels is triggered by the condensation reactions between Si-OH groups, stabilising the nanostructure with high cross-linking of Q^4(3Al) and Q^4(2Al) sites. Figure 2.3(b) displays the N-A-S-H models (Si/Al ratio ≈ 1.5) with rising degree of disorder from crystalline to defective and amorphous structures [96]. Regarding the internal bond angle of O-Si-O, the tetrahedra in N-A-S-H gels shows limited distortion compared to the crystalline structure [97]. The external bond angle of T-O-T can vary between 120° and 180° in polymerised SiO_2 and AlO_2 [96, 98, 99].

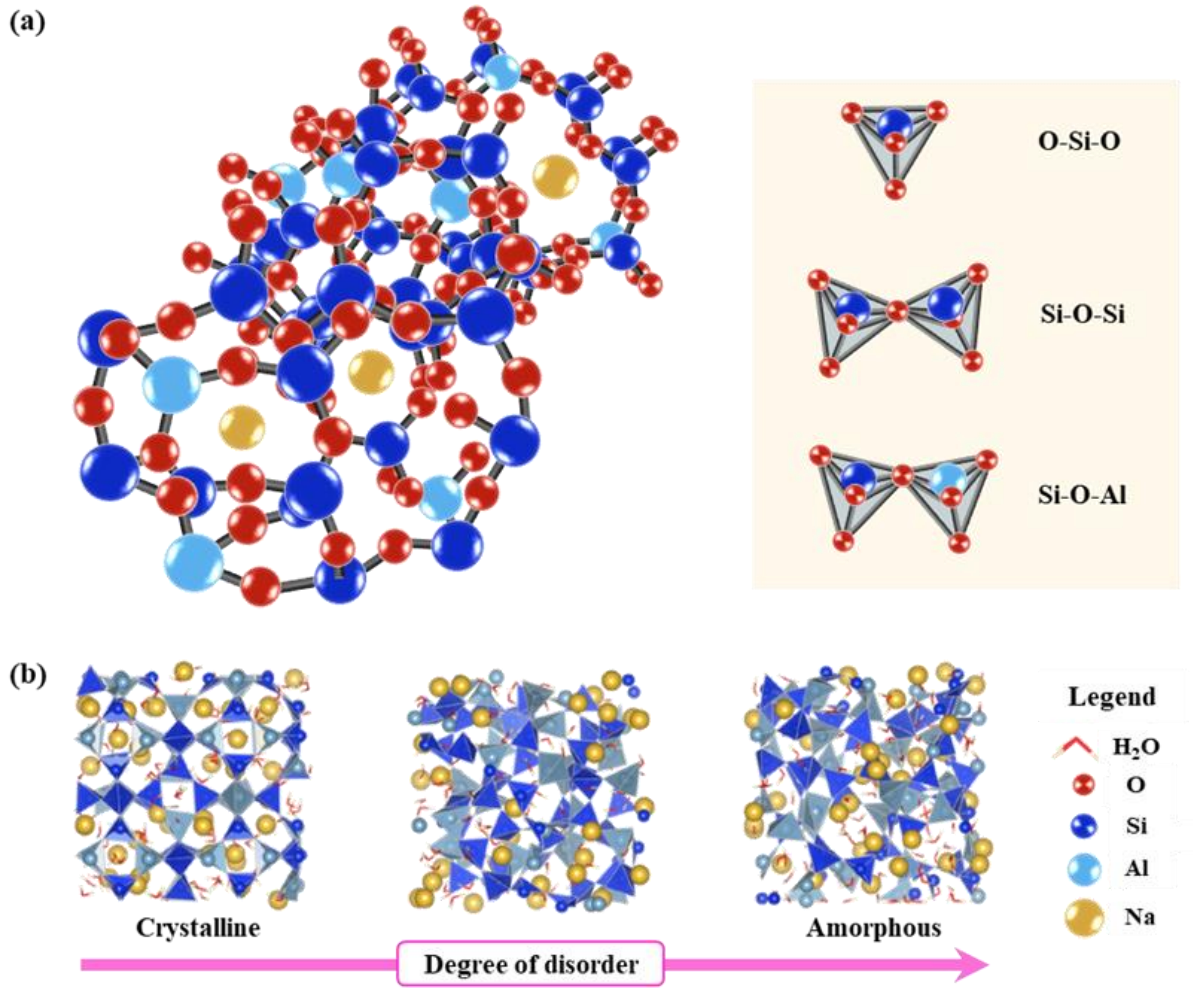

Figure 2.3. Nanostructure of N-A-S-H regarding (a) 3D view and (b) simulation from crystalline to amorphous N-A-S-H with Si/Al ≈ 1.5 (adapted from [96, 100]).

The gel development can be described by the change of reaction degree in terms of curing time. Consequently, the volumetric model for alkaline activation can be built to track the change of volume fractions of solid gel particles. Figure 2.4(a) demonstrates the volume changes of solid gel particles in AAF and AAMK [101]. Compared with AAF, AAMK exhibits a faster reaction, leading to a more rapid formation of solid gel particles by approximately 32.3%, while it contains a 26.6% higher open porosity based on the proposed model [101, 102]. The N-A-S-H gel matrix and gel pores will be further discussed at the next level in the following section.

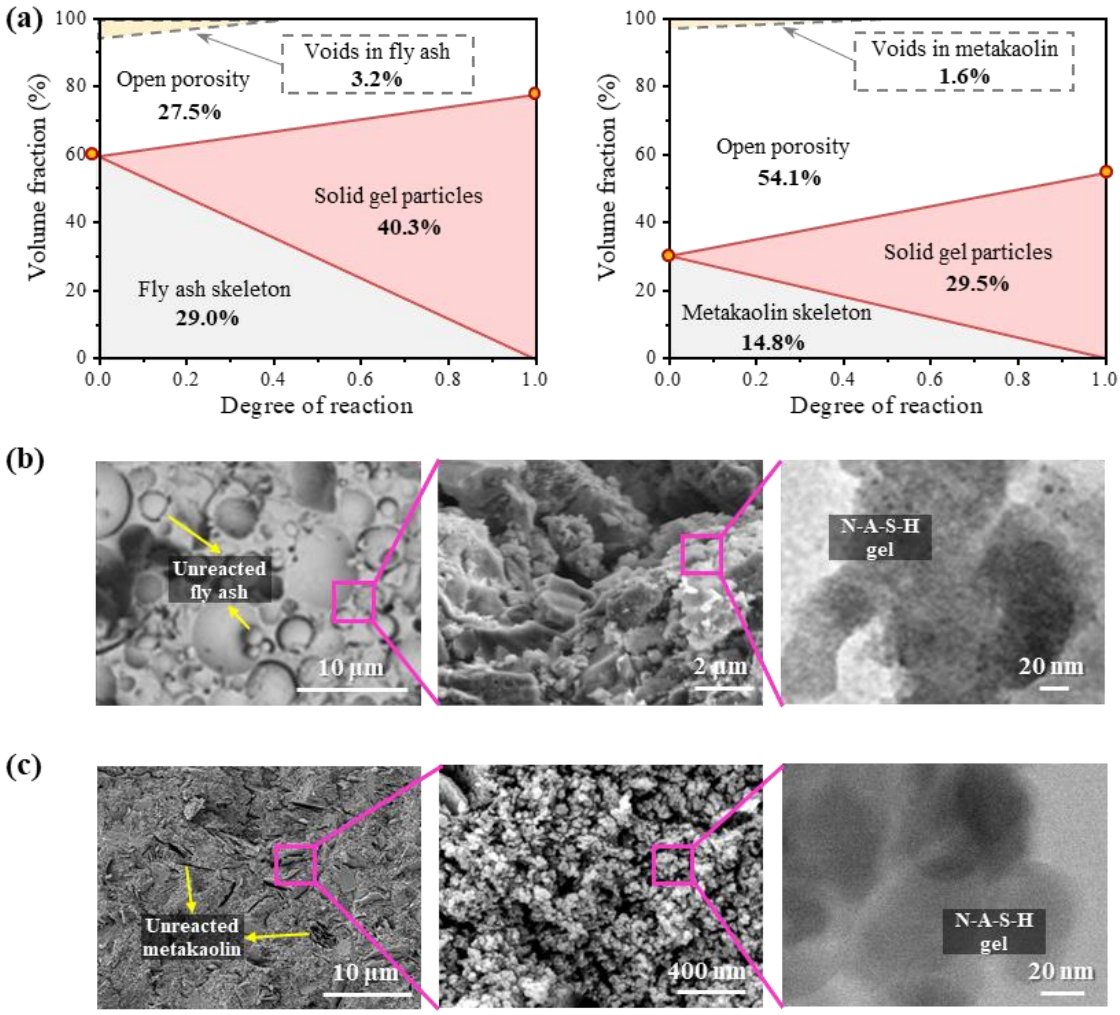

Figure 2.4. Comparison of nanostructures in terms of (a) Volumetric model of alkaline activation in AAF and AAMK [101], (b) SEM and TEM images of N-A-S-H gels in AAF [22, 103-105], and (c) SEM and TEM images of N-A-S-H gels in AAMK [106].

C-A-S-H solid gel particle

The nanostructure of C-A-S-H has been described by analogy according to the structure of aluminium-containing minerals resembling disordered tobermorite-like [107-111]. This structure is formed of silicate chains inter-linked by layers of CaO. Figure 2.5(a) introduces the nanostructure of C-A-S-H, which contains CaO layers, interlayer region and a so-called dreierketten arrangement with SiO_4 tetrahedra chains. The schematic illustration of Q^n in an interconnected silica structure is given in Figure 2.5(b). As for the interlayer region, both alkali cations (Ca^+ and Na^+) and chemically-bonded H_2O are enclosed within the gel structure [84].

Here, alkali cations play a crucial role in neutralising the overall negative charge deduced by the substitution of Si^{4+} by Al^{3+} within the tetrahedral chain sites. Also, the nanostructure of C-A-S-H can be highly dependent on Ca/Si ratio [107]. For low Ca/Si ratios, aluminium substitutions are prone to be tetrahedrally coordinated by silica sites, owing to tetrahedral replacement in the silica chains of C-S-H gel [112, 113]. Whereas, high Ca/Si ratios can result in random distribution of aluminium due to the substitution in the interlayer region, on the particle surfaces or other reaction products [107, 114, 115]. Aluminium substitutions would therefore occur in octahedrally coordinated sites alongside hints of pentahedral coordination (with a ratio of octahedral/pentahedral coordination of around 3.5) [116, 117].

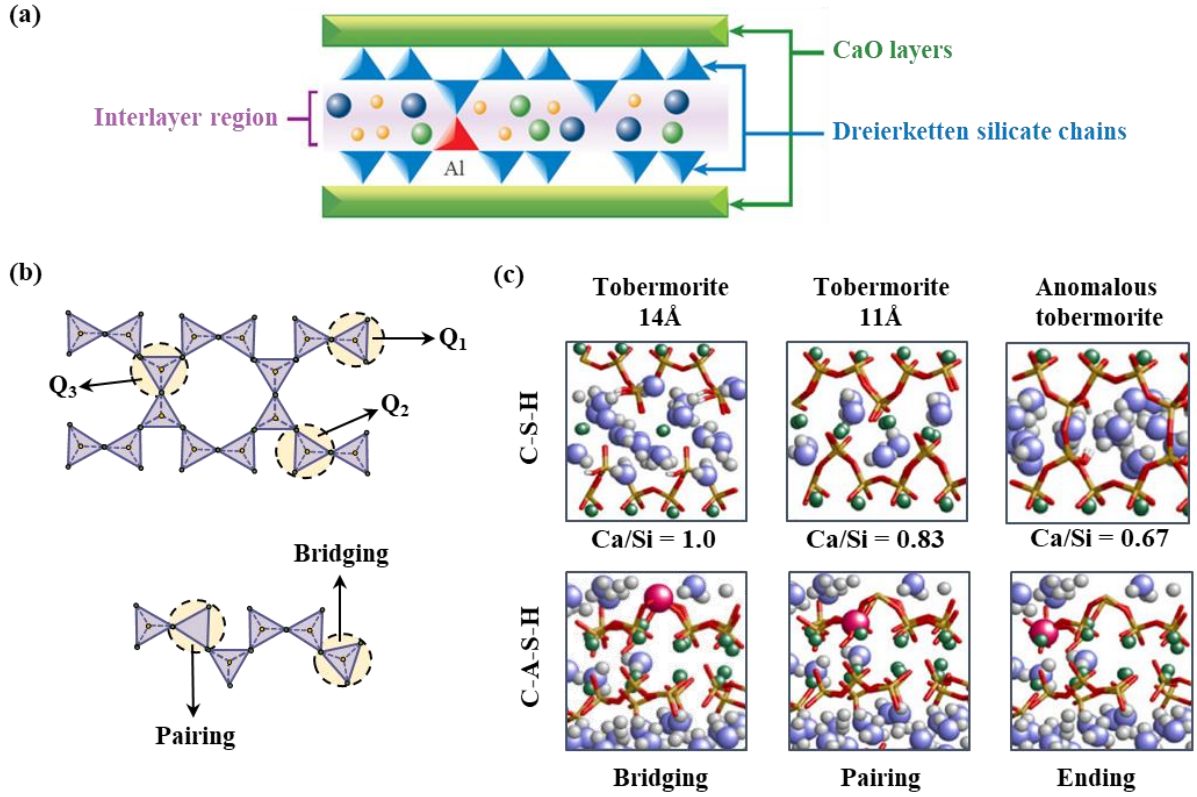

Figure 2.5. Nanostructure of C-A-S-H: (a) Overall tobermorite-like structure, (b) Schematic illustration of Q^n in a silica chain and possible substitution positions for aluminium atom, and (c) Structure of tobermorites in C-S-H and C-A-S-H with aluminium atom in the bridging, pairing and ending sites of a silica chain. (adapted from [64, 107]).

Different substitution positions of aluminium atoms have been proposed in C-A-S-H system, including bridging, pairing and ending sites, as depicted in Figure 2.5(c). In the context of

chemical stability, the substitution of Si^{4+} by Al^{3+} significantly reduces the Gibbs free energy, leaving around 8 eV difference from the embedding energy of Si^{4+} [107]. Hence, there is a pronounced preference for aluminium occupancy in the bridging sites, attributing to energy disparities between distinct polymorphs and thermal energy [107, 118, 119]. The incorporation of Al^{3+} into the bridging SiO_4 tetrahedra leads to alterations in the Si-Al skeleton and the interlayer H_2O within the C-A-S-H gel [83]. This process enhances the crystalline arrangement and cross-linking degree by transitioning the layered C-S-H structure into a cross-linked C-A-S-H structure [84, 120-122].

N-C-A-S-H solid gel particle

With the incorporation of fly ash and slag, their different dissolutions and reaction mechanisms can trigger the interaction between different precursors in blend precursor system [46]. Especially, free Ca^{2+} can modify N-A-S-H gels during the reaction process by partially replacing Na^+, attributing to the strong polarising power of the aqueous Ca^{2+} relative to Na^+ [46, 84, 88]. This results in the formation of N-C-A-S-H gel, as illustrated in Figure 2.6(a). Owing to the strong binding of Ca within the structure of C-A-S-H, the influence of Na+ on the formation of N-C-A-S-H is relatively insignificant [88]. It may be difficult to distort Ca^{2+} by the presence of Na^+ due to the difference in polarising power between the two [123, 124].

Following this rearrangement process, the N-C-A-S-H gel exhibits mineral characteristics that bridge the gap between N-A-S-H and C-A-S-H gels. This means that it can maintain the inherent 3D aluminosilicate framework structure while tending to possess a composition more akin to that of C-A-S-H gel. However, the reorganisation and formation of N-C-A-S-H can strongly depend on different factors such as calcium content and pH conditions within the gel structure. Figure 2.6(c) demonstrates the transmission electron microscope (TEM) images of the gel morphologies under high-, medium-, and low-calcium environments. With high calcium content (CaO/SiO_2=3.2; SiO_2/Al_2O_3=2), a more lime-rich cluster can be observed, which indicates a combination of crystalline and amorphous phases. Under the medium-calcium condition, only a single phase of C-A-S-H gel is captured, which shows various clusters without the appearance of crystalline. As for the low-calcium environment (CaO/SiO_2=0.24; SiO_2/Al_2O_3=3), N-C-A-S-H gel can be identified with more globular-like morphology and relatively smaller angularity compared to C-A-S-H gel [39, 88].

In terms of pH conditions, a pseudo phase diagram has been reported to illustrate the stability and compatibility of N-A-S-H gel structure in terms of pH values, as displayed in Figure 2.6(b). The critical pH value of 12 is corresponding to the transition point between C-A-S-H and N-C-A-S-H pH measurements [88, 125]. When the pH condition is below 12, N-A-S-H would be either stable or accepting the ion exchange by Ca to form N-C-A-S-H. A full exchange might also appear to form C-A-S-H, whereas the gel would remain in a 3D aluminosilicate structure instead of 2D [126]. When the pH value is around 12, the gel would degrade to C-A-S-H with the presence of free Ca [88].

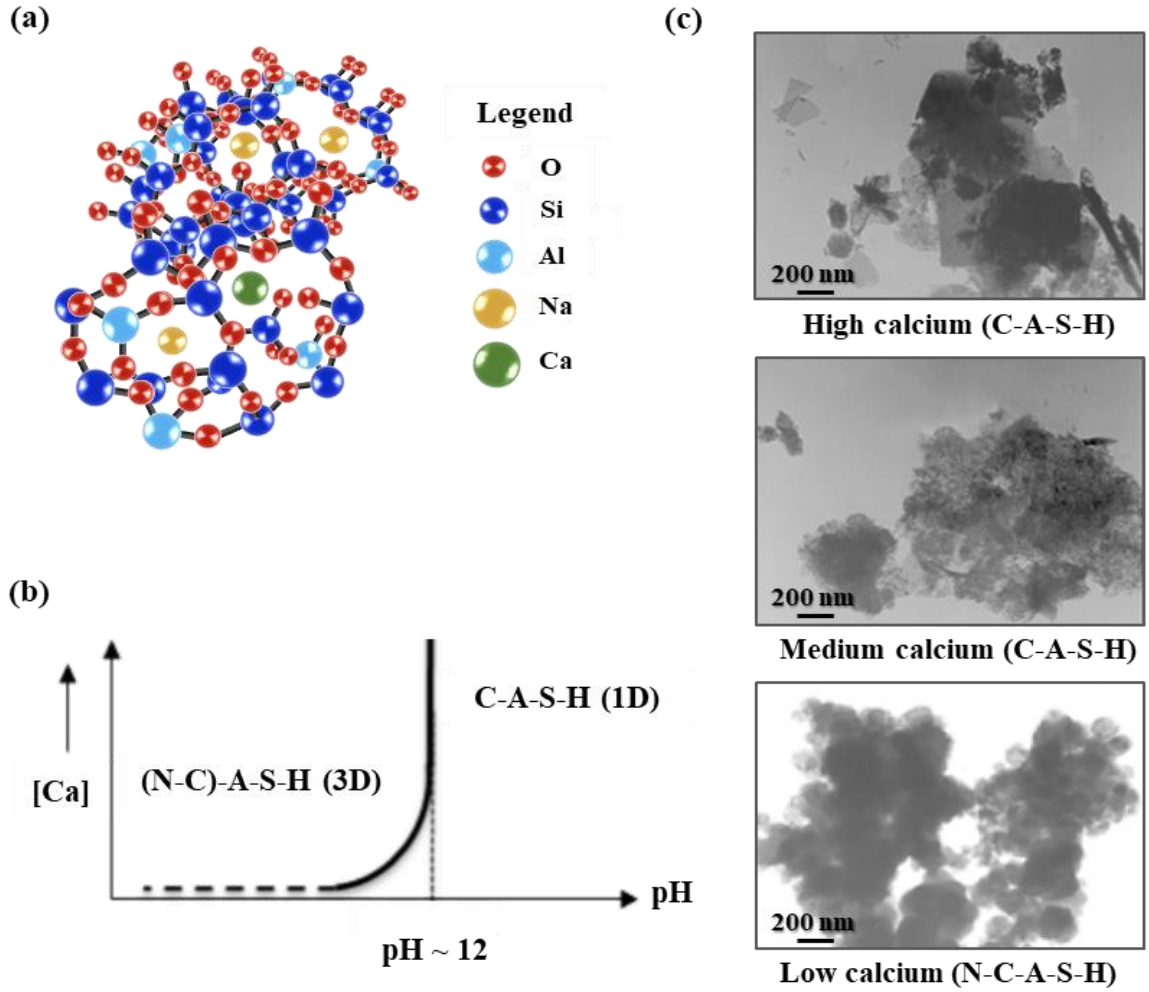

Figure 2.6. Nanostructure of N-C-A-S-H: (a) Overall 3D structure, (b) Schematic illustration of the stability and degradation of N-A-S-H with pH, and (c) Morphologies of C-A-S-H and N-C-A-S-H gels under different calcium conditions detected using TEM [88].

2.3.2 Level I: Gel matrix

At Level I, the gel matrix is agglomerated by the solid gel particles and gel pores. The agglomeration process of N-A-S-H and C-A-S-H solid gel particles is commonly described by simplifying agglomeration model of C-S-H gel particles, which is recognised as the colloidal model [84, 127-129]. The tobermorite-like solid phases mentioned at Level 0 are assumed as the fundamental units, which are also identified as the basic building blocks [84]. The globules are then formed by packing of these blocks [126]. After further clustering of the globules, gel matrix is formed, as illustrated in Figure 2.7. Herein, the inherent properties of 'globules' (i.e. solid gel particles) and gel pores (associated with the packing density of 'globules') will be discussed in depth based on the characterisation of nanostructure and micromechanical properties of different gel matrix.

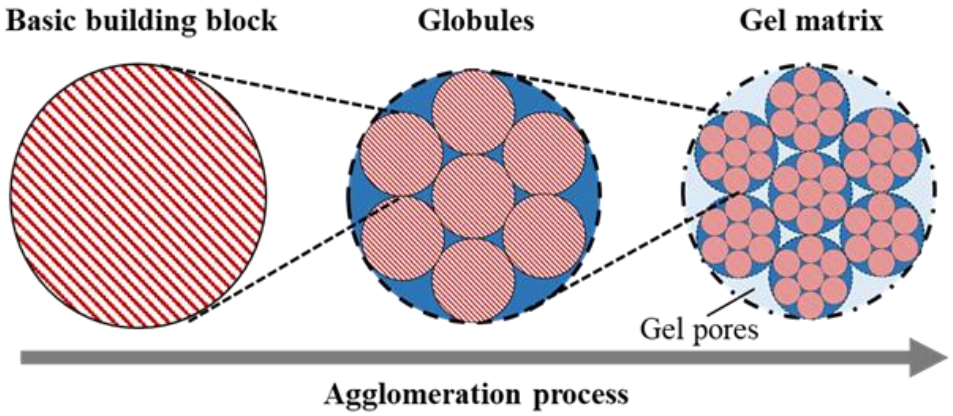

Figure 2.7. Agglomeration of gel matrix [127].

N-A-S-H gel matrix

The N-A-S-H gel matrix consists of primary globular polymeric entities with diameters of 0.8-2.0 nm, which are packed in a dense structure based on hydrolysis-polycondensation process [128, 130, 131]. A 3D network of aluminosilicates can be formed during the process, comprising Si-O-Si and Si-O-Al bonds in a highly cross-linked structure [131-134]. These bond formations coincide with the release of water into larger pores, facilitating the agglomeration of monomeric species into polymeric clusters, which subsequently develop into particles and consequently form gels [84]. It was mentioned that N-A-S-H gels are contingent upon the degree of reversibility [65]. When the polycondensation process approaches near irreversibility,

it results in the formation of a space-filling gel, which eventually undergoes interconnection to create a continuous gel structure [102]. If the polycondensation rate exceeds the rate of bond breaking, the gels can develop with the inclusion of new monomers [135]. As such, reorganisation takes place in the N-A-S-H gel, which can restructure the gel into a more stable state. The morphology of the gel can be observed in Figure 2.4 (b) and (c) based on scanning electron microscopy (SEM) and transmission electron microscopy (TEM) images.

The nature of N-A-S-H gel nanostructure can be dependent on different factors, including curing time, temperature, and alkaline activator type [94, 126, 136, 137]. Figure 2.8 demonstrates the change of N-A-S-H gel nanostructure based on various curing conditions and activators. In general, longer curing time can benefit the formation of silica-rich products, favouring the strength development in geopolymer matrix. At the curing time of 3 h in Figure 2.8(a), the peaks ranging from around -92.1 to -112.3 ppm correspond to the presence of Q^4(nAl) sites, which are recognised as the N-A-S-H gels with a 3D structure containing Si in a variety of environments [126]. The dominance of Q^4 sites at 3 h indicates the formation of various Si-O-Al connections in aluminosilicate prepolymer structures, which can be attributed to the dissolution of active aluminate ions together with silicate ions [138]. With the increase of curing time, the spectral peak of ^{29}Si nuclear magnetic resonance (NMR) tends to shift positively with a focus on Q^4 sites. The presence of Q^1 and Q^2 at approximately -78 and -83 ppm can be ascribed to the gradual replacement of Si-O by Al-O during the polycondensation when increasing the curing time [123, 138]. As the reaction progresses to 24 h, the N-A-S-H gel becomes Si-richer, in which the determined volume fractions of Q^4(4Al), Q^4(3Al), Q^4(2Al) and Q^4(1Al) are 14.3%, 18.3%, 18.9% and 13.9%, respectively (Figure 2.8(b)). This indicates that the extension of curing time can lead to the dissolution of active silicate and give rise to the silicate content, which promotes the strength development in matrix [138-140].

Figure 2.8(c) shows the ^{29}Si NMR patterns of AAF cured at 40, 60 and 80 °C. When the curing temperature increases from 40 to 80 °C, there is a shift of the major spectral peak associated with Q^4(3Al) from -92.1 to -91.4 ppm. The heat curing was found to favour the dissociation of the -O-Si-O- and -O-Si-O-Al-O- bonds in fly ash and thus promote the pozzolanic reaction [138]. The presence of peaks at around -103 to -108 ppm was found after 80 °C curing. These peaks corresponded to the Q^4(2Al) and Q^4(1Al) sites, which are identified as Si-rich N-A-S-H gels in comparison with the Q^4(3Al) site (Al-rich N-A-S-H gels) [39, 141].

This suggests the formation and transformation of short-chain N-A-S-H gels from Al-rich to Si-rich, triggered by the curing at elevated temperatures up to 80 °C [138].

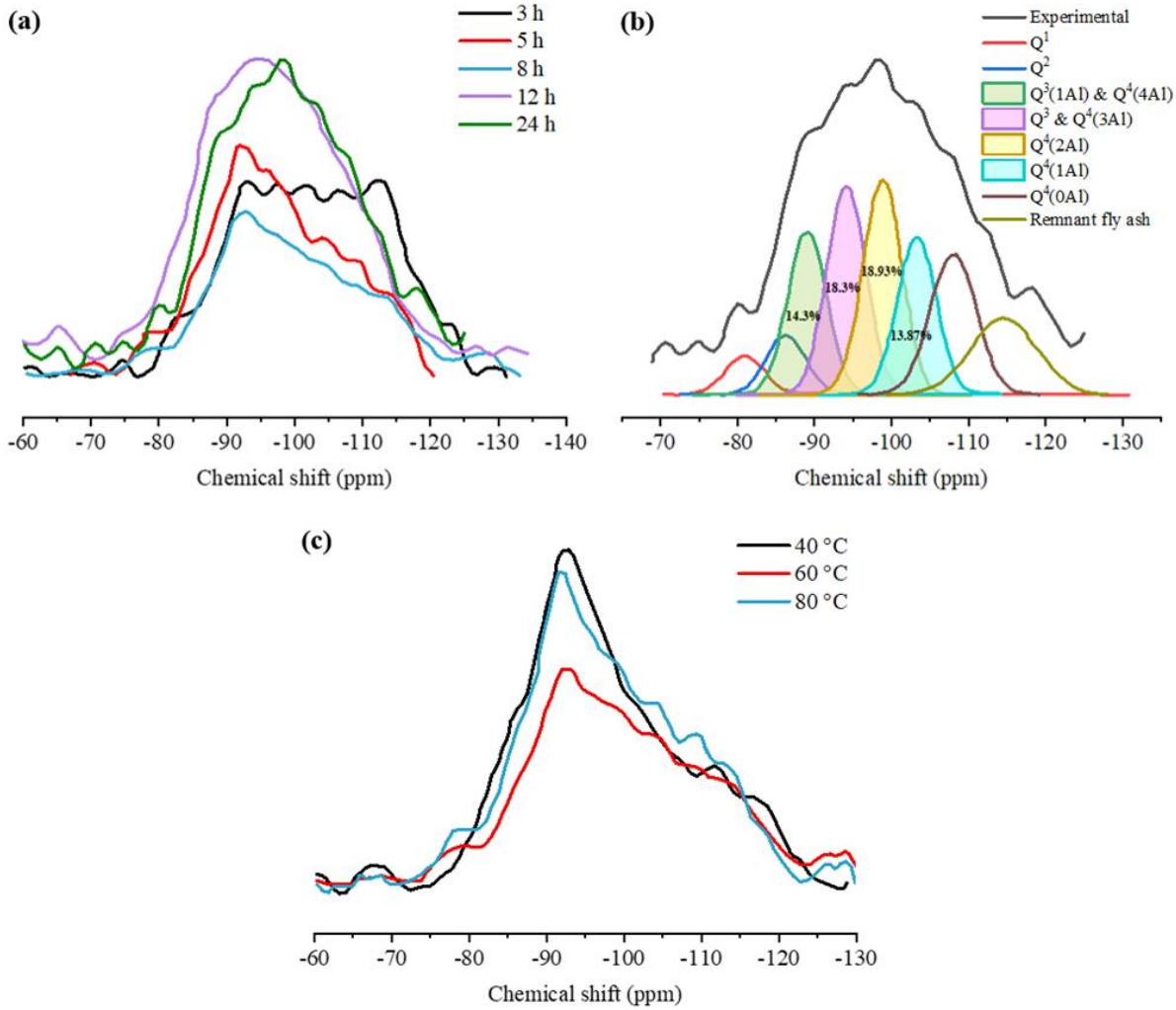

Figure 2.8. ^{29}Si NMR spectra of AAF against (a) curing time with (b) the deconvolution, and (c) curing temperature (data from [138, 142]).

C-A-S-H gel matrix

Compared with the C-S-H gel formed in PC paste, the C-A-S-H gel was found to maintain a lower Ca/Si ratio of around 0.9 to 1.2 [126]. The nanostructure of C-A-S-H can be dependent on the Al/Si ratio within the gel. Figure 2.9 depicts the effect of incorporating aluminium on the structure of C-A-S-H based on the NMR results and TEM images. In the C-S-H gel, the ^{29}Si NMR pattern is deconvolved with respect to Q^1, Q^2_p and Q^2_b (Figure 2.9(a)), which respectively

refers to the terminal silicate tetrahedra and Q^2 with the pairing and bridging positions, as mentioned previously [143-145].

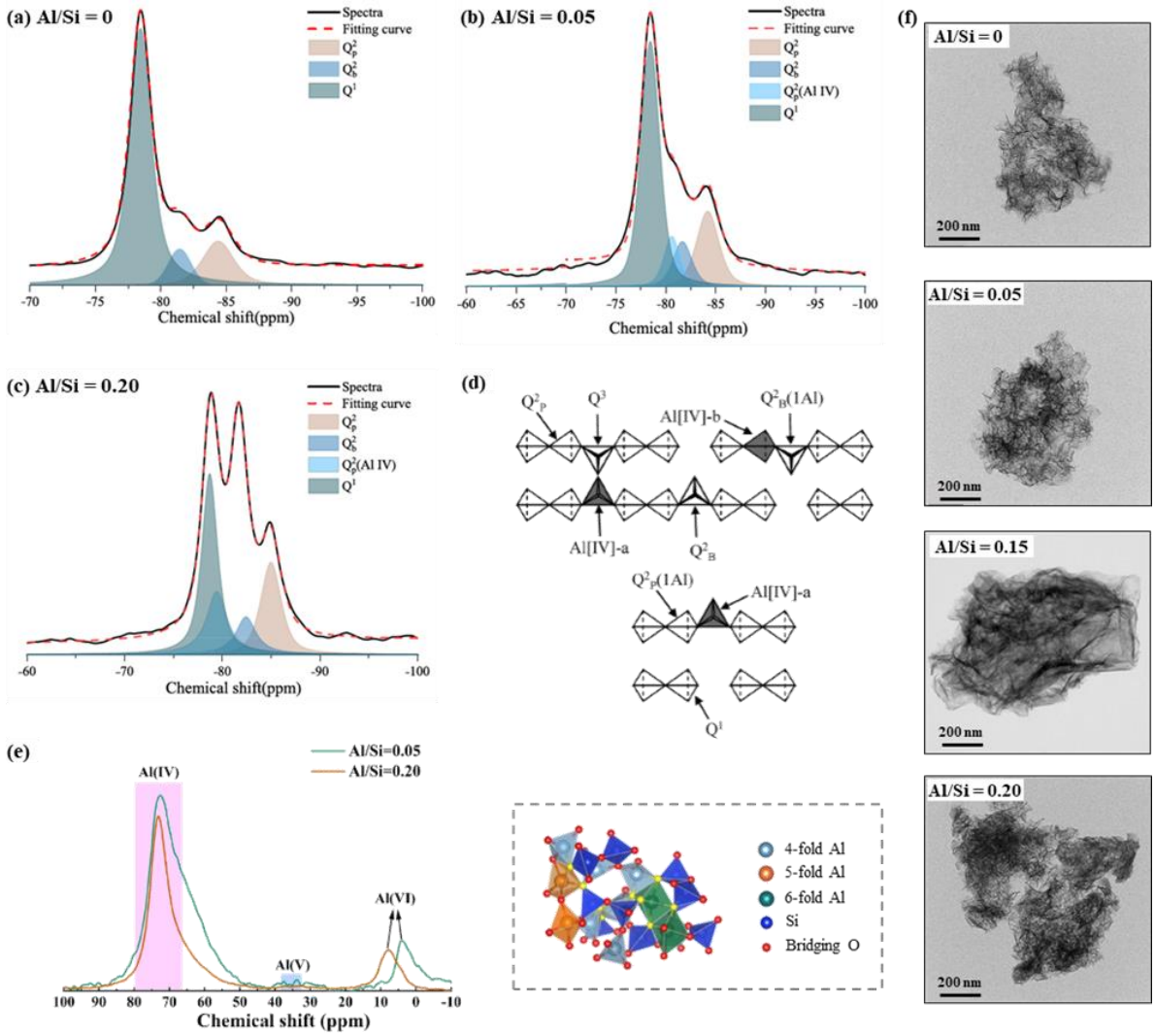

Figure 2.9. ^{29}Si NMR spectra of (a) C-S-H and C-A-S-H with (b) Al/Si=0.05 and (c) Al/Si=0.20, with (d) deconvolution based on alumino-silicate chains in C-A-S-H; (e) ^{27}Al NMR spectra of C-A-S-H with different Al/Si ratios and (f) Corresponding TEM images (adapted from [143, 145, 149, 150]).

Obviously, Q^1 dominates the structure when Al/Si ratio is 0, which takes up 75.6% of the gel. With the increase of Al/Si ratio to form C-A-S-H gels, as shown in Figure 2.9(b-c), the deconvolution of them reveals the existence of Q^2_p(Al IV), corresponding to the pairing silicate tetrahedron with the bridging Al (IV) [146-148]. This can be ascribed to the incorporation of aluminium, which occupies bridging sites and transfer the initial Q^1 into new Q^2_p(Al IV) sites

[114, 143]. As a result, the silicate chain can be elongated with the increased fraction of Q^2 by 33.4% and the reduction of Q^1 down to 42.4% when the Al/Si ratio reaches 0.20 [143, 147]. Moreover, the rise of Al/Si ratio from 0.05 to 0.20 can result in the increasing amount of Q^2_p(Al IV) by 24.1%, implying that the aluminium is mainly occurred as IV-fold coordinated. Different structures in the alumino-silicate chains within C-A-S-H gels are illustrated in Figure 2.9(d).

Other than the IV-fold coordinated aluminium (Al(IV)), there are also V-fold (Al(V)) and VI-fold (Al(VI)) coordinated signals, which can be associated with the dissolved aluminium in C-A-S-H interlayers and the third aluminate hydrate (i.e. an Al-rich phase precipitated on the surface of C-A-S-H gel), respectively [117, 145, 151]. The spatial impression of Al(IV), Al(V) and Al(VI) is schematically illustrated together with the ^{27}Al NMR spectra of C-A-S-H at Al/Si ratios of 0.05 and 0.20 shown in Figure 2.9(e). At both Al/Si ratios, the predominant peak represents Al(IV), which may be charge-balanced by Ca^{2+}(presented as $Al(IV)_{-a}$ in Figure 2.9(d)) and Al(V) and/or Al(VI) (denoted as $Al(IV)_{-b}$) [149]. As for the nanomorphology, Figure 2.9(f) presents the change of C-A-S-H gels with the increase of Si/Al ratio. A foil-like shape can be observed in all specimens, which tends to become darker, denser and more compact when rising Al/Si ratio [129, 143, 145, 152, 153]. This indicates that the substitution of Si by Al can potentially modify the charge distribution in globules and give rise to more significant attraction between them [129, 143].

Two types of packing referring to low-density and high-density were proposed to describe C-A-S-H gels [84, 127, 154, 155]. The low-density packing configuration bears resemblance to the random close packing, while the high-density packing configuration aligns closely with the face-centred cubic lattice packing arrangement [84, 156]. C-A-S-H gels exhibit diverse ranges of packing density, spanning from 0.63 to 0.79, and gel porosity ranging from 21% to 37% [84, 154]. These characteristics are influenced by the spatial availability for C-A-S-H gel packing, with denser packing approached to the precursor particles and looser packing in regions further from them [154, 157, 158]. As for the aforementioned nature of activator, the activator type can modify the structure of C-A-S-H gels. In particular, C-A-S-H gels with SH exhibit a comparatively higher gel porosity ranging from 21% to 37%, whereas those activated by SS demonstrate a lower value from 21% to 29% [154].

N-C-A-S-H gel matrix

As the formation of N-C-A-S-H gels follows the aforementioned process, the agglomeration of N-C-A-S-H gel particles should be similar to N-A-S-H [46, 88, 128]. However, the polarising effect of Ca^{2+} can induce the rearrangement of the aluminosilicate structure by distorting the Si-O-Al bonds, resulting in the formation of Si-O-Ca bonds [89]. This structural modification leads to less polymerised structures in N-C-A-S-H gel matrix with a decreasing degree of cross-linking, which can finally result in a comparable structure to C-A-S-H gels [88]. Figure 2.10 presents the evolution of nanostructure in AAFS from 1 to 28 d. A negative shift of the broad peak from -84.2 to -85.7 ppm together with the change of the broad band centre from -107.2 to -105.9 ppm denotes the further polymerisation with a higher degree of cross-linking of gels over time [39]. As N-C-A-S-H gels are associated with Q^3(1Al) and Q^4(4Al) sites located at around -88 ppm, the increase of curing ages can lead to a higher composition of N-C-A-S-H gels from around 11.1% at 1 d to 14.6% at 28 d [46, 141].

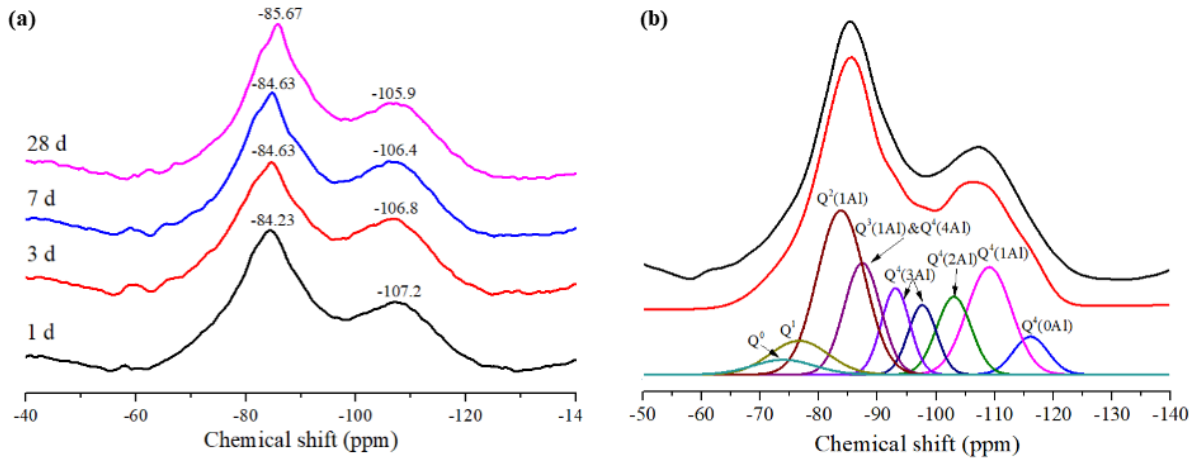

Figure 2.10. ^{29}Si NMR spectra of AAFS at different curing ages from 1 to 28 d with (b) the deconvolution results on 28 d [39].

2.3.3 Level II: Paste

Level II refers to the paste level, which is composed of unreacted precursors, reaction products (i.e. gel matrix in Level I) and pores. At this level, the unreacted precursors including fly ash and slag are reviewed and discussed in terms of the dissolution and reaction mechanisms. The evolution of pore structures and reaction products is also reviewed at paste level.

Unreacted particles

It is recognised that the reaction of precursor that leads to the formation of reaction products is essential to the determination of multiscale properties of AAC [46, 87, 159]. The morphology and chemical compositions of precursors such as fly ash and slag have been extensively investigated through SEM and EDS tests [48, 160-162]. The distribution and microstructural evolution of these particles can be heterogeneous and highly dependent on their particle sizes, precursor systems (single or blend system), activator types, curing ages and local alkaline environment [43, 84, 133, 163, 164]. Figure 2.11 demonstrates the particle dissolution and reaction of fly ash and slag particles in AAFS paste at different curing ages by XCT, along with the corresponding SEM and BSEM images. The time-dependent evolution of particle structure can be directly observed.

For both fly ash and slag particles, the reaction process includes the dissolution of particle and the development of surrounding matrix [43]. In the unreacted fly ash particle, the dissolution occurs with the rupture of Si-O-Si and Al-O-Al bonds, which exhibits inconsistent degree of reaction in different directions with an increase of irregularity from a spherical to more angular shape as time goes by. Due to the heterogeneity of fly ash particles, in which the distribution of inert crystal phases and reactive amorphous phases can be random, the parts that contain more amorphous phases are prone to react faster than the rest of particles [43, 165]. The formation and precipitation of reaction products are localised in the dissolved area of fly ash particles, which can be identified as inner and outer products based on the relative position to the initial particle boundary [84]. The initial formation of inner products has been found to physically impede the diffusion of ions, which can be difficult to penetrate from outside the particle into N-A-S-H gels as the reaction proceeds [43, 128, 163].

As for the unreacted slag particle, it shows a less spherical shape compared to fly ash in Figure 2.11. The dissolution of slag particles occurs by breaking the Ca-O and Si-O-Si bonds. Similar to fly ash, the dissolution of slag exhibits inhomogeneous characteristics with increasing irregularity of the remnant particle from 1 to 28 d. The formation of C-A-S-H gels can be further observed with the increase of curing ages, acting as a physical barrier that surrounds the remained core particles and thereby slows down the further reaction process when approaching 28 d [84, 166]. It is worth noting that in a blend precursor system like AAFS, the interaction between fly ash and slag particles can also be crucial to the microstructure evolution,

since different ions are dissolved from these particles (i.e. Si and Al from fly ash; Ca, Si and Al ions from slag) [43, 48, 162]. The interaction mechanisms between both particles were characterised in two stages: the early stage from 1 to 3 d and later stage from 7 to 28 d. No apparent interaction between fly ash and slag particles was detected during the early stage, whereas the diffusion of Ca^{2+} had a pronounced effect on accelerating the formation of C-A-S-H and N-A-S-H gels. It can also trigger the formation of hybrid gels as Si ions near fly ash particles would prefer the reaction with Ca^{2+} to form N-C-A-S-H gels [43, 162].

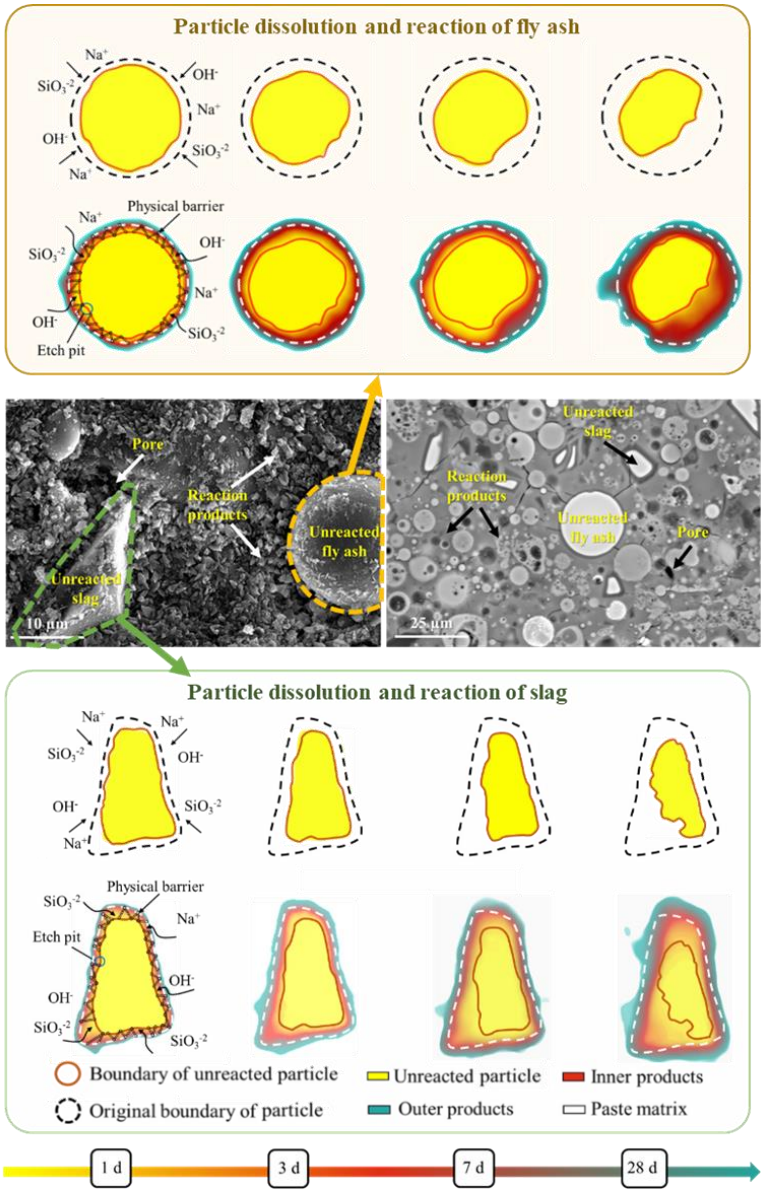

Figure 2.11. Dissolution of fly ash and slag and formation of reaction products in AAFS (adapted from [43, 84]).

Reaction products

The microstructure of reaction products in AAC can be affected by different factors such as activator type, curing time and slag content, which are generally characterised using SEM and EDS techniques. The chemical compositions of reactions products can be analysed using the ternary CaO-SiO_2-Al_2O_3 and SiO_2-Al_2O_3-Na_2O diagrams. Figure 2.12 illustrates the effect of slag content and alkaline activator on the chemical compositions of reaction products. The mixture of reaction products including C-A-S-H, N-A-S-H and N-C-A-S-H gels with other minor phases can be detected. For N-A-S-H gels, the Al/Si ratio of Si-rich N-A-S-H gels is close to 0.5, whereas Al-rich N-A-S-H gels may approach an Al/Si ratio of more than 2 depending on the compositions [167]. The N-A-S-H-rich region is commonly identified with the Al/Si ratio ranging from 0.08 to 0.5 and Ca/Si ratio of 0-0.3 [48, 88]. In terms of C-A-S-H gels, they are characterised at the region with the Ca/Si ratio varying roughly between 0.67 and 3, as shown in Figure 2.12(a). Additionally, the hybrid N-C-A-S-H gel was segmented into two different types, which includes low-calcium substituted N-(C)-A-S-H gel from the reaction of fly ash and C-(N)-A-S-H gel with low sodium content formed by the activation of slag [167]. The Ca/Si ratio of N-(C)-A-S-H gels was reported to locate within the range of around 0.14-0.33, while C-(N)-A-S-H gels tend to have a higher Ca/Si ratio of approximately 0.45-10 [46, 88, 124, 168, 169].

Figure 2.12(b-d) presents the influence of alkaline activators on the compositional changes within the paste [48]. Compared with AAFS activated by the combination of sodium hydroxide and sodium silicate, the specimens activated by sodium hydroxide exhibit relatively higher Ca/Si and Al/Si ratios with more inhomogeneous chemical distribution. This implies that increasing amount SiO_2 may depress the precipitation of zeolite crystal and preferentially trigger the formation of N-C-A-S-H instead of C-A-S-H [46, 48]. The statistical distribution of Ca/Si and Al/Si ratios based on the EDS results is shown in Figure 2.12(e-f), indicating a more pronounced effect of slag content on the chemical compositions of binder gels in AAFS in comparison with the activators [48]. With the incorporation of slag from 0 to 80%, the chemical composition of reaction products moves from low-calcium towards high-calcium region, inferring the change of binder gel contribution from N-A-S-H-rich to C-A-S-H-rich in the blend precursor system. As per the findings on different binder gel matrix at Level I, the phase

transformation at paste level can be quantified in terms of change of volume fractions in binder gels.

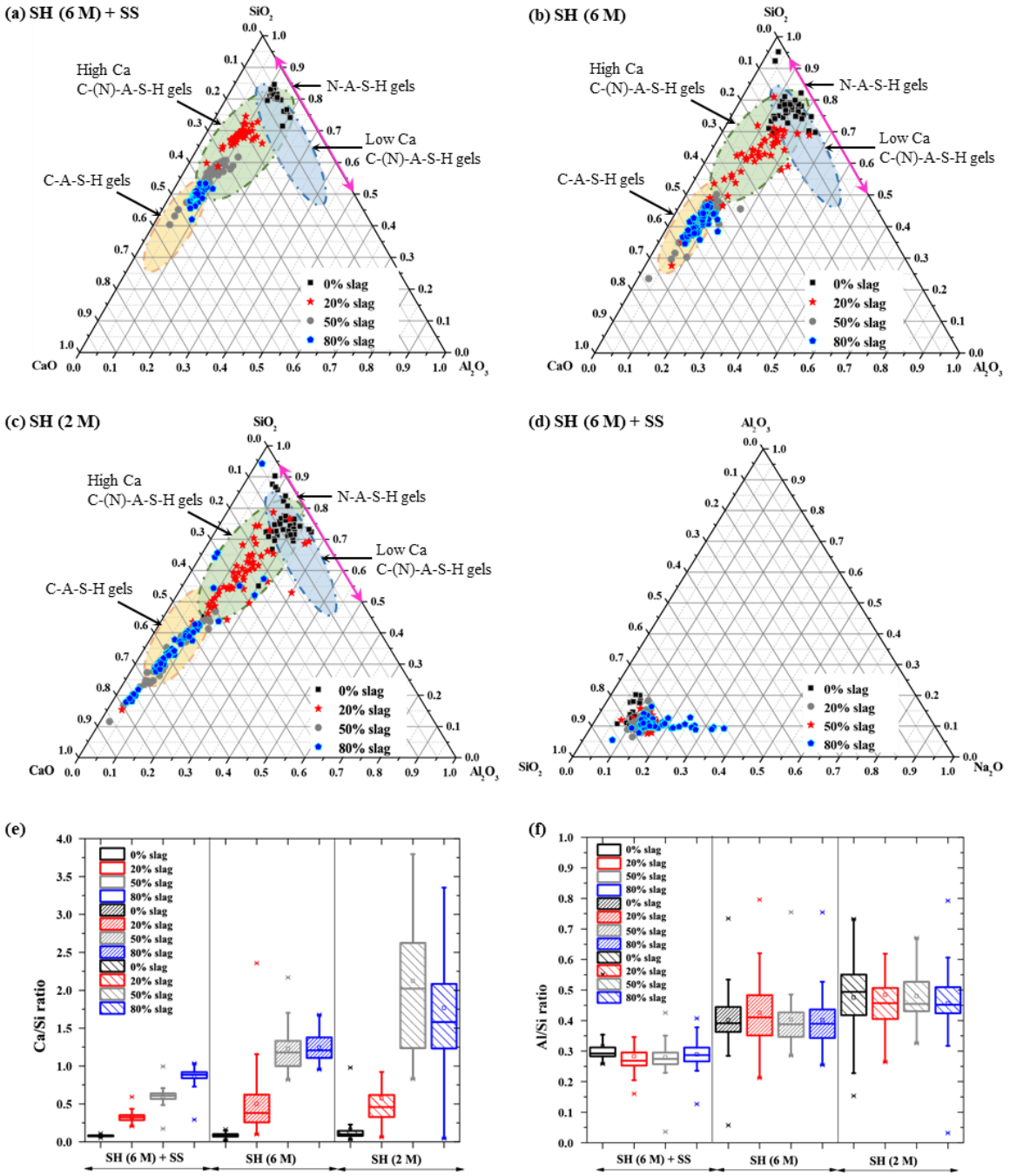

Figure 2.12. Composition ternary diagram in (a-c) CaO-SiO_2-Al_2O_3 and (d) SiO_2-Al_2O_3-Na_2O for AAFS with various slag contents and alkaline activators, accompanied by the statistical distribution of (e) Ca/Si and (f) Al/Si ratios based on the EDS analysis (adapted from [48, 84, 88, 170, 171].

Figure 2.13 illustrates the microstructure and phase assemblage of reaction products and unreacted particles in AAFS characterised using NMR. From 1 to 28 d, C-A-S-H denotes a gel structure with more links in the chain, which takes up 34.9% of the paste at 28 d [39]. The volume fraction of N-C-A-S-H stabilises at around 14.6% after 28 d, suggesting an enhancement in the cross-linking of gel structure as the curing time increases. Furthermore, a higher degree of polymerisation can be found in N-A-S-H gels, occupying approximately 35.9% to 42.6% of AAFS paste at up to 28 d of curing [39]. The understanding of reaction products and identification of individual phases can provide microstructural basis for the characterisation of micromechanical properties and macroscopic performance of AAC.

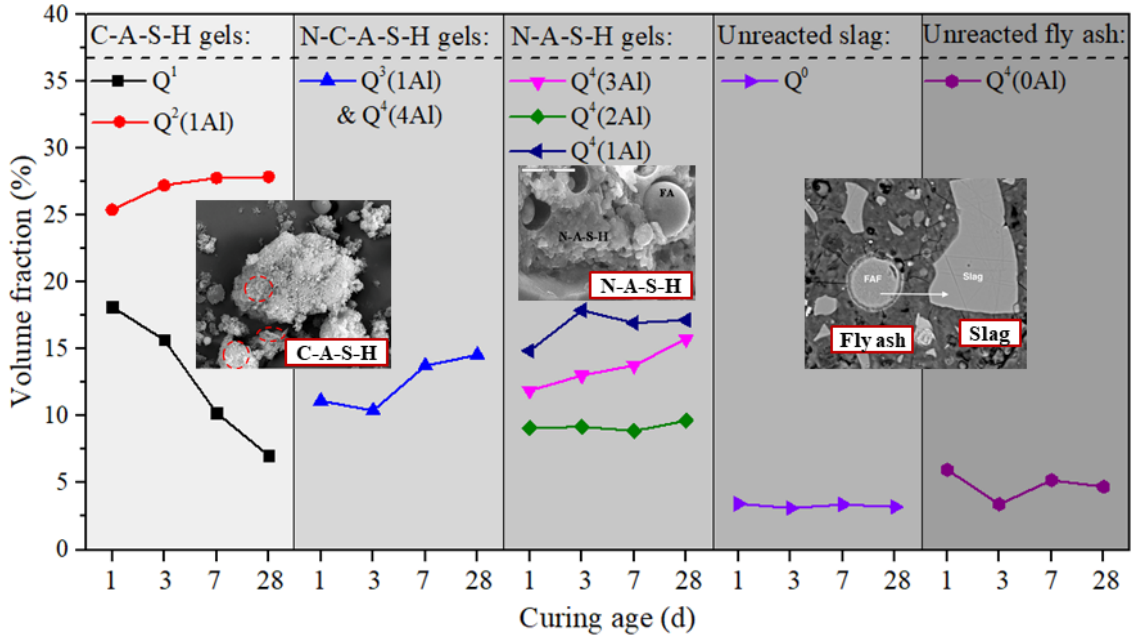

Figure 2.13. Phase assemblage of AAFS paste at different curing ages (adapted from [39, 48, 145, 172]).

Pores

The multiscale pore structure of cementitious materials can be characterised in different ways. In PC concrete system, the pores are distinguished as gel pores (0.5-10 nm), capillary pores (10 nm-10 μm), and air voids (> 10 μm) [84, 173]. However, the pore size distribution in AAC can differ from that in PC system due to the discrepancy in chemical compositions and reaction kinetics. The pore structure in AAC can be categorised in three different types, corresponding to the length scale from Level 0 to Level II in this review [174]. Level 0 represents molecular

pores (< 2 nm) existing in solid gel particle networks. Level I is associated with nano pores (2-100 nm) from gel interstices in gel matrix. Level II stands for micro and meso pores (100 nm-10 μm), which can be composed by a combination of cracks, hollow voids induced by partially reacted particles, defects and fillers in AAC paste [174]. Pores with a size of greater than 10 μm are referred to macro pores induced by air bubbles, which can be recognised at AAC paste, mortar and concrete levels.

At paste level, the pore structure exhibits heterogenous characteristics, which can be significantly influenced by the dispersion of unreacted particles. In low-calcium AAC system, the unreacted fly ash particles can not only introduce interior pores with hollow structures but also trigger the propagation and localisation of micro-cracks at the interfacial transition zone between remnant particles and reaction products [2, 175-177]. Compared with AAMK, AAF shows a wider range and less homogeneous pore size distribution [37, 174]. Due to the higher water-to-binder ratio required for AAMK, AAF also exhibits a lower proportion of pores at the micro level [17]. The pore structure can be altered by the calcium content in AAC. For the Ca-rich AAS paste, the mean pore size and overall porosity tend to be lower in comparison with those of AAF, resulting from the mitigation of large pores since slag can impede the merging of pores in matrix [174, 177-179]. Regarding the blended system, the increase of slag content to no less than 50% in AAFS exhibits a noticeable reduction in porosity with rising tortuosity. Higher slag content can lead to the dominance of the space-filling C-A-S-H gels rather than N-A-S-H gels, which affects the formation of pore network with reduced permeability in AAFS [84, 177]. Figure 2.14 shows the SEM images of AAFS with increasing slag content from 0 to 100%. When subjected to elevated temperatures from 20 to 800 °C, the pore structure can experience a drastic change with increasing porosity by approximately 71%, accounting for 24% of the total volume of AAFS paste [141]. The pore structure evolution in AAC at high temperatures can be associated with the damage mechanisms including further geopolymerisation, pore pressure accumulation, thermal gradient, phase decomposition, recrystallisation and viscous sintering [22, 25, 34, 52, 180].

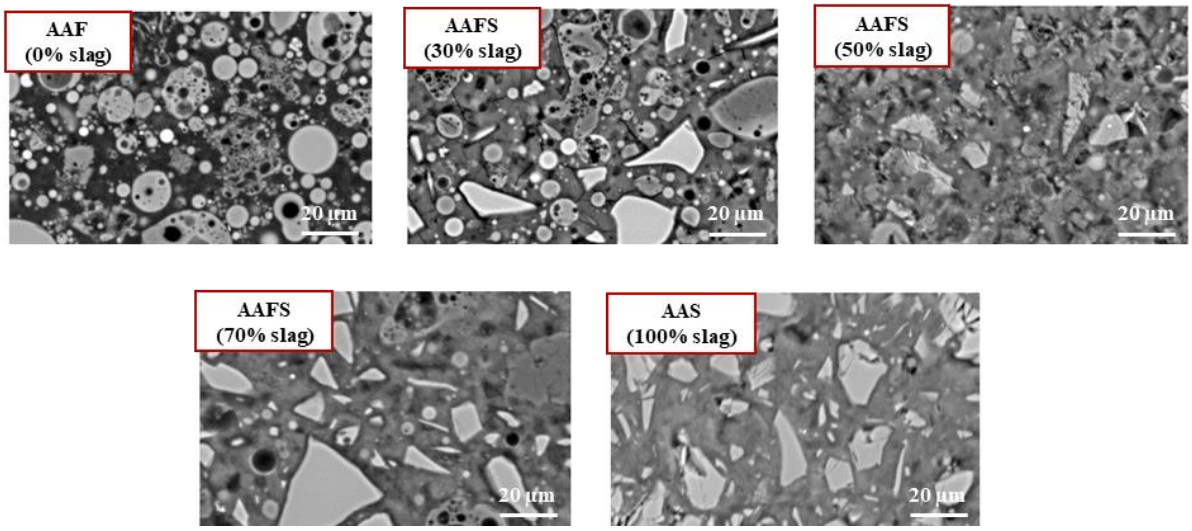

Figure 2.14. Microstructural features of AAF, AAS and AAFS with increasing slag content from 30% to 70% (adapted from [181]).

2.3.4 Level III: Mortar and concrete

The AAM mortar and concrete consists of paste (discussed in Level II), aggregate and ITZ between them. Herein, the microstructural characteristics and micromechanical properties of ITZ in AAC are reviewed, along with a summary of macroscopic performance of AAM mortar (with fine aggregates) and concrete (with both fine and coarse aggregates).

Interfacial transition zone

ITZ is defined as the interlayer between aggregate and bulk paste and considered as one of the most essential phases that can be responsible for the development of micro-cracks in concrete subjected to loading, affecting the macroscopic properties of cementitious materials [182-185]. In AAF, a well-formed layer of ITZ with dense and uniform structure can be observed at high magnifications 20,000×, which adheres to the surface of aggregate due to wall effect and bonding [185]. Figure 2.15 displays the evolution of ITZ in AAFS at different curing ages from 3 h to 28 d. As seen in Figure 2.15(a), the ITZ morphology exhibits the occurrence of microcracks, which can be distinguished as bond cracks that develop in between aggregates and bulk paste, and matrix cracks that propagate from aggregate edges towards paste [84, 186]. A major bond crack appears in ITZ after 3 h curing. The formation and propagation of bond cracks within ITZ can be ascribed to the different deformation behaviour between aggregates and

paste. As the curing time increases, a tighter bonding between the two phases can be observed, while the bond crack is gradually healed in ITZ by further formation of reaction products. At the curing ages of 3 to 28 d, the formation of matrix cracks can be identified, owing to the different gel compositions and shrinkage performance [187, 188].

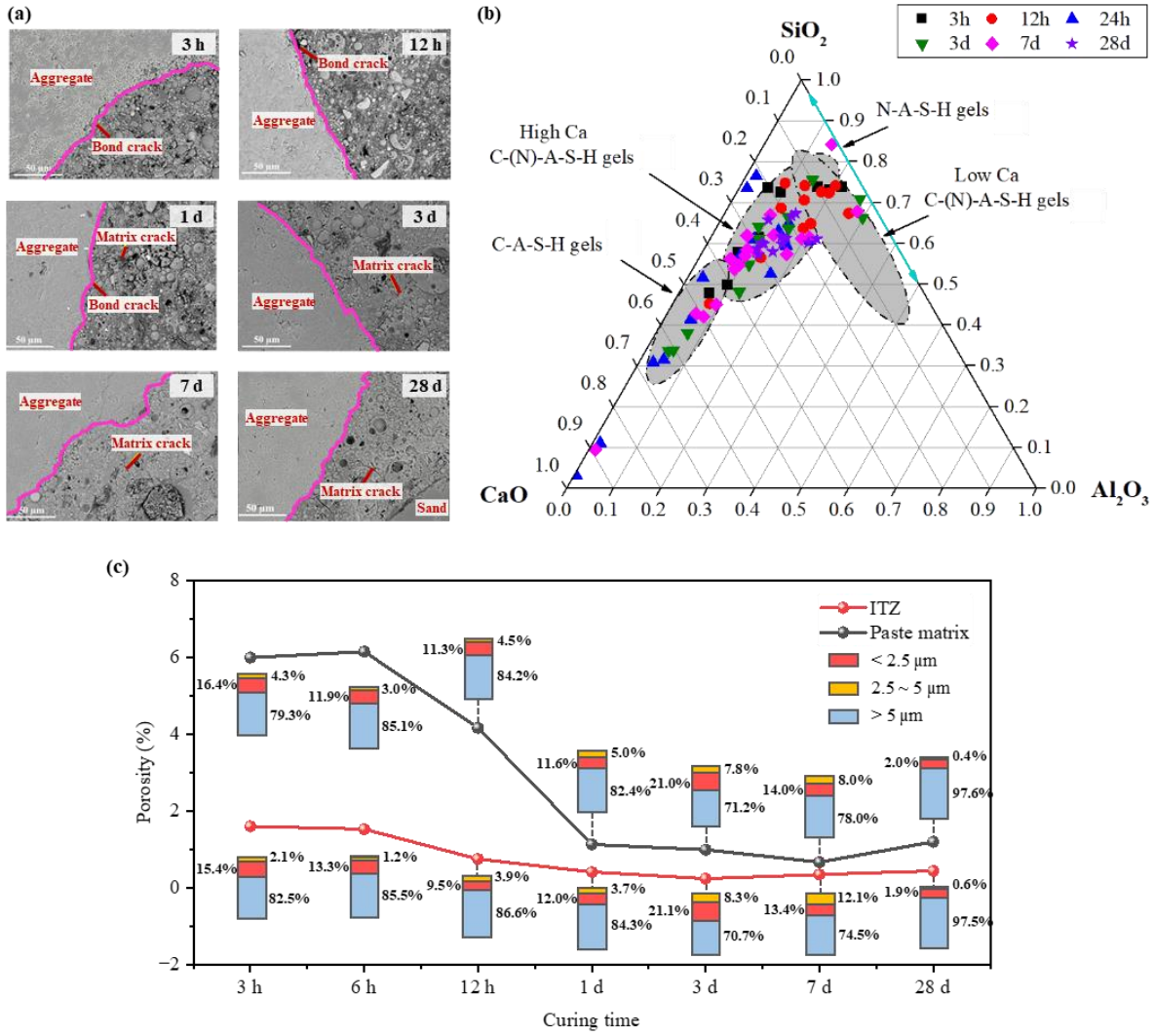

Figure 2.15. Microstructural evolution of ITZ at different curing ages: (a) morphology, (b) chemical compositions, and (c) overall porosity and volume fractions of pores with diverse sizes, including < 2.5, 2.5~5 and > 5 μm (adapted from [39, 84]).

Therefore, for reaction products, the chemical composition in ITZ at up to 28 d is summarised in the ternary diagram in Figure 2.15(b). A typical ITZ in AAC can consist of high gel content by more than 65% with the layer thickness of 30 μm [185]. The ITZ in AAFS tends to be associated with low-calcium C-(N)-A-S-H gels instead of N-A-S-H from 3 to 12 h, owing

to the inclusion of Ca that impedes the formation of N-A-S-H [88, 170]. With the further dissolution of fly ash and slag particles, the reaction products in ITZ cluster more in high-calcium C-(N)-A-S-H and C-A-S-H regions. It is noteworthy that the formation of ITZ may be affected by crystallisation in AAM, as the unreacted particles and their crystals can be low in the vicinity of aggregates due to the wall effect [185, 187, 189, 190]. Figure 2.15(c) shows the overall porosity and porosity within ITZ and bulk paste, indicating a relatively higher porosity of bulk paste than ITZ at 3 h to 28 d. There exists a significant discrepancy of approximately 3.5% at 3 h, which drops rapidly until 1 d. This can be attributed to the formation of reaction products in bulk paste that significantly refines the pore structure from 12 h to 1 d [39].

2.4 Multiscale micromechanical properties of AAC

Besides microstructural characteristics, the micromechanical properties of AAC from Level 0 to Level III are reviewed in this section. Afterwards, the relationships between microstructure and mechanical properties in AAC are analysed and discussed in depth.

2.4.1 Level 0: Solid gel particle

N-A-S-H solid gel particle

For the solid gel particles at nanoscale, it is very challenging to directly characterise the mechanical properties [83, 191]. Herein, the investigation has primarily relied on simulation studies. It was found that the level of structural disorder can significantly influence the mechanical properties of solid gel particles, as illustrated in Figure 2.3(b). Crystalline structure (order structure) is generally considered to exhibit better mechanical performance compared to amorphous structure (disorder structure) [96, 120].

As a sol-gel system, N-A-S-H contains solid particles dispersed in a liquid, which is heterogeneous with local aggregation into clusters [102]. With the increasing appearance of solid particles, the connections among clusters would lead to a percolation threshold indicated by a noticeable change of properties [101]. N-A-S-H has the nature of a true gel, referring to inconsistent gel porosity, excessive shrinkage, and strong sample disintegration (under sealed conditions) [192, 193]. Thus, the micromechanical responses have been suggested to be

obtained at the level of solid gel particles downscaling from the gel matrix at Level 1 [101]. Using the Mori-Tanaka method, the elastic modulus of solid gel particles in AAF and AAMK was determined as 48.2 and 25.5 GPa, respectively [101]. This implies the possible difference among the existence of solid gel particles in different single precursor systems. The gel synthesised from AAMK was revealed to be richer in solid gel particles and twice as compliant as those found in the gel derived from AAF, while slightly different chemical compositions were also noticed in the previous experimental studies [101, 194, 195].

C-A-S-H solid gel particle

Micromechanical properties of C-A-S-H can be associated with the nanostructure in terms of degree of cross-linking and chemical compositions. The increase of cross-linking level tends to enhance its mechanical responses [84, 120]. Specifically, the increase of Al/Si ratio in C-A-S-H solid gel has been suggested to enhance its crystalline order and cross-linking degree, and therefore the mechanical responses [84]. The inclusion of Al branch structures serves to impede tensile loading and strengthen the soft interlayer region within the C-A-S-H solid gel [83, 84]. This, in turn, augments both the interlayer cohesive strength and stiffness [120, 121]. On the other hand, the alumino-silicate tetrahedral chains were reported to be less stiff than plain silica chains, suggesting the possibility of weakening the mechanical performance by increasing the Al content [107]. The overall mechanical properties can be determined by a combination of different factors, such as geometrical transformation, structure changes, Ca/Si ratio and charge neutraliser (Ca^{2+} or Na^{+}).

In terms of the aforementioned Al substitution positions, the mechanical properties of atomistic models with respect to tobermorite 14Å, tobermorite 11Å and anomalous tobermorite (Figure 2.5(c)) were calculated. When the Al substitutions are located in silica chain pairing sites, the elastic modulus of solid gel ranges from 67.8 to 109.6 GPa. The elastic modulus of all models varies between 49.8 and 109.6 GPa at the bridging position. The anomalous tobermorite model exhibits the highest mechanical properties compared with others [107]. This reveals a noticeable dependence of mechanical performance on the configuration of aluminium atoms in C-A-S-H. Moreover, with the occurrence of calcium-aluminium replacement and decrease of Ca/(Al+Si) ratio, the main chain length seems to increase (more Q^2, Q^3, Q^4 and less Q^0 and Q^1 sites), thereby leading to the growth of elastic modulus [107, 154, 196, 197]. This implies that

potential cross-links between layers, specifically Q^3 sites leading to the formation of a 3D nanostructure, which might positively affect the loading path between adjacent layers [107].

N-C-A-S-H solid gel particle

The N-C-A-S-H can promote the enhancement of spatial heterogeneity of composition within the microstructure [48]. In the blend precursor system, the formation kinetics of N-C-A-S-H have been increasingly investigated, while the micromechanical properties are barely studied especially on the scale of solid gel particles. A few studies attempted to conduct qualitative and quantitatively analysis on the micromechanical responses of N-C-A-S-H gels based on nanoindentation tests [39, 171]. It was reported that the elastic modulus of N-C-A-S-H fell between that of N-A-S-H and C-A-S-H, being higher than the former and lower than the latter as the curing time increased from 1 to 28 d. The mechanical performance of N-C-A-S-H can possibly correspond to the aforementioned reorganisation in N-A-S-H by free Ca^{2+} to form N-C-A-S-H, leading to a retained N-A-S-H-like aluminosilicate framework and similar composition with C-A-S-H [39, 88]. To thoroughly explore the micromechanical responses of N-C-A-S-H, molecular dynamics simulations can be employed to link the nanostructure with the mechanical performance of solid gel particles.

2.4.2 Level I: Gel matrix

N-A-S-H gel matrix

To characterise the micromechanical features, different attempts have been made to explore the local elastic modulus and hardness of N-A-S-H gels in AAF and AAMK [198-205]. To identify the N-A-S-H phase from the nanoindentation results, statistical deconvolution can be performed, the first peak of which in the frequency distribution plot of elastic modulus corresponds to the N-A-S-H gel phase with the lowest elastic modulus [199]. The following peaks are associated with partially and unreacted precursors as these particles possess a higher elastic modulus compared to the gel phase [198]. After the identification of N-A-S-H gel phase, the micromechanical properties of N-A-S-H gels can be determined, which are affected by different factors such as alkaline concentration and Si/Al ratio.

With the rise of Na_2O-to-fly ash weight ratio from 6% to 10%, the elastic modulus and hardness of N-A-S-H gels in AAF vary in the ranges of 12.7-15.5 GPa and 0.59-0.73 GPa, respectively [198]. A higher alkaline concentration can boost the activation of unreacted fly ash, leading to the enhancement of micromechanical properties in AAF. As for the Si/Al ratios, the elastic modulus of N-A-S-H gels tends to grow with the increase of Si/Al ratios, which is the result from a greater density of binder gels induced by the rising Si content [200, 206]. Moreover, the Si-O bonds were found to exhibit a higher bond strength than Al-O bonds, indicating that a higher elastic modulus can be achieved in N-A-S-H gels if increasing the Si-O bonds with a higher Si/Al ratio [207]. On the other hand, to consider the micromechanical performance of pure N-A-S-H gels, it would be very challenging to separate them from other reaction products like the unevenly distributed crystal phase due to heterogeneity of AAC [198]. The future research can be focused on the development of other characterisation techniques to determine the micromechanical properties of pure N-A-S-H gels.

C-A-S-H gel matrix

Considering the micromechanical properties of C-A-S-H gel matrix, it is summarised that the elastic modulus of individual phases in AAS follows an ascending order of pore < reaction products < unreacted slag [208-212]. The reaction products in AAS can be divided into two different groups based on their micromechanical performance, including outer reaction product consisting of C-A-S-H gels and inner reaction product composed by the combination of C-A-S-H gels and layered double hydroxides [213-215]. With different types of alkaline activators, the volume fraction of C-A-S-H gels can be affected. The C-A-S-H gels were found to take up 68.0% and 47.3% of the reaction products when activated by SH and SS, respectively [213]. Since the microstructure features are generated faster in SH-activated slag (within a few hours) than SS-activated slag, the corresponding strength development tends to be slower in the later one [161, 216-218]. The alkaline concentration (molarity) and silica modulus were found to have limited influences on the elastic modulus of C-A-S-H gels [218]. It was reported that the elastic modulus of C-A-S-H gels and inner reaction product in AAS were stabilised at around 26 GPa and 35 GPa, respectively, no matter which activator was used [213, 219]. Thus, the micromechanical responses of C-A-S-H gels can be dependent on the distance to unreacted particles, degree of reaction and chemical compositions modified by alkaline activators.

N-C-A-S-H gel matrix

The micromechanical properties of N-C-A-S-H gels are mostly studied via nanoindentation tests on blended AAC with calcium-rich precursors like AAFS [84, 171]. In terms of the level of cross-linking, the order was proposed as: N-A-S-H < N-C-A-S-H < C-A-S-H gels [84]. Correspondingly, the elastic modulus of N-C-A-S-H gels tends to lie between that of N-A-S-H and C-A-S-H gels based on their different microstructural features. Comparing the N-(C)-A-S-H and C-(N)-A-S-H gels, the former exhibits the Si/Al ratio of around 6, whereas the later has a Si/Al ratio of around 3 [220]. Accordingly, the elastic moduli of N-(C)-A-S-H and C-(N)-A-S-H gels were detected, which were around 15.5 GPa and 17.8 GPa, respectively [220]. It was proposed that a relatively higher Si/Al ratio of up to 4.3 in the gel showed lower level of dissolution and thus lower elastic modulus compared to the gel with a lower Si/Al ratio at around 2.4 [220]. This indicates that the variation of elastic modulus in N-C-A-S-H gels is associated with the degree of dissolution from the precursors, which is significantly affected by the alkalinity of different alkaline activators [202, 220]. The elastic modulus of N-C-A-S-H gels was found to go up continuously from around 19.0 GPa to 22.7 GPa with the curing time from 1 to 28 d [84].

2.4.3 Level II: Paste

Unreacted particles

The micromechanical properties of unreacted precursors in AAC have been experimentally explored via nanoindentation tests. In AAF paste, the elastic modulus of unreacted fly ash particles is dependent on their mineral features with an overall range from around 30 to 140 GPa [212, 221, 222]. Among different chemical compositions of fly ash, the Fe-rich ones achieve the highest elastic modulus, ranging from 71.0 to 137.7 GPa, whereas Ca-rich fly ash particles exhibit a relatively lower value, i.e. 75.7-91.2 GPa [222]. The elastic modulus of Si-rich fly ash is around 82.9 GPa, while the worst performance has been reported in Al-rich fly ash with an elastic modulus of 33.3-65.4 GPa [222]. As for AAS paste, the elastic modulus of unreacted slag is in the range of 46-70 GPa, with the hardness of approximately 6 GPa [218, 223]. In terms of blend AAFS paste, the combination of fly ash and slag as a whole unreacted particle phase is tested with an overall elastic modulus of more than 65 GPa [84, 223]. Whereas,

the individual particles are analysed in AAFS with an elastic modulus of around 71.6 and 48.5 GPa in fly ash and slag, respectively [84]. As the curing time increases from 1 to 7 d, the elastic modulus of fly ash exhibits a reduction by up to 9.56%, while that of slag is stabilised at around 49 GPa. This can be attributed to the discrepancy between dissolution and reaction mechanisms of both types of precursors as mentioned previously.

Reaction products

In recent years, the micromechanical properties of reaction products are increasingly studied at paste level in different types of AAC. In AAF, the elastic modulus of N-A-S-H is dependent on the aforementioned curing conditions and choice of alkaline activators, which varies from 4 to 20 GPa [84, 212, 221, 222]. C-A-S-H in AAS tends to exhibit a higher elastic modulus than N-A-S-H, ranging from 12 to 47 GPa with the hardness of 0.3-2.5 GPa, which is strongly associated with the mix design [84, 154, 218]. For the N-C-A-S-H gel in AAFS, the elastic modulus was found to go up from 15.6 to 23.9 GPa as the curing time reaches 28 d [39]. This implies that the transformation among different reaction products can be crucial to the evolution of their micromechanical properties.

Microstructure-mechanical property relationships in paste

The relationships between microstructural features and mechanical properties of AAM can be summarised from gel matrix at Level I to paste at Level II. At Level I, the factors that affect the micromechanical performance of gel matrix are mainly associated with two aspects: solid gel particles from Level 0 and gel pores [84]. Considering different types of AAM paste, the evolution of compressive strength in AAF, AAS, AAMK and AAFS from 1 to 28 d is demonstrated in Figure 2.16. As seen in Figure 2.16(a-c), the overall trend of compressive strength shows a continuous rise in single precursor systems at up to 28 d. For low-calcium AAF and AAMK pastes, the 28 d compressive strengths are in the ranges of around 8-54 and 30-66 MPa, respectively. AAS paste exhibits a higher compressive strength of approximately 75-85 MPa at 28 d, while the compressive strength of AAFS paste is highly dependent on the inclusion of slag, indicating a broad range from around 30 to 100 MPa at 28 d (Figure 2.16(d)). This can be attributed to the effect of chemical compositions, internal structure, phase

transformation and gel porosity on the micromechanical properties of gel matrix and compressive strength of paste in AAM.

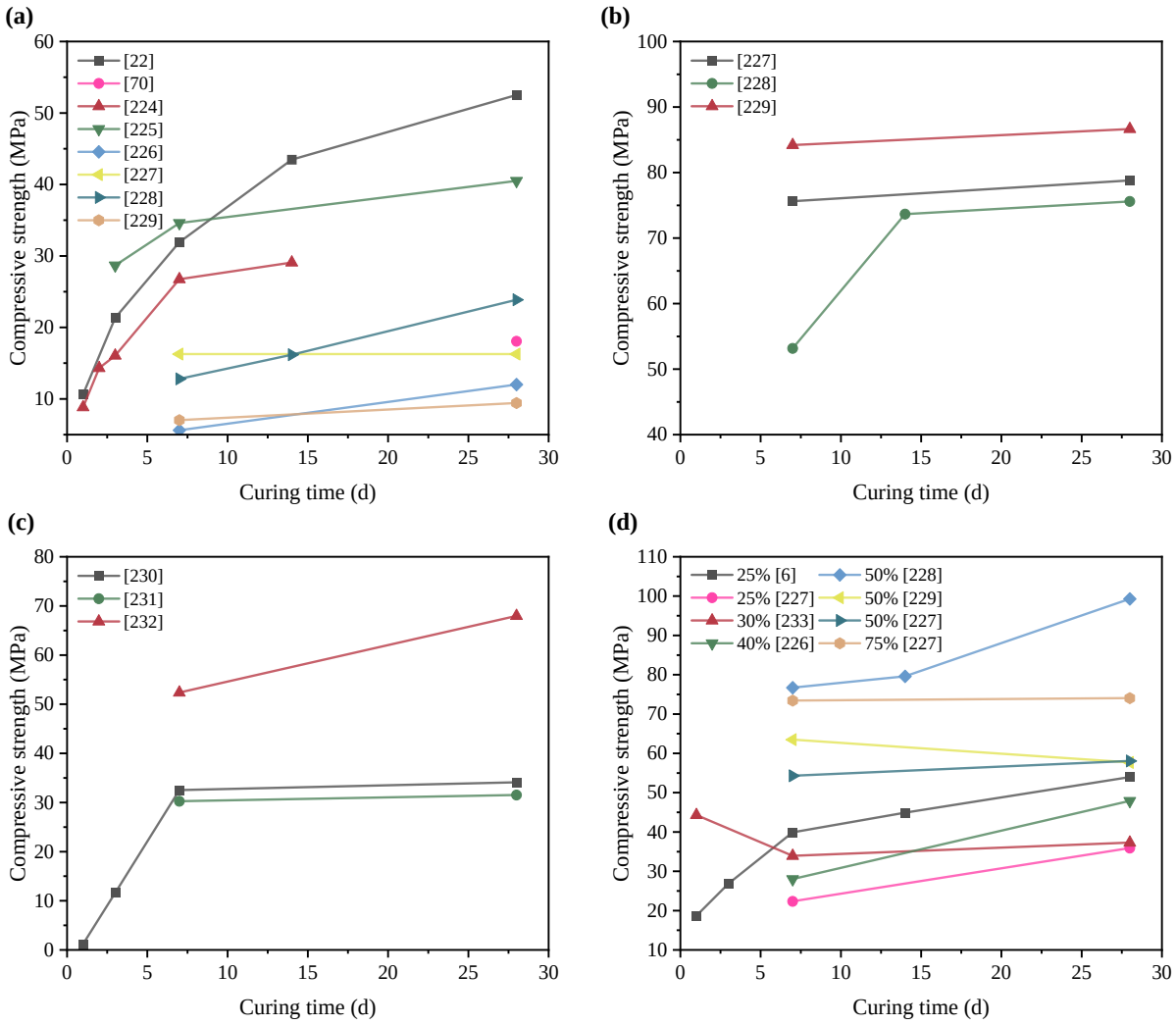

Figure 2.16. Compressive strength of different types of paste: (a) AAF [22, 70, 224-229], (b) AAS [227-229], (c) AAMK [230-232], and (d) AAFS with various slag contents [6, 226-229, 233].

Firstly, the chemical compositions were found to influence the elastic modulus of different binder gels. For AAF paste, a higher Si/Al ratio can lead to the increase of elastic modulus of N-A-S-H gels, as the bond strength of Si-O bonds is higher than that of Al-O bonds [198, 207]. With different types of alkaline activators, the degree of dissolution can be modified in gel matrix that results in the change of local elastic modulus in the heterogenous structure. In AAS paste, the volume fraction of C-A-S-H gel was reported to increase from 47.3% to 68.0% when

replacing SS by SH as the alkaline activator, which indicates a faster reaction and formation of microstructure features with the use of SH, resulting in a more rapid strength development within the gel structure [213] Secondly, the internal structure referring to level of disorder can also influence the micromechanical properties of different types of gel. Comparing with N-A-S-H gels, C-A-S-H gels were observed to contain hints of crystalline phase with order structure. Correspondingly, they exhibit a lower level of disorder with a higher elastic modulus (35-47 GPa) than N-A-S-H gels (11-20 GPa), since N-A-S-H gels possess highly cross-linked amorphous structure with a more pronounced level of disorder [84, 209, 234]. For AAFS, N-C-A-S-H gels have a level of disorder in between C-A-S-H and N-A-S-H gels, which corresponds to the elastic modulus of around 19-23 GPa [39]. Therefore, the phase transformation between different binder gels within gel matrix can be crucial for the micromechanical performance of AAFS [39]. This suggests that the N-C-A-S-H gels can be formed by the exchange of Ca and Na from the original N-A-S-H gels, leading to the change of volume fractions of different reaction products and thus the modification of micromechanical properties [88]. Finally, among the mentioned three types of gel matrix, N-A-S-H gels exhibit the most porous structure, whereas C-A-S-H gels are the most compact phase with the greatest gel density [212]. This implies that a lower gel porosity can contribute to better micromechanical properties of gel matrix in AAM.

The mechanical properties can be associated with the dissolution of unreacted particles, microstructural properties of different reaction products from Level I and overall pore structure. Regarding unreacted particles, the discrepancy in mechanical properties between fly ash and slag is induced by physical chemistry and degree of dissolution, with elastic modulus of around 72 and 49 GPa, respectively. For reaction products, the phase assemblage of binder gels can significantly contribute to the mechanical properties, influenced by factors such as slag content (i.e. Ca-rich precursors), alkalinity and type of alkaline activators and curing conditions. Regarding pore structure, AAS has lower porosity compared to AAF as the merging of pores in paste tends to be impeded by slag [235].

2.4.4 Level III: Mortar and concrete

Interfacial transition zone

The micromechanical properties of ITZ can be highly associated with the gel compositions, reaction products, pore structure and other factors that modify aggregates and bulk paste in AAC. To enable the comparison between ITZ and paste with respect to micromechanical properties, different techniques such as nanoindentation and nanoscratch have been employed in the previous studies to explore the mechanical responses and heterogeneity of ITZ in AAC [84, 187, 188, 190, 236-241]. Nanoindentation is adopted to investigate the localised ITZ regions, whereas nanoscratch can provide the overall information of ITZ surrounded by different aggregate surfaces [184, 187, 242]. Compared with AAF bulk paste, the comparable mechanical properties obtained in ITZ can be associated with the formation of N-A-S-H gels that provide a strong bond between aggregate and bulk paste [84, 237, 243]. In AAF, the elastic modulus and hardness of ITZ typically range from 17.2-36.7 GPa and 0.76-1.78 GPa, respectively, depending on the locations of ITZ referring to top, bottom and lateral positions, as shown in Figure 2.17(a) [187]. ITZ at the top surface of aggregate exhibits the highest elastic modulus and hardness, while ITZ at the lateral surface of aggregate has the worst micromechanical properties. the micromechanical properties of ITZ in AAS are dependent on the alkaline activators, in which the mean hardness of ITZ is 76.8% of that of AAS paste [241, 244]. In particular, the use of SS in AAS can introduce excess SiO_2, which potentially boosts the formation of C-A-S-H gels and refine the pore structure in ITZ [216, 240]. Thus, the ITZ in AAS activated by SS exhibits great mechanical properties with low porosity [216, 245].

The micromechanical properties of AAFS are influenced by the evolution of reaction products and microstructural characteristics against curing age [44]. Figure 2.17(b) illustrates the comparisons of elastic modulus between ITZ and AAFS paste with the evolution of reaction products over curing age at up to 28 d. As the micromechanical properties are dependent on the nature of binder gels in terms of packing density, structure disorder and gel porosity, the elastic modulus of C-A-S-H gels was found to be the highest, followed by N-C-A-S-H and N-A-S-H gels [212, 218]. Hence, the increase of N-C-A-S-H and C-A-S-H gels in ITZ can lead to a comparative growth of elastic modulus by 57% to around 21.2 GPa after 12 h curing, as seen in Figure 2.17(b). This can be attributed to the high reactivity of slag that results in the more

rapid dissolution of Ca and thus the formation of C-A-S-H gels [246-249]. In addition, according to the aforementioned porosity in ITZ at various curing ages, the decrease of porosity at up to 12 h curing can also contribute to the development of elastic modulus within ITZ, resulting from the refinement of initial microcracks and thus enhance the ITZ structure to provide better micromechanical response. After 28 d of curing, the elastic modulus of ITZ in AAFS can eventually stabilise at approximately 13.2 GPa [44]. Compared with AAFS paste, ITZ exhibits a more compact microstructure with higher elastic modulus at up to 28 d of curing, implying a stronger interfacial bonding between aggregates and bulk paste in AAC compared to traditional PC concrete [250-252]. Since the reaction products and microstructural morphology play crucial roles in the determination of micromechanical properties, it is necessary to explore the modification of AAFS matrix with different slag contents in the future.

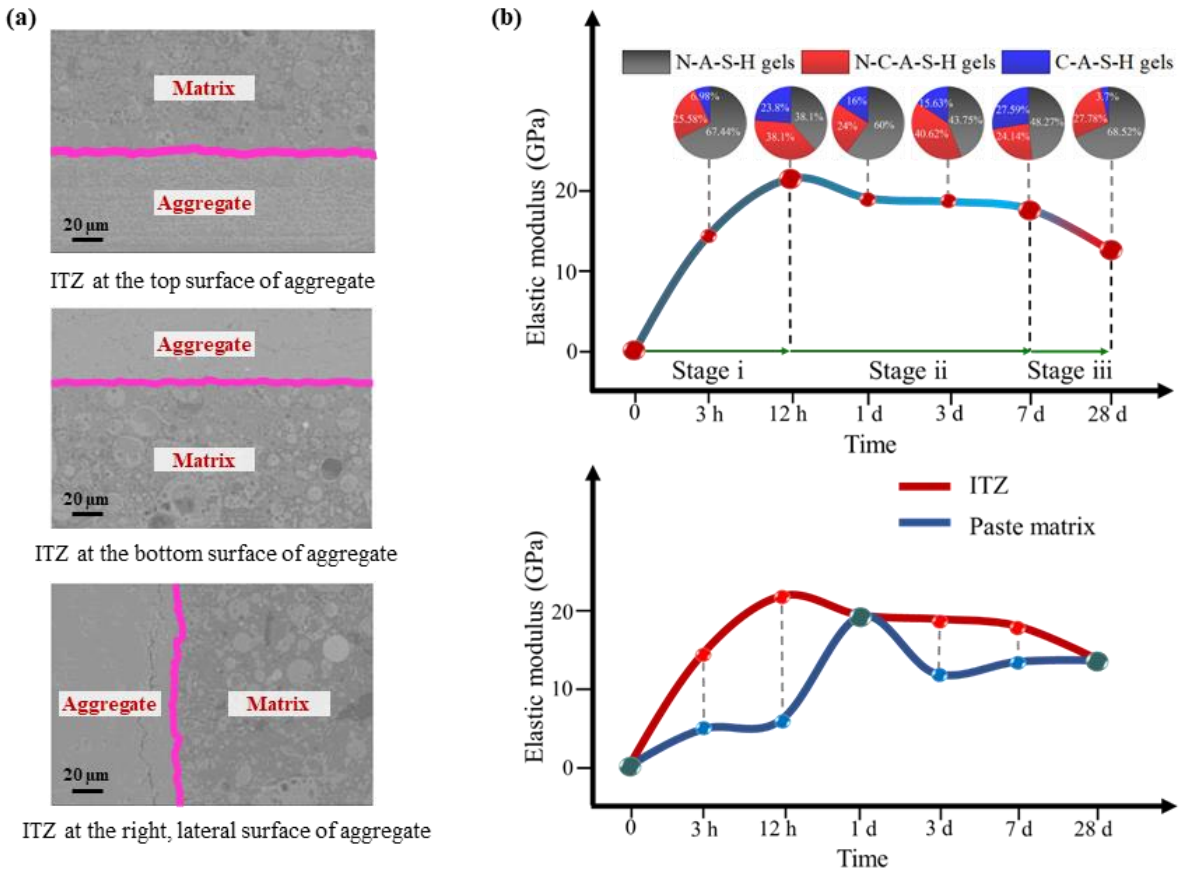

Figure 2.17. (a) Different positions of ITZ related to aggregates, and (b) Evolution of elastic modulus in ITZ and bulk paste in AAFS (adapted from [39, 187]).

Microstructure-mechanical property relationships in mortar/concrete

With the inclusion of fine and coarse aggregates, the mechanical properties in terms of strength and stiffness of AAC at Level III are closely associated with the paste and ITZ, especially their microstructural features including chemical compositions and phase assemblage among N-A-S-H, C-A-S-H and N-C-A-S-H [235]. The macroscopic mechanical properties of AAM mortar and concrete including compressive, splitting tensile and flexural strengths have been extensively investigated and summarised in pervious reviews which indicate the importance of alkaline activators, type of precursors, liquid/binder ratios, binder/sand ratios and curing regime [15, 67, 122, 253, 254]. Figure 2.18 demonstrates the compressive strength of AAC. In general, all four types of AAC experience continuous strength gain as the curing time increases from 1 to 28 d. At least 80% of compressive strength can be achieved within 7 d of curing in almost all types of AAC, attributed to the fast reaction process and early development of geopolymeric network. The progressive strength growth from 7 to 28 d in AAC is related to further reaction and rearrangement of gel structure towards a stable status with the increasing curing age.

For AAF mortar and concrete, the compressive strength is mostly in the range of 5- 30 MPa at 28 d, depending on different factors. For instance, elevated curing at around 80-90 °C can shorten the time to achieve the ultimate compressive strength by reaching 90% of the total strength within the first few hours of mixing [15]. Upon heating at higher temperatures of up to 400 °C, the compressive strength of AAF can be enhanced by further geopolymerisation, which can reach up to around 160% of the original strength at 20 °C [2, 26, 31]. AAS mortar and concrete exhibit better compressive strength than AAF, which can reach up to about 80 and 52 MPa at ambient temperature, respectively (Figure 2.18(b)). However, they exhibit worse high-temperature resistance compared to AAF, due to the decomposition of $CaCO_3$ at up to 600 °C [23, 24, 53]. The compressive strength of AAFS is dependent on the slag content. As seen in Figure 2.18(d), when the slag content rises from 10% to 30% in AAFS concrete, the compressive strength can be enhanced from 28 MPa to around 60 MPa at 28 d of curing [12, 84]. Therefore, the compositions of unreacted particles, phase assemblage of reaction products and propagation of cracks can be crucial to the development of compressive strength, depending on the mix design of AAFS paste and selection of fine and coarse aggregates. The static mechanical properties of AAC have been systematically studied, while the dynamic properties

of AAC linking to microstructural evolution and micromechanical properties have been rarely explored.

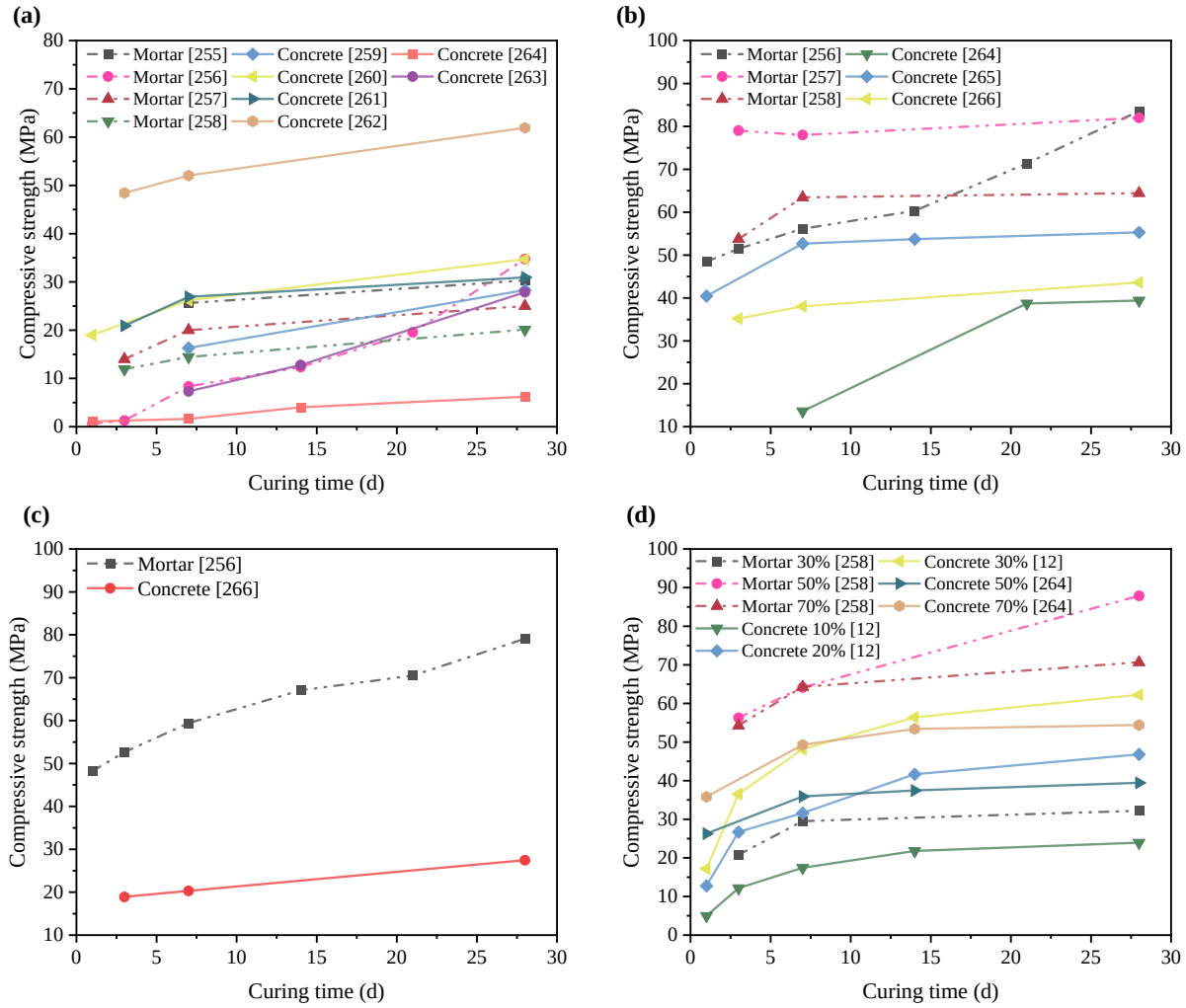

Figure 2.18. (a) Compressive strengths of different types of AAC: (a) AAF [255-264], (b) AAS [256-258, 264-266], (c) AAMK [256, 266], and (d) AAFS with various slag contents [12, 258, 264].

2.5 Behaviour of AAC at elevated temperatures

In recent years, an increasing number of studies have been focused on the behaviour of different types of AAC at elevated temperatures. Table 2.6 summarises the experimental studies on the behaviour of AAC at elevated temperatures, including single and blend precursor systems (AAF, AAS, AAMK and AAFS). This section presents a state-of-the-art review and provides

comprehensive discussions from microscopic characteristics to macroscopic performance of AAC at elevated temperatures. As illustrated in the outline of this section in Figure 2.19, firstly, the heating and cooling methods are briefly introduced. Then, the behaviour of AAC subjected to elevated temperatures in terms of phase stability, microstructural evolution, thermal stability, thermal deformation, and compressive, tensile and flexural strengths are systematically reviewed and analysed. Afterwards, the damage mechanisms in PCC and AAC are discussed, with potential mitigation approaches including the modification of AAC and incorporation of fibres were summarised and discussed in detail.

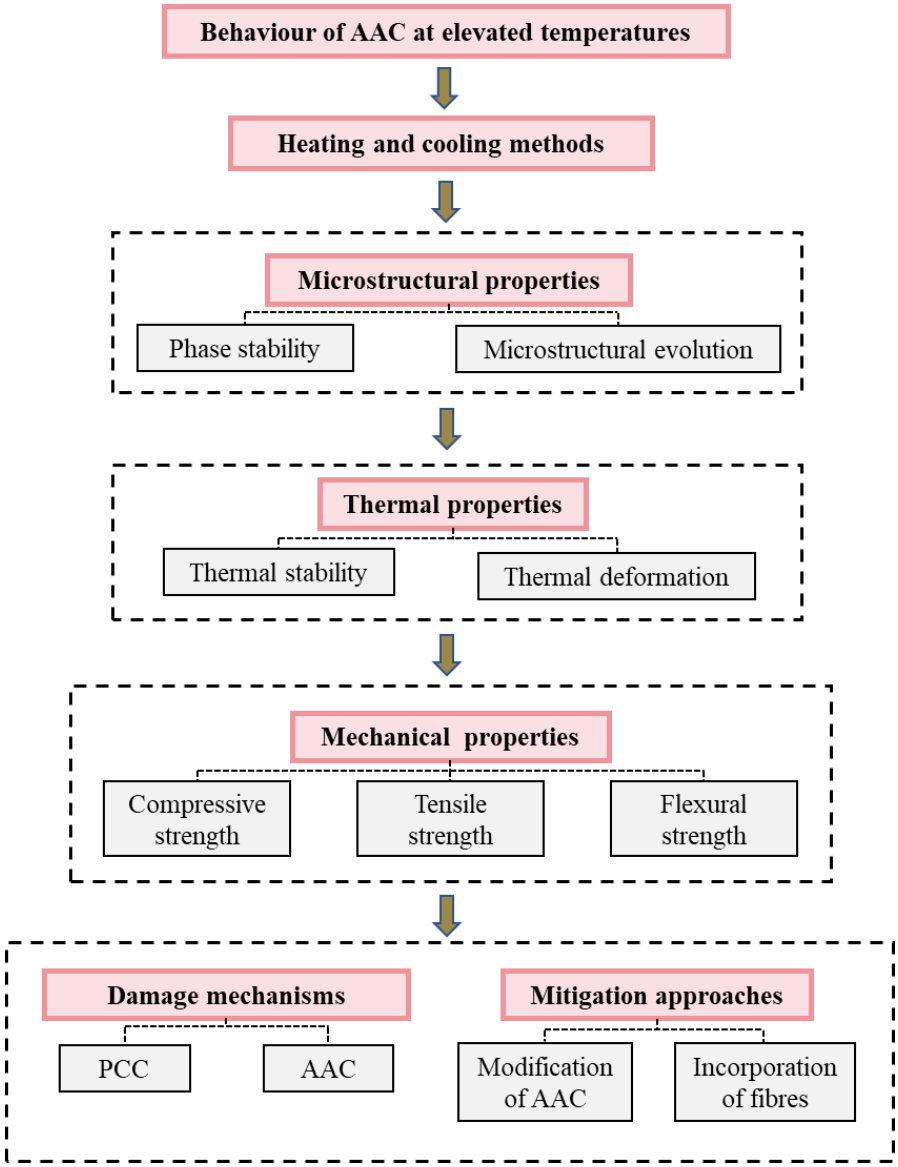

Figure 2.19. Outline of this section.

2.5.1 Heating and cooling methods

The heating and cooling conditions have pronounced effects on the measurement of temperature-dependent properties of both PCC and AAC. In general, the thermal stress induced by temperature gradient in concrete is highly related to heating rate, which can significantly affect the mechanical performance of concrete after high temperature exposure [4, 52]. Two main heating procedures are commonly employed: (1) simulation of the real fire situation following a standard heating curve, and (2) constant heating rate [3, 267, 268].

A standard heating rate is set based on the specified heating curves to predict the real fire conditions. Figure 2.20(a) illustrates the standard fire curves given in ISO 834-1 [269], ASTM E119 [270], KSF 2257 [271] and JIS A 1304 [272], indicating a logarithmic relationship between the growing temperature and heating time to reflect the real fire circumstance [273-276]. This heating method has been extensively employed to investigate the resistance of concrete to pore pressure and spalling [3, 277-280]. However, concrete can be significantly damaged by thermal gradient and thus become structurally unstable with such a rapid increase of temperature in a short time period.

Therefore, the second method of increasing the temperature constantly at a relatively lower heating rate is applied more frequently to reach the target temperature [281-285]. Figure 2.20(b) demonstrates the heating and cooling process of concrete with a fixed heating rate. A lower heating rate can minimise the thermal stress and isolate the effect of vapour pressure inside the matrix. However, a slow heating rate may not completely prevent spalling of specimens due to the existence of pore pressure induced damage as a result of moisture vaporisation and pore pressure build-up [4]. The previous studies examined the heating rates between 0.5 and 30 °C/min such as 1 °C/min [4, 285], 2 °C/min [286], 4 °C/min [287] and 10 °C/min [284, 288, 289]. Once the target temperature is attained at a constant speed, the temperature level is usually maintained for a certain period of time (1-2 h) to ensure that there is no temperature gradient inside the specimen while preventing the effect of long holding time on the mechanical properties of specimens [3].

The mechanical properties can be tested during and after heating process [283, 290-299]. Due to the potential safety concerns on hot specimens, the tests are commonly conducted after cooling. To measure the residual properties of specimens at ambient temperature, the test

samples can be either cooled down instantly in water or naturally in furnace (air). It was reported that water cooling could cause 15.1% more deterioration in strength of the specimens than furnace cooling after exposure to 1100 ºC, which can be attributed to the high heat transfer capacity of water with a rapid cooling process, leading to the generation of an unneglectable temperature gradient inside the concrete specimens [3, 300]. Thus, the non-uniform distribution of thermal stress can cause damage to concrete and a strength loss.

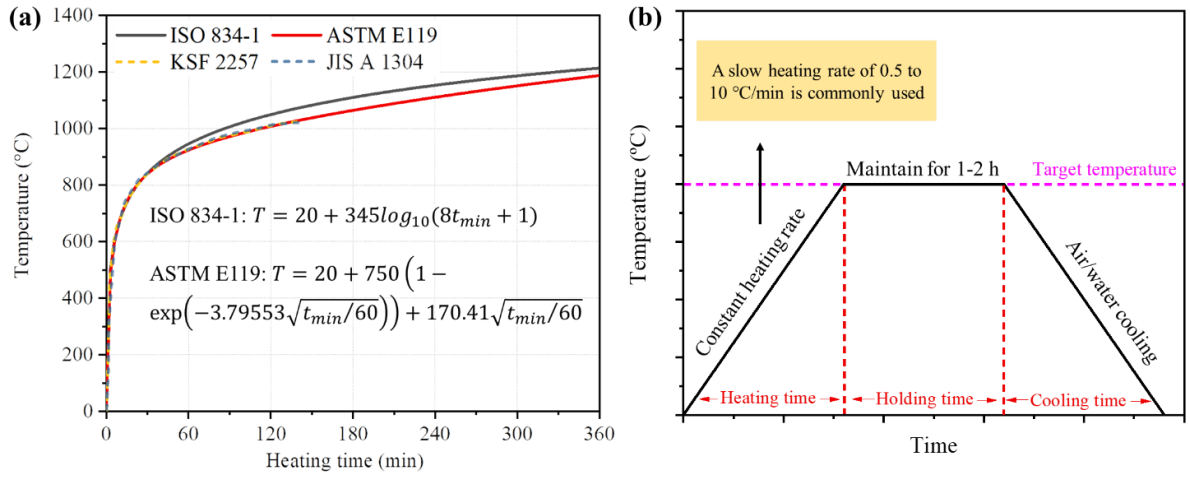

Figure 2.20. Heating methods following (a) standard fire curves (T is the fire temperature and t_{min} is the heating time) and (b) constant heating process (adapted from [3, 275])

It is worth noting that the measurement on specimens after cooling to room temperature may not fully represent the real situation for concrete structures in a fire circumstance [290, 301]. Hot and residual compressive strengths of concrete specimens could be similar to each other [302, 303]. However, it was also observed that there could be a large discrepancy between the temperature-dependent properties of concrete during exposure to elevated temperatures and after cooling [299, 301, 304]. At 100-105 ºC, both the compressive and tensile strengths of hot specimens are much lower than those after cooling from the same temperature, which can be ascribed to the pore pressure-induced damage during heating [301, 304]. At a higher temperature level of 600 ºC, the strength of hot specimens suffers from inner tensile stresses induced by the thermal incompatibility between different phases (i.e. shrinkage of matrix and expansion of aggregates at elevated temperatures), which can further deteriorate the mechanical behaviour of specimens during exposure to high temperatures [299]. Due to the high facility requirements to undertake tests on hot specimens, the available data obtained from in-situ

measurements are still limited. Table 2.6 summarises the recent experimental studies on ACC with different heating and cooling methods.

2.5.2 Phase stability

Phase stability can reflect the fundamental changes in AAC at elevated temperatures, which can explain the underlying damage mechanisms and essentially affect the macroscopic performance of AAC at elevated temperatures.

Single precursor system

Phase transformation can affect the behaviour of AAC in single precursor systems subjected to elevated temperatures. The matrix structural evolution can be evaluated through XRD analysis [30]. Figure 2.21 gives a summary of the main phase changes observed in different types of AAC. In AAF, the geopolymerisation can primarily result in the formation of amorphous aluminosilicate gel (three-dimensional N-A-S-H type gel) to promote strength and durability at ambient temperature [10, 48, 89]. The main semi-crystalline phases include quartz (SiO_2), mullite ($Al_6Si_2O_{13}$), magnetite ($Fe + 2Fe_2 + 3O_2$) and hematite (Fe_2O_3) [30, 305, 306]. Quartz is a common phase in unreacted fly ash particles with a high melting point of 1713 ºC, which can be primarily in origin and formed from the Al_2O_3-SiO_2 system [307]. Mullite is a refractory with a melting point of 1830 ºC [308] that is stable at both room and elevated temperatures and contributes to thermal resistance, mechanical properties and thermal stability with low thermal conductivity and expansion [309-312]. As summarised in Table 2.1, before 300 ºC, the reduction of Si-O-Al and Si-O-Si can be observed, implying the absorption of weak bond molecules at this stage [31]. The phase changes mainly happen with the appearance of new crystalline phases including albite ($NaAlSi_3O_8$) and nepheline ($NaAlSiO_4$) after exposure to 300-1000 ºC, whereas other phases are relatively stable at 1000 ºC. The formation of albite and nepheline is associated with the disappearance of minority zeolite crystalline phases including hydroxysodalite ($Na_4Al_3Si_3O_{12}OH$) and herschelite ($NaAlSi_2O_6 \cdot 3H_2O$) after exposure to 600 ºC [33]. Also, the appearance of nepheline phases can contribute to the mass loss of AAF matrix at 750 ºC [53, 313].

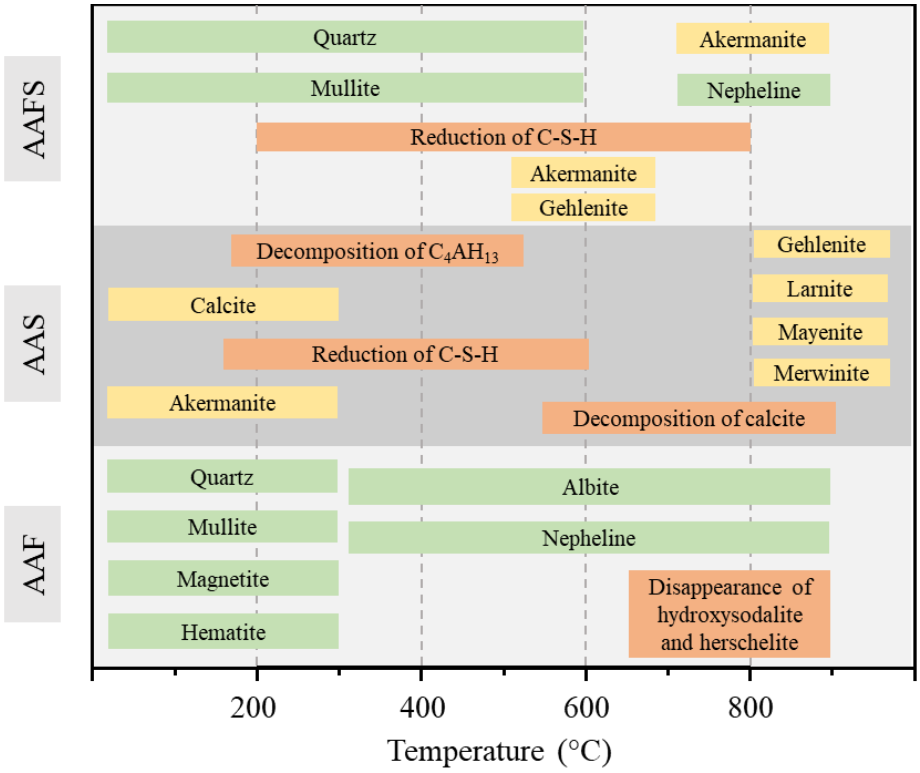

Figure 2.21. Schematic diagram of phase changes in different types of AAC at elevated temperatures.

It is noteworthy that alkaline activators can affect the phase stability of AAF at elevated temperatures. Potassium-based (KOH and K_2SiO_3) and sodium-based (NaOH and Na_2SiO_3) activators are the most commonly used ones to produce AAC. At 400 ºC, more mullite can be detected in AAF with 2% nano silica activated by potassium activators compared to sodium activators, which is a high temperature phase that can contribute to the strength gain of AAF exposed to elevated temperatures [314]. A slightly higher content of amorphous phase can be observed in AAF made from potassium activators compared to the sodium counterparts, which can enhance the mechanical strength of AAF at elevated temperatures. Furthermore, the molarity of alkaline solutions can also influence the crystalline phases of AAF. The increase of molarity of NaOH solutions can improve the residual strength of AAF at high temperatures, which can be ascribed to the high amount of sodium oxide contained in the solutions, enhancing the aluminosilicate phase to promote further geopolymerisation. The formation of Na-based crystalline phases such as albite and nepheline that have great thermal stability with high

melting points can improve the thermal resistance and thus mitigate the strength loss of AAF at elevated temperatures [315, 316].

Table 2.1. Summary of phase changes of AAC at elevated temperatures.

Ref.	Precursor	Main findings
[30]	Fly ash	Appearance of crystalline phases (albite, anorthite, and magnetite) after 800 ºC
[31]	Fly ash	Increase in the amorphous phase content after 800 ºC
[306]	Fly ash	Appearance of albite and nepheline at 300 ºC, and more albite was observed at 900 ºC
[33]	Fly ash	Hydroxysodalite and herschelite disappeared to form albite and nepheline after 600 ºC
[317]	Fly ash	Disappearance of hydroxysodalite and formation of nepheline at 800 ºC
[312]	Fly ash	Peaks of quartz, mullite and hematite and appearance of albite and nepheline at 1000 ºC
[38]	Slag	Formation of new crystalline phases of gehlenite, larnite and mayenite at 1000 ºC
[318]	Slag	Crystallisation to form akermanite, diopside and wollastonite at 1200 ºC
[319]	Slag	Increase of akermanite and formation of gehlenite and merwinite at 800 ºC
[320]	Slag	Increase of albite and sodium-aluminium-silicate after exposed to 800 ºC
[321]	Metakaolin	Formation of new crystalline phase of nepheline at 900 ºC
[322]	Metakaolin	Formation of nepheline after firing to 1000 ºC
[32]	Fly ash and slag	No formation of new crystalline phase after exposed to 700 ºC
[25]	Fly ash and slag	No new crystalline phases detected and decomposition of calcite at 600 ºC (50% slag)
[56]	Fly ash and slag	Formation of akermanite, gehlenite, anorthite and nepheline at 800 ºC (25, 50, 75% slag)
[34]	Fly ash and slag	New crystalline phases: anorthite, nepheline and wollastonite at 600 ºC

In AAS, the unreacted slag has high calcium concentration that contains crystalline phases such as calcite ($CaCO_3$) and akermanite ($Ca_2Mg(Si_2O_7)$) [32, 38]. After mixing with alkaline activators (i.e. NaOH and Na_2SiO_3), the strength of AAS is developed with the formation of a C-(A)-S-H type gel. Compared to AAF, there are additional hydrated phases in AAS due to the high calcium content, which can impair the thermal resistance and stability [10]. No obvious new phases appear in AAS until the temperature goes up to 300 ºC, where the decomposition of C_4AH_{13} occurs along with the drop in C-S-H gel content, indicating the structural evolution of C-S-H layers [25]. After exposed to 600 ºC, the calcium hydrates decompose with de-carbonation of calcite at around 756 ºC [25, 38]. With the rise of exposure temperature to 800-1000 ºC, the new crystalline phases such as gehlenite ($Ca_2Al_2SiO_7$), larnite (Ca_2SiO_4), mayenite

($Ca_{12}Al_{14}O_{33}$) and merwinite ($Ca_3Mg(SiO_4)_2$) can be observed. The crystallisation of amorphous phases leads to a more ordered structure with these stable crystalline phases, which can enhance the mechanical properties of AAS matrix due to sintering effect and densification at high temperatures [38, 61, 323, 324]. Minor crystalline phases such as diopside ($CaMgSi_2O_6$) and wollastonite ($CaSiO_3$) disappear when the temperature goes up to 1150 ºC [318].

For AAS made from SS solution, there is an increase of the amount of akermanite in matrix when exposed to 800 ºC compared to lower temperatures. When continuing heating until 1200 ºC, the development of akermanite is further promoted due to high temperature environment [325]. However, the formation of this crystalline phase is not directly associated with the mechanical properties of AAS at elevated temperatures.

Regarding AAMK, amorphous aluminosilicate gel exists with the crystalline phases such as quartz and anatase (TiO_2) [10]. High-temperature exposure up to 300 ºC has a limited effect on the phase changes or transformation. The new crystalline phase of nepheline can be detected as the temperature goes up to 900 ºC due to geopolymerisation along with reordering of amorphous aluminosilicates [321, 322, 326]. In general, AAF exhibits better thermal stability and less damage than AAMK after high temperature exposure as AAMK contains more free moisture and thus can lead to a more pronounced pore pressure within the matrix [10, 327].

Blend precursor system

As a combination of AAF and AAS, the reaction products in AAFS are more complex, mainly consisting of N-A-S-H (from AAF), C-A-S-H (from AAS) and N-C-A-S-H (a hybrid of AAF and AAS) gels [32, 328]. In AAFS matrix, the fly ash/slag ratio is the dominant factor that affects the formation of different phases [25]. The XRD patterns of AAFS before and after exposure to up to 400 ºC exhibit insignificant differences, except a slight reduction of C-S-H phase that indicates the dehydration. There is almost no difference between the crystalline phases of AAF and AAFS (with no more than 20% slag) at 600 ºC, which mainly contains quartz and mullite [25], while akermanite and gehlenite can be detected in AAFS containing no less than 50% slag [34]. At 700 ºC, AAFS with 40% slag content can contain C-S-H with traces of calcite as seen in the XRD patterns [32]. Moreover, the intensity of C-S-H in AAFS reduces significantly at elevated temperatures, while there is no obvious impact on that in AAS,

implying that the incorporation of fly ash and slag can change the nature and the main binding phases [25].

At 800 ºC, crystalline phases such as akermanite, gehlenite, anorthite ($CaAl_2Si_2O_8$) and a small amount of nepheline can be observed in AAFS [56], along with the disappearance of C-S-H phase, indicating full crystallisation or dehydration in all AAFS mixtures containing slag dosages of 25%, 50% and 75%, which is consistent with the previous research [34]. As the C-S-H gel is susceptible to high temperature damage, AAFS with higher slag content is prone to suffering more serious strength retrogression due to the higher calcium concentration that results in the formation of additional hydrates compared to AAF [10, 56]. In addition, the amounts of gehlenite and anorthite are strongly related to the Ca/Al ratio in AAFS as higher slag content can lead to the dominant formation of gehlenite, while the opposite situation can lead to the dominant formation of anorthite [56].

Regarding other blend types of AAC such as alkali-activated fly ash-metakaolin and alkali-activated slag-metakaolin systems (see Table 2.6), a new crystalline phase can be detected in alkali-activated fly ash-metakaolin specimens when exposed to 500-700 ºC, resulting from the sintering reaction of unreacted fly ash particles [329] and the slag content and alkalinity can affect the existence of C-S-H phase in alkali-activated slag-metakaolin system [330]. However, the phase stability of AAC in blend precursor system at elevated temperatures has not been systematically explored with respect to different factors such as types of alkaline activators, curing condition and so on. Thus, further research is required to gain an in-depth understanding of the phase changes and the effects of different factors on the phase stability of AAFS at elevated temperatures.

2.5.3 Microstructural evolution

Single precursor system

Microstructure of AAC at elevated temperatures can be affected by various factors in relation to different damage mechanisms. The changes in porosity, pore size and pore connectivity of AAC with exposure temperatures are directly related to moisture transport inside the matrix and pore pressure-induced damage [5]. Figure 2.22 demonstrates an example of AAF exposed to elevated temperatures. At ambient temperature, AAF matrix exhibits a porous structure with

unreacted spherical/semi-spherical fly ash particles, N-A-S-H gel as a dense and bulky base and some stripe-shaped substances by abundancy of alkaline [30, 32], which is corresponding to the semi-crystalline phases such as quartz and mullite mentioned in the previous section. After exposed to 200 ºC, many unreacted fly ash particles can be observed [31]. The microstructural evolution of AAF is mainly associated with the evaporation of free moisture, which can cause the accumulation of entrapped vapour pressure and initiation of microcracks [17].

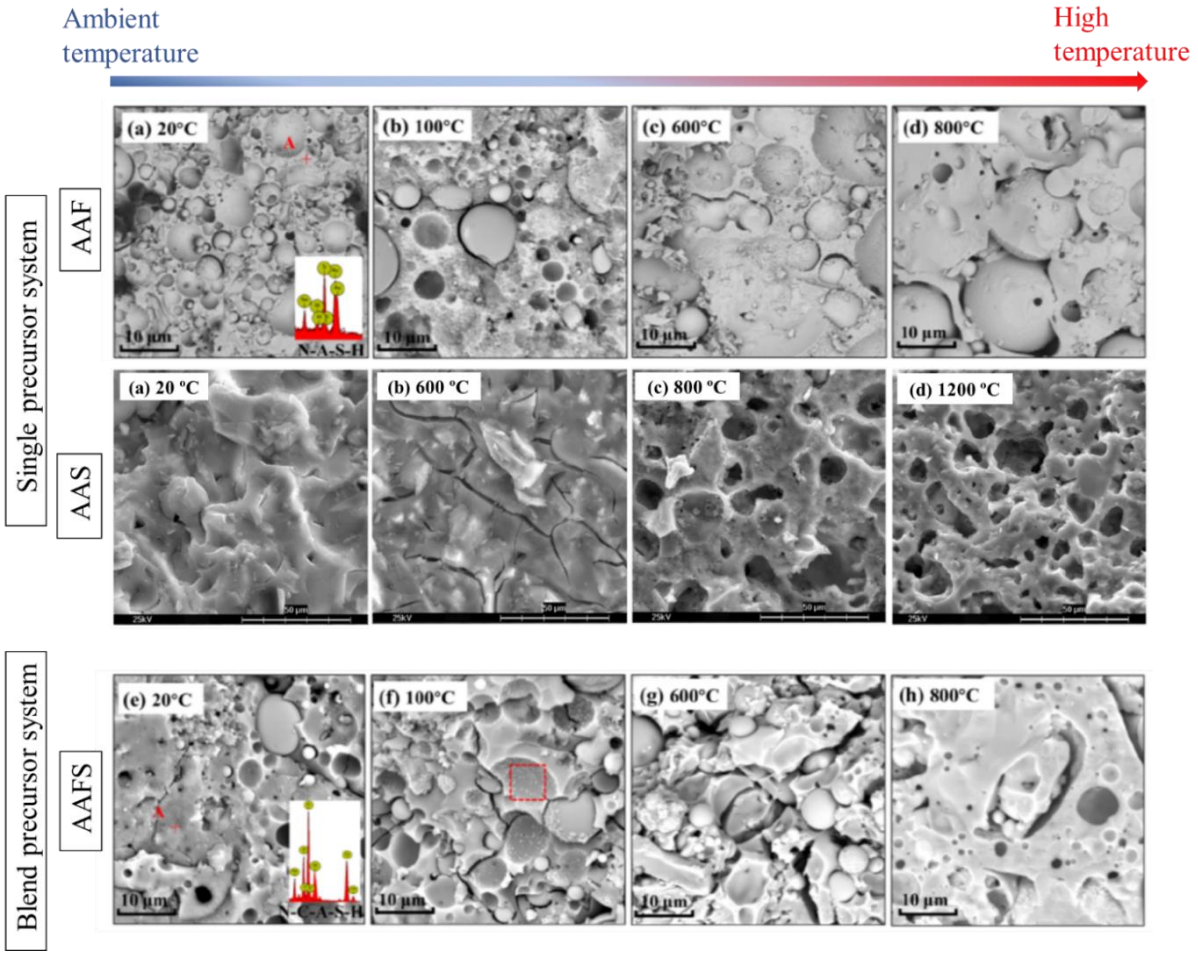

Figure 2.22. SEM micrographs of AAF, AAS and AAFS samples exposed to different temperature levels, (adapted from [22, 318]).

From 200 ºC to 400 ºC, further evaporation of bound moisture between alkali-activated binder and unreacted fly ash particles occurs with the development of microcracks [30]. As the temperature goes up from 400 ºC to 600 ºC, more porous internal structures can be detected with either few or nonreacted fly ash particles remaining [30, 31]. Also, sintering reaction and densification take place at about 550 ºC and above [5]. At 800 ºC, further augment of voids and

thermal stress induced microcracks could lead to a significant loss of strength of AAF matrix [26, 30, 31]. AAF with class F fly ash has a looser and more honey-comb shaped structure, while AAF with class C fly ash exhibits a denser matrix [30]. This indicates the influence of precursor type and mix proportion on the microstructural features of AAF at elevated temperatures. Above 800 ºC, the melting of matrix with a smoother texture and less impurities can be detected in AAF due to viscous sintering that heals the microcracks at high temperatures [10, 32, 331, 332]. Figure 2.23 illustrates the pore size distribution of AAF at elevated temperatures. The main peak shifts from a smaller pore size (< 0.1 µm) to a larger one (> 1 µm) after exposure to 800 ºC, indicating the sintering and densification effect on the pore structure changes of AAF. New crystalline phases such as albite and nepheline can also be observed with the disappearance of hydroxysodalite and herschelite at this temperature level, and there is an increase in pore size and volume compared to the unexposed AAF at 800 and 1000 ºC.

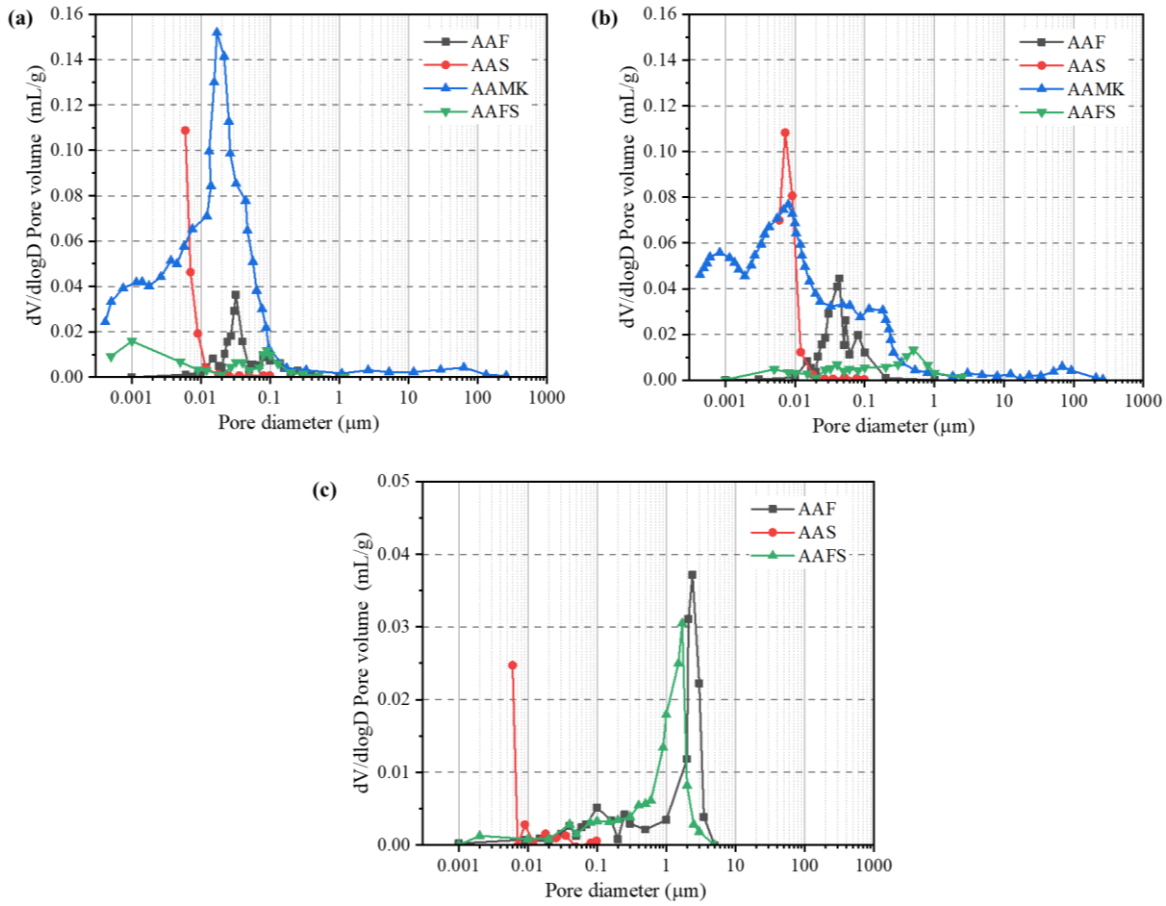

Figure 2.23. Pore size distribution of AAC at (a) ambient temperature and exposed to (b) 400 ºC and (c) 800 ºC (data from [22, 318, 333]).

In AAS concrete, the matrix shows a smooth surface with some unreacted slag particles and microcracks at ambient temperature [38, 334]. C-A-S-H gel is structurally stable due to the adhesive forces from those saturated small pores [318]. As temperature rises, the moisture is gradually released from the small pores and migrates inside AAS matrix. The evaporation of free moisture and slight decomposition of C-A-S-H gel lead to the development of microcracks and deterioration of AAS matrix at up to 200 ºC [318]. From 200 ºC to 600 ºC, the initiation and propagation of microcracks take place due to the dehydration of binder and reduction of C-S-H gel [38, 318, 319]. Consequently, the strength could be further degraded due to the loss of water [318]. Partially reacted slag particles appear in various sizes with irregular shapes and the amount of unreacted slag particles decreases accordingly. Upon exposure to 600 ºC, the pore size and volume increase with the appearance of larger cracks [38, 318, 319]. The stability of C-A-S-H structure suffers from high temperature exposure and the dehydroxylation and crystallisation happen, leading to the damage in AAS matrix as the temperature rises from 600 ºC to 800 ºC [38]. The phase transformation (e.g., formation of akermanite) at 800 ºC correspondingly results in the evolution of microstructure and mechanical properties, as akermanite has a week and porous structure that leads to densification, increase of pore sizes and strength loss of AAS at this temperature level [62, 318-320, 335]. From 800 ºC to 1000 ºC, the shrinkage of gel and densification occur in AAS matrix due to melting and sintering, leading to the formation of a smooth and compact structure [38]. Less microcracks along with the reduction of gel pores in a connected network can be observed at this stage, implying the self-healing of AAS matrix after exposed to 1000 ºC [38, 327, 336].

Blend precursor system

At ambient temperature, unreacted fly ash and slag particles can be found within AAFS matrix. The unreacted fly ash particles exhibit the aforementioned quartz and mullite, whereas calcite can be identified in the unreacted slag particles [25, 46, 88, 123, 337]. When the temperature increases to 200 ºC, the porosity of AAFS matrix drops (reduction of fraction of pores with diameter of 5-10 nm) along with the strength rise, which can be ascribed to the formation of an additional highly cross-linked gel product, making the matrix denser [34, 56]. At 300 ºC, the microstructure of the gel is stable without obvious changes. For AAFS containing 40-50% slag, there exist C-A-S-H type gel and/or N-(C)-A-S-H gel with a slight decomposition of C-A-S-H

gel [25, 32]. For AAFS matrix with low slag content (≤ 20%), the primary binding phase of low calcium N-(C)-A-S-H type gel is structurally stable at 300 ºC [32], while the remnant fly ash particles continue to react (i.e. a shift of T-O bond towards a higher rate of recurrences indicating the strengthened Si content in N-A-S-H gel [25, 338]), which promotes the formation of N-A-S-H or N-(C)-A-S-H gel, leading to a more homogeneous structure with strength gain at 300 ºC [32].

From 200 ºC to 400 ºC, the porosity of AAFS (pore diameter of 0.005-6 μm) is further reduced and the reaction of the residual fly ash particles continues at elevated temperatures, leading to the rise in strength [34]. On the other hand, the strength of AAFS is found to decrease at 300-500 ºC, due to the moisture evaporation and the replacement of Ca by Na that degrades the thermal stability of zeolite materials at elevated temperatures [32, 318]. Moreover, as the slag content in AAFS drops from 40% to 20%, the strength loss reduces, while AAFS with higher slag content is less stable at elevated temperatures as the slag has a high CaO content with relatively lower glass transition point [32]. After exposed to 600 ºC, further dehydration of C-A-S-H phase takes place with the presence of crystalline phases of akermanite and gehlenite, while the formation of anorthite is associated with N-(C)-A-S-H gel [34]. At 600 ºC, calcite disappears in AAFS with 50% slag and N-(C)-A-S-H is recognised as the dominant binder gel in AAFS with 10% slag [25].

At 800 ºC, the pore size of AAFS matrix increases (pore diameter > 6 μm) with the disappearance of C-S-H phase [34]. The C-A-S-H gel produced from slag is fully dehydrated along with the crystallisation of akermanite and gehlenite, while the N-A-S-H gel generated from fly ash is partially crystallised with the formation of nepheline and the N-(C)-A-S-H gel come from both fly ash and slag is crystallised to form anorthite [34]. The porosity of AAFS matrix declines with the increase of slag content from 25% to 75% [56], as the fly ash-related products of anorthite and nepheline have porous structure. Therefore, the fly ash/slag ratio can greatly affect the crystalline phases and microstructure of AAFS. In general, the increase of slag content in AAFS can result in a higher strength loss due to thermal instability of CaO, but it can also lead to a denser and more compact microstructure, reducing the deterioration of AAFS at elevated temperatures [32]. In comparison with AAF, AAFS exhibits a higher proportion of gel pores < 0.01 μm, indicating that a higher degree of reaction takes place in AAFS matrix at ambient temperature, as seen in Figure 2.22(a) [22]. Similar pore size

distribution of AAFS and AAF can be observed at 800 ºC, where the main fraction of pores is at around 2 µm, owing to further geopolymerisation, contraction of gel matrix and sintering effect.

2.5.4 Thermal properties

Thermal stability

Thermal stability of AAC plays a crucial role in its behaviour at elevated temperatures, which can be estimated through thermogravimetric analysis (TGA). Figure 2.24 presents the mass loss of PCC and different types of alkali-activated paste at elevated temperatures [10], indicating that AAF paste exhibits the lowest mass loss of less than 2% in comparison with AAMK, AAS and PCC paste. The majority of mass loss of AAF paste occurs at 100-200 ºC, which can be ascribed to free water evaporation [10, 27, 339]. After the initial decline, the mass of AAF paste gradually tends to be stable at 250-800 ºC [27]. The slight mass loss at this stage can be attributed to the liberation of water during further geopolymerisation and the formation of new crystalline phases such as albite and nepheline [10].

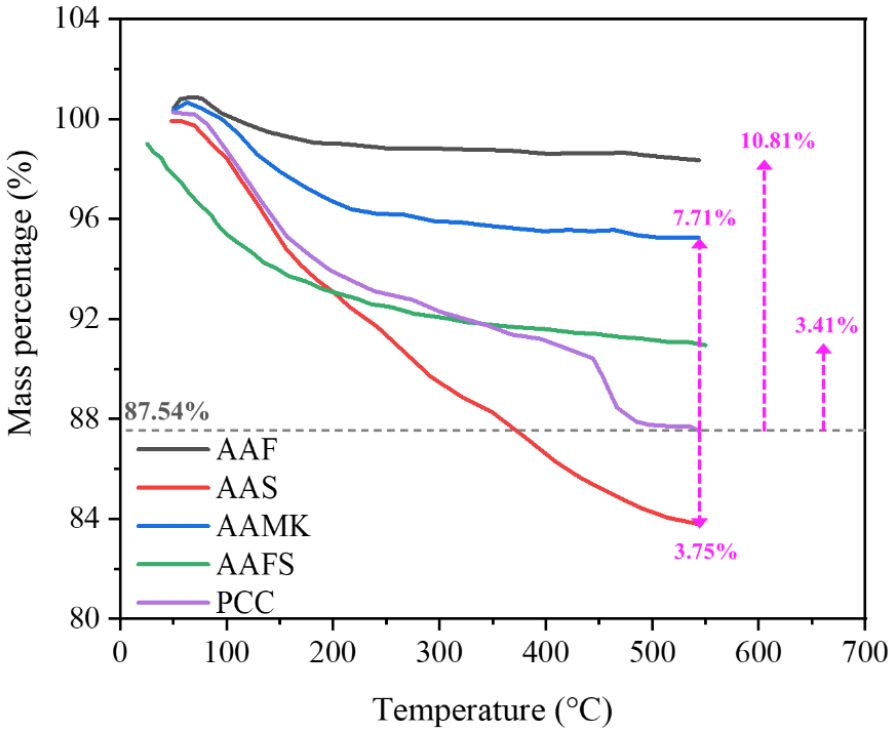

Figure 2.24. Mass loss of AAC and PCC at elevated temperatures (adapted from [10, 22]).

Compared to AAF, AAMK paste performs slightly worse with a mass loss of approximately 4.75%. The relatively higher water/solid ratio and the volatilisation of free water and absorbed water in aluminosilicate gel phases were the main reasons for the mass loss in AAMK paste [10]. AAS paste shows the largest mass loss of roughly 16.21% compared to AAF and AAMK pastes, which can be ascribed to the volatilisation of both physically absorbed and chemically bonded water. With the increase of temperature until 550 ºC, AAS exhibits a gradual mass loss (3.75% more than PCC), while PCC experiences a rapid mass loss at 450 ºC due to the dehydration of $Ca(OH)_2$ [10]. As mentioned in Section 4.1.1, AAS has less thermal stability compared to AAF due to the high calcium content, leading to the formation of additional hydrated phases. Furthermore, a sudden mass loss of AAS paste can be found at around 800 ºC, corresponding to the decomposition of calcite [340]. For AAFS paste, the sensitivity of mass loss to high temperatures is dependent on the incorporation of slag. The increase of slag content in AAFS paste can result in an increase of the mass loss [32]. Thus, not all the alkali-activated materials can possess better thermal resistance than PCC in terms of mass loss (which is around 12.46%) and the choice of precursor can significantly affect the thermal stability of AAC at elevated temperatures.

Thermal deformation

At elevated temperatures, the thermal deformation of AAC needs to be considered, which can influence the thermal compatibility among different phases in AAC. As per previous studies [53, 54, 341, 342], the thermal expansion of AAF consists of a few stages, as illustrated in Figure 2.25. From ambient temperature to around 100 ºC, there is a slight expansion in AAF due to water evaporation. At 100-300 ºC, a capillary shrinkage takes place, corresponding to the dehydration of AAF matrix. At 300-550 ºC, the contraction of AAF matrix continues. As the temperature rises to around 650 ºC, viscous sintering can consume fly ash particles in AAF, leading to densification and thus shrinkage of matrix [22]. After 800 ºC, the collapse of AAF matrix can be detected. Compared to sodium-based AAF, potassium-based AAF exhibits lower mass loss and volumetric shrinkage due to the higher content of amorphous phase [314]. AAF shows relatively better thermal stability without significant mass loss compared to other types of AAC such as AAS and AAFS, which can be attributed to the stable gel structure with relatively low calcium content as mentioned before [22, 53].

For AAS, a slight thermal expansion can be observed from ambient to 150 ºC, which is similar to that of AAF, followed by thermal contraction until 800 ºC. A relatively significant thermal shrinkage of more than 25% can be detected in AAS, resulting from the thermal incompatibility and aforementioned phase transformation within AAS matrix, which is around 8 times greater than the thermal shrinkage of AAF at 800 ºC [343]. AAMK exhibits a less significant thermal contraction of approximately 13% at 800 ºC compared to AAS, which can be attributed to the capillary strain, dehydroxylation reactions and sintering and densification effects after exposure to 105-800 ºC [321].

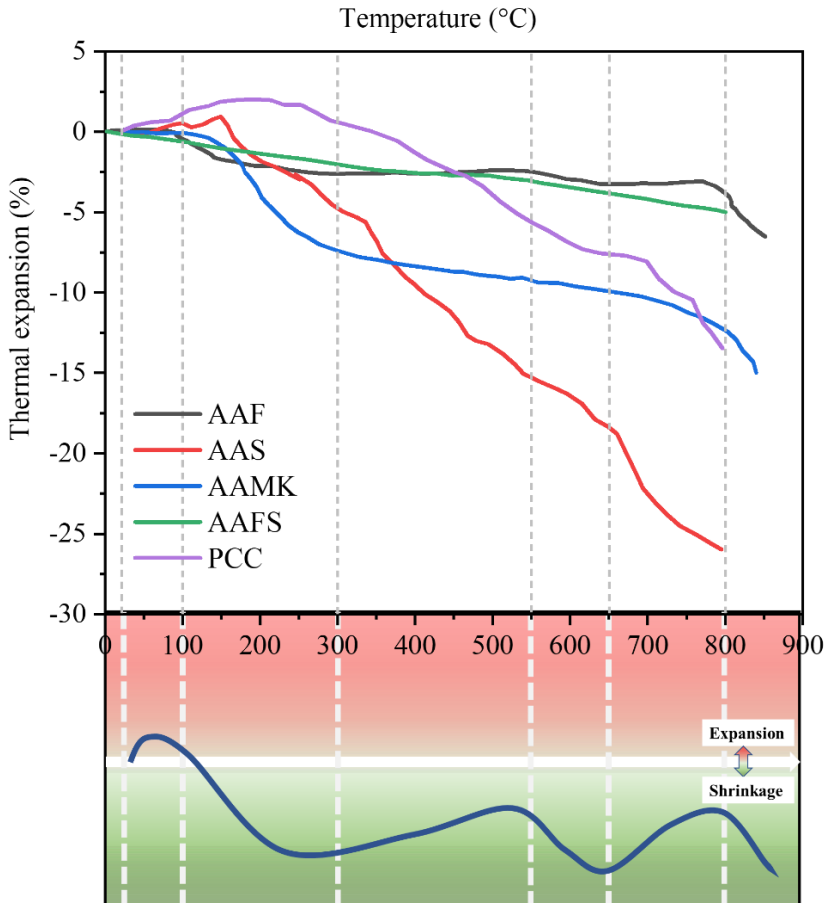

Figure 2.25. Thermal deformation of AAC and PCC at elevated temperatures, along with a schematic illustration for AAF (adapted from [18, 53, 321, 343, 344]).

In the blend precursor systems, AAFS with 50% slag has a similar thermal strain of roughly 4% in comparison with that of AAF after exposed to 800 ºC due to the inclusion of slag that leads to a greater thermal shrinkage [344]. For alkali-activated fly ash-metakaolin pastes, the similar thermal deformation can be detected compared to AAF, where a sharp shrinkage takes

place at 100-300 ºC. Contrarily, a slight thermal expansion can be observed in alkali-activated fly ash-metakaolin mortars from ambient temperature to 800 ºC, which can be ascribed to the combined effect of both expansion of aggregates and contraction of paste. This can also result in the development of microcracks between different phases and thus the microstructural evolution of AAC.

Single precursor system

A summary of the existing studies on the relative compressive strength (i.e. ratio of residual compressive strength to original compressive strength) of AAF paste, mortar and concrete at various temperatures is presented in Figure 2.26. AAF tends to gain strength at elevated temperatures (≤ 600 ºC) due to the interconnected small pore network that facilitates the release of moisture pressure at heating and further geopolymerisation that activates the unreacted fly ash particles [5]. Sintering reaction also happens at elevated temperatures, which can lead to stronger inter-particle bonding to enhance strength and offset the strength loss induced by crack initiation and propagation or facilitate AAF matrix to accommodate the deformation of aggregates [61, 345, 346]. After 600 ºC, the compressive strength of exposed AAF experiences a moderate or significant decline compared to the unexposed counterpart. The strength loss of AAF paste is lower than that of AAF concrete as the inclusion of aggregates can lead to thermal incompatibility between AAF paste and aggregates in concrete [27]. At elevated temperatures, AAF matrix tends to experience shrinkage while aggregates undergo expansion, which can thereby cause damage to the microstructure and reduce the compressive strength [27, 347, 348].

The type and size of aggregates can affect the compressive strength loss of AAF concrete. The inclusion of basalt and slag based aggregates leads to a strength loss of 58.4% and 64.6% respectively in AAF concrete after exposure, which can be explained by the closeness of the thermal expansion of these aggregates compared to AAF paste and the original strength characteristics of these aggregates, while other types of aggregates such as quartz aggregates, expanded clay aggregates, and lightweight aggregates were also used [305, 332, 345, 349-351]. Quartz aggregates can cause obvious strength loss due to the large coefficient of thermal expansion, while expanded clay aggregates with a relative lower thermal expansion and porous structure can help mitigate the strength loss [332, 345]. The use of natural lightweight aggregates (e.g., basaltic pumice) can improve the residual compressive strength [24, 50, 305,

332]. Moreover, the smaller size (2-10 mm) of aggregates can cause explosive spalling in AAF concrete at up to 505 ºC, whereas about 30% of residual strength still exists for that with larger size (10-20 mm) of aggregates [27]. The high stiffness of aggregates can restrain shrinkage of AAF at elevated temperatures and the induced radial and tangential stresses surrounding the aggregates leads to cracking [352]. As it is hard for smaller aggregates to produce effective aggregate bridging due to lack of shape irregularity, the use of appropriate aggregate size and various grading of aggregates can help retain the compressive strength of AAF after exposure to high temperatures.

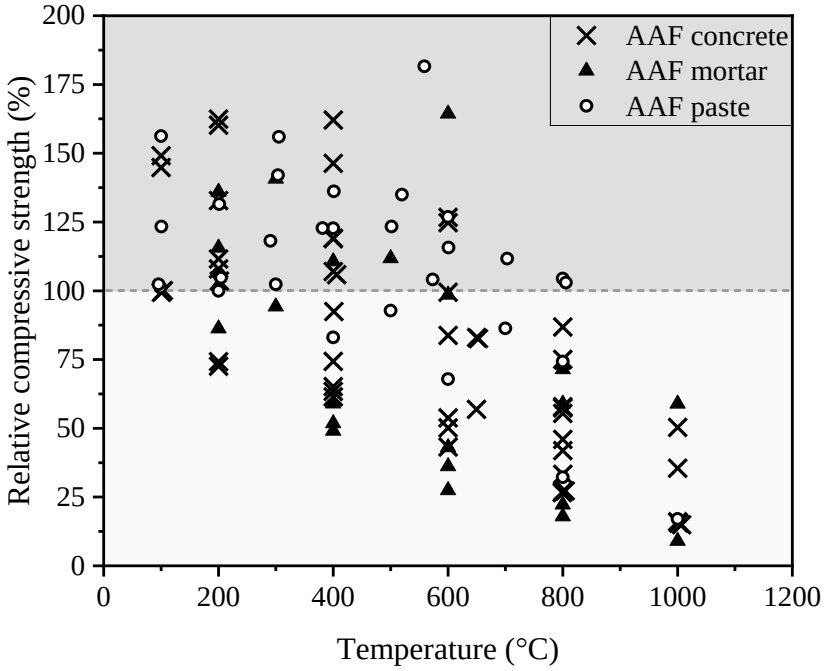

Figure 2.26. Relative compressive strength of AAF paste [24, 27, 28, 35, 339, 353], mortar [25, 314, 353-357] and concrete [26, 31, 50, 354, 358-362].

Apart from aggregate, the mix proportion of AAF paste can also affect the mechanical performance of AAF concrete at elevated temperatures where Si/Al ratio is one of the most crucial factors. AAF concrete with a higher Si/Al ratio (2.2) performs much better than that with a lower Si/Al ratio (1.7) [306], and thus raising the Si content in alkali-activated mixtures is recommended. In addition, the Si/Al ratio ranging from 2.0 to 3.0 can promote strength loss by up to 80%, whereas a ratio of less than 2.0 is more optimal with a 132% strength increase compared to the unexposed specimen [363]. This indicates that Si/Al ratio is a critical parameter in alkali-activated formulations, which needs to be tailored for AAF to achieve a desirable

compressive strength after exposure [5]. Other factors (e.g., curing condition) can also affect the change of compressive strength of AAF at elevated temperatures. The experimental study on the effect of ambient and heat curing on the mechanical properties of AAF after high-temperature exposure indicated that the ambient-cured AAF concrete experienced lower strength deterioration than the heat-cured one after exposed to 1000 ºC [26]. Thus, the residual compressive strength of AAF at elevated temperatures is dependent on many factors such as compatible aggregates and optimal alkali-activated formulation.

Figure 2.27 displays the relative compressive strength of AAS paste, mortar and concrete at elevated temperatures, indicating that the compressive strengths of AAS paste, mortar and concrete reduce significantly against exposure temperature, where the highest strength loss appears at around 800 ºC [25, 38, 318, 320, 325, 328, 332, 343, 364-369]. The retention strength ranges from 0 to approximately 50% at this temperature level. This can be attributed to the dehydration of AAS matrix and decomposition of calcite [38]. Some of the specimens exhibit an enhanced compressive strength at 200 ºC and 400 ºC, which can be mainly ascribed to the acceleration of hydration process by heating, activating the slag particles with strength gain [320, 364]. It is noteworthy that after obvious decline of strength at 800 ºC, AAS pastes and mortar specimens start to gain strength when the temperature continues to rise until 1000 ºC. This can be explained by the densification of AAS matrix during viscous heating, which causes a reduction of voids and thereby enhances the compressive strength [38]. Also, the formation of new crystalline phases such as gehlenite and larnite contribute to the densification of AAS after high temperature exposure. Among AAF, AAMK and AAS, AAS tends to have the lowest thermal/fire resistance whereas AAF performs best and thus can be regarded as a good choice in high-temperature resistance applications. This is also consistent with that presented in the previous section that AAF shows the best thermal stability compared to other types of AAC.

Figure 2.28 shows the experimental results of relative compressive strength of AAMK paste and mortar as a function of exposure temperature collected from literature [321, 332, 370-373], indicating that AAMK possesses a dense and homogeneous microstructure without prominent pore structure evolution at elevated temperatures [373]. Thus, the moisture is prone to be trapped inside the dense pore structure, leading to the accumulation of pore pressure and thus a significant strength reduction. Most results of the relative compressive strength are below 100% at elevated temperatures ranging from 100 ºC to 900 ºC, suggesting that the compressive

strength of AAMK after exposure is retained or gained less than that of AAF. This is because sintering reaction takes place in AAF matrix at elevated temperatures, which can rearrange the pore structure with evolution of pores with large size to smaller ones. A large number of small pores can provide channels for free water and vapour to escape without pore pressure build-up [373, 374], while metakaolin-based AAC matrix tends to have a higher moisture content with a denser pore structure compared to AAF, which would be subjected to a higher risk of pore pressure induced damage at elevated temperatures [5].

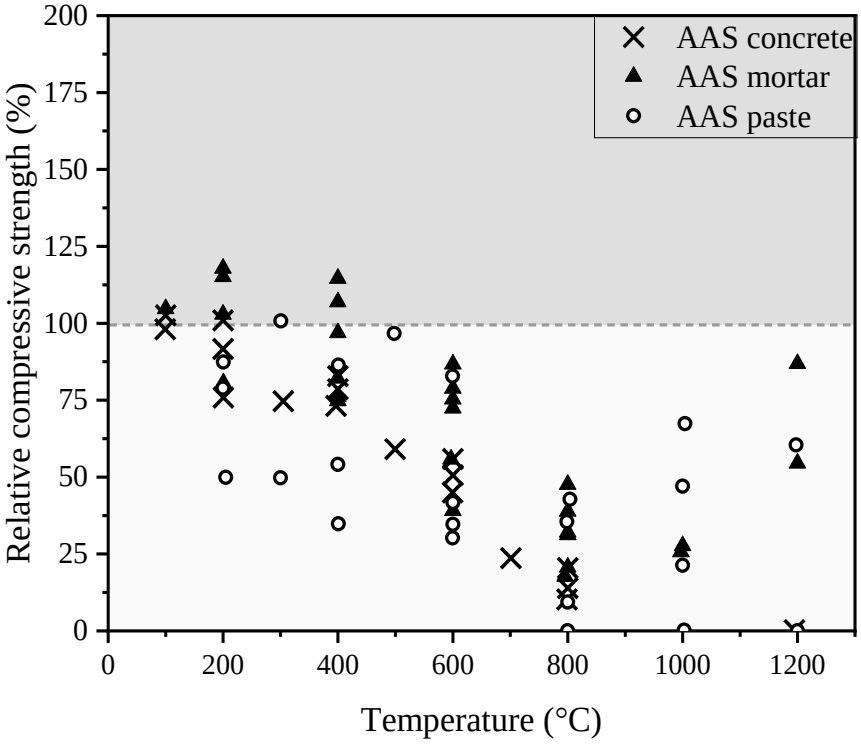

Figure 2.27. Relative compressive strength of AAS paste [25, 38, 318, 368, 369], mortar [320, 325, 328, 332, 366, 367] and concrete [343, 364, 365].

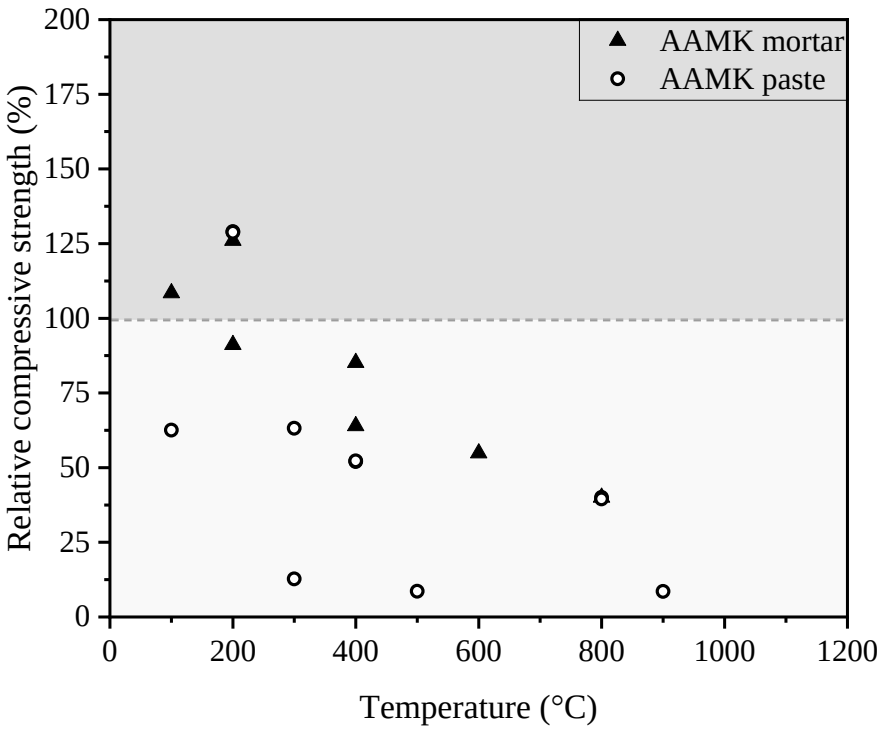

Figure 2.28. Relative compressive strength of AAMK paste [321, 371-373] and mortar [332, 370].

Blend precursor system

Figure 2.29 presents a summary of the relative compressive strength of AAFS paste, mortar and concrete at elevated temperatures, indicating a similar change trend as that for AAS system, with a slight increase of residual strength after exposure to 200-600 ºC. The most essential factor that affects the mechanical behaviour of AAFS at elevated temperatures is the fly ash/slag ratio. The effect of fly ash/slag ratio by weight on relative compressive strength of AAFS is depicted in Figure 2.30. AAF concrete and AAS concrete have the highest and lowest retention strength at up to 600 ºC, respectively, while the residual strength of AAFS concrete is in between those two. Moreover, the increase of initial strength could lead to a more significant strength loss after exposure as the slag content increases from 0 to 100% [5, 375]. Ductility of AAFS matrix is a governing factor in the level of thermal incompatibility induced damage. AAFS matrix with higher ductility can better accommodate the thermal shrinkage and expansion that occurs in different phases and thus reduce the compressive strength loss after exposure to high temperatures [5, 23].

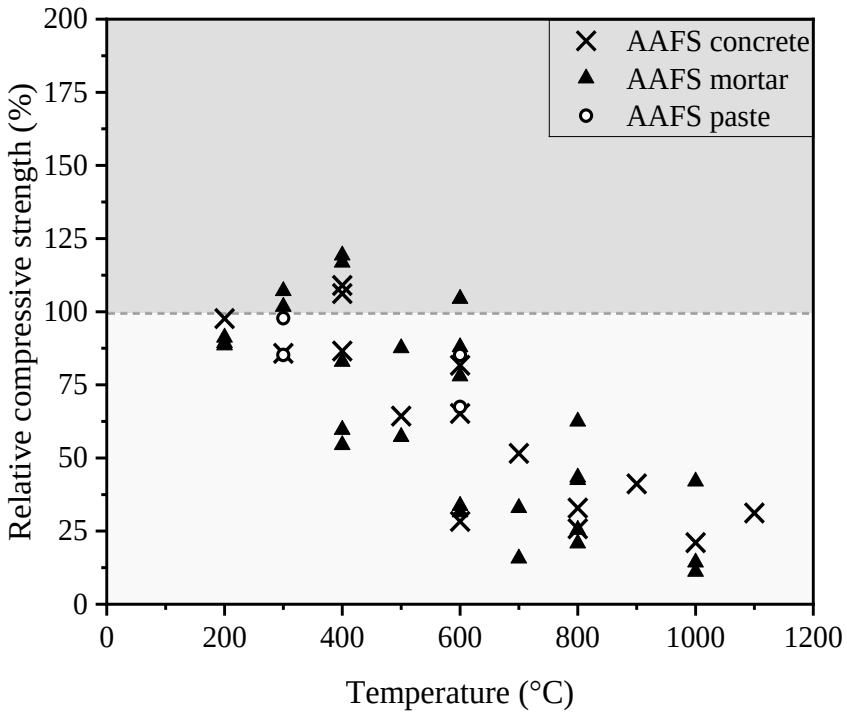

Figure 2.29. Relative compressive strength of AAFS paste [25], mortar [25, 32, 328, 355, 376] and concrete [57-60].

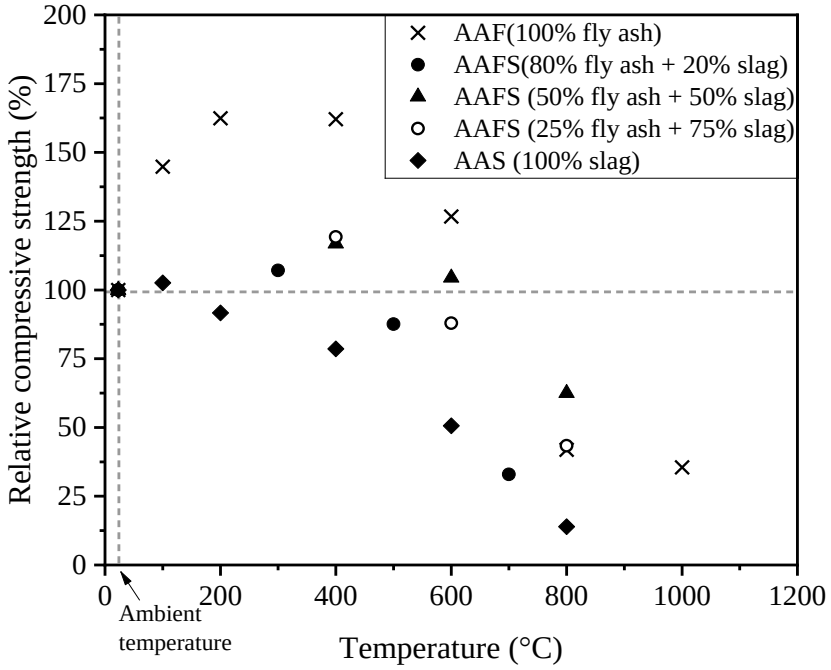

Figure 2.30. Effect of fly ash/slag ratio on the relative compressive strength of AAF [26], AAFS [32, 372] and AAS [305] concrete at elevated temperatures.

2.5.5 Tensile strength

Figure 2.31 displays the residual tensile strength of AAC obtained from literature [57, 347, 360, 377, 378]. Similar to relative compressive strength, AAC containing fly ash including AAF, AAFS and alkali-activated fly ash-metakaolin concrete exhibits a slight enhancement of tensile strength at elevated temperatures until 400 ºC. This can be ascribed to the further geopolymerisation that activates the unreacted precursor particles inside the matrix as well as the occurrence of sintering reaction. Without fly ash, the tensile strength of AAS declines continuously, which is consistent with the compressive strength change with exposure temperature. A combined effect of further geopolymerisation and thermal incompatibility is regarded as the cause for the tensile strength drop at elevated temperatures, similar to the compressive performance.

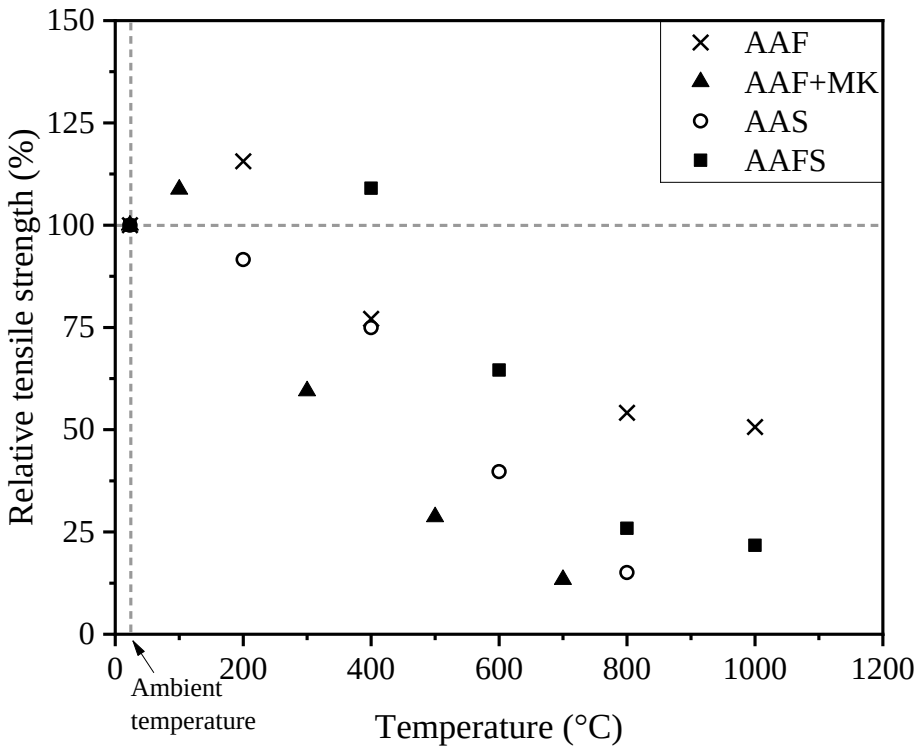

Figure 2.31. Relative tensile strength of AAC at elevated temperatures [57, 347, 360, 377, 378].

2.5.6 Flexural strength

The relative flexural strength of different types of AAC at elevated temperatures is illustrated in Figure 2.32. A similar tendency can be observed for tensile and flexural strengths of AAC at elevated temperatures. In comparison with compressive strength, flexural strength is more sensitive to the initiation and propagation of micro-cracks inside AAC matrix [340]. Therefore, the micro-cracks induced by matrix shrinkage when exposed to high temperatures can cause a comparative drop in flexural strength of AAC [320], as seen from all specimens in Figure 2.32. Moreover, the microstructural evolution (e.g., pore structure characteristic changes) can significantly affect the flexural strength degradation at elevated temperatures [347]. The large number of small pores distributed in AAF can accommodate the pore pressure induced by heating to reduce the flexural strength loss, while other types of AAC may show a more rapid decline when the exposure temperature rises.

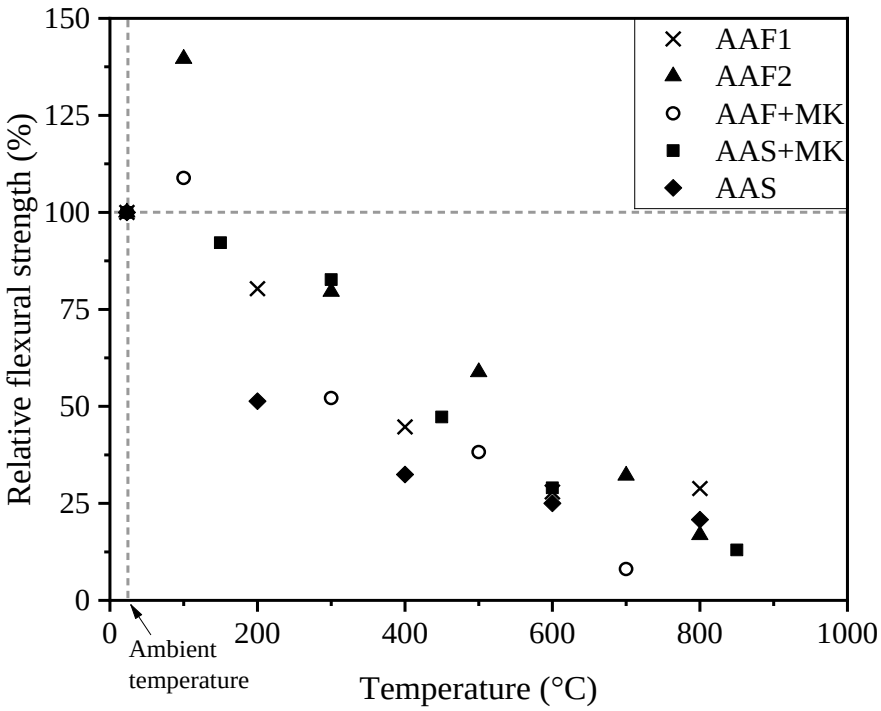

Figure 2.32. Relative flexural strength of AAC at elevated temperatures [35, 330, 347, 356, 366].

2.5.7 Damage mechanisms

Up to now, the damage mechanisms in PCC has been extensively studied with a variety of approaches proposed to improve its thermal and fire resistance, whereas very few attempted to explore the inherent mechanisms in AAC at elevated temperatures. The proposal damage mechanisms of both types of concrete are summarised below.

Portland cement concrete

The damage mechanism of PCC at elevated temperatures has been extensively studied. Figure 2.33 displays a schematic illustration of pore pressure induced damage evolution in PCC at elevated temperatures. In general, up to 100 ºC, the concrete specimen is fully in the moist zone with free-water evaporation. When the temperature continues to rise, the dehydration of hydration products in concrete takes place from the heated surface to the inner region.

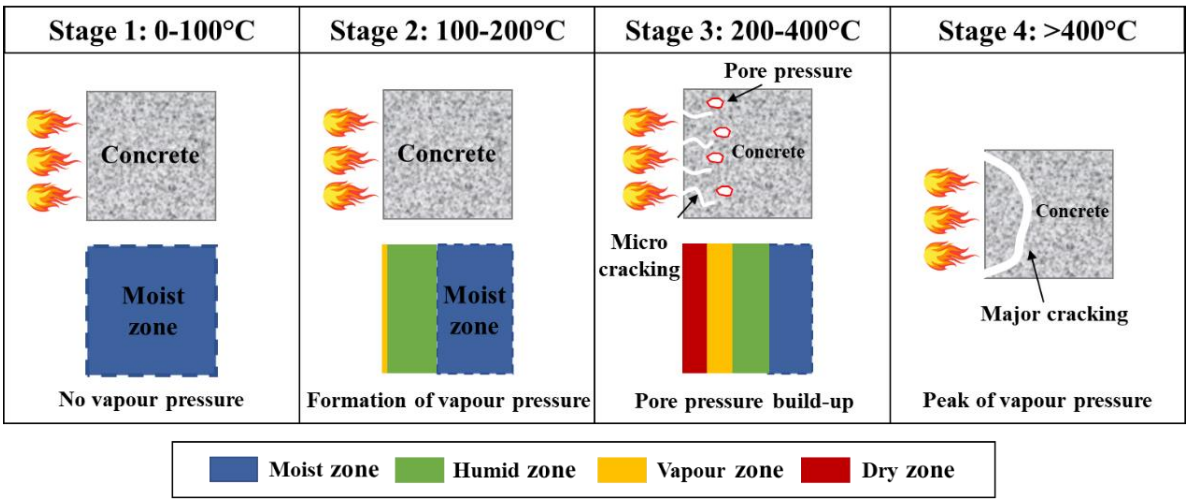

Figure 2.33. Schematic illustration of damage evolution in Portland cement concrete (PCC) at elevated temperatures (adapted from [384]).

Afterwards, the decomposition of C-S-H gels starts and the chemically bounded water is released. As the moisture flows towards the cold side of the concrete, the damage would occur with the initiation of cracks at the region with moisture accumulation [284, 291, 379-383]. It is widely accepted that the high-temperature-induced damage of concrete can be mainly attributed to pore pressure build-up from trapped moisture inside matrix and thermal stress. Thus, three

mechanisms were proposed to explain the damage evolution in PCC system, including pore pressure induced damage, thermal stress induced damage, and phase transformation.

The mechanism of pore pressure induced damage is associated with air and moisture migration in concrete. At elevated temperatures, moisture travels towards both directions of the heated surface and the inner matrix. Since the temperature remains lower inside the concrete, moisture can condense to form a "moisture clog". With the accumulation and expansion of condensed water vapour, a significant amount of potential energy is formed inside the pore network of concrete. Saturated vapour pressure, dilation of liquid water and partial pressure of enclosed air are all retained in the pores [385]. Consequently, the pore pressure builds up and the pore pressure induced stress would continue to increase until the maximum stress that can be maintained within the structure is exceeded, as a result of which damage would occur in concrete due to a violent release of energy.

However, pore pressure induced damage is not the only cause that leads to concrete failure [386]. The measured pore pressure can be relatively lower than tensile strength of concrete matrix, while the damage in concrete mainly results from the thermal stress induced by the temperature gradient inside concrete, i.e. the second mechanism [387, 388]. In this case, the damage occurs due to concrete failure in compression at the heated surface. The exposed surface experiences not only compressive stresses but also tensile stresses from the inner parts due to restrained thermal expansion [385]. Thereby, the heating rate has a pronounced effect on the temperature gradient in concrete, which directly results in thermal stress induced damage. A higher heating rate tends to cause a greater temperature gradient.

From the previous studies on damage mechanisms of concrete at elevated temperatures, it is challenging to define the temperature-induced damage by a single factor, whereas the combined effect of both pore pressure and thermal stress induced damage is considered [389]. During heating, the thermal stress forms on the exposed surface, leading to the initiation of multi-cracks parallel to the heated surface, which are then filled and saturated with vapour pressure resulting in damage in concrete [385]. Furthermore, the heating rate can play a significant role in the damage mechanisms of concrete exposed to elevated temperatures. Following the standard fire heating rate, thermal stress induced damage is the dominant factor, while pore pressure induced damage is the main contributor to concrete failure if the slow heating rate is employed [388].

After exposure to 100 ºC, physically bound water evaporates and chemically bound water can be released from the C-S-H layer, along with the decomposition of C-S-H gel that leads to an unstable structure. At 400-600 ºC, calcium hydroxide (CH) in PCC can decompose into calcium oxide and water. After 700 ºC, the decarbonation of calcium carbonate ($CaCO_3$) takes place. When the temperature reaches 800 ºC, all chemically bound water can be fully evaporated [379].

Alkali-activated concrete

In comparison with the PCC system, AAC exhibits better high-temperature resistance [10, 194, 390]. This is because alkali-activated aluminosilicate gels in AAC differ from cement paste in PCC [27, 194]. A sodium or potassium-based alkaline activator is needed to react with silica- and alumina-rich phases, due to the non-hydrated aluminosilicate gel binding phases in AAC matrix, leading to the generation of gels without much chemically bounded or physically absorbed water compared to C-S-H gels in PCC [10]. Thus, an open pore structure of AAC matrix is formed, which can result in a higher resistance to withstand elevated temperatures of up to 600-1200 ºC with less strength loss compared to PCC [24, 391].

The damage mechanisms in AAC at elevated temperature were found to be similar to PCC system, which include: (1) thermal incompatibility, (2) pore pressure build-up, and (3) phase transformation [23], as illustrated in Figure 2.34. The first mechanism occurs when heat flow transfers in AAC. As different phases in AAC (i.e. matrix and aggregates) have different thermal conductivity and thermal capacity, there exist non-uniform distribution of heat flow and inhomogeneity of thermal stress inside AAC, leading to the initiation of cracks and strength degradation [23]. At the initial state, there is no expansion or shrinkage in AAC. When exposed to elevated temperatures, the expansion of aggregates and contraction of AAC matrix take place. The microcracks are then formed inside AAC due to the reversible expansion and irreversible shrinkage after heating, which have a detrimental impact on residual strength of AAC [26]. However, it was found that the mechanical performance of AAF at elevated temperatures was unstable. As the temperature rises, viscous sintering takes place, which denotes the collapse of nano-pores and development of interparticle bonding, resulting in the self-healing of micro-cracks and densification of concrete matrix [392]. Moreover, further

chemical reaction can enhance the strength of AAF, whereas the thermal incompatibility induced damage has a reverse effect [23].

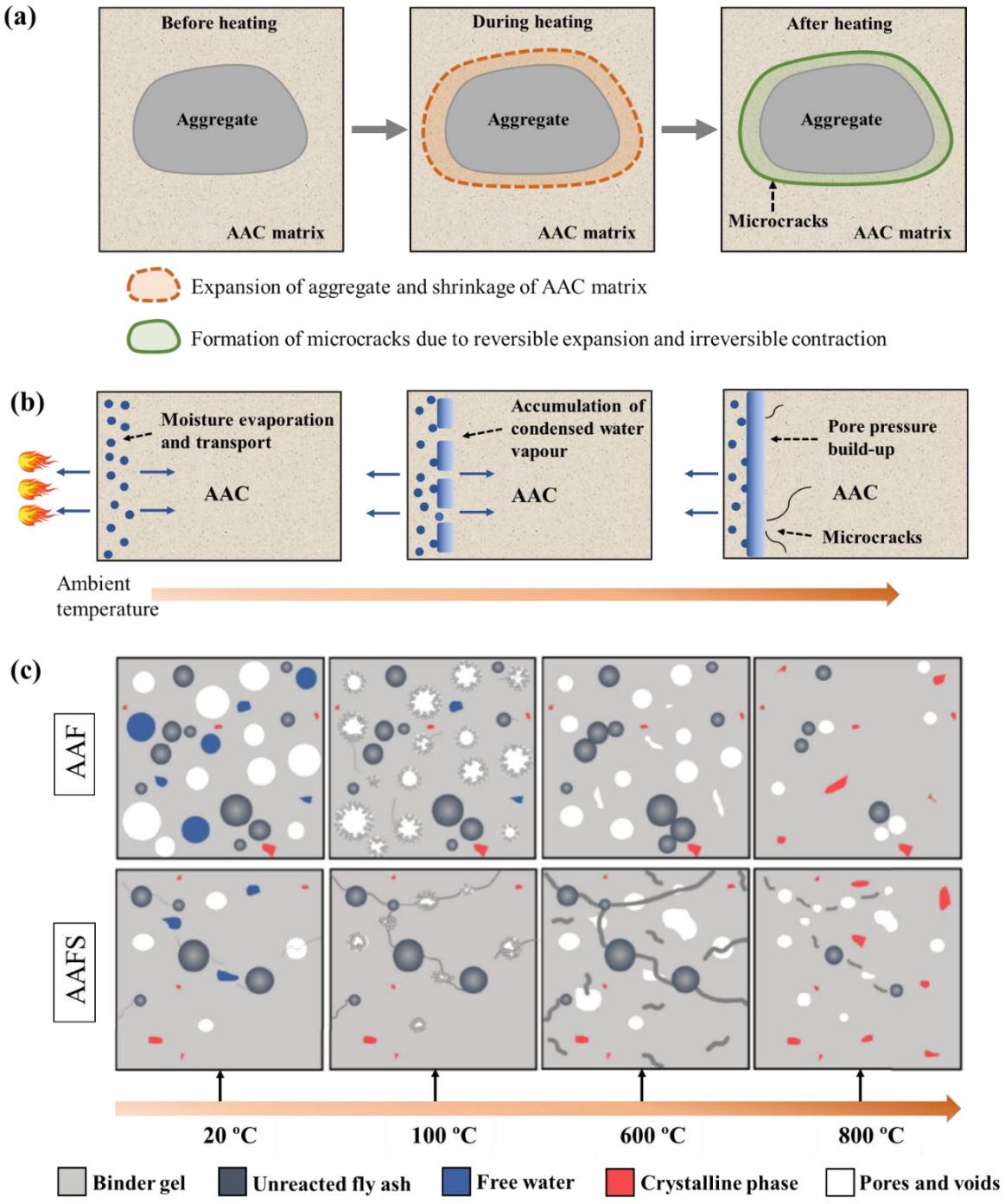

Figure 2.34. Damage mechanisms of AAC at elevated temperatures: (a) thermal incompatibility, (b) pore pressure build-up, and (c) phase transformation (adapted from [22, 26, 384, 393]).

The pore pressure effect is associated with the transportation of water/moisture and accumulation of pore pressure as mentioned above for PCC, which is considered as one of the main contributors to the deterioration of AAC during exposure to high temperatures. The trapped moisture and vapour can result in cracking and damage to the pore structure. For different alkali-activated systems, AAF concrete performs better than AAMK at elevated temperatures, due to more small pores in AAF concrete with an inter-connected network that can hinder the vapour pressure build-up in pores [27].

The phase transformation is related to the effects of different raw materials, alkali cations and calcium content and can form a combined effect together with pore pressure build-up on AAC at elevated temperatures [17, 23, 394]. Figure 2.34 displays a comparison of the damage evolution in single and blend precursor systems (i.e. AAF and AAFS) at elevated temperatures. At ambient temperature, AAF has a porous structure with some unreacted fly ash particles and free water. At 100 ºC, the pore pressure induced by water evaporation can be released through the porous network in AAF without formation of major cracks. Meanwhile, further geopolymerisation takes place, leading to strength gain as the newly formed gels can fill the cracks and voids left by free water. After exposure to 100-600 ºC, AAF remains stable with no significant loss of structural integrity and change of crystalline phases. The shrinkage of AAF matrix and viscous sintering can be detected at 600 ºC and new crystalline phases are formed after 800 ºC. The re-crystallisation process can weaken the gel skeleton with a less compact texture, while the sintering reaction can continue to compact and strengthen the AAF matrix by filling the pores and cracks [22]. Thus, there is a combined effect of both strength gain and loss on AAF, which may retain the residual strength of AAF when exposed to 800 ºC.

Regarding the blend precursor systems, AAFS exhibits a relatively more compact structure with less unreacted particles and residual water before high temperature exposure, which can be ascribed to the incorporation of slag that accelerates the reaction process, resulting in a denser matrix compared to AAF [22]. Some microcracks can be observed in AAFS matrix at this stage. When exposed to 100 ºC, the initiation of new cracks and propagation of existing cracks can happen in AAFS due to the pore pressure trapped in a compact structure with poor internal connectivity. Meanwhile, AAFS experiences further geopolymerisation that can strengthen the internal structure by filling the pores and voids. At 600 ºC, gel decomposition occurs in AAFS, resulting from slag that forms hybrid N-C-A-S-H gel with lower thermal

stability compared to N-A-S-H gel in AAF [22]. The decomposition of hybrid gels can lead to the initiation of small cracks, and thus significantly deteriorate the strength of AAFS at this stage. Similar to AAF, the formation of new crystalline phases and viscous sintering are the dominant factors that affect the residual strength of AAFS at 800 ºC. Nevertheless, AAFS suffers more from the decomposition of matrix leaving larger cracks and voids compared to AAF, and thus a greater strength loss. In general, the addition of slag plays a key role in the damage mechanism of AAFS, which has a more complex and unstable gel structure compared to the single precursor system, i.e. AAF.

2.5.8 Damage mitigation approaches

Tailoring precursors

As discussed above, the mechanical properties of AAC at elevated temperatures can be affected by different factors, among which Si/Al is one of the critical factors. Table 2.2 summarises the relevant studies on the effect of Si/Al ratio on mechanical properties of AAC. It is indicated that a higher Si/Al ratio can lead to a better residual strength of AAC after exposure to high temperatures.

Table 2.2. Effect of Si/Al ratio on mechanical properties of AAC at elevated temperatures.

Ref.	Precursor	Si/Al ratio	Main findings
[306]	Fly ash	1.7-2.2	The residual strength of samples with Si/Al ratio of 2.2 is the highest.
[61]	Fly ash	1.2-8.8	The residual strength of AAC with Si/Al ratio of 1.2 is 18% at 1000 ºC, whereas it is 400% for AAC with Si/Al ratio of 8.8 at 1000 ºC.
[321]	Metakaolin	1.03-2.00	The highest strength (6 MPa which is about 9% of the original strength) occurs when Si/Al ratio is 1.75, whereas it is 0% for samples with Si/Al ratio of 1.03.
[363]	Fly ash	<2	The use of low Si/Al ratio (<2) can result in a 132% increase of compressive strength after exposure of 1000 ºC.
[396]	Fly ash	1-3	The AAF gel with Si/Al ratio of 2 exhibits superior performance compared to those with lower Si/Al ratio.

As the Si/Al ratio rises from 1.2 to 8.8, the residual strength of AAC is improved from 18% to around 400% of the original strength at 1000 ºC [61]. This can be mainly explained by the fact that the higher Si content can result in higher conversion of fly ash particles into amorphous aluminosilicate alkali-activated gel [53, 306]. Furthermore, the increase of Si/Al ratio can lead

to the rise in initial temperature of gel crystallisation [395]. A range of Si/Al ratio of 1-3 was generally studied in literature. It was found that higher Si/Al ratio resulted in superior performance of AAF and AAMK after exposure to high temperatures [53, 61, 306, 321, 363, 396], implying the importance of Si/Al ratio to AAC mix design.

Incorporating additives

To improve the mechanical behaviour of AAC at elevated temperatures, some additives such as quartz and silica fume are used to maintain the dimensional stability of AAC and increase the Si/Al ratio [53, 306, 312]. The increase of quartz powder dosage (up to 30%) can lead to a higher degree of reactivity and sintering in AAF at 1000 ºC and thus enhance the residual strength of the matrix [312]. The incorporation of fine filler particles such as silica powder and ceramic powder into AAC can reduce the thermal shrinkage and thus improve the residual strength after exposed to high temperatures [53, 312]. AAMK containing fine ceramic powders can achieve a higher compressive strength at 1000 ºC, as the addition of fine particles can improve the pore size and shape distribution while filling the gap between large aggregates [53, 397]. As ceramic powder exhibits good volume stability, an effective barrier can be formed inside the matrix to mitigate the thermal stress induced damage [397]. The thermal shrinkage can be effectively improved, and thus the damage mechanism associated with thermal incompatibility can be tackled. However, the additives do not always benefit AAC. For instance, silica fume was found to have a negative impact on AAC at elevated temperatures in some cases [291, 398, 399]. AAMK containing silica fume has a lower residual strength compared to the plain specimens after exposure to 800 ºC, while reversed results can be observed at ambient temperature [291]. This can be ascribed to the denser internal structure of AAMK after adding silica fume, which impedes the escape of vapour pressure and thus deteriorate the pore pressure induced damage [3]. Hence, it is crucial to select the appropriate additives and precursor type for mitigating the damage of AAC at elevated temperatures.

Adopting appropriate aggregates

Aggregate is an essential phase for AAC. The commonly used aggregates can be divided into two categories: conventional aggregates and recycled aggregates [53]. The conventional aggregates include carbonate aggregates (specific heat between 150 ºC and 400 ºC) and

siliceous aggregates (specific heat at about 500 ºC) [288, 400, 401]. Carbonate aggregates have a 10 times greater heat absorption capacity than siliceous aggregates after exposure to 600 ºC, which can be attributed to the emission of carbon dioxide from the decomposition of carbonate at high temperatures [53].The effects of different types of aggregates on the thermal behaviour of AAC discussed previously suggest that the use of some appropriate aggregates (e.g., expanded clay aggregates) can mitigate the thermal incompatibility between different phases in AAC and thus the damage at elevated temperatures.

Recycled aggregates such as recycled ceramic aggregates, crumb rubber and glass waste have been increasingly adopted to tackle the environmental issue of industrial wastes. The use of recycled ceramic aggregates can negatively affect the flowability of concrete at ambient temperature, whereas they have a negligible effect on the compressive strength of concrete with a slight improvement after exposed to 800 ºC [402]. The addition of crumb rubber can reduce the residual strength of concrete by around 30% and 25% compared to the plain concrete at room temperature and 600 ºC, respectively [403]. Glass wastes have high fire-resistant capacity and thus can benefit concrete after exposed to 600 ºC as the molten glass can fill the microcracks in the matrix induced by pore pressure and thermal gradient to prevent crack growth [404]. The use of recycled aggregates can generally enhance the fire-resistance of concrete, while the type and dosage of them need to be considered to maintain the fresh properties of AAC at room temperature and mechanical performance at elevated temperatures. This can be attributed to the higher porosity of recycled aggregates compared to natural aggregates, which allows for the release of pore pressure and thereby reduces high-temperature induced damage in AAC.

Adding fibres

The addition of fibres is another important approach to mitigating damage in concrete at elevated temperatures. As seen in Table 2.6, the existing studies on the behaviour of fibre reinforced AAC are very limited. It was reported that the incorporation of fibres can extend the plastic deformation of concrete and thus influence the failure patterns [3, 53]. The commonly used fibres include steel, synthetic (e.g., polypropylene (PP), polyvinyl alcohol (PVA) and polyethylene (PE)), glass, basalt, carbon and natural fibres, the physical and thermal properties of which are summarised in Table 2.3 [3, 53]. Here, special focus is placed on steel fibre, PP fibre and hybrid fibre composed of them.

Table 2.3. Physical and thermal properties of fibres for AAC [277, 371, 405-414].

Fibre type	Tensile strength (MPa)	Young's modulus (GPa)	Elongation ratio (%)	Specific gravity	Melting point (ºC)
Steel	200-2760	200	0.5-35	7.8	1370
PP	552-690	3.45	~25	0.9	170
PVA	1000-1600	22-42	6-7	1.3	220-240
PE	~690	0.14-0.41	~10	0.95	141.4
Glass	1034-3792	72	1.5-3.5	2.5-2.7	860
Basalt	872-2800	40-89	3.15	2.8	1500-1700
Carbon	1550-6960	159-965	2.5-3.2	1.8	Over 3000
Nylon	750-1000	2.5-5.17	15-30	1.14	231-252
Jute	400-800	13-26.5	1.8	1.3-1.45	-

Steel fibres are widely adopted for PCC because of their excellent mechanical performance, flexibility and availability [415]. Steel fibre reinforced concrete (SFRC) can achieve higher tensile strength, toughness, strain and energy absorption capacity and better impact resistance compared to plain concrete [3, 416, 417]. Due to their high melting point and strong thermal stability, the residual strength of fibre-reinforced concrete can be retained at a certain level [3, 53, 359]. The studies on steel fibre-reinforced concrete containing different supplementary cementitious materials are summarised in Table 2.4. At ambient temperature, the increase of steel fibre content from 1% to 3% can result in the enhancement of compressive strength of concrete [418, 419]. After exposed to high temperatures, the effect of steel fibre in concrete varies with different aspects such as fibre dosage and temperature level [3, 25, 53]. There exists a positive relation between compressive strength of concrete at 400 ºC and steel fibre dosage (from 0% to 1%), whereas an opposite impact appears after exposed to 600 ºC [298, 420]. However, concrete reinforced with 1-2% steel fibres can improve the residual compressive strength of concrete compared to plain concrete at up to 1000 ºC, indicating that temperature-induced damage can be effectively mitigated through the incorporation of steel fibres [53, 380, 421].

Moreover, the incorporation of steel fibres was found to effectively improve the residual tensile strength of concrete due to their high tensile strength. At ambient temperature, SFRC has better tensile strength and strain capacity compared to plain concrete, which can be

attributed to the fibre bridging effect [288, 422]. The tensile strength reduction of SFRC is slower than that of plain concrete from ambient temperature to around 400 ºC due to the high thermal conductivity of steel fibres that can transmit heat through concrete from the heated side to the cold side more homogeneously in SFRC. Thus, the thermal stress-induced damage can be mitigated with a more uniform temperature profile at the early stage of heating [421]. However, the strength loss can be increased more rapidly when the temperature exceeds 400 ºC until 800 ºC is reached [417]. Compared to plain concrete, SFRC has around 48% and 41% more residual strength after exposed to 400 ºC and 600 ºC, respectively [3, 417].

Table 2.4. Behaviour of steel fibre reinforced concrete (SFRC) at elevated temperatures.

Ref.	Replacement material	Dimension of fibre		Volume fraction (%)	Main findings
		Length (mm)	Diameter (μm)		
[424]	Fly ash, silica fume	25	417	0, 1	Heating up to 800 ºC, SFRC has 55% more residual strength compared to the plain one.
[300]	Fly ash, silica fume	25	417	0, 1	After exposed to 1100 ºC, SFRC has a 76% increase of residual strength.
[294]	Fly ash	60	900	0.5, 0.75	SFRGC showed higher residual strength than PCC. The original temperature is retained until 400 ºC.
[288]	Fly ash	25	500	0, 1, 3	Steel fibres improved the tensile strength via crack-bridging at elevated temperatures.
[409]	Fly ash	13	160	0, 0.5	Steel fibres had almost no effect on the permeability of concrete at 20-300 ºC.
[425]	Fly ash, silica fume	30	600	0, 0.5	Steel fibres improved the residual strength up to 300 ºC but spalling could not be prevented.
[283]	Fly ash, slag	38	114	0, 0.5	The addition of steel fibres did not obviously affect the compressive strength at 800 ºC.
[420]	Fly ash, slag, silica fume	60	750	0-1	The residual tensile strength of SFRC (optimal 0.75%) is much greater than that of PFRC.
[419]	Slag, silica fume	13.2	220	0, 1, 2, 3	A higher content (3%) of steel fibres could not enhance the residual compressive strength.
[281]	Slag	32.6	950	0-2	The addition of slag and steel fibres (optimal 1%) improved splitting strength of concrete.
[291]	Metakaolin, silica fume	25	417	0, 1	The addition of steel fibres greatly improved the toughness at elevated temperatures.

Regarding the effect of steel fibre content (wt%) on tensile behaviour of concrete at elevated temperatures, for SFRC containing 10% slag, the optimal fibre content was found to be 3% with the best residual tensile strength compared to those with 1-2% of steel fibre after exposure to 800 ºC while 1% of steel fibre addition showed better performance in residual tensile strength at 400 ºC for concrete with 40% slag [417]. Regarding the application of steel fibres in AAC at elevated temperatures, there are only few preliminary studies on the physical and mechanical performance of AAF. AAF with 1.5% steel fibre dosage exhibited a 15.4% and 13.07% strength gain compared to plain AAF at ambient temperature and after exposure to 800 ºC, respectively [423]. However, the research on the effect of steel fibres on different types of AAC in terms of phase stability, pore structure and microstructural evolution at high temperatures is lacking.

Synthetic fibres are mainly produced from raw industrial materials or recycled from plastic wastes. The addition of recycled polymer fibres in concrete can provide a sustainable and feasible solution for the consumption of disposed plastics which can cause environmental pollution [415]. The most commonly used synthetic fibres include PP, PVA, PE and PET fibres. Among them, PP is commonly used to reduce the high temperature-induced damage and prevent spalling [3, 267]. Some relevant studies on the behaviour of PP fibre reinforced concrete (PFRC) are briefly summarised in Table 2.5.

Unlike steel fibres that have a strong thermal stability, PP fibres have a relatively low melting point of around 170 ºC. Thus, the mechanism of using PP fibres to improve the thermal performance of concrete is associated with the melting of fibres in concrete matrix. Figure 2.35 schematically illustrates the microstructural evolution of PFRC at elevated temperatures. It was reported that the residual strength of concrete reinforced with 0.17% PP fibres went up first until 350 ºC, followed by a slight drop between 350 ºC and 450 ºC and a significant decline after 450 ºC [430]. This is because at the early stage of heating, the matrix might not be influenced by the addition of PP fibre while the further hydration of cement pastes or geopolymerisation in AAC with the increase of temperature can lead to strength gain for concrete [420, 431]. Compared to plain concrete, the incorporation of PP fibres was found to improve the residual compressive strength by up to 13% when the temperature was increased from 400 ºC to 600 ºC [421]. The enhancement of residual strength is because of the coefficient of thermal expansion of PP fibres, which is around 10 times greater than that of other phases in concrete. This leads to the initiation of multiple microcracks that can improve the

interconnection between pores and thus provide the pathways for vapour pressure to escape and prevent pore pressure accumulation [4, 52, 385]. The length of PP fibres can also affect the compressive strength of PFRC. When the fibre length increased from 6 mm to 12 mm, the residual strength can be slightly improved by about 4% after exposure to 600 ºC [421]. PP fibres should be large enough to have a better dispersion in concrete [285].

Table 2.5. Behaviour of PP fibre reinforced concrete (PFRC) at elevated temperatures.

Ref.	Replacement material	Dimension of fibre		Volume fraction (%)	Main findings
		Length (mm)	Diameter (μm)		
[424]	Fly ash, silica fume	19	53	0, 0.22	After 800 ºC, PFRC had a 4.4% strength reduction compared to the control sample.
[300]	Fly ash, silica fume	19	53	0, 0.22	Heating up to 1100 ºC, the addition of PP fibres helped with the strength retention.
[425]	Fly ash, silica fume	30	-	0, 0.05	The spalling resistance of HPC was increased with the addition of PP fibre, whereas the residual strength slightly suffered from that.
[426]	Fly ash, silica fume	3-30	40	0, 0.05, 0.1, 0.15	The effectiveness of PP fibre was dependent on the melting point, fibre length and volume.
[427]	Fly ash	19	70	0.05, 0.1	When the volume fraction of PP fibre was more than 0.05%, the spalling was resisted.
[428]	Fly ash	19	-	0, 0.05, 0.1, 0.15	The optimal volume fraction of PP fibre was found to be 0.05%.
[283]	Fly ash, slag	20	-	0, 0.11	The PP fibre could reduce the residual tensile strength of concrete without an obvious effect on compressive strength.
[429]	Fly ash, slag	20		0, 0.11	Both specimens with and without PP fibres experienced strength degradation.
[281]	Slag	19	-	0-0.133	The optimal dosage of PP fibre was 1%.
[420]	Fly ash, slag, silica fume	65	850	0-0.2	The residual strength was around 20% for specimens with PP fibres after exposed to 900 ºC.

Besides the compressive strength, the addition of PP fibres can enhance the residual splitting tensile strength of concrete [432-435]. Compared to plain concrete, PFRC has around 27% more retained tensile splitting strength at elevated temperatures [434]. Nevertheless, the effect of PP fibres on the residual tensile strength is dependent on the matrix proportions, fibre content and fibre length. PP fibres with 12 mm length perform better on mitigating the tensile loss in PFRC compared to those with 6 mm length [421, 434].

To combine the advantages of different types of fibres, hybrid fibre reinforced concrete has been increasingly studied. For instance, steel fibres are used to restrict the initiation and propagation of microcracks together with PP fibres that can improve the internal connectivity

of concrete, and thus can enhance the thermal behaviour of concrete at elevated temperatures. The residual compressive strength of hybrid steel and PP fibre reinforced concrete was higher than that of plain concrete at temperatures between 20 ºC and 300 ºC [279]. Concrete reinforced with 1% steel and 0.22% PP fibres showed a relatively greater compressive strength retention than PFRC while worse than SFRC when exposed to 800 ºC [291], as PP fibres have a much lower melting point than steel fibres and lose strength quickly when the melting point of around 170 ºC is achieved while steel fibres have a better thermal stability to function properly when the temperature continues to rise [3]. A hybrid of high tensile strength fibres (e.g., steel fibres and carbon fibres) and low melting point fibres (e.g., PP and PVA fibres) can maximise the damage mitigation effect in concrete at high temperatures, where hybrid steel and PP fibre reinforced concrete exhibits the most superior mechanical behaviour [3]. In regard to AAC at elevated temperatures, a combination of glass and basalt fibres was employed to mitigate the compressive and flexural strength losses of AAF at elevated temperatures, where glass fibres provided superior bonding and bridging effect due to less agglomerated distribution [436].

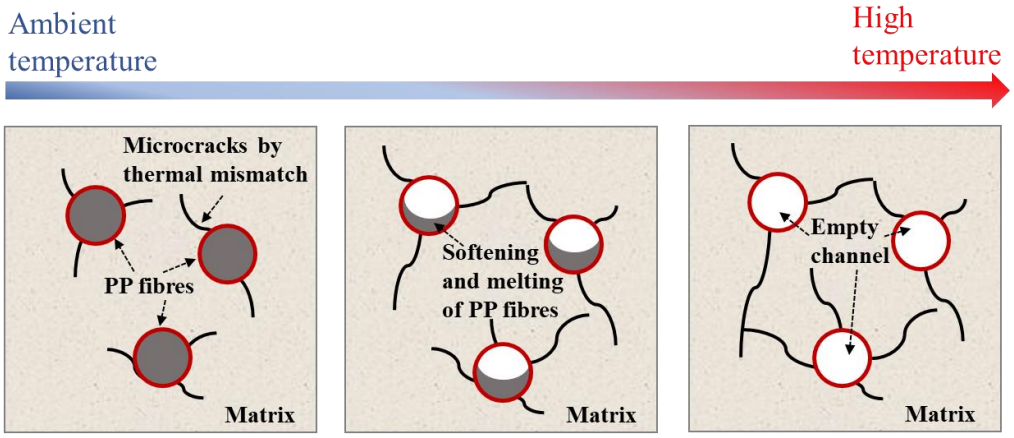

Figure 2.35. Schematic illustration of damage evolution in Portland cement concrete (PCC) at elevated temperatures (adapted from [384]).

2.6 Summary

In this chapter, the multiscale microstructural characteristics and micromechanical properties of AAC at ambient temperature is systematically reviewed. Meanwhile, the behaviour of different types of AAC at elevated temperatures is discussed with respect to microstructural

features as well as thermal and mechanical properties. Afterwards, the proposed damage mechanisms of PCC and AAC are summarised with their corresponding damage mitigation approaches. Up to now, the high-temperature performance of AAF, AAS and AAMK has been extensively investigated, whereas the fundamental understanding of the behaviour of AAFS at elevated temperatures is still lacking, particularly from a multiscale point of view. The main conclusions can be drawn below:

- Regarding single precursor systems such as AAF, AAS and AAMK, the reaction process consists of different steps, including dissolution of precursors, rearrangement, gelation and solidification to form N-A-S-H gels in low-calcium AAF and C-A-S-H gels in high-calcium AAS. As for blend precursor system, the hybrid N-C-A-S-H gels are formed in AAFS due to the local chemical interactions between different precursors during alkaline activations, leading to the heterogeneity of composition distribution in the microstructure.
- The elastics modulus of different reaction products in AAC follows an order of N-A-S-H gels (11-20 GPa) < N-C-A-S-H gels (19-23 GPa) < C-A-S-H gels (35-47 GPa), which strongly affects the macroscopic mechanical strengths of AAF, AAS and AAFS.
- The damage mechanisms of AAC at elevated temperatures can be summarised in three aspects: thermal-induced damage due to phase incompatibility between matrix and aggregates, pore pressure-induced damage due to vapour pressure build-up, and phase transformation during the heating process.
- AAFS with lower slag content (10-20% by weight) contains the similar crystalline phases as found in AAF, including quartz and mullite, while the C-S-H phase exists in AAFS when the slag content reaches 40-50%. The slag content has a significant influence on the microstructural characteristics and macroscopic properties of AAFS at elevated temperatures.

The most urgent challenges and limitations are summarised as follows:

- The existing studies on microstructural characteristics of AAFS are mainly focused on ambient temperature, while the damage evolution in AAFS at elevated temperatures has not been explored from a multiscale point of view. In particular, the solid gel particles in

nanostructure of AAFS at elevated temperatures has not been thoroughly studied to understand the high-temperature performance of this material.

- The investigation on microstructural evolution and visualisation of internal morphological changes in AAFS after 20-800 ºC exposure has never been vividly visualised in 3D views.
- The micromechanical properties regarding elastic modulus and hardness of different solid phases in AAFS at elevated temperatures have not been explored.
- The evolution of microstructure in terms of phase assemblage and pore structure of AAFS subjected to high temperatures and its macroscopic properties including thermal and mechanical performance have not been linked to each other to explore the underlying damage mechanisms at different temperature levels.

Table 2.6. Summary of raw materials, curing conditions, heating and cooling methods, characterisation and main findings collected from studies on AAC at elevated temperatures.

Ref.	Precusor	Alkaline activator	Additive	Fibre	Curing method	Heating method	Cooling method	Characterisation	Main findings
[26]	Fly ash	SH (8 and 14 M) + SS	-	-	24 h at 25, 40 and 80 °C oven curing, then ambient curing	Exposed to 100-1000 °C at 5 °C/min for 2 h	Naturally cool down	Compressive strength, mass loss, SEM, TGA	AAC surface had more deterioration due to temperature gradient. The strength loss after 600 °C can be ascribed to dehydration of reaction gels.
[30]	Fly ash	SH (10 M) + SS	-	-	24 h at 60 °C oven curing, then ambient curing	Exposed to 100-1200 °C for 2 h	Naturally cool down	Compressive and bond strengths, mass loss, TGA/DTG, XRD, SEM-EDS	The decrease of Si/Al ratio led to AAC strength loss. Class C fly ash caused denser microstructure and great mechanical performance after exposed to 800 °C.
[437]	Fly ash	SH + SS	-	-	24 h at 60 °C oven curing, then ambient curing	Exposed to up to 1200 °C in 5 mins and hold for 2 h	Naturally cool down	Compressive and bond strengths, mass loss, TGA/DTG, XRD, SEM	No spalling occurred at 1200 °C. AAC exhibited better bond strength at 1200 °C compared to PCC. As the porous structure in AAC provided the channels for moisture to escape, with more stable crystalline phase.
[31]	Fly ash	SH (10 M) + SS	-	-	24 h at 75 °C oven curing, then ambient curing	Exposed to up to 200-800 °C at 5 °C/min and hold for 2 h	Naturally cool down	Compressive strength, mass loss, SEM, FTIR, XRD, TGA	The crystalline network in AAC was sensitive to the temperature increment. It kept stable at 600 °C, while the formation of new crystalline phases at 600-800 °C resulted in strength gain.
[354]	Fly ash	SH + SS	Bamboo ash (5-100%)	-	-	Exposed to 200-800 °C for 1 h	Air and water cooling	Compressive strength, mass loss, UPV	AAC with 100% fly ash showed 62% strength loss when exposed to 400-800 °C

[360]	Fly ash	SH (8 M) + SS	-	PVA and steel (both 0.75%)	24 h at 60 °C heat curing, then ambient curing	Exposed to 1000 °C at 5 °C/min for 2 h	Air and water cooling	Tensile and compressive strengths	Water cooling can cause more obvious strength loss. Compared to PVA, the steel fibre reinforcement for AAC was more obvious.
[361]	Fly ash	SH + SS	-	-	24 h at 20 °C curing then ambient curing	Exposed to 100-800 °C at 2 °C/min for 1 h	Naturally cool down	Compressive strength, mass loss, SEM, TGA	The compressive strength increased up to 200 °C, due to secondary geopolymerisation between fly ash and alkaline activator but dropped after 200 °C due to dehydroxylation of N-A-S-H gel.
[353]	Fly ash	KOH (8 M) + K_2SiO_3	-	Carbon and basalt (0.5-1%)	24 h at 70 °C curing then ambient curing	Exposed to 200-800 °C at 5 °C/min	-	Compressive strength, mass loss, MIP, SEM	1% is the optimal dosage of carbon and basalt fibres for AAC. AAC containing carbon fibres showed less cracks at 600 °C and more compact microstructure than that with basalt fibres.
[438]	Fly ash	SH + SS	Micro silica (0-10%) granular filler	-	24 h at 80 °C curing then ambient curing	Exposed to 200-800 °C at 10 °C/min for 2 h	-	Compressive strength, thermal expansion and conductivity, XRD, TGA, FTIR, MAS-NMR analysis	5% is the optimal dosage of micro silica for fly ash -based AAC. Thermal conductivity of AAC decreased with the rise of temperature. Normal AAC exhibited around 2.5% thermal expansion.
[358]	Fly ash	SH (14 M) + SS	-	Rubber (10% by weight)	48 h at 90 °C curing then ambient curing	Exposed to 200-800 °C at 4.4 °C/min for 2 h	Naturally cool down	Compressive strength mass loss, XRD, TGA/DTG, FTIR	The compressive strength went up as the temperature increased from 600 to 800 °C. N-A-S-H was formed when increasing the temperature. Zeolite turned into nepheline and albite during the recrystallisation process at 600-800 °C.
[314]	Fly ash	SH (8 M) + SS	Nano silica	-	24 h at 70 °C curing then	Exposed to 200, 400, 600 and 800 °C	Naturally cool down	Mass loss, volume change, thermal shrinkage, XRD	Replacement of 10% of fly ash with fine silica can enhance thermal resistance of fly ash-based AAC.

		KOH (8 M) + K_2SiO_3			ambient curing				
[439]	Fly ash	SH + SS	-	Steel, PP	Ambient temperature curing	Exposed to 100, 200 and 300 °C	-	Compressive, splitting tensile, flexural strengths, flexural toughness	Fly ash-based AAC exhibited softening behaviour when subjected to elevated temperatures. The addition of fibres can improve the tensile strength and flexural toughness of AAC.
[359]	Fly ash	SH (10 M) + SS	-	-	24 h at 100 °C curing then ambient curing	Exposed to 200-800 °C at 5.5 °C/min for 1 h	Naturally cool down	Crack width, ductility, flexural behaviour	The load carrying capacity of AAC degraded rapidly when exposed to more than 600 °C.
[356]	Fly ash	SH + SS	-	-	48 h at 50-100 °C curing then ambient curing	Exposed to 200-800 °C at 7 °C/min	Naturally cool down	Compressive and flexural strengths, mass loss, UPV, SEM	Fly ash-based AAC had better compressive and flexural performance than that of PCC. After exposure to 800 °C, the compressive strength of AAC was improved from 7.63 MPa to 40.7 MPa.
[440]	Fly ash	SH (12 M) + SS	Light-weight fly ash aggregate	-	-	Exposed to 100-800 °C at 5 °C/min and held for 2 h	-	Elastic modulus, Compressive strength	There was a drop in strength when exposed to up to 200 °C, followed by a slight increase until 400 °C due to further geopolymerisation, and no strength loss occurred at 800 °C due to disintegration of reaction gels and phase transformation.
[312]	Fly ash	SH + SS	Quartz powder (0-30%)	-	24 h at 105 °C curing then ambient curing	Exposed to 400-1000 °C at 6.67 °C/min and held for 2 h	Naturally cool down	Compressive strength, workability, mass loss, XRD, SEM	The inclusion of quartz powder in fly ash and slag-based AAC improve thermal resistance due to the increase of Si/Al ratio.

[294]	Fly ash	SH (8 M) + SS KOH (8 M) + K_2SiO_3	-	Steel (0.5% and 0.75%)	24 h at 60 °C steam curing then 105 °C for 24 h	Exposed to 200-800 °C at 8 °C/min and held for 2 h	Naturally cool down	Elastic modulus, tensile and compressive strengths	Steel fibre reinforced AAC retained the compressive strength until 400 °C. AAC made from K-based activator had better tensile strength at elevated temperatures compared to that made from Na-based one.
[377]	Fly ash	SH + SS	-	-	72 h at 80 °C curing then ambient curing	Exposed to 200-1000 °C at 4.5 °C/min	Naturally cool down	Elastic modulus, Compressive strength, SEM	AAC retained around 60% of strength and stiffness when exposed to over 400 °C while fly ash particles was observed to collapse to form a homogeneous and compact structure when exceeding 600 °C.
[315]	Fly ash	SH (10-16 M) + SS	-	-	24 h at 105 °C curing then ambient curing	Exposed to 200-800 °C at 1 °C/min	-	Compressive strength, thermal expansion, physical appearance	The strength of AAC reduced when exposed to 400 °C but went up at 600-800 °C due to further geopolymerisation.
[362]	Fly ash	SH (14 M) + SS	-	-	24 h at 60 °C curing	Exposed to 400-1000 °C at ISO834 for 2.5 h	Naturally cool down	Compressive strength, mass loss, spalling	No spalling occurred in AAC. After exposed to 400 °C, the residual strength of AAC kept at around 93-107%.
[28]	Fly ash	SH + SS	-	Cotton fibres	-	Exposed to 200-1000 °C at 5 °C/min and held for 2 h	Naturally cool down	Compressive and flexural strengths, fracture toughness, TGA, SEM	The addition of cotton fibres can help inhibit crack development when AAC is subjected to elevated temperatures, owing to additional porosity and small channels.
[441]	Fly ash	SH + SS	-	-	72 h at 80 °C curing then ambient curing	4.5 °C/min	-	Compressive strength, thermal expansion, SEM	AAC experienced shrinkage induced by loss of moisture and densification of the matrix structure due to sintering effect.
[24]	Fly ash	SH (8 M) + SS	-	-	18 h at 60 °C curing then	Exposed to 200-550 °C at 5	Naturally cool down	Elastic modulus,	As the temperature increased to 200-300 °C, the compressive strength of AAC increased due to further geopolymerisation.

					ambient curing	°C/min and held for 1 h		compressive strength, thermal strain, creep, TGA	
[305]	Fly ash	SH + SS	Light-weight aggregate	-	24 h at 70 °C curing then ambient curing	Exposed to 400-800 °C at 4.4 °C/min and held for 1 h	Naturally cool down	Compressive strength, thermal expansion, TGA/DTG, XRD, SEM-EDS	The strength of AAC dropped after exposed to 400-600 °C due to dehydration and dehydroxylation. After exposed to 800 °C, the damage occurred due to sintering effect.
[350]	Fly ash	SH + SS	Light-weight aggregate	-	24 h at 70 °C curing then ambient curing	Exposed to 100-800 °C at 4.4 °C/min and held for 1 h	Naturally cool down	Compressive strength, thermal expansion, SEM	The residual strength of lightweight AAC increased when exposed to 100-300 °C, followed by a strength loss due to vapour effects and difference in thermal expansion between different phases in AAC.
[306]	Fly ash	SH + SS	-	-	24 h at 85 °C curing then ambient curing	Exposed to 300-900 °C at 8.5 °C/min and held for 2 h	Naturally cool down	Compressive strength, mass loss, shrinkage, water sorptivity, SEM-EDS, XRD	A rapid increase in volumetric strain of AAC happened when subjected to more than 600 °C. The sintering effect can be detected at elevated temperatures. The thermal performance of AAC with higher Si/Al ratio was better than that with lower Si/Al ratio.
[339]	Fly ash	SH + SS	-	-	18 h at60 °C curing then ambient curing	Exposed to 100-680 °C at 5 °C/min and held for 1 h	Naturally cool down	Compressive strength, thermal strain, TGA	A glass transition point was detected in AAC with the increase of temperature to 560 °C. AAC exhibited brittle failure at any temperature level.
[27]	Fly ash	SH (7 M) + SS	-	-	24 h at 80 °C curing then ambient curing	Exposed to up to 800 °C at 4.4 °C/min and held for 1 h	Naturally cool down	Compressive strength, Thermal expansion, TGA/DTG	The residual strength of AAC at elevated temperatures was dependent on sample size. The thermal incompatibility was the dominant effect on the strength loss of AAC.
[23]	Fly ash	SH (10 M) + SS	-	-	24-96 h at 55-80 °C curing	Exposed to up to 800 °C at 4.4	Naturally cool down	Compressive strength, mass loss, TGA	Two opposing processes can affect the strength behaviour of AAC: (1) sintering

					then ambient curing	°C/min and held for 2 h			effect to enhance strength, and (2) thermal incompatibility that deteriorates the matrix.
[348]	Fly ash	SH (7 M) + SS	-	-	24 h at 80 °C curing then ambient curing	Exposed to up to 800 °C at 5 °C/min and held for 1 h	Naturally cool down	Compressive strength, thermal expansion, TGA/DTG	Thermal incompatibility due to matrix shrinkage and aggregate expansion at elevated temperatures is the main cause for the strength loss of AAC.
[346]	Fly ash	SH + SS	-	-	24 h at 70 °C curing then ambient curing	Exposed to 100-1000 °C at 5 °C/min and held for 1 h	Naturally cool down	Compressive strength, mass loss, thermal expansion, SEM, XRD	Sintering can improve the interparticle bonding to enhance the residual strength of fly ash-based AAC at elevated temperatures while the strength loss was due to dehydration.
[391]	Fly ash	SH (10 M) +SS	-	-	Water curing	Fire heating to 500 and 1000 °C for 2 h	Naturally cool down	Compressive strength, Mass loss, FTIR, SEM	AAF exhibited higher fire resistance compared to PCC. Further geopolymerisation could lead to a denser microstructure in AAF.
[436]	Fly ash		-	Hybrid glass and basalt fibre	24 h at 80 °C curing then ambient curing	Exposed to 300-800 °C at 5 °C/min and held for 2 h	Naturally cool down	Flowability, compressive and flexural strengths, mass loss, SEM	Hybrid glass and basalt fibres could mitigate strength loss of AAF after high temperature exposure more efficiently compared to their single use. Glass fibres can provide bonding effect.
[442]	Fly ash	SH + SS	-	-	24 h at 85 °C curing then 23 °C water curing for 27 d	Exposed to 200-1000 °C at 4 °C/min and held for 1 h	Naturally cool down	Compressive strength Thermal diffusivity TGA, FTIR, XRD, SEM	Further geopolymerisation with an increase of N-A-S-H gel was detected after AAF was exposed to 200 °C. A phase transformation from amorphous to new crystalline phases took place after exposure to 600 °C.
[443]	Fly ash	SH + SS	-	-	24 h at 60 °C curing then 25	Exposed to fire at 500 and 1200 °C and held for 2 h	-	Compressive strength, FTIR	A higher structural integrity was found in AAF compared to PCC. A more compact and denser internal structure was obtained in

					°C water curing for 28 d				AAF matrix after high temperature exposure.
[423]	Fly ash	SH + SS	-	-	-	Exposed to 200-800 °C at 8 °C/min and held for 2 h	Naturally cool down	Compressive and flexural strengths, UPV, SEM	The inclusion of steel fibres enhanced thermal resistance of AAF in terms of physical and mechanical properties such as compressive and flexural strengths.
[364]	Slag	SH (10 M) + SS	0-100% recycled concrete aggregate	-	24 h at 80 °C curing then 23 °C water curing for 27 d	Exposed to 100-800 °C for 1 h	Air, oven and water cooling	Compression strength, mass loss, UPV, microstructures	The microstructure of ACC deteriorated with the increase of temperature and decrease of Ca/Si ratio while increase of Si/Al ratio. ITZ was weakened.
[366]	Slag	SH + SS	Calcined perlite (0, 25 and 50%)	-	48 h at 70 °C oven curing, then ambient curing	Exposed to 105 °C for 48 h, then 400-800 °C at 6 °C/min	Naturally cool down	Compressive and flexural strengths, mass loss, XRD, SEM-EDS	With the increase of temperature, the residual flexural and compressive strengths of AAS decreased and the mass loss of AAS increased.
[38]	Slag	SH (10 M) + SS	-	-	Ambient curing (29 °C)	Exposed to 200-1000 °C at 10 °C/min for 1 h	-	Compressive strength, mass loss, TGA/DTG, SEM, XRD, FTIR	Crack healing of AAC happened at 800-1000 °C. No spalling occurred at elevated temperatures. The compressive strength dropped by 90.6% at 800 °C due to decomposition but went up at 1000 °C due to rearrangement of crystalline.
[365]	Slag	SH + SS	Quartz powder and Quartz sand	-	-	Exposed to 200-800 °C at 5 °C/min for 1.5 h	Naturally cool down	Compressive strength, mass loss, SEM-EDS	No spalling in AAC was observed when exposed to 800 °C. The strength was retained at around 50% at 600 °C.
[378]	Slag	SH + SS	-	-	Water curing at 23 °C	Exposed to 200-800 °C at 2.7 °C/min for 1 h	Naturally cool down	Tensile strength, mass loss, SEM, MIP	The crack grew in C-A-S-H gel and the crack number and size in AAS increased

									with the rising temperature. At 800 °C, the pore size ranged from 0.01-10 μm.
[320]	Slag	SH + SS	-	-	Ambient curing	Exposed to 200-800 °C at 15 °C/min and held for 2 h	Naturally cool down	Compressive and flexural strengths, TGA, SEM, XRD	The compressive strength of slag-based AAC dropped by around 80% when exposed to 800 °C. More microcracks can be observed in ambient-cured AAC compared to heat-cured AAC.
[318]	Slag	Dried water glass	-	-	-	Exposed to 200-1200 °C at 5 °C/min and held for 1 h	Naturally cool down	Compressive and flexural strengths, bulk density, shrinkage, SEM, MIP, XRD FTIR, MAS NMR	Crystallization of predominantly akermanite of slag-based AAC when exposed to above 600 °C was the main reason for the strength gain of up to 180%.
[368]	Slag	SH (2-6 M) + SS	-	-	24 h at 38 °C curing	Exposed to 300-1000 °C at 5 °C/min	Naturally cool down	Compressive strength, SEM	AAC had thermal stability when exposed to up to 500 °C.
[369]	Slag	SS	-	-	24 h at 45 °C curing	Exposed to 200-1000 °C at 6.67 °C/min (2 h)	Naturally cool down	Compressive strength, XRD, SEM-EDX	As the NaO_2 concentration in AAC increased, the reaction products became more compact and denser.
[325]	Slag	Water glass	-	-	Ambient curing	Exposed to 200-1000 °C at 10 °C/min (2 h)	Naturally cool down	Bending strength, thermal properties, MIP, SEM, XRD	The porosity of slag-based AAC increased significantly when subjected to 1200 °C.
[343]	Slag	Hydrated lime	-	-	24 h at 23 °C curing	Up to 1200 °C at 2.5 °C/min (2 h)	Naturally cool down	Compressive strength, thermal expansion, TGA	The residual strength of AAC at 200 and 800 °C are 76% and 10%, respectively.
[444]	Slag	SH (12 M)	Glass powder	-	Ambient curing	Exposed to 150-750 °C and held for 1 h	Air and water curing	Compressive and tensile strengths, mass loss, sorptivity	The strength of AAS decreased with the increase of glass powder dosage. Crack initiation and propagation took place after

								SEM	exposed to 450 °C, along with gel structure deterioration.
[370]	Metakaolin	SH + SS	Red sand	PVA (0.5%, 1%)	Ambient curing (40 °C)	Exposed to up to 200 and 400 °C at 17 °C/min and held for 3 h	Naturally cool down	Compressive and bond strengths	A sharp drop in bond strength can be observed in the plain AAC. The addition of PVA fibres can improve the bond strength of AAC at 200 °C.
[321]	Metakaolin	SH + SS	-	-	Ambient curing	Exposed to 300 and 900 °C at 5 °C/min for 1 h	Naturally cool down	Compressive strength, crack pattern, thermal expansion, SEM, XRD, FTIR	AAMK experienced strength growth without appearance of new crystalline phases when exposed to up to 300 °C but exhibited poor volume stability, leading to thermal shrinkage.
[371]	Metakaolin	SH + SS	Basalt microfibril (5-15%)	-	Ambient curing	Exposed to 200-800 °C at 5 °C/min for 1 h	-	Compressive strength, TGA, SEM-EDS, XRD	The inclusion of basalt microfibrils can help enhance thermal resistance of AAC due to more microcracks and larger voids, and the pore-filling effect of basalt microfibrils.
[372]	Metakaolin	SH+SS	-	Micro carbon fibres	-	Exposed to 200-800 °C at 5 °C/min for 1 h	Naturally cool down	Compressive strength, volume resistivity, TGA, SEM-EDS	The addition of carbon microfibres led to more compact structure in AAC due to the pore-filling effect. The strength loss of AAC at elevated temperatures was due to thermal incompatibility.
[445]	Metakaolin	SH (5 and 10 M), SS (10 M)	Calcium hydroxide	-	Ambient curing	Exposed to 300-900 °C at 10 °C/min for 2 h	Naturally cool down	Compressive strength, MIP, XRD, FTIR, SEM-EDS	10% calcium hydroxide resulted in the formation of nepheline after AAMK was exposed to 900 °C. Sintering and densification took place. The optimum AAMK mixture contained calcium hydroxide with low activator concentration.

[446]	Metakaolin	SH (5 M) + SS	Nano-silica fume	-	-	Exposed to 500-1000 °C	-	Compressive strength, bulk density, FTIR, XRD, TGA,/DTG	The addition of nano-silica fume can improve thermal performance of AAMK with a maximum addition of 5%.
[22]	Fly ash and slag	SH + SS	-	-	24 h at 60 °C curing then ambient curing	Exposed to 100-800 °C at 10 °C/min for 1 h	Naturally cool down	Compressive strength, bulk density, skeleton density, open porosity, UPV, MIP, SEM-EDS, TG/DSC, FTIR, XRD	AAF exhibited better thermal stability after exposed to 600 °C, compared to AAFS with low slag content. The decomposition of hybrid N-C-A-S-H gel in AAFS led to loss of residual strength and matrix structure.
[50]	Fly ash and slag	SH +SS	Basaltic pumice aggregate	-	48 h at 80 °C oven curing, then ambient curing	Exposed to 100-800 °C at 6 °C/min for 3 h	Naturally cool down	Compressive strength, water absorption, SEM-EDS, XRD, PLM	The increase of slag content in AAFS resulted in a decrease in compressive strength of AAFS after exposed to elevated temperatures.
[32]	Fly ash and slag	SH (10 M) + SS	-	-	24 h at 70 °C oven curing, then ambient curing	Exposed to up to 300-700 °C at 10 °C/min and held for 2.5 h	Naturally cool down	Compressive strength, mass loss, volume change, TGA/DTG, SEM-EDS-XRD	AAC containing 100% fly ash had the best mechanical performance at 500 °C and 700 °C, while fly ash-slag based AAC had low strength loss at 500 °C and 700°C.
[51]	Fly ash and slag	SH (12-20 M) + SS	-	-	24 h at 60, 70 °C oven curing	Exposed to 200 °C for 1 h	-	Compressive and flexural strengths	The compressive strength of AAC with 20 M was less than that of AAC with 16 M, which increased with the increase of sodium silicate.
[328]	Fly ash and slag	SH + SS	-	-	48 h at 80 °C oven curing then ambient curing	Exposed to 200-800 °C	-	Compressive and flexural strengths, physical properties, SEM, EDS, PLM, XRD	The inclusion of fly ash in slag-based AAC can increase the thermal resistance and reduce the mass loss. Na content in AAC increased at elevated temperatures.

[355]	Fly ash and slag	SH (8-14 M) + SS	-	-	24 h at 60-100 °C heat curing and ambient curing	Exposed to 200-2000 °C at 4 °C/min	Naturally cool down	Compressive strength, mass loss, setting time, SEM-EDS	The addition of slag in fly ash-based AAC led to effective polymerisation and strength gain. When AAC exposed to 600 °C, there was a change from crystalline phase to amorphous phase.
[57]	Fly ash and slag	SH + SS	-	-	-	Exposed to 400-1000 °C at a rate of ISO834	Naturally cool down	Compressive strength and splitting tensile strengths	Compared to PCC, AAC had more obvious surface change after exposed to 400-600 °C.
[447]	Fly ash and slag	SH + SS	Waste ceramic powder	-	Ambient curing	Exposed to 400-900 °C	Air cooling	Compressive strength, mass loss, UPV, TGA, XRD, SEM-EDX, FTIR	The addition of waste ceramic powder at dosages of 50-70% can improve thermal resistance of slag-based AAC at up to 900 °C. However, when adding fly ash into the mixture, the strength dropped.
[25]	Fly ash and slag	SH + SS	-	-	Ambient curing	Exposed to 300 and 600 °C at 4 °C/min for 1.5 h	-	Compressive strength, XRD, FTIR, SEM	The change in slag content in fly ash-slag based AAC resulted in various mechanical responses when exposed to elevated temperatures. The recommended mixture consisted of 90% fly ash and 10% slag.
[58]	Fly ash and slag	SH + SS	-	-	48 h at 40 °C curing, then ambient curing	Exposed to 300-1100 °C at 2 °C/min	-	Compressive strength, DTG, XRD, SEM	Fly ash and slag-based AAC exhibited the lowest compressive strength when exposed to 700 °C. At 700 °C, the porosity reduced while a new crystalline phase was found along with sintering at 1000 °C.
[59]	Fly ash and slag	SH + SS	-	-	-	Exposed to 400 °C for 1 h; 600 °C for 1 h, 600 °C for 2 h	Naturally cool down	Compressive, tensile and flexural strengths	The cracks in AAC induced by elevated temperatures were more intense and wider than those in PCC.

[376]	Fly ash and slag	SH (14 M) + SS	-	-	60 °C oven curing for 5-168 h	Exposed to 200-800 °C at 5 °C/min	Naturally cool down	Compressive and flexural strengths, bulk density, apparent porosity, water absorption	The recommended curing condition was 48 h at 60 °C for the mixture made from 14 M SH. 400 and 600 °C were identified as the critical temperature points, at which the compressive strength of AAC dropped and physical changes occurred.
[60]	Fly ash and slag	SH + SS	Silica fume	-	Ambient curing	Exposed to 200-800 °C at 10 °C/min and held for 2 h	Natural and water cooling	Compressive strength, mass loss, UPV, FTIR, SEM	AAC after water cooling had a more significant degradation at elevated temperatures compared to the ones with natural air cooling.
[375]	Fly ash and slag	SH (8 M) + SS	-	-	22 h at 80 °C curing then ambient curing	Exposed to up to 800 °C at 2.5 °C/min and held for 1 h	Naturally cool down	Compressive strength, Stress-strain	The increased compressive strength of AAC after exposed to 800 °C was ascribed to the further hydration of unreacted particles and sintering reaction.
[36]	Fly ash and slag	SH (3.5-10 M) + SS	Zirconia, Alumina, Zinc oxide, Silica fume	-	Ambient curing	Exposed to 200-800 °C at 10 °C/min and held for 2 h	Naturally cool down	Compressive and tensile strengths, water absorption, TGA, SEM	AAF had more resistance to temperature compared to AAFS. The presence of more compact and homogeneous gels appeared after exposure to 800 °C.
[344]	Fly ash and slag	SH (4 M)	Soda lime waste glass		Ambient curing	Exposed to 200-800 °C at 5 °C/min and held for 2 h	Naturally cool down	Compressive strength, mass loss, thermal expansion, SEM	The reduced compressive strength of AAFS after high temperature exposure was owing to the increase of slag content. The melting of waste glass at 600-800 °C led to the increase of thermal resistance.
[448]	Fly ash and slag	SH (10 M) + SS	-	PVA fibres	Ambient curing	Exposed to 105-800 °C at 10 °C/min and held for 2 h	Naturally cool down	Compressive and tensile strengths, mass loss, UPV, DSC, TGA, XRD, MIP, SEM	Mechanical properties of PVA fibre reinforced AAFS was affected by phase composition, microstructure evolution and fibre bridging effect. The sintering effect occurred after 600 °C in AAFS, leading to

									the reduction of small gel pores and increase of larger pores due to formation of cracks.
[329]	Fly ash and metakaolin	KOH + K_2SiO_3	Silica fume	-	-	Exposed to 100-700 °C at 5, 8 and 12 °C/min	-	Compressive strength, spalling, Sorptivity, XRD	AAC had better spalling-resistance and higher water absorptivity than PCC. The sintering reaction occurred at 700 °C.
[449]	Fly ash and metakaolin	KOH + K_2SiO_3	-	-	Ambient curing	Exposed to 100, 300, 500 and 700 °C at 5 °C/min	-	Compressive, splitting tensile and bond strengths	The bond strength of AAC reduced when exposed to 300 °C. The bond strength and tensile strengths of AAC dropped at a greater pace compared to its compressive strength.
[347]	Fly ash and metakaolin	KOH + K_2SiO_3	-	-	Ambient curing	Exposed to 100-700 °C	-	Compressive, tensile, bond and bending strengths, thermal expansion TGA/DTG, DSC	The flexural, compressive, tensile and bond strengths of AAC increased up to 100 °C, followed by a decrease when exposed to 300-700 °C. The mass loss was induced by thermal incompatibility and dehydration.
[35]	Fly ash and metakaolin	KOH + K_2SiO_3	-	-	-	Exposed to up to 800 °C at 10 °C/min and held for 2 h	Naturally cool down	Compressive and bending strengths, thermal expansion TGA/DTG, SEM-EDS, MIP	Compared to fly ash-based AAC, AAMK concrete had a more compact and denser microstructure due to greater thermal shrinkage and less pore evolution.
[333]	Fly ash and metakaolin	SH + SS	-	-	24 h at 40 °C curing then curing at 40 °C	Exposed to 100-800 °C at 2 °C/min and held for 2 h	Naturally cool down	Compressive strength, mass loss, thermal shrinkage, MIP, SEM	A strength gain of fly ash and metakaolin-based AAC happened when exposed to up to 500 °C, whose microstructure became denser after 400 °C.
[37]	Fly ash and metakaolin	SH (10 M) + SS	-	-	24 h at 40 °C curing then curing at 40 °C	Exposed to up to 1000 °C at 2 °C/min	Naturally cool down	Compressive strength, mass loss, thermal shrinkage, SEM	A denser and more compact microstructure of metakaolin and fly ash-based AAC was detected after exposed to 400 °C due to sintering effect and geopolymerisation.

[332]	Slag and metakaolin	SH and SS	Clag brick waste powder	-	24 h at 105 °C heat curing then water curing	Exposed to up to 800 °C	-	Compressive strength, SEM	With the increase of temperature from 100 to 400 °C, the compressive strength went up.
[330]	Slag and metakaolin	-	PVA resin powder	-	-	Exposed to 150-850 °C at 3 °C/min and held for 1 h	Naturally cool down	Compressive and flexural strengths, mass loss, volume shrinkage, XRD, SEM	The compressive strength increased at 150-300 °C, followed by a decrease at 450-800 °C due to dehydration of AAC matrix.
[367]	Slag and tailing	SH + SS	-	-	Ambient curing	Exposed to 200-1200 °C at 10 °C/min and held for 2 h	Cool down by electric fan	Compressive strength, thermal expansion, TGA, DSC, XRD, FTIR	AAC experienced cracking and shrinkage due to dehydroxylation at 300-700 °C and thermal expansion of AAC can be observed after 800 °C.
[450]	Slag and palm oil fuel ash	SH (12 M) + SS	-	-	-	Exposed to 100-800 °C at 5 °C/min	Naturally cool down	Compressive strength, TGA, DSC, XRD, FTIR	The substitution of slag by palm oil fuel ash indicated the role of aluminium in the development of C-(A)-S-H gel.
[357]	Fly ash and palm oil fuel ash	SH + SS	-	-	24 h at 65 °C curing then ambient curing	Exposed to 200-1000 °C at 5 °C/min and held for 2 h	Naturally cool down	Compressive strength, TGA, XRD, SEM	All the mixtures can gain strength when exposed to up to 500 °C. The pore size increased significantly with the increase of temperature to 800 °C.

Note: SH – sodium hydroxide; SS – sodium silicate; PVA – polyvinyl alcohol.

Chapter 3 Multiscale Microstructural Characteristics of AAFS Paste at Elevated Temperatures

3.1 Introduction

According to Chapter 2, AAFS paste is considered as a multiphase heterogeneous composite material, consisting of unreacted fly ash and slag particles, reaction products and pores [39]. Hence, the microstructural features of AAFS can be characterised at three different levels, as schematically illustrated in Figure 3.1. Level 0 denotes the nanostructure of solid gel particles that are the elementary components of crystalline and amorphous phases in AAFS [39, 43-45]. The addition of a calcium source leads to the coexistence of N-A-S-H and C-A-S-H gels, with partial replacement of sodium from N-A-S-H gel to form N-C-A-S-H gel that has a higher degree of cross-linking [22, 46-48]. These three types of reaction products dominate the AAFS paste, which take up more than 90% of the binder weight [48]. Level I corresponds to the chemical composition of the AAFS gel matrix, which is agglomerated by the solid gel particles and gel pores. Level II stands for AAFS paste at micro-scale, composed of gel matrix, unreacted fly ash and slag particles and pores. To systematically understand the microstructural evolution of AAFS at elevated temperatures, it is vital to investigate both individual phase assemblage from nano- to micro-scale and pore structure characteristics.

This chapter thoroughly investigates the multiscale microstructural evolution of AAFS paste at elevated temperatures. A series of advanced characterisation techniques including nuclear magnetic resonance (NMR), X-ray diffraction (XRD), Fourier transform infrared spectroscopy (FTIR) were undertaken to characterise the nanostructures and phase assemblage of AAFS paste after exposure to various temperatures (20, 105, 200, 400, 600 and 800 °C) at Levels 0

and I. Meanwhile, the microstructural evolution of AAFS paste in terms of morphology changes, crack development and pore structure characteristics were monitored using backscattered electron microscopy-energy dispersive spectrometry (BSEM-EDS), mercury intrusion porosimetry (MIP) and X-ray microcomputed tomography (XCT). Based on the obtained experimental results, the inherent mechanisms of damage evolution in AAFS at elevated temperatures were analysed and discussed in depth from a multiscale point of view. It should be noted that part of this chapter has been presented in a peer-reviewed journal paper: W. Tu, G. Fang, B. Dong, M. Zhang, Multiscale study of microstructural evolution in alkali-activated fly ash-slag paste at elevated temperatures, *Cement Concrete and Composites*, 143 (2023) 105258.

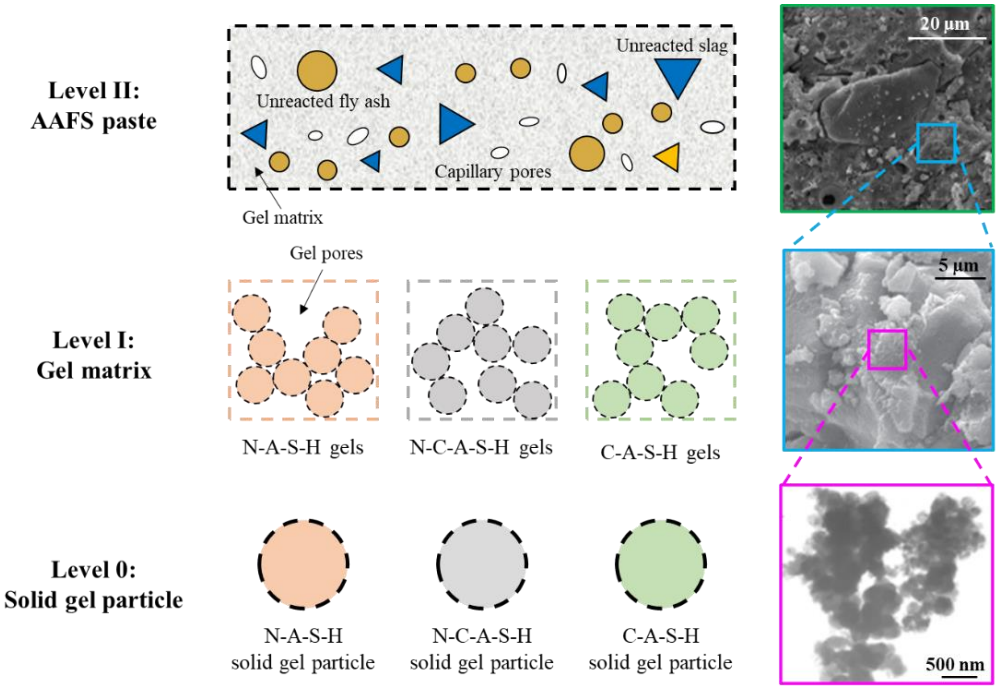

Figure 3.1. Schematic diagram of multiscale microstructure of AAFS paste (adapted from [39, 58, 88, 162]).

3.2 Raw materials

Low-calcium (Class F) fly ash and ground granulated blast-furnace slag were used as precursors, the chemical compositions of which measured by means of X-ray fluorescence spectrometry (XRF) are presented in Table 3.1. Figure 3.2 presents the morphologies of fly ash

and slag particles. It can be seen that fly ash exhibits more spherical particle shapes, whereas slag particles are more irregular. The particle size distribution of both materials is presented in Figure 3.3. A mixture of 10 M sodium hydroxide (SH) and sodium silicate (SS) was used as alkaline activators, where SH solution was prepared by incorporating 400 g NaOH pellets (analytical level of 99 wt.%) into 1 L water. It was then stored for 24 h to release heat and cool down to ambient temperature before mixing. The modulus (molar ratio of SiO_2/Na_2O) of SS solution (Na_2O: 8.5 wt.%, SiO_2: 27.0 wt.%, H_2O: 64.5 wt.%) was set as 2.0. The polycarboxylate-based superplasticiser (SP, Sika®ViscoFlow®2000) was added to ensure the workability of AAFS mixtures [12, 39, 45, 451].

Table 3.1. Chemical compositions (wt.%) of fly ash and slag.

Oxide	SiO_2	Al_2O_3	Fe_2O_3	CaO	K_2O	MgO	TiO_2	Na_2O	SO_3	P_2O_5	MnO
Fly ash	47.51	28.68	7.28	8.02	1.52	1.46	1.00	1.05	0.68	2.35	-
Slag	32.61	16.90	0.33	39.61	0.30	7.28	0.55	0.38	-	0.03	0.26

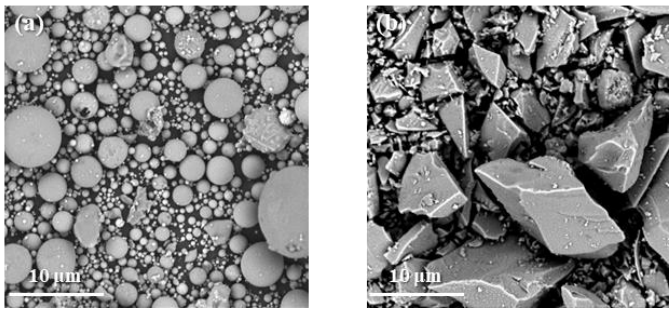

Figure 3.2. SEM images of (a) fly ash and (b) slag.

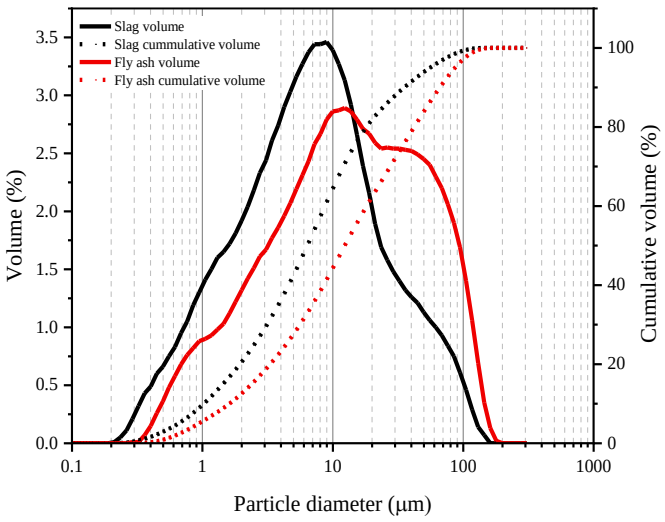

Figure 3.3. Particle size distribution of fly ash and slag.

3.3 Mix proportion

The mix proportion of AAFS paste adopted here was obtained based on the optimal mixture determined from previous studies [6, 43], which could meet the criteria for engineering application in terms of fresh and hardened properties (e.g., workability, setting time and 28 d compressive strength) according to ACI M318-05 [452, 453]. Based on previous experimental work, the workability of AAFS decreases with an increase in slag content (10-30%) and the molarity of the SH solution (10-12 M), as well as with a decrease in the alkaline activator-to-precursor (AL/P) ratio. Conversely, the compressive strength of AAFS improves with higher slag content and increased SH molarity. Considering the combined effects on both fresh and hardened properties, AAFS paste with 20% slag content and 10 M SH was selected as the optimal mixture according to these criteria. The fly ash-to-slag ratio, AL/P ratio, SS-to-SH ratio and SP-to-precursor (SP/P) ratio were set as 4, 0.4, 0.2 and 0.01, respectively. The Na_2O content was kept as 7.78 wt.% of the precursors (equivalent to 5.5 wt.% of the whole mixture). The mixture quantity is given in Table 3.2.

Table 3.2. Mix proportion (kg/m^3) of AAFS

	Fly ash	Slag	SH	SS	SP
Quantity	320	80	53	107	4

Note: SH – sodium hydroxide; SS – sodium silicate; SP – superplasticiser.

3.4 Sample preparation

The mixing process of AAFS paste includes two steps: dry mix of fly ash and slag for 3 min, and incorporating SS, SH and SP into the mixture and mixing for another 3 min. The fresh AAFS paste was cast into the cylindrical plastic moulds (⌀15 × 100 mm) and 40 mm cubic moulds after mixing, and placed on a vibrating table for 2 min. The AAFS paste specimens were then sealed with plastic film and cured in a standard curing room (20 ± 2 ºC, 95% relative humidity) for 28 d before testing.

After 28 d, the small cylindrical samples (⌀15 × 5 mm) were cut by operating a low-speed diamond saw (see Figure 3.4) with wet-cutting system. The position was kept the same when cutting different samples to ensure the representativeness. Figure 3.5 illustrates the preparation

of cylinder and crushed specimens. Six cylindrical samples were prepared from each tube for the BSEM-EDS test, whereas the crushed specimens from the cone of the cube were used in the MIP test. The sample images are shown in Figure 3.6.

Followed by cutting, the solvent exchange method was used to stop hydration inside the specimen, which was a commonly used method to eliminate free water from the hardened specimens with negligible impact on its inner microstructure [45]. As seen in Figure 3.7(a), the isopropanol solution was prepared as the organic solvent. The specimens were then placed in the isopropanol solution for 48 h to ensure free water was removed. Afterwards, the samples were stored in the vacuum drying rack for another 48 h before testing.

Figure 3.4. Instrument of low-speed diamond saw.

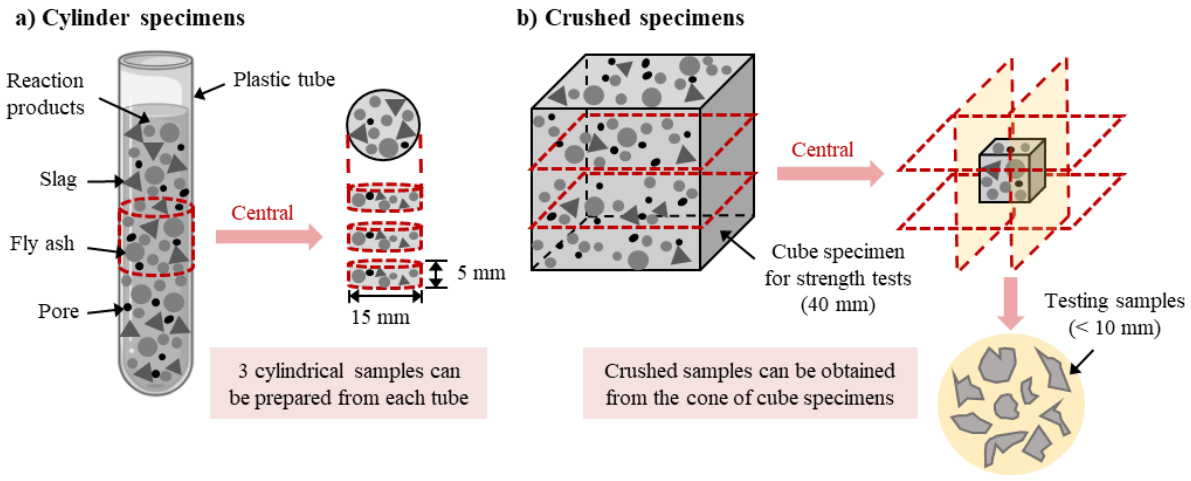

Figure 3.5. Schematic illustration of a) cylinder and b) crushed specimen preparation.

Figure 3.6. Images of cylinder and crushed specimens.

To obtain a comparatively smooth surface for BSEM tests, further preparation was required to fill the pores on the testing samples by impregnating epoxy solution as seen in Figure 3.7(b). This process was to smoothen the surface and stabilise the microstructure of specimens without alteration when subjected to grinding and polishing as seen in Figure 3.8 [45]. At first, the epoxy solution was prepared by mixing Part A (epoxy resin) with Part B (hardening agent) solution with a mass ratio of: Part A/Part B = 3. After stirring for 3-5 min, the vacuum impregnation was performed in a vacuum mosaic containing the testing specimen (i.e. it was placed in a plastic mould with a diameter of 30 mm to ensure the top surface was fully impregnated by epoxy). Finally, the specimen was stored in a vacuum drying rack for 24 h and then demoulded after the epoxy got hardened.

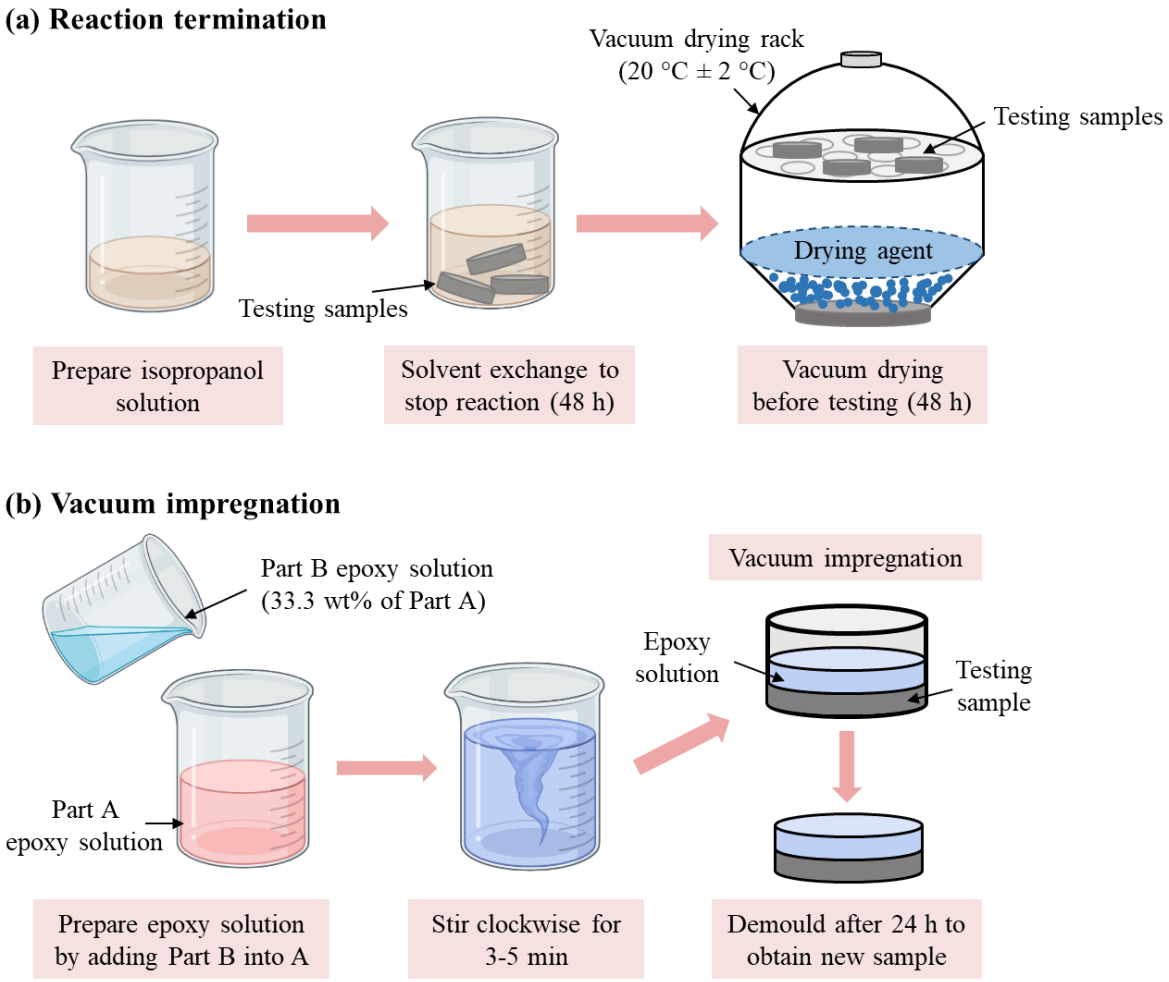

Figure 3.7. Sample preparation process regarding: (a) reaction termination and (b) vacuum impregnation.

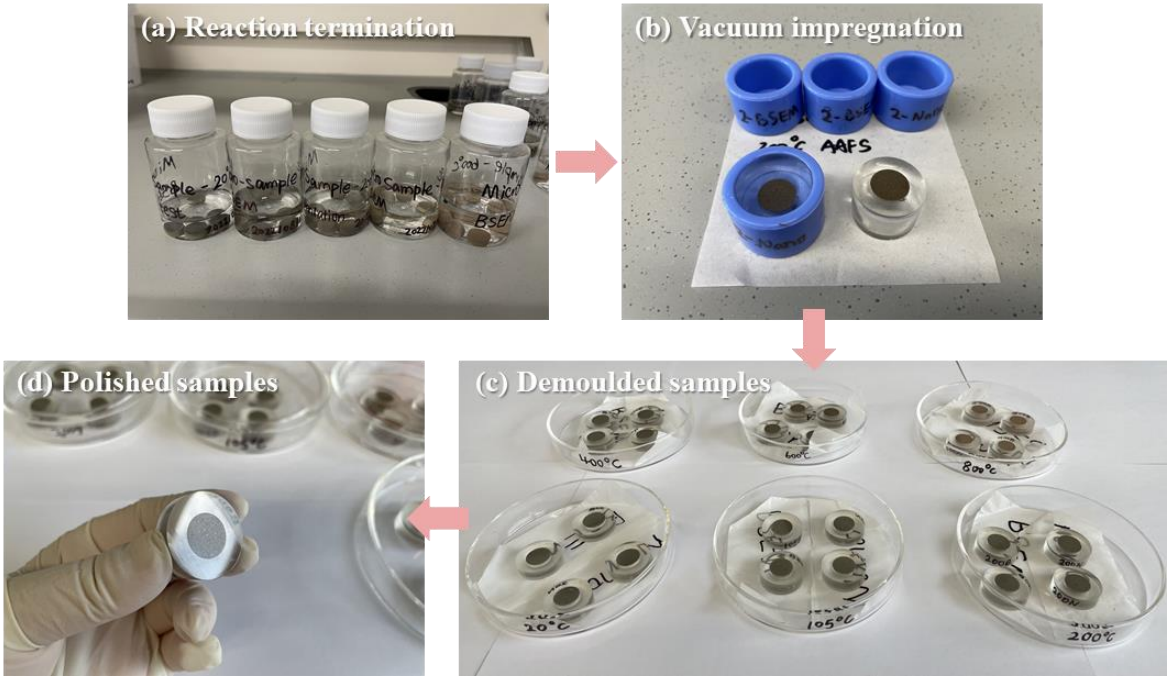

Figure 3.8. Images of vacuum impregnation process.

3.5 Heating method

After 28 d of curing, the surfaces of specimens were dried and cleaned prior to heating. Herein, the heating rate was set as 10 °C/min to attain the target temperatures of 105, 200, 400, 600 and 800 °C, apart from ambient temperature. The samples were placed in an electrical furnace with a computed heating curve. When the target temperature was reached, it was maintained for 120 min to ensure uniform distributed temperatures within the specimen, and thus a thermal equilibrium state could be achieved [454]. Afterwards, the specimen was naturally cooled down to room temperature.

3.6 Test methods

3.6.1 Nuclear magnetic resonance

To characterise the nanostructure of AAFS paste, ^{29}Si NMR test was performed to study the reacted AAFS paste prior to and after high temperature exposure. It can be used to analyse the

structural compositions of unreacted particles and reaction products by revealing the silicate structure in binding gels [34, 39, 49, 56]. Herein, the solid-state ^{29}Si NMR instrument (BRUKER, AVANCE 400WB, Germany) was used under the conditions: ^{29}Si resonance frequency of 79.48 MHz, spinning speed of 5 kHz, pulse length of 4.97 μs and a relaxation delay of 5 s with 2048 scans. The powder samples (< 40 μm) were prepared for this test. This experimental work was conducted at the Institute for Advanced Study, Shenzhen University, China.

3.6.2 X-ray diffraction

The phase compositions of AAFS specimens were detected by means of XRD [39, 454]. This is one of the most commonly used techniques to characterise the chemical features in cementitious materials. Similar to NMR test, powder specimens with size of less than 40 μm were used for XRD measurement (see Figure 3.9). To estimate and quantify the amorphous phases of AAFS prior to and after high temperature exposure, the internal standard method of Rietveld-based quantitative X-ray diffraction (QXRD) was also applied.

To prepare for the QXRD test, the powder samples with a diameter of smaller than 40 μm were obtained by manually grinding the crushed AAFS paste. A standard crystalline material of ZnO was incorporated into AAFS paste and ground together with the original sample to ensure the homogeneous distribution. The addition of ZnO is considered as an internal standard method to analyse and quantify the amorphous and crystalline phases. Figure 3.10 illustrates the preparation of both XRD and QXRD samples. Herein, the XRD instrument (XRD, D8 ADVANCE, Malvern Panalytical, Netherlands) was used under the conditions: CuKα X-ray radiation at the intensity of 40 kV- 40 mA with the slit system of RS = 0.1 mm and DS = SS = 0.6°; the 2θ scanning rate of 6°/min. The step size was set as 0.02° with $2\theta = 90°$.

Figure 3.9. Instrument of XRD.

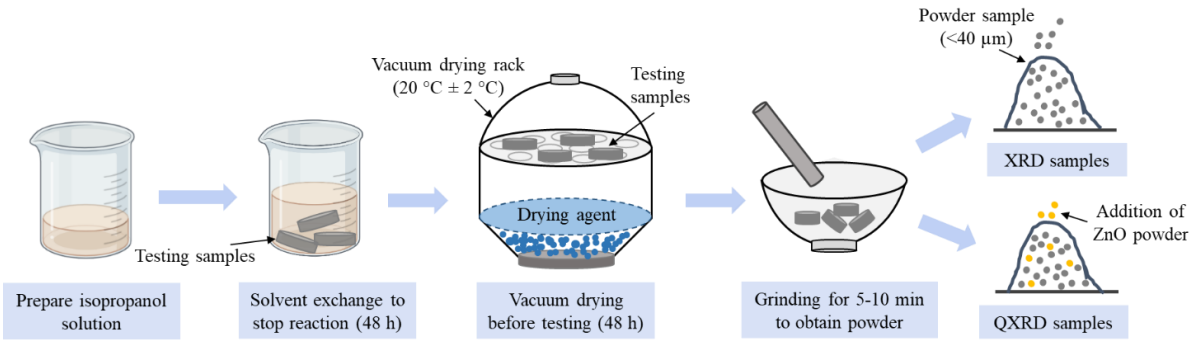

Figure 3.10. Preparation of XRD and QXRD samples.

3.6.3 Fourier transform infrared spectroscopy

To characterise the features of amorphous phase in AAFS paste at elevated temperatures, FTIR is used to scan and analyse chemical properties of samples by infrared light. Powders smaller than 25 μm were prepared, using a Shimadzu, IR Tracer-100 (Japan). 16 times of scanning from 4000 to 400 cm^{-1} with a resolution of 4 cm^{-1} were performed.

Figure 3.11. Instrument of FTIR.

3.6.4 Backscattered electron microscopy–energy dispersive spectrometry

The morphology changes and phase assemblage of AAFS paste were characterised using BSEM-EDS. AAFS paste specimens experienced grinding and polishing after the vacuum impregnation using a machine (BUEHLER, EcoMetTM 250, USA) as seen in Figure 3.12. Grinding was performed for 5 min at 50 r/min with a loading of 5 N with ethyl alcohol as a cooling medium and lubricant using paper grits of 400 (37 μm), 800 (19 μm) and 1200 (15.3 μm). Polishing was performed for 15 min at 70 r/min using diamond suspensions with grits of 2500 (5.5 μm), 3000 (5 μm), 5000 (2.7 μm) and 7000 (1.25 μm). Ultrasonic cleaning was applied after these operations and the polished specimens were stored in vacuum bags until testing. A schematic illustration of sample preparation process is given in Figure 3.13.

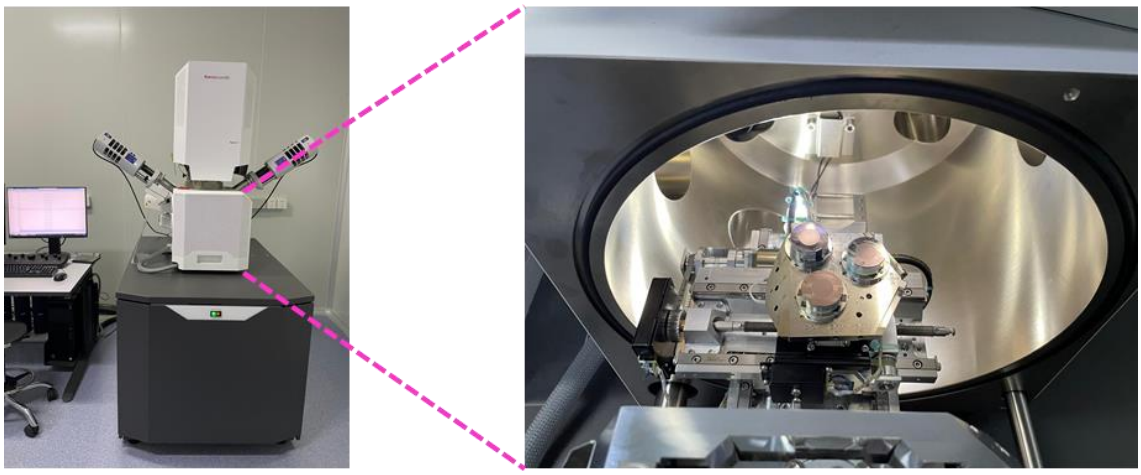

Figure 3.12. Instrument of BSEM-EDS.

Before the BSEM test, a thin layer of carbon coating was applied on the specimen to improve the conductivity. During the test, the working distance was 10 mm with the acceleration voltage set as 15 kV and the spot size of 6 nm. BSEM images (pixel size of 20 nm) were obtained at a magnification ranging from 30× to 4000×. Furthermore, the EDS analysis was conducted under the conditions: beam energy of 15 keV, probe current of 600 pA, and beam spot size of about 450 nm. The working distance was 8.5 mm with a take-off angle of 35º. The counting rate was set as 50000 counts per analysis with dead times of 30% and acquisition time of 50 s.

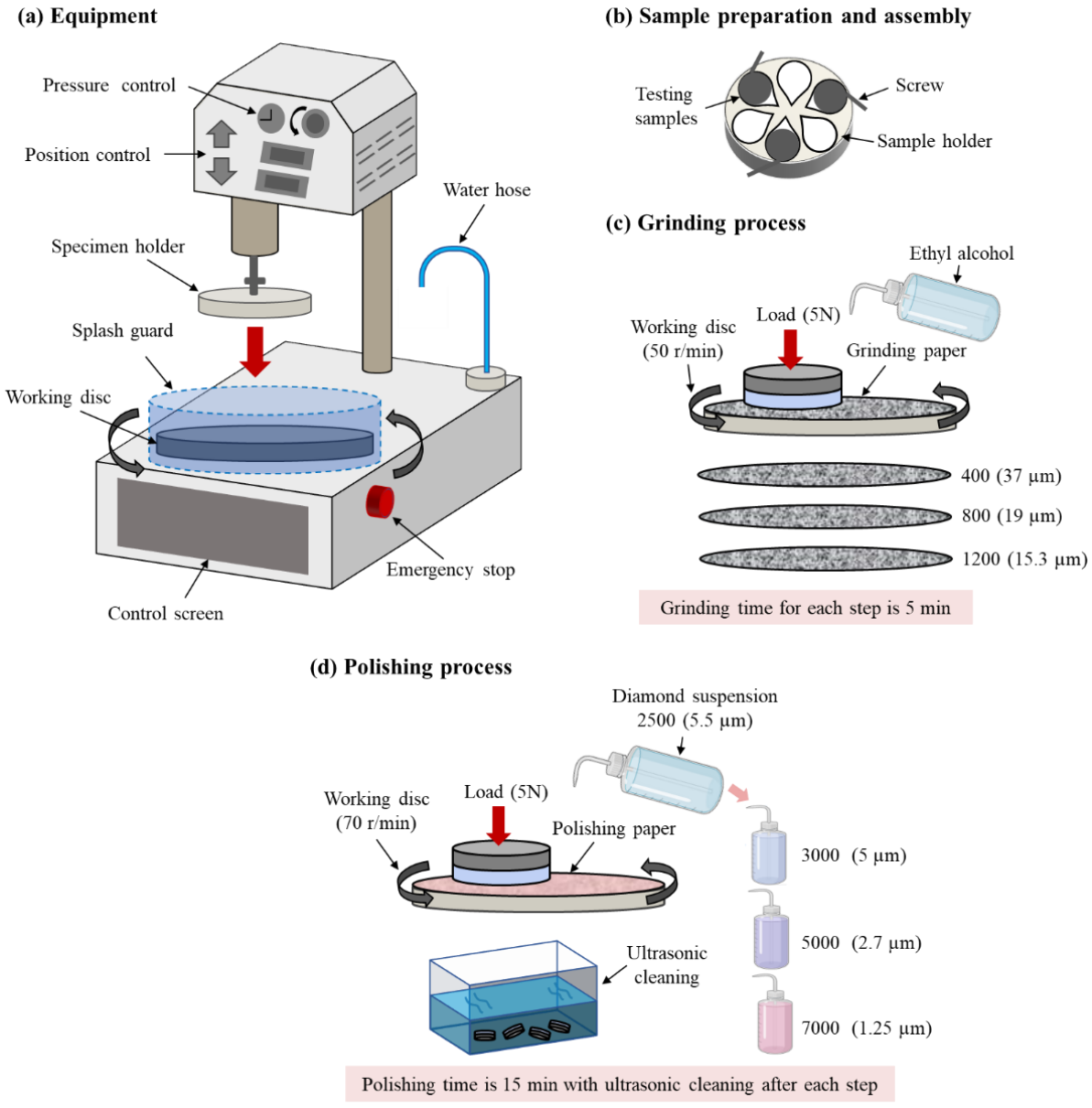

Figure 3.13. Grinding and polishing process.

3.6.5 Mercury intrusion porosimetry

The pore structure of AAFS paste was characterised using MIP (AutoPore IV 9500). The pore diameters ranging from 0.001 μm to 1000 μm were measured with MIP. The pressure applied for MIP test was from 0 to 414 MPa. The surface tension of mercury employed here was 0.485 N/m. The contact angle between the mercury and the pore surface was 130° [455].

3.6.6 X-ray microcomputed tomography

As a non-destructive method, XCT was used to explore the 3D microstructural evolution of AAFS paste at elevated temperatures. Figure 3.14 illustrates the XCT test setup and image processing procedure. XRadia-Micro XCT-400 scope (Zeiss, Germany) was employed for XCT scanning at 59 kV and 150 μA (magnification of 0.4×).

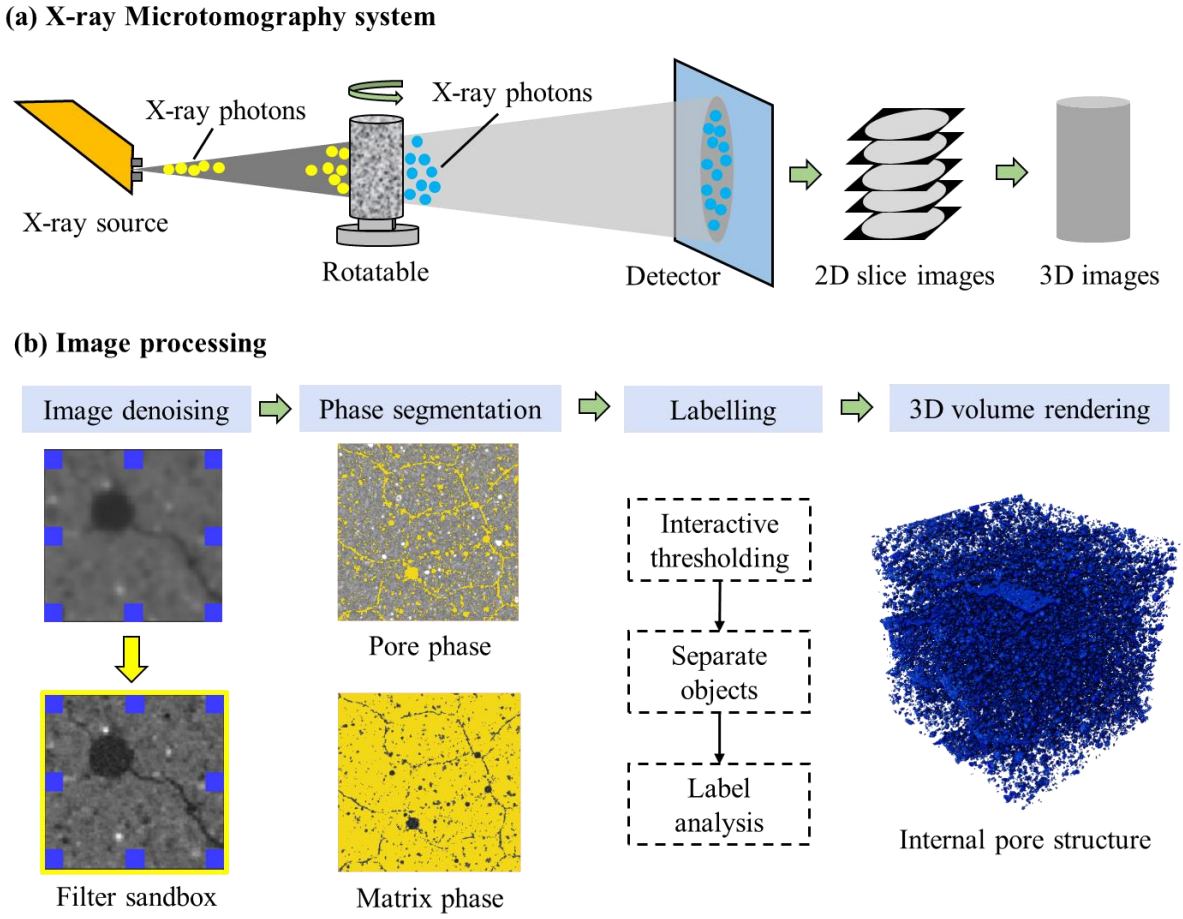

Figure 3.14. (a) XCT setup and (b) image processing procedure.

The scanning time for each test is about 7 h to complete 2501 projections (angle step of 0.144º from -180º to 180º) with a 10 s exposure of every projection. The field of view and spatial resolution was 1.5 mm (x = y = z) and 1.56 µm (x = y = z), respectively. 2D slice images of the specimen were obtained from the detector to construct 3D images, which were further analysed using the software Avizo. Firstly, the images were denoised using the filter sandbox tool to better separate the edges of different phases (e.g., between cracks and matrix). Afterwards, different phases were segmented through interactive thresholding and separate objects. The labelling was then carried out using label analysis to quantify the volume fractions of different phases and size distribution. Finally, the internal pore structure of specimens could be visualised using 3D volume rendering.

3.7 Results and discussion

In this section, the multiscale microstructural evolution of AAFS at 20-800 °C is investigated with respect to nanostructure of AAFS solid gel particles, chemical compositions, solid phase assemblage and pore structure changes.

3.7.1 Nanostructure arrangement

The ^{29}Si NMR spectra was obtained to investigate the nanostructure of AAFS solid gel particle at ambient and high temperatures. To determine the chemical surroundings of silicon tetrahedra in different phases, Q^n(mAl) structure units were commonly employed (n is the number of oxygen bridges between different silicon tetrahedral and m represents the number of aluminium tetrahedra) [456]. The ^{29}Si NMR spectra of fly ash and slag were deconvolved and depicted in Figure 3.15. The presence of fly ash particles was reflected by five Q^4 structures in an overlapped peak: Q^4(4Al) (-87 ppm), Q^4(3Al) (-95 ppm), Q^4(2Al) (-103 ppm), Q^4(1Al) (-110 ppm) and Q^4(0Al) (-116 ppm). On the other hand, a broad peak at approximately -75 ppm was shown in slag particles, which can be assigned to the presence of Q^0 and Q^1 sites [39]. Two traces of signals corresponding to Q^2(1Al) and Q^3(1Al) sites were also found at -83 and -88 ppm, respectively [457].

To monitor and characterise the evolution of reaction products in AAFS at different temperatures, the Q sites from the raw materials were assumed to be stable, while the relative changes of intensities corresponded to the development of different reaction products, including C-A-S-H, N-C-A-S-H and N-A-S-H gels. Figure 3.15(c) displays the ^{29}Si NMR spectrum of AAFS paste at ambient temperature, with deconvolution of the signals that can be assigned to the presence of several Q sites based on the previous NMR studies of AAFS [34, 47, 49, 123].

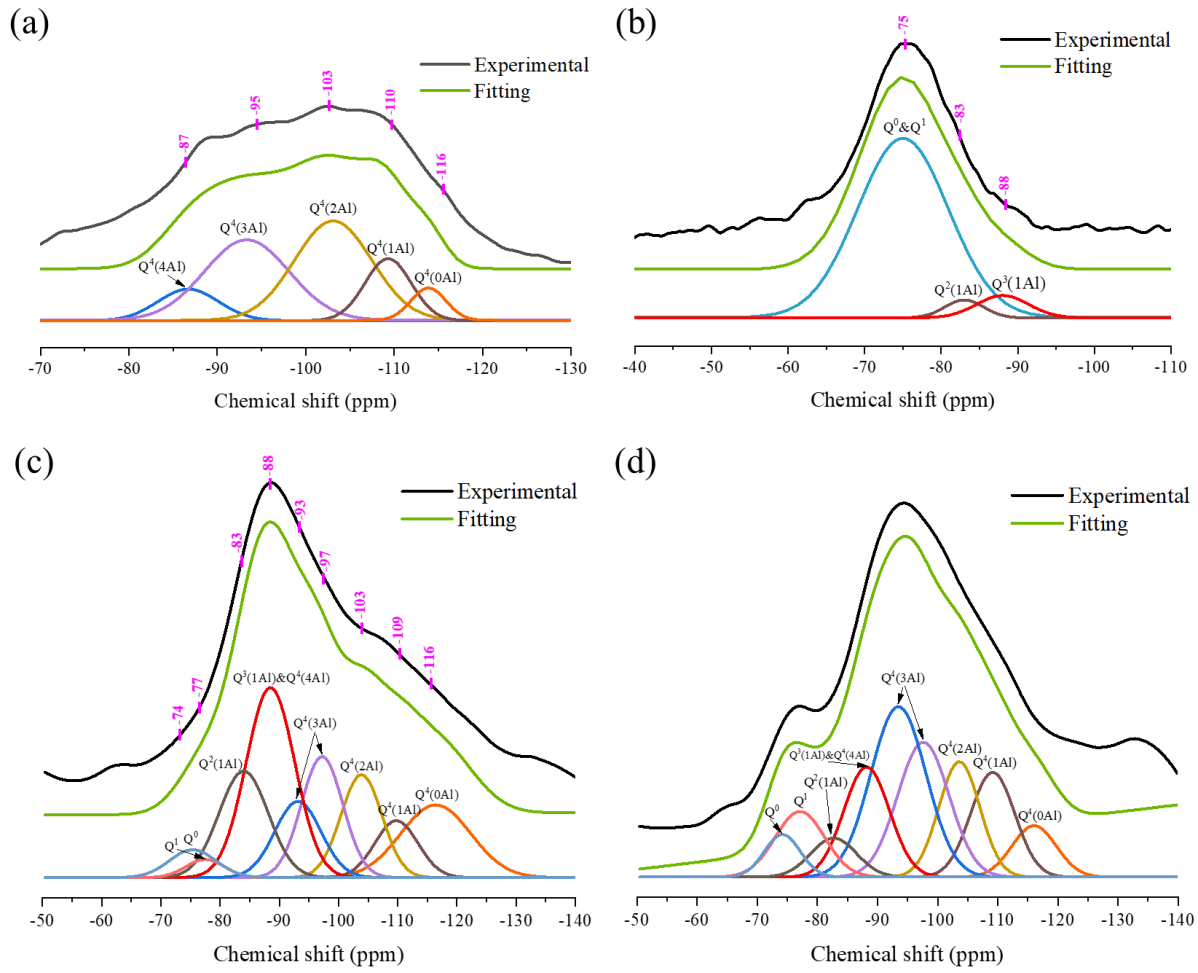

Figure 3.15. ^{29}Si NMR spectra of (a) fly ash, (b) slag, and AAFS paste at (c) 20°C and (d) 800 °C.

The spectrum exhibited a broad peak between -70 and -100 ppm, implying a significant portion of Q^0 (unreacted slag), Q^1 and Q^2 (C-A-S-H) from the slag solely and Q^3 (highly cross-linked N-C-A-S-H) from the reaction of both raw precursors. The coverage area between -90 and -120 illustrates the presence of Q^4 (N-A-S-H and unreacted fly ash) sites. The location of

different Q^n sites can be referred to the previous NMR analysis [39], which is summarised in Table 3.3. There was a notable drop of Q^2 and Q^3, whereas the amount of Q^4(3Al) in AAFS went up remarkably as the temperature rises from 20 to 800 °C. The quantification of different phases based on the deconvolution results is also presented in Table 3.3.

Table 3.3. Area percentages of 29Si NMR spectra of AAFS paste at elevated temperatures.

Temperature (°C)	Slag	Reaction products							Fly ash
		C-A-S-H		N-C-A-S-H	N-A-S-H (Al-rich)		N-A-S-H (Si-rich)		
	Q^0	Q^1	Q^2(1Al)	Q^3(1Al) & Q^4(4Al)	Q^4(3Al)		Q^4(2Al)	Q^4(1Al)	Q^4(0Al)
	-74	-77	-83	-88	-93	-97	-103	-109	-116
20	3.53	1.90	14.24	25.14	9.56	13.68	11.48	6.67	13.81
105	5.17	7.98	20.80	20.35	15.56	10.43	7.87	6.84	5.00
200	5.68	7.07	24.52	21.77	7.10	14.35	5.36	9.48	4.66
400	8.27	16.45	17.01	16.65	10.10	11.48	9.13	5.81	5.12
600	5.97	10.31	11.61	15.09	8.58	26.91	5.04	11.31	5.18
800	3.85	8.21	4.50	12.69	23.81	17.52	11.95	11.71	5.75

With respect to the evolution of different phases in AAFS paste at different temperatures, the ^{29}Si NMR spectra is shown in Figure 3.16. As the temperature rose from ambient to 200 °C, the broad peak at Zone b slightly shifted to a lower value from -88.39 to -86.39 ppm, followed by a right shift of the peak at -94.38 ppm after 800 °C exposure. This indicated the increase in the intensity of sites corresponding to C-A-S-H gel from 20 to 200 °C and a considerable drop with the dehydration of C-A-S-H gel when the temperature exceeded 400 °C [154]. By further evaluating of AAFS nanostructure changes at elevated temperatures, the volume fractions of Q^n(mAl) structure units corresponding to unreacted particles and reaction products are presented in Figure 3.17. An increase of the content of Q^2(1Al) from 14.24% to 24.52% can be found after 200 °C exposure. From 400 to 800 °C, the amount of Q^2(1Al) sites went down to 4.5%, suggesting that C-A-S-H gels were no longer the dominant reaction products in AAFS at 800 °C. This is in good agreement with the previous studies, which reported the mitigation of the peaks assigned to C-S-H gel in the XRD pattern of AAFS at 400 °C [34, 458]. The decomposition of C-A-S-H gels and the formation of N-A-S-H gels occurred simultaneously [34, 459, 460], with a reduction of Q^4(0Al) sites from 13.81% to 5.75% and an increase of Q^4(3Al) from 23.24% to 41.33%. Since Q^4(0Al) was assigned to the highly polymerised Al-rich N-A-S-H gel, a higher degree of cross-linking was found in AAFS. This is demonstrated

in Zone c of Figure 3.16, with a right shift of the peak from -107.87 to -110.37 ppm upon exposure at 200 °C and disappearance of the peak after 200 °C exposure. Meanwhile, Q^4(2Al) and Q^4(1Al) sites were recognised to represent more stable Si-rich N-A-S-H types of gel. It is noteworthy that a new peak in Zone a appears at -75.90 ppm after exposure to 800 °C, indicating the formation of gehlenite with monomeric Si [56, 461].

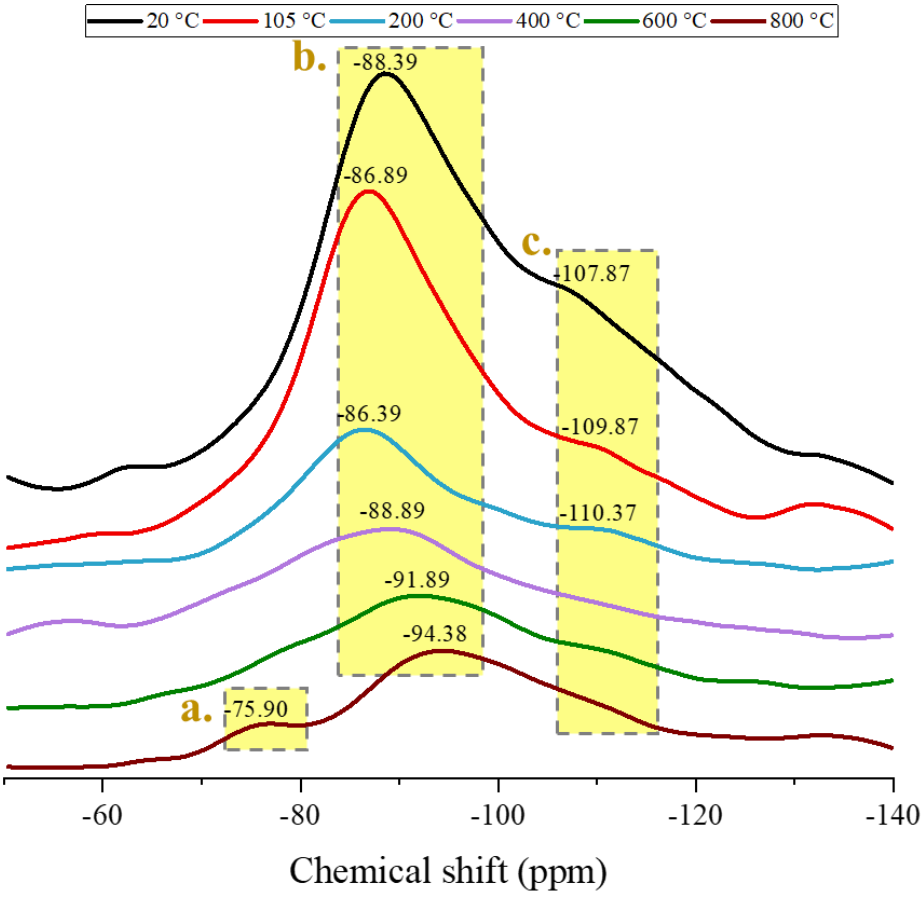

Figure 3.16. ^{29}Si NMR spectra of AAFS paste at elevated temperatures.

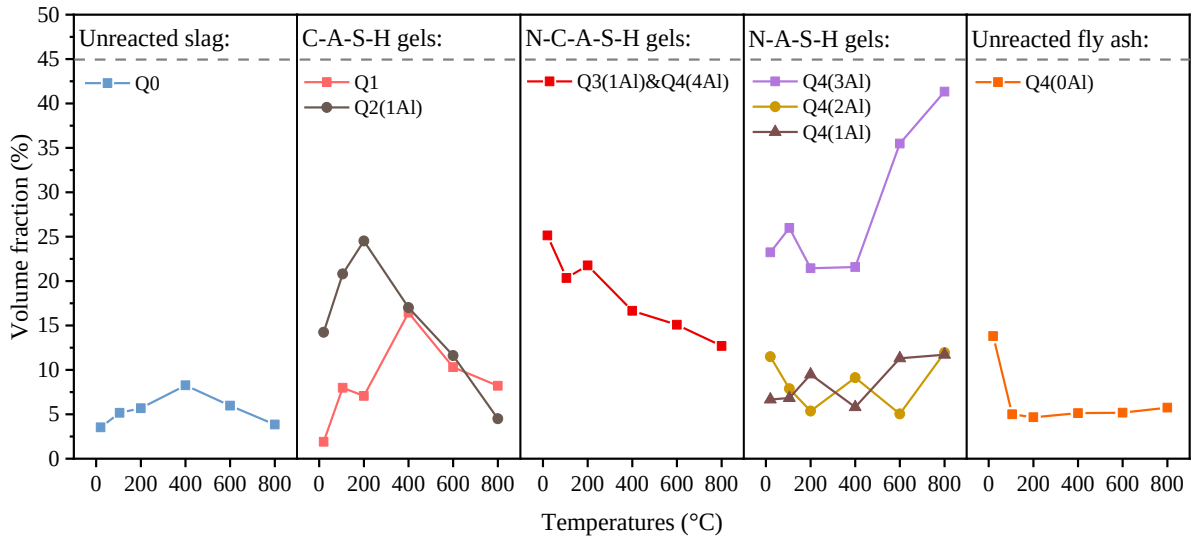

Figure 3.17. Volume fractions of different phases in AAFS paste at elevated temperatures.

3.7.2 Crystalline phase characterisation

To understand the chemical composition of AAFS gel matrix and track the transformation of different crystalline phases, XRD analysis was carried out to provide the information on AAFS paste at ambient and high temperatures. Figure 3.18(a) displays the XRD patterns of raw fly ash and slag. The peaks in the XRD spectra of fly ash were mainly associated with quartz (SiO_2), mullite ($Al_6Si_2O_{13}$) and magnetite (Fe_3O_4), whereas a diffuse band at 25-35° 2θ was depicted in the XRD spectra of slag, corresponding to the presence of glassy phase [55, 56]. Figure 3.18(b) shows the XRD results of AAFS paste at different temperatures. At ambient temperature, the crystalline phases presented in AAFS paste were similar to those in the raw fly ash, including quartz, mullite, hematite (Fe_2O_3) and magnetite, which were consistent with those reported in the previous XRD results of AAFS paste [22]. Both quartz and mullite were physically stable when subjected to elevated temperatures, as they had a relatively high melting point of 1713 °C and 1830 °C, respectively [307, 308]. A wide and diffusive band at around 20-35° 2θ reflected the amorphous phases, suggesting the presence of aluminosilicate gels [123]. The peak at around 30° 2θ indicated the presence of calcite [462]. The diffuse hump at around 29-31° 2θ was associated with C-S-H gels, which were formed from the polymerisation of the dissolved active calcium out of slag with silica provided by sodium silicate in a strong

alkaline environment [463, 464]. Also, the Si from C-S-H gels could be possibly replaced by Al to form C-(A)-S-H gels [55].

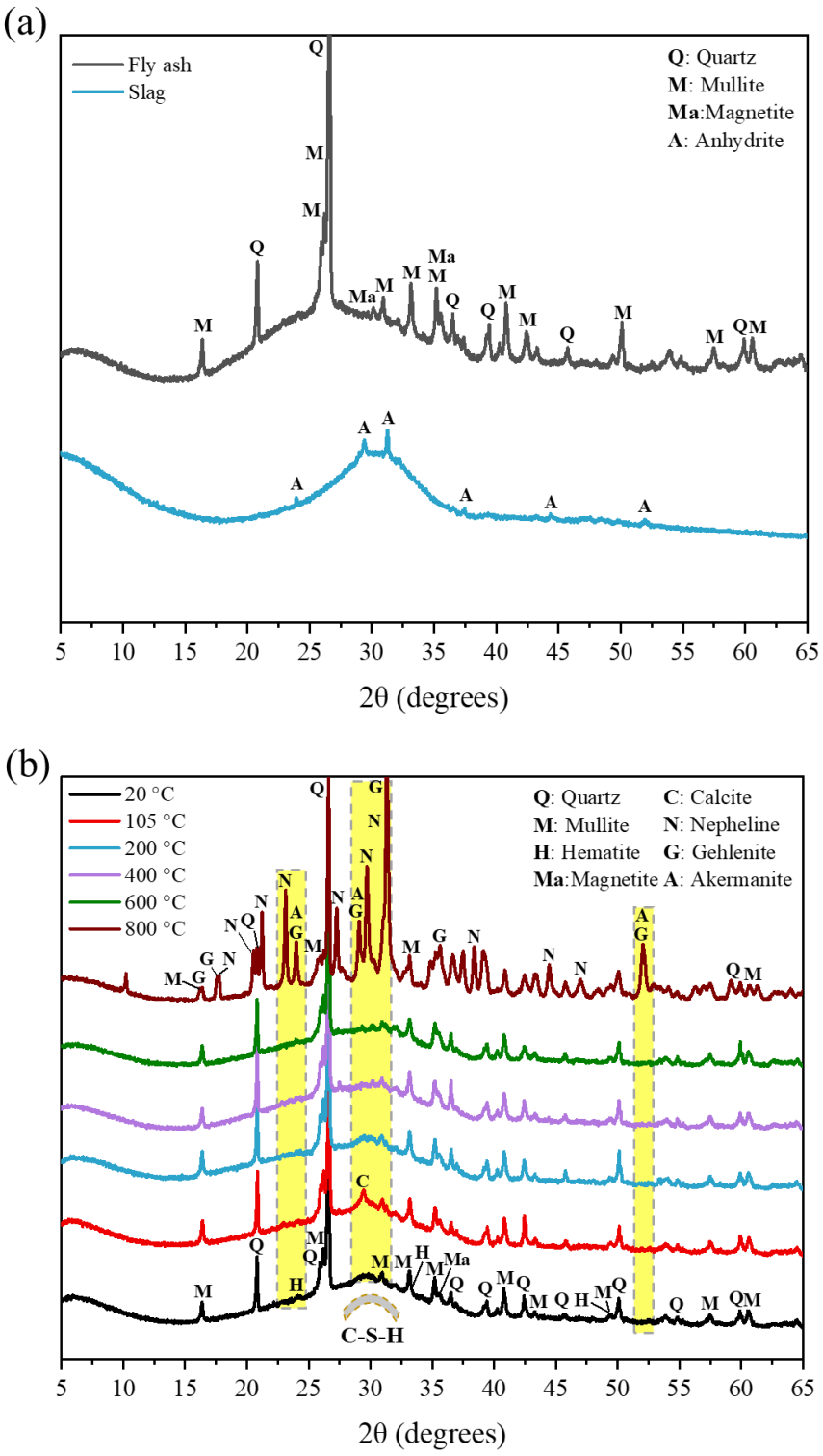

Figure 3.18. XRD patterns of (a) precursors, and (b) AAFS paste at elevated temperatures.

After high temperature exposure, the decrease of the intensity of C-S-H phase was observed at 200 °C, implying the decomposition of C-S-H gels, while no obvious changes can be identified until 800 °C was reached. New crystalline phases including nepheline ($NaAlSiO_4$), gehlenite ($Ca_2Al(AlSiO_7)$) and akermanite ($Ca_2MgSi_2O_7$) can be observed, implying the full crystallisation and decomposition of N-A-S-H, C-(A)-S-H and hybrid gels at 800 °C. The formation of nepheline corresponded to the partial crystallisation of N-A-S-H gel, while gehlenite and akermanite were associated with the transformation of C-(A)-S-H gel. The findings from ^{29}Si NMR also supported that the reduction of C-A-S-H content corresponding to Q^1 and $Q^2(1Al)$ could happen from 200 to 800 °C. Consequently, more cross-linked Q^4 sites occurred, which can be ascribed to the presence of nepheline [56].

Figure 3.19 presents the mineralogical compositions of AAFS paste at elevated temperatures acquired with Rietveld refinement. It can be seen that the crystalline phases of quartz and mullite were thermally stable after 800 °C exposure, which slightly fluctuated around 6.9% and 9.5%, respectively, while the amorphous content dropped dramatically from 79.6% to 33.5% at 800 °C, along with the appearance of nepheline and gehlenite, taking up 26.3% and 21.5%, respectively. This indicated that the partial recrystallisation of amorphous aluminosilicates in AAFS paste was approximately 57.9% of the total amorphous phase. As nepheline was formed from the crystallisation of N-A-S-H gel, while the formation of gehlenite was associated with the crystallisation of C-A-S-H gel, the calculated phase content implied that the crystalline phase transformation of AAFS paste at 800 °C could be more sensitive to N-A-S-H induced phases [180]. Furthermore, it is worth noting that the content of calcite went up from 2.9% to 4.4% when the temperature rose to 105 °C, followed by a drop to 2.2% at 400 °C. After 400 °C, calcite was not detected in AAFS paste, indicating the decomposition of this phase, as mentioned above.

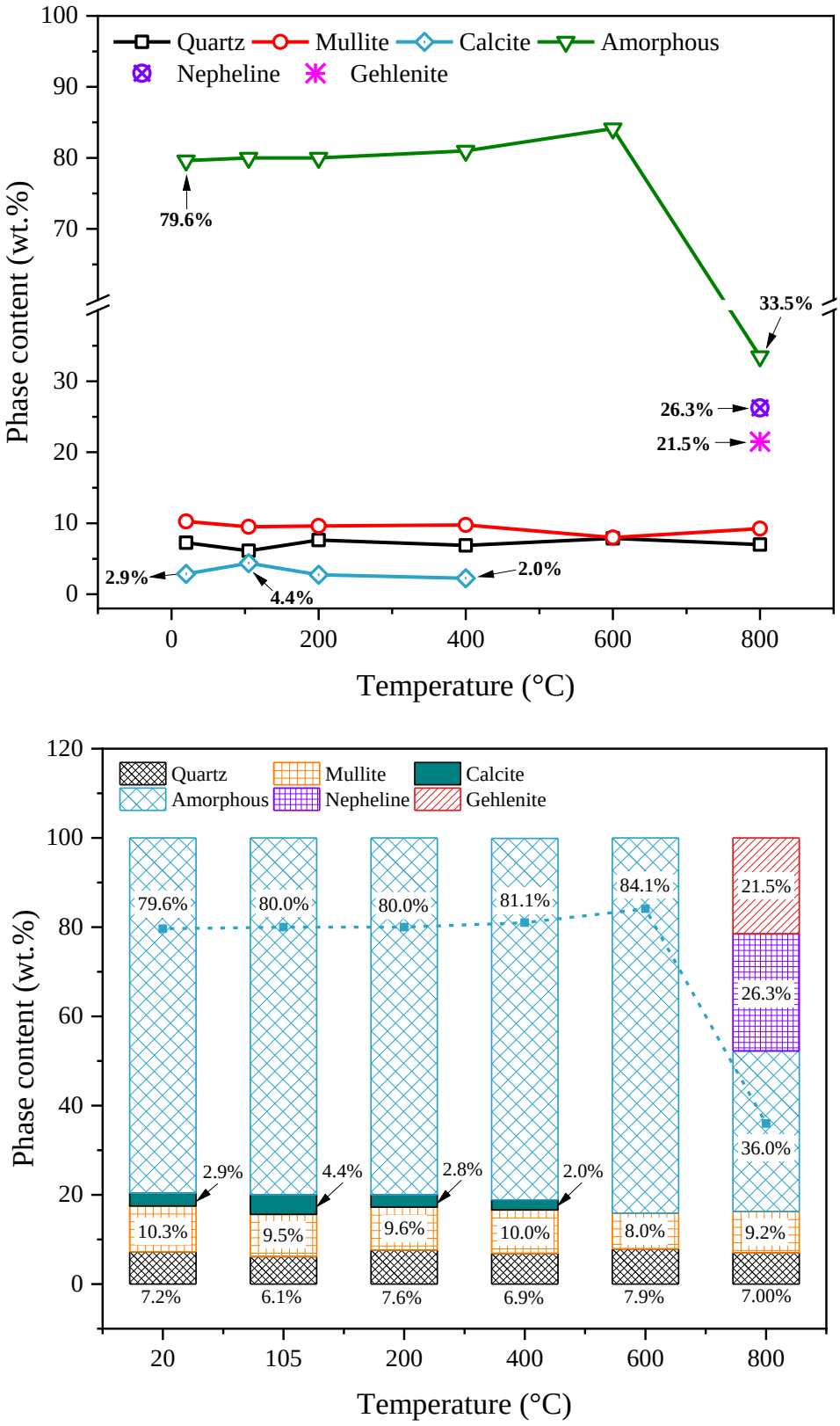

Figure 3.19. Mineralogical compositions of AAFS paste at elevated temperatures.

3.7.3 Amorphous phase identification

FTIR test results can be used to study the chemical changes of AAFS paste at elevated temperatures. Figure 3.20 illustrates the FTIR spectra of raw precursors and AAFS paste at different temperatures. As seen in Figure 3.20(a), the major band at around 1008 cm^{-1} can be observed in raw fly ash, which was associated with the asymmetric stretching vibration of Si-O-T bonds, where T stood for Si or Al units [180, 465]. The band ranging from around 680 to 800 cm^{-1} corresponded to the stretching vibrations of Si-O-Si and the weak peak at 1486 cm^{-1} could be ascribed to the O-C-O bonds associated with the presence of calcite [22, 180]. Similar to raw fly ash, the main band observed at 860 cm^{-1} in slag was related to Si-O-T bonds. The discrepancy between the band positions of fly ash and slag (i.e. 1008 and 860 cm^{-1}) was due to the chemical and structural differences of these two materials [39, 46]. The vibration band at 1488 cm^{-1} can be assigned to the stretching vibration of O-C-O bonds [22], which implied the existence of calcite as confirmed in the XRD patterns in Figure 3.18(b). Moreover, the absorption band observed at around 670 cm^{-1} can be attributed to the T-O stretching vibrations (see Figure 3.20(a)).

Figure 3.20(b) demonstrates a comparison among FTIR spectra of AAFS paste at different temperatures. At ambient temperature, the alkali-activation provided an intense band centred at 962 cm^{-1}, assigning to the asymmetric stretching vibrations of Si-O-T bonds. Knowing that C-A-S-H gels were located at 950 cm^{-1} and the wavenumber representing N-A-S-H gels was centred at 1020 cm^{-1}, the position that corresponded to the reaction products of AAFS paste (i.e. 962 cm^{-1}) was located between C-A-S-H and N-A-S-H gels, implying the coexistence of both types of gels and the presence of N-C-A-S-H gel [39, 46, 88, 171]. With the rise of temperature, the Si-O-T bonds shifted to left towards a higher value of wavenumber, which reached 970 and 993 cm^{-1} at 400 and 800 °C, respectively. This indicated that the formation of C-A-S-H gels could potentially make a pronounced impact on the reaction products in AAFS at 20 °C, since the wavenumber of 962 cm^{-1} was closer to 950 cm^{-1} than 1020 cm^{-1}. However, the rising temperature to up to 800 °C could lead to the promotion of further polymerisation and thus the development of N-A-S-H gels with a higher cross-linking structure (i.e. 993 cm^{-1} was closer to 1020 cm^{-1}) [39]. This was also confirmed in the ^{29}Si NMR results that there was an around 21.3% loss of C-A-S-H gels, while the volume fraction of N-A-S-H gels went up by

about 57.1% from 20 to 800 °C. This suggested the transformation of gel matrix in AAFS paste from a potentially C-A-S-H dominated to N-A-S-H dominated structure with the coexistence of N-C-A-S-H, attributing to the presence of Ca from slag. Moreover, the absorption area tended to be broader and deeper as the temperature went up, indicating a more disordered structure in the AAFS gel matrix due to high temperature exposure, which agreed well with the previous study on AAFS at elevated temperatures [22, 62].

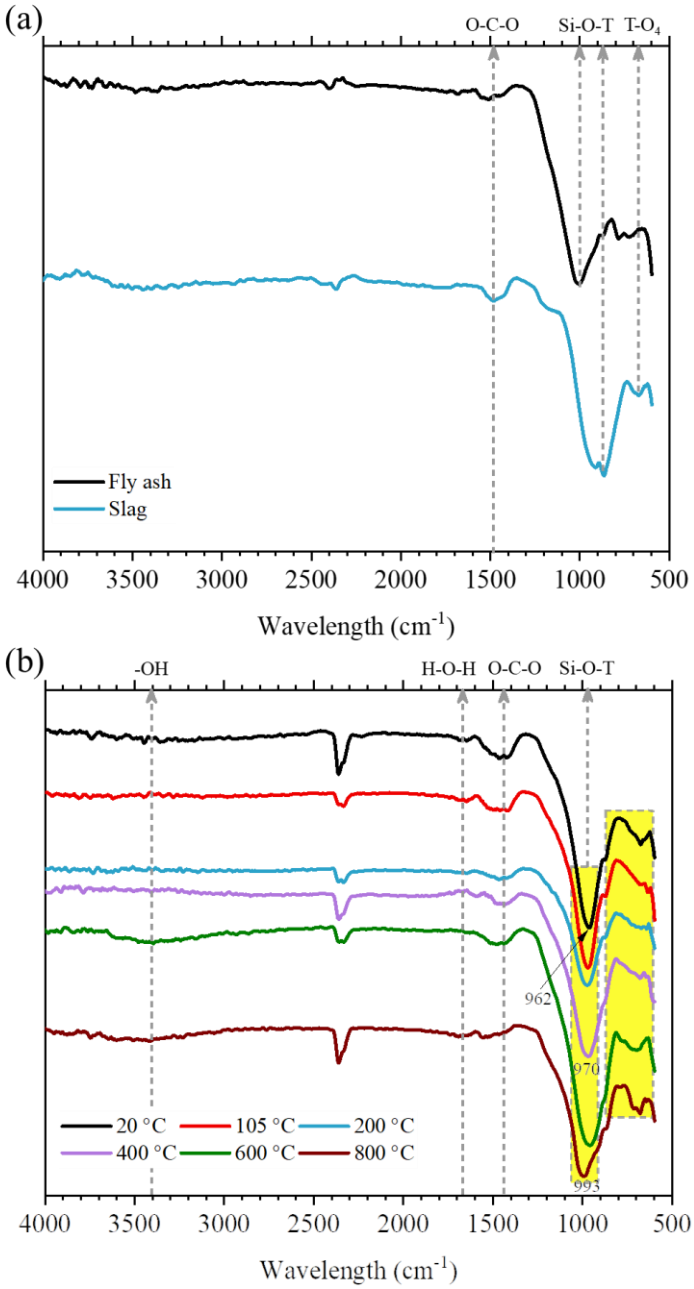

Figure 3.20. FTIR spectra of (a) precursors, and (b) AAFS paste at elevated temperatures.

The signal at around 2360 cm^{-1} was assigned to CO_2 vibration, while the vibration band located at around 1670 cm^{-1} was associated with H-O-H bonds that represented both physically- and chemically-bonded water in the gel matrix and disappeared after 400 °C exposure [22, 466, 467]. This indicated that moisture was fully lost in AAFS paste. Similarly, the vibration band at about 1440 cm^{-1} was linked to the carbonates from soluble alkali species, which also became invisible after 600 °C. Furthermore, the highlighted broad band from around 600 to 860 cm^{-1} was recognised as the quartz band, which did not experience an obvious change after high temperature exposure, suggesting the thermal stable feature of quartz, as mentioned in the XRD results [22, 180].

3.7.4 Solid phase assemblage

AAFS paste is composed of different phases, including unreacted fly ash and slag particles, reaction products and pores [39]. These phases can be assembled using BSEM images which track the evolution of AAFS paste at various temperatures based on the morphology changes. After analysing the grey values of BSEM images, different phases can be quantitatively identified. The BSEM images of AAFS after high temperature exposure are shown in Figure 3.21. At 20 °C, both unreacted fly ash and slag particles can be observed. The activation of small fly ash particles was more noticeable than the relatively larger particles, which can be explained by the fact that finer particles were easier consumed and activated than coarser ones at ambient temperature [468, 469]. The dissolution of slag particles at this stage was ascribed to a higher vitreous phase of more than 90% involved in the alkaline activation compared to that of fly ash (around 50% vitreous phase) [39, 468]. Hence, the degree of activation in slag was more pronounced than fly ash, which was consistent with the NMR and FTIR results, confirming the dominant presence of slag induced C-A-S-H gels. Also, there were some visible micro-cracks in AAFS paste at 20 °C, due to autogenous, chemical and drying shrinkage during the curing process [6]. Moreover, the interfacial transition zone (ITZ) between reaction products and unreacted particles was defined as the weak zone, which led to the development of cracks [22].

When the exposure temperature went up to 105 °C, the reaction of fly ash and slag particles continued with the initiation and propagation of wider cracks along the edge of unreacted precursors, which implied that the cracks were prone to develop around the interfacial transition

zone between unreacted particles and reaction products. The development of cracks at this stage could be the result of the evaporation of free moisture that led to the propagation and localisation of cracks at the relatively weaker interface [22]. At 200 °C, the unreacted particles were gradually consumed to form hybrid N-C-A-S-H gels. The cracks kept growing due to the loss of physically- and chemically-bound water and the transport of moisture that resulted in the accumulation of pore pressure [2, 4, 52]. With the rising temperature to up to 400 °C, the cracks were both wide and lengthened. This can be ascribed to the migration of moisture from both physically and chemically bonded water that resulted in the pore pressure build-up. Fully reacted particles were found at 400 °C. Some fly ash particles exhibited hollow structures, which may leave a porous spherical-shaped region, as highlighted in Figure 3.21.

A pronounced morphological change was depicted in AAFS paste from 400 to 600 °C, at which the cracks turned into large cavities with drastic deterioration. After 600 °C exposure, the presence of small and widen cracks indicated that AAFS paste experienced discontinuity due to pore pressure-induced and thermal stress-induced damage, along with decomposition of hybrid gels [4, 22]. In particular, the decomposition of silica gel could take place at 700-800 °C, resulting in thermal expansion and thus the widening and lengthening of cracks [142, 171, 438]. Slag particles could barely be observed, while some holes were detected on the surface of residual fly ash particles. At 800 °C, a porous structure with traces of consumed precursor particles was shown. There were few unreacted particles at this stage and micro-cracks were not observed. This can be attributed to melting and viscous sintering, which corresponded to the collapse of nano-pores and evolution of interparticle bonding, allowing the self-healing of micro-cracks and densification of AAF matrix by filling small voids [2, 392].

Based on BSEM images, the greyscale histogram can be obtained and deconvolved into four Gaussian curves for image segmentation to divide the phases in AAFS paste into three different groups: pore phase including pores and cracks in black owing to the low atomic number [43, 44], reaction products in dark grey, and unreacted fly ash and slag particles in light grey, as illustrated in Figure 3.22(a) and (b).

With a greyscale from 0 to 250, the threshold value between pore phase and reaction products was assigned at the interaction point between Gauss 1 (pore and cracks) and Gauss 2 (reaction products) of 54. The boundary between reaction products and unreacted particles was defined using the second interaction point between Gauss 2 (reaction products) and Gauss 3

(unreacted particles), which was 181. Thus, the image was processed based on the categorised grey values: pores (0-54), reaction products (54-181) and unreacted particles (181-250). For consistency and comparison purposes, the same thresholding method was adopted to process all images at different temperatures.

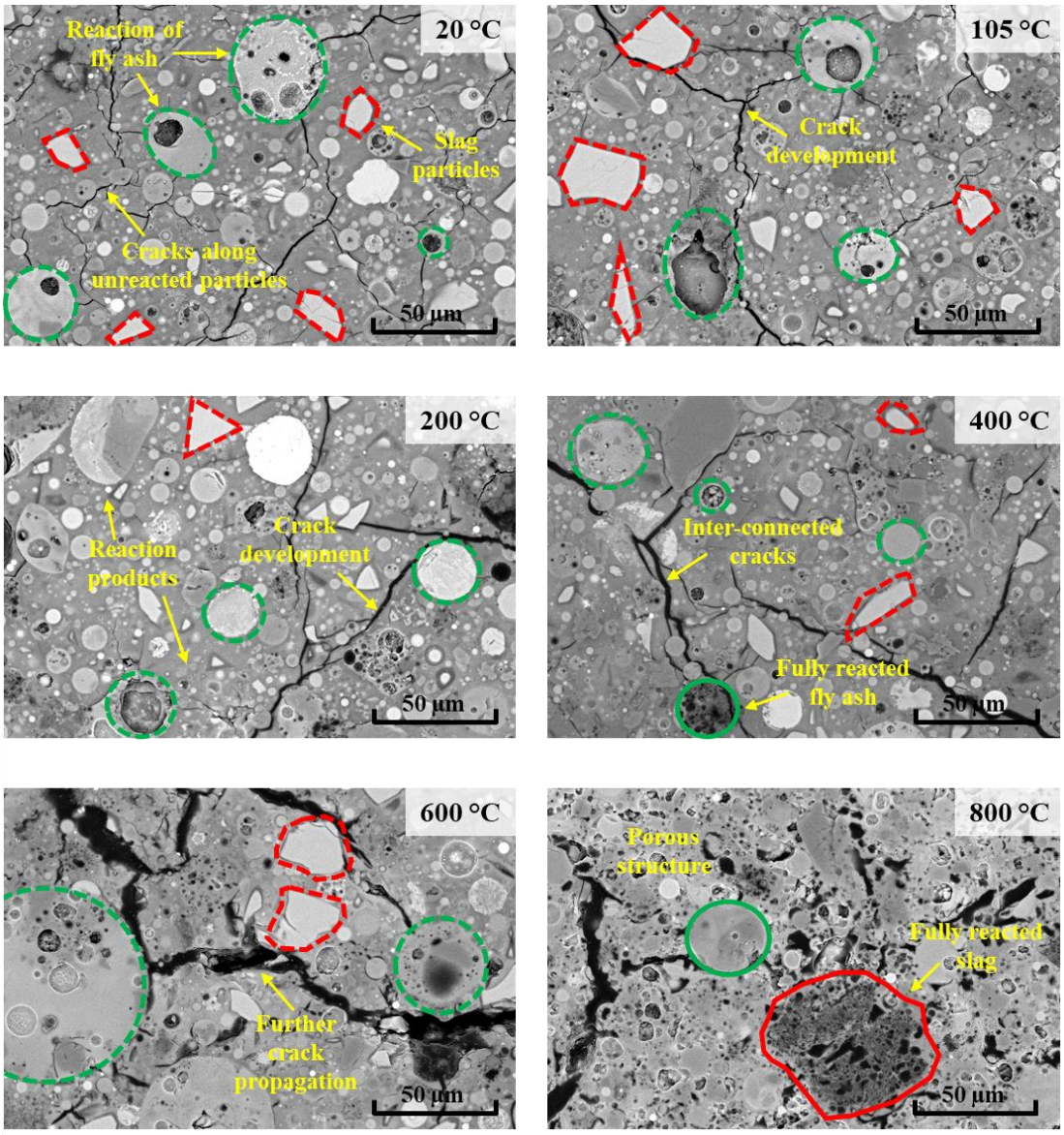

Figure 3.21. BSEM images of AAFS paste at elevated temperatures.

After image segmentation, the content of each phase can be determined, as shown in Figure 3.22(c). All three phases are colour-coded separately in green (unreacted particles), red (reaction products) and blue (pores and cracks). Overall, unreacted particles with the highest volume fraction of 29.7% can be found in the paste specimen at 20 °C, followed by a gradual

decline to 18.8% at up to 400 °C and a sudden drop by approximately 36.3% when reaching 600 °C. Due to the continuous high temperature exposure and sintering effect, the unreacted particles only takes up 4.01% of the total volume at 800 °C, as observed from the segmented image with almost negligible green regions [470-472].

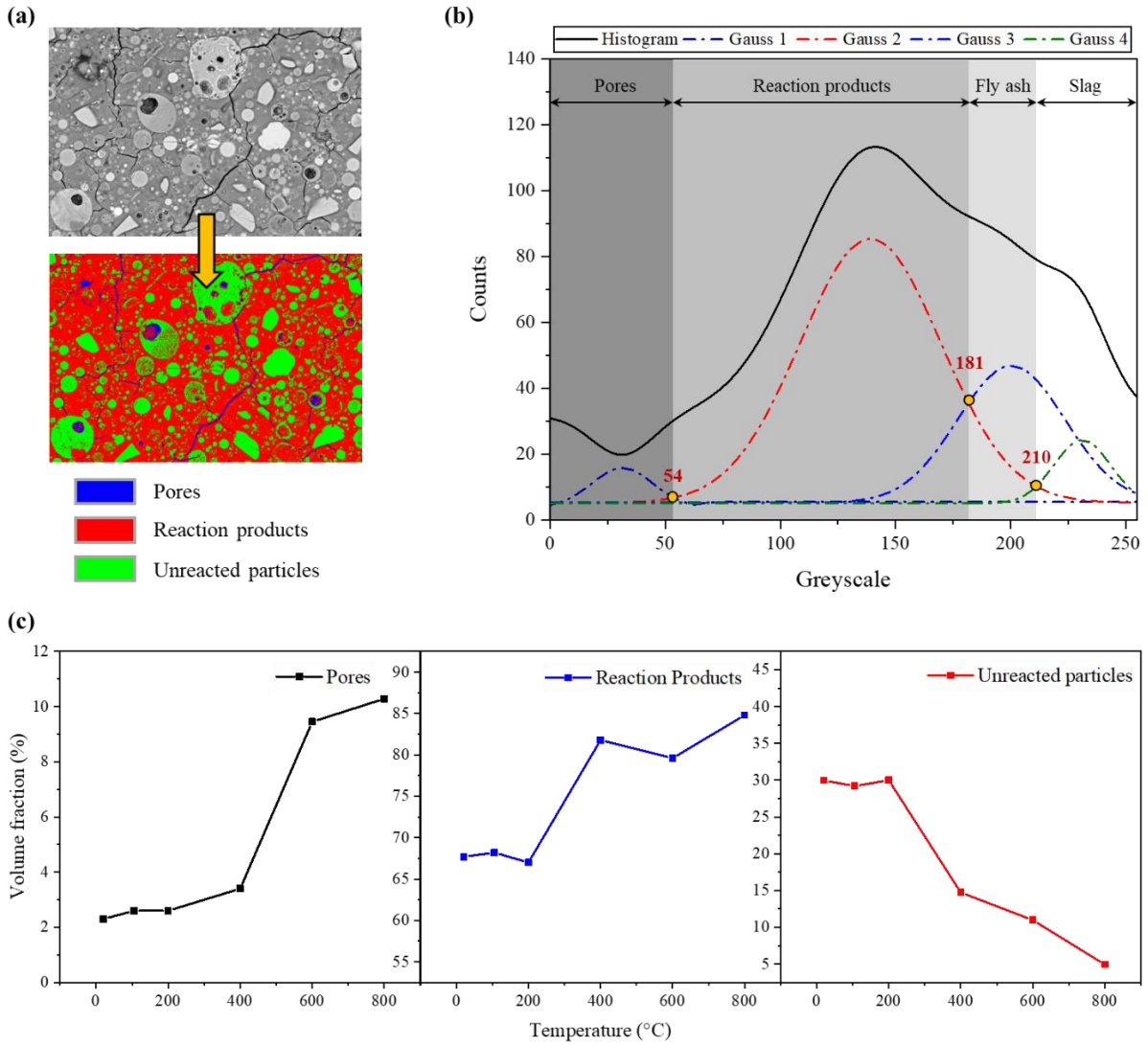

Figure 3.22. BSEM image processing: (a) segmentation of different phases, (b) greyscale histogram, and (c) quantification of volume fractions.

Regarding reaction products, a continuous increase from around 67.5% to 82.7% happens when the temperature rises from 20 to 400 °C, while there is a slight increase of the volume fraction from 82.7% to 85.1% after 800 °C is reached, as a result of the drastic phase transformation at this stage of heating [24, 25, 30, 33]. In terms of pores and cracks, the volume

fractions went up gradually with rising temperature from room temperature to up to 400 °C, with a sudden jump from approximately 3.4% to 9.5% after reaching 600 °C. Afterwards, there is a comparative increase from 9.5% to 10.3%, as the temperature reaches °C.

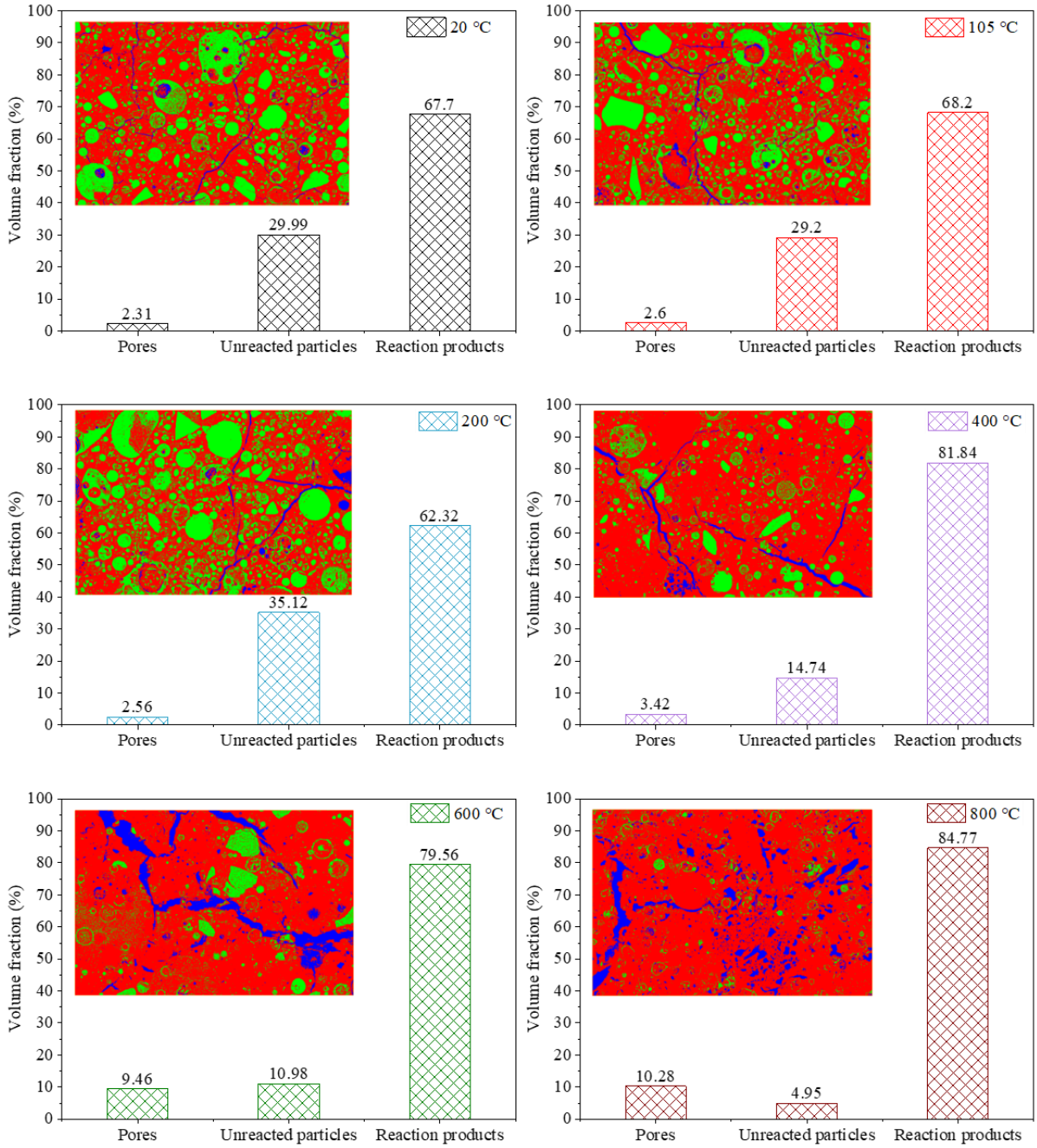

Figure 3.23. FTIR spectra of (a) precursors, and (b) AAFS paste at elevated temperatures.

After image processing, phase assemblage in AAFS paste at elevated temperatures can be summarised (Figure 3.23). At all temperature levels, reaction products were the dominant phase, while volume fractions of pores and cracks continued to go up until exceeding that of unreacted particles at 800 °C. The continuous consumption of unreacted particles can contribute to the strength development, while the initiation and propagation of cracks can lead to damage in AAFS paste [34]. To further investigate the gel compositions in reaction products of AAFS paste, the local element maps regarding Si, Al, Ca and Na in the specimen at elevated temperatures are displayed in Figure 3.24, indicating that part of Si and Ca concentrate at the region of unreacted fly ash and slag particles. Whereas, the rest of the mentioned elements are relatively evenly distributed in the reaction products, consisting of N-A-S-H gels (i.e. SiO_4 and AlO_4 tetrahedra in a highly cross-linked structure with shared O atoms [83]), C-A-S-H gels (i.e. silicate chains inter-linked by layers of CaO [107, 109, 110]), and N-C-A-S-H (i.e. modification of N-A-S-H gels by partially replacing Na^+ with free Ca^{2+} to form the hybrid structure [46, 84, 88]).

Figure 3.25 illustrates the compositional ternary diagram of CaO-SiO_2-Al_2O_3 in AAFS matrix at elevated temperatures from 20 to 800 °C based on the EDS point scanning results focusing on the reaction products. As per the existing studies on the compositional ranges of different types of reaction products [48, 84, 88, 170, 171], the majority of the points are within the region of C-A-S-H and high Ca C-(N)-A-S-H gels in reaction products from 20 to 200 °C. As the temperature rises to 400 and 600 °C, the spots tend to shift towards right and concentrate at the region with relatively less Ca involvement. After 800 °C exposure, more spots appear in the low-calcium region, which are categorised as N-A-S-H and N-C-A-S-H gels.

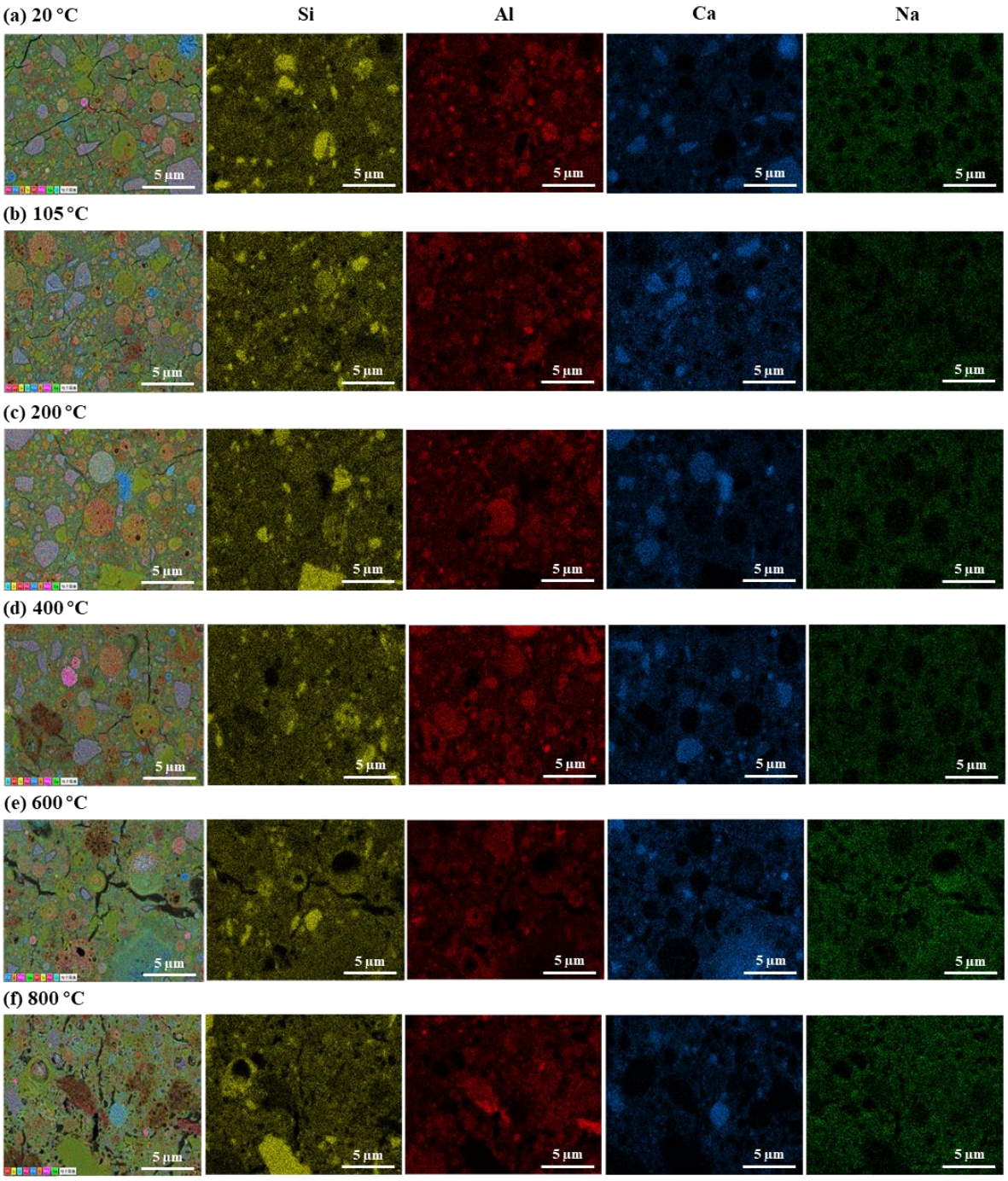

Figure 3.24. Element maps (Si, Al, Ca and Na) of AAFS paste at elevated temperatures.

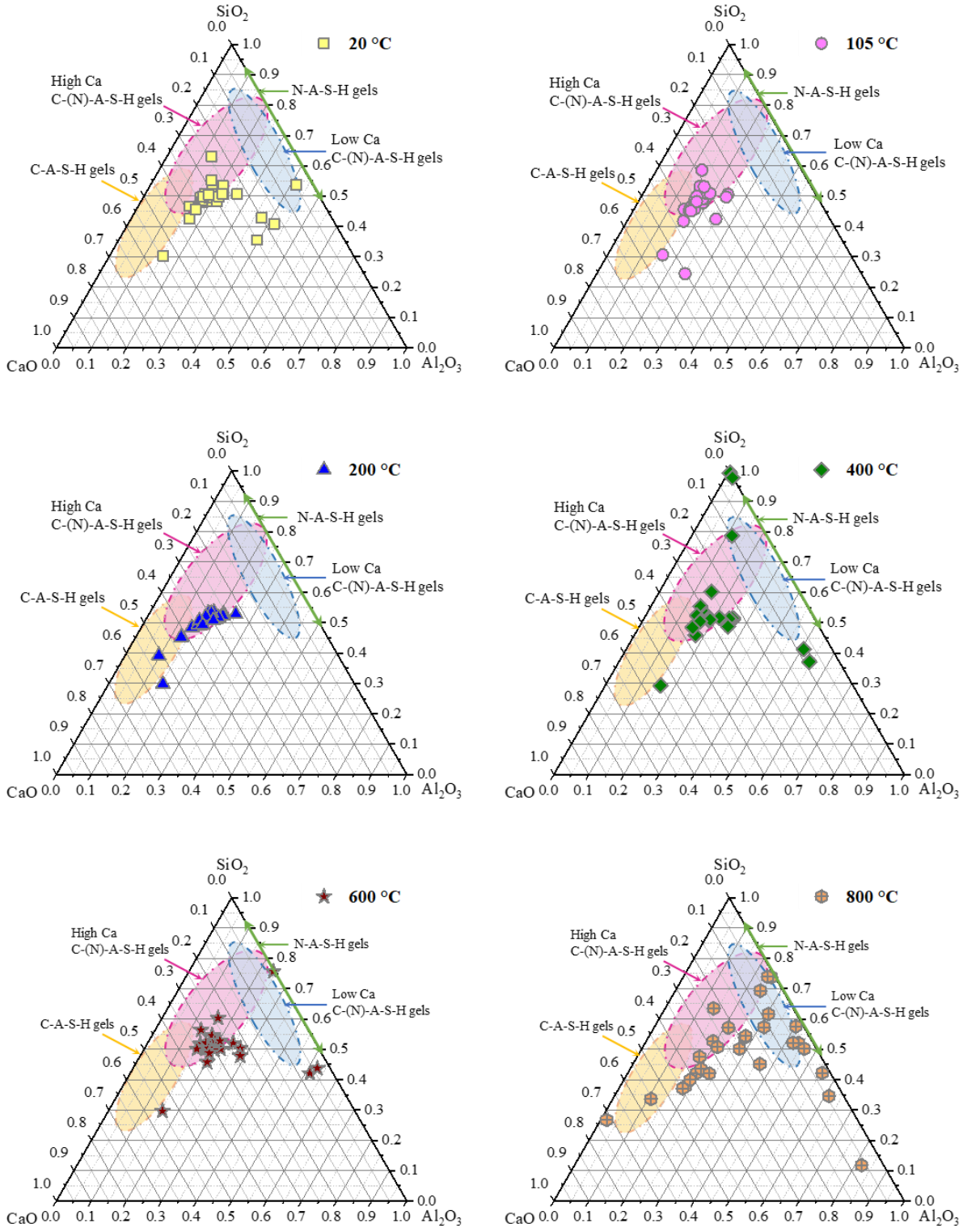

Figure 3.25. Compositional ternary diagram of CaO-SiO_2-Al_2O_3 in AAFS at elevated temperatures (Note: compositional ranges of binder gels adapted from [48, 84, 88, 170, 171]).

To quantitatively analyse the gel compositions, the statistical distribution of Al/Si and Ca/Si ratios in AAFS at elevated temperatures is demonstrated in Figure 3.26. As seen in Figure 3.26(a), the average Al/Si ratio stays around 0.36-0.46 in the paste after heating at up to 400 °C, which can be recognised as Si-rich N-A-S-H gels (i.e. the Al/Si ratio of Si-rich N-A-S-H gels is around 0.5 [167]). From 400 to 800 °C, there is a noticeable increase of the Al/Si ratio from approximately 0.40 to 0.79, implying an increase of Al-rich N-A-S-H gels in the reaction products of AAFS paste after 400 °C exposure. This is consistent with the nuclear magnetic resonance (NMR) results from the previous research that the silicon tetrahedra with a $Q^4(3Al)$ structure referring to highly cross-linked Al-rich N-A-S-H gels exhibits a significant increase of volume fraction from 21.6% to 41.3% at 400-800 °C [141].

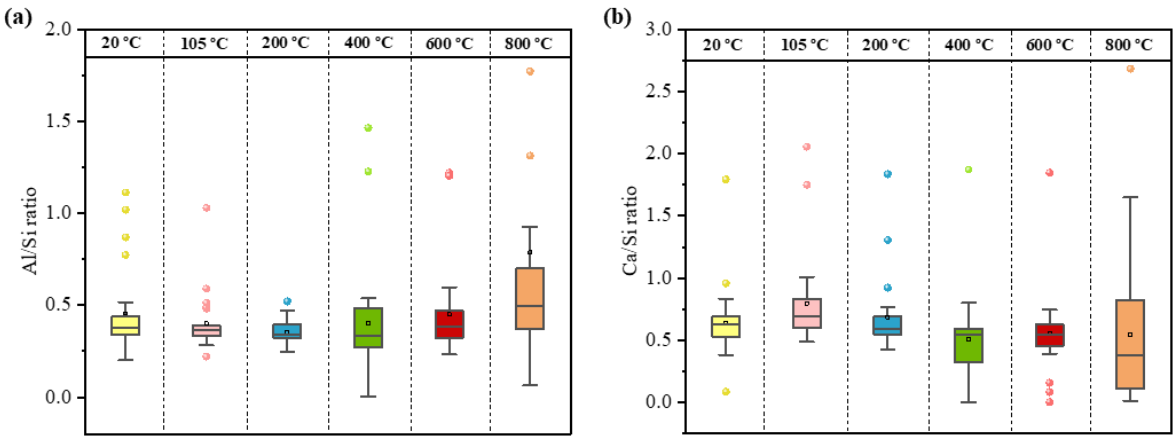

Figure 3.26. Statistical distribution of (a) Al/Si and (b) Ca/Si ratios in AAFS at elevated temperatures based on the EDS analysis.

In terms of Ca/Si ratio in the paste, a rise in the average ratio from around 0.64 to 0.81 at 20-105 °C occurs, attributing to the continuous dissolution of slag and further geopolymerisation triggered by temperature curing. As the temperature goes up from 200 to 800 °C, there is an overall trend of decline in Ca/Si ratio of the specimen from 0.68 to 0.55 with a slight fluctuation at 400-600 °C (see Figure 3.26(b)). This can be ascribed to the release of free Ca^{2+}, decomposition of C-A-S-H gels and potential phase transformation from C-A-S-H (Ca/Si ratio of around 0.67-3) to N-(C)-A-S-H (Ca/Si ratio of around 0.14-0.33) and C-(N)-A-S-H (Ca/Si ratio of around 0.45-10) gels at up to 800 °C [46, 88, 124, 167-169].

3.7.5 Pore structure analysis

Pore size distribution by MIP

Apart from solid phases, a combination of pores, inherent voids and cracks that formed the whole pore structure of AAFS paste was also a crucial phase at the paste level. The evolution of pore structure characteristics of AAFS paste at elevated temperatures obtained from MIP test is presented in Figure 3.27, where the pore size is defined and categorised into three distinct size ranges for better description: small pores (2-50 nm), medium pores (50-7500 nm) and large pores (> 7500 nm) [22, 473].

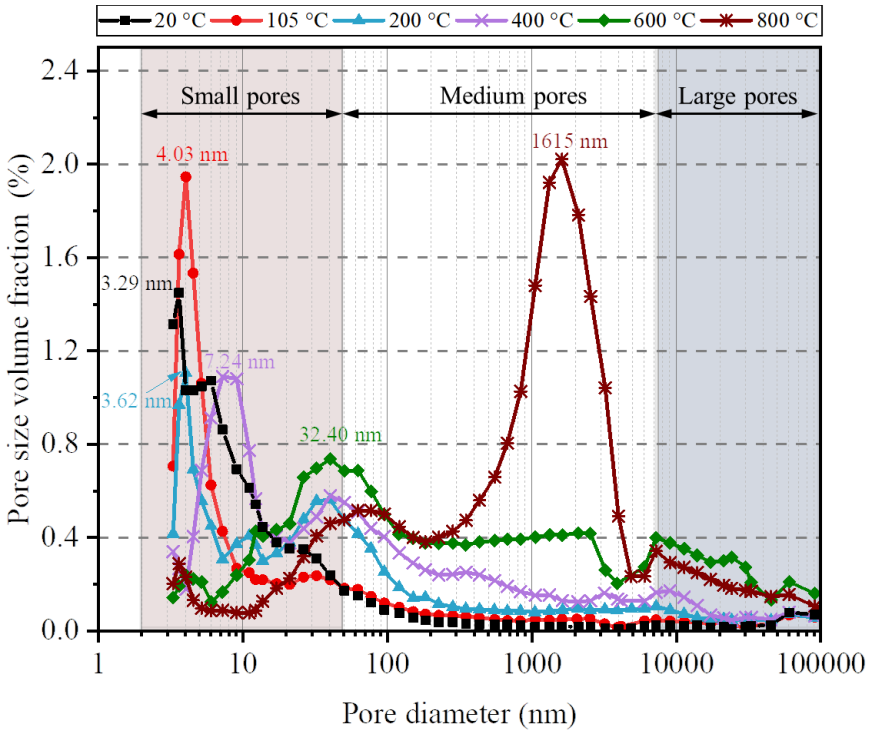

Figure 3.27. Pore size distribution of AAFS paste at elevated temperatures.

At ambient temperature, the highest peak appeared with the pore size of 3.29 nm, indicating that originally the majority of the pores formed were gel pores (i.e. ≤ 10 nm). Similarly, the pore sizes corresponding to the highest volume fractions for AAFS exposed to 105 °C and 200 °C were 4.03 nm and 3.62 nm, respectively. After 400 °C, pores with diameter of 7.24 nm dominated the matrix structure. The pore size continued to shift to a larger size of 32.4 nm when subjected to 600 °C, belonging to capillary pores (i.e. 10-50 nm). At this stage, the majority of

the pores were distributed between small and medium sizes. When the temperature reaches 800 °C, a broad peak at 1615 nm was detected, implying a sharp and drastic change of pore size distribution from small to medium pores. Figure 3.28 demonstrates the cumulative pore volume of AAFS at elevated temperatures. In general, the total pore volume fraction (also known as porosity) roughly remained at the original level until 400 °C, followed by a significant increase by more than 10% after 800 °C exposure.

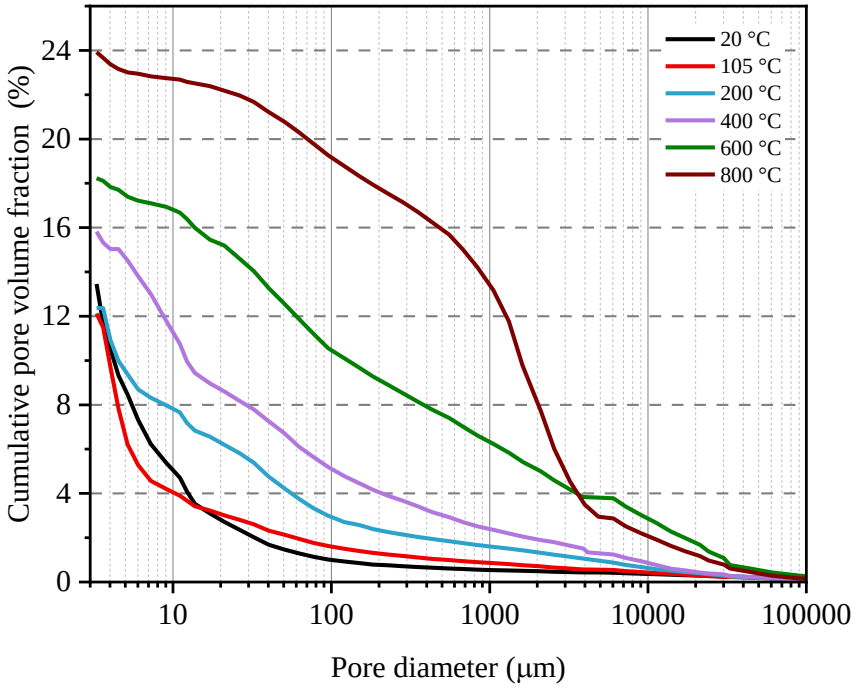

Figure 3.28. Cumulative pore volume of AAFS paste at elevated temperatures.

To further estimate the development of pores within different size ranges, Figure 3.29 provides the compositions of different pores that contribute to the total porosity in AAFS paste at ambient and high temperatures. There was a slight reduction of overall porosity from 13.45% to 12.37 % when the temperature rose from 20 to 200 °C, due to a combined effect of water evaporation and further geopolymerisation that promoted the development of binder gels with a higher cross-linking level and thus resulted in continuous refinement of pores [34, 55]. A relatively significant drop of 16.59% can be observed in the volume fraction of small pores from 105 to 200 °C, implying that the reaction process might be slowed down at this stage as the degree of reactivity was positively proportional to the volume fraction of gel pores [22]. Meanwhile, there was a rise of the proportions of medium and large pores by 20.65% and 2.7%, respectively. This can be attributed to the transport of moisture from heated surface to inner

area, allowing the pore pressure build-up that led to the initiation and propagation of microcracks and the development of an inter-connected network in AAFS paste.

From 200 to 600 °C, a great number of medium pores were generated, while a further mitigation of small pores by 38.51% can be found. As seen in the BSEM images, AAFS matrix experienced lengthening and widening of cracks as the exposure temperature went up, confirming the growth of medium and large pores. Simultaneously, the remarkable mitigation of small pores at 600 °C implied that the sintering effect might take place since gel pores could collapse to form larger pores and also, they could be filled by melting and densification [2]. Figure 3.30 illustrates the detailed proportion of gel and capillary pores within the group of small pores, which confirms a rapid decrease of gel porosity with rising temperature from 400 to 600 °C. Furthermore, it is noteworthy that the volume of gel pores increased at up to 105 °C, confirming the further reaction process and formation of new binder gels. At 800 °C, the volume fractions of both gel and capillary pores dropped to less than 10%, whereas medium pores became the dominant group with a proportion of 77.72%.

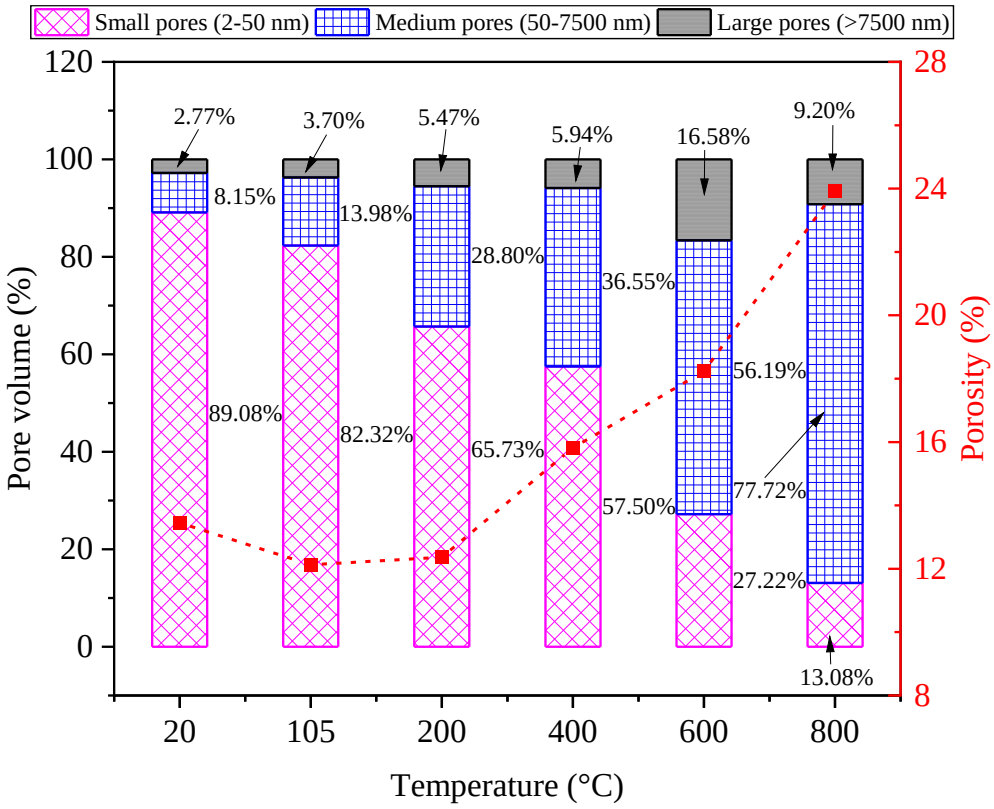

Figure 3.29. Pore volume fractions of AAFS paste at elevated temperatures.

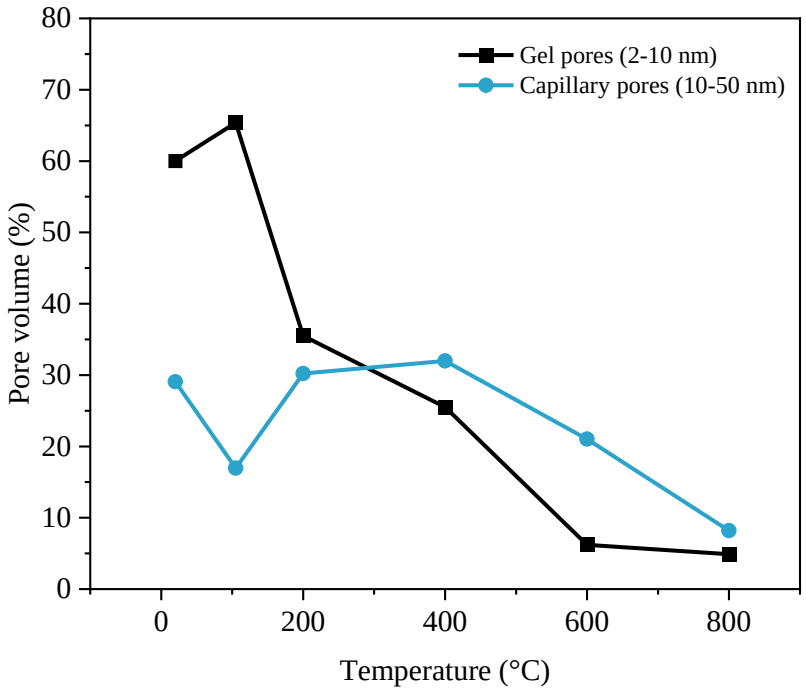

Figure 3.30. Detailed pore volume distribution within 2-50 nm.

Pore structure characteristics by XCT images

MIP can provide the information on internal pore structure and the formation of cracks by measuring pore throat size, whereas the relatively larger pores with small pore throat size might not be accurately characterised [22, 474-476]. The spatial distribution of pores and cracks was analysed based on the obtained XCT images to investigate the microstructural evolution in AAFS paste before and after high temperature exposure. By analysing XCT images, the evolution of larger pores and cracks in AAFS paste could be captured. According to the voxel size of 13.9 µm, the smallest pore that can be detected had an average diameter of 27.8 µm (i.e. a cube is formed by the arrangement of 8 voxels) [477, 478]. After denoising, segmentation, labelling and sieving on the XCT images, the pore structure evolution of AAFS paste at elevated temperatures was obtained and demonstrated in Figure 3.31. Due to the difficulty of singling out the cracks from the pores since they shared the similar grey value, the label and sieve analysis was performed based on the inter-connected pore volume including both pores and cracks [477].

The surfaces of paste specimens were excluded to minimise discrepancy in the visualisation and calculation based on the colour map due to art effect (i.e. accidental combination of colours

at the edges of testing samples, which tends to be brighter and whiter than the original colour). At ambient temperature, the spatial heterogeneity of pores can be observed. With the rising temperature to up to 600 °C, the development of micro-cracks can be detected, which triggered the formation of macro-cracks and cavities when the temperature continued to rise until 800 °C was reached. At 800 °C, there existed some quasi-diagonal damage planes in AAFS paste, which can be attributed to the micro-crack coalescence [477-480].

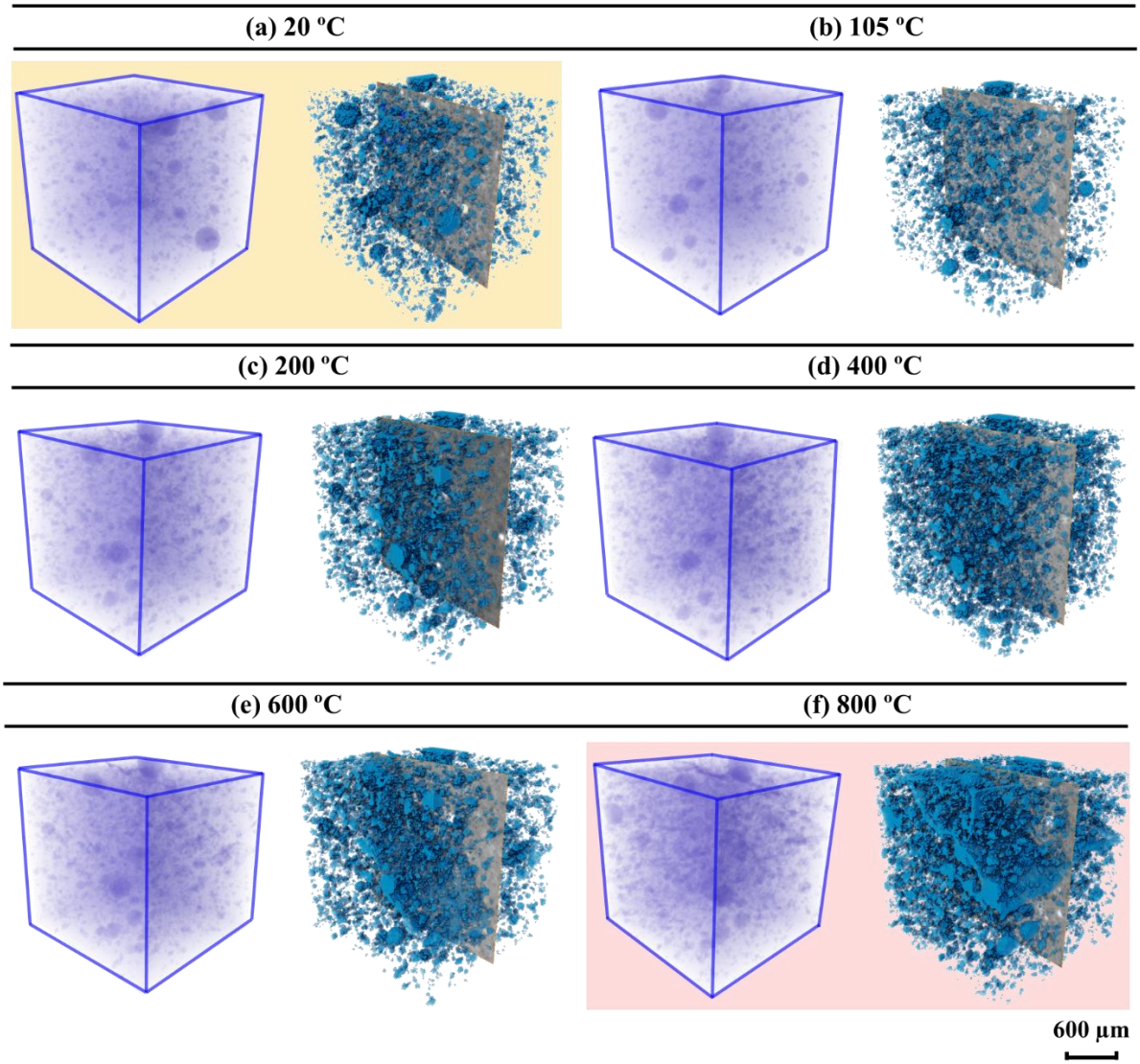

Figure 3.31. 3D pore structure evolution of AAFS paste at elevated temperatures.

Afterwards, the inter-connected pore structure was visualised in Figure 3.32. The pore volume was categorised into three ranges: 0-0.02 mm^3, 0.02-0.04 mm^3 and 0.04-0.06 mm^3 based on the quantification of pore size distribution, which varied from 0 to 0.06 mm^3 in the

shown representative volume element. Figure 3.33 illustrates the size distribution of pores with respect to mean diameter. At up to 105 °C, there were few visible pores with a volume larger than 0.02 mm^3. As the temperature increased to up to 600 °C, the gradual development of inter-connected pore network could be observed. After 800 °C exposure, the number of pores corresponding to 0.02-0.04 mm^3 rose dramatically, while several major cracks and voids could be found, which indicated the drastic deterioration of inner structure in AAFS paste and the increase of internal pore connectivity at 800 °C. The number of pores with diameter of less than 0.1 mm dropped comparatively when the temperature went up from 20 to 800 °C, while the number of pores with diameter of 0.2 mm increased by approximately 300%. Moreover, pores larger than 0.45 mm only existed after 400 °C exposure, which can be associated with the completed water evaporation process and thermal stress induced by temperature gradient.

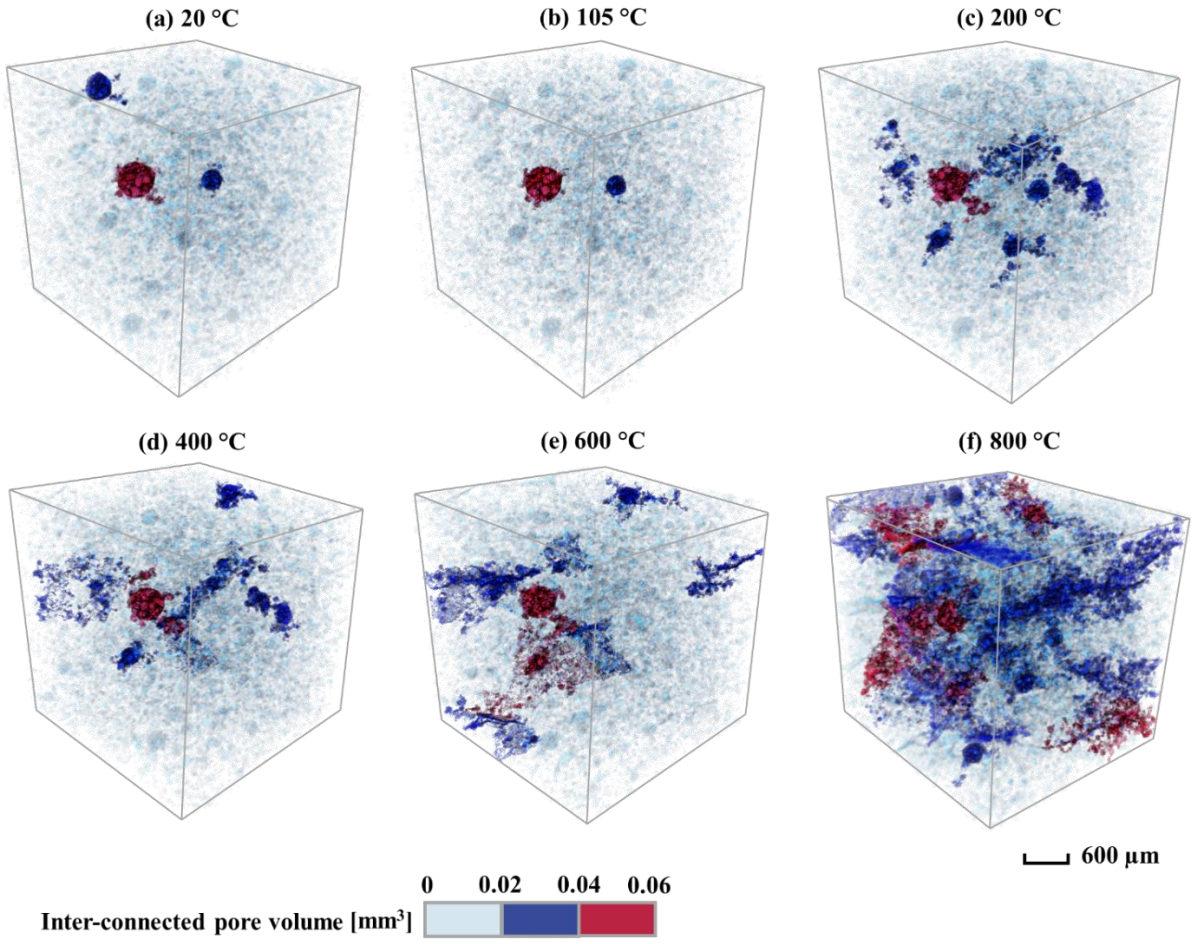

Figure 3.32. Evolution of inter-connected pores and cracks in AAFS paste at elevated temperatures obtained from XCT imaging.

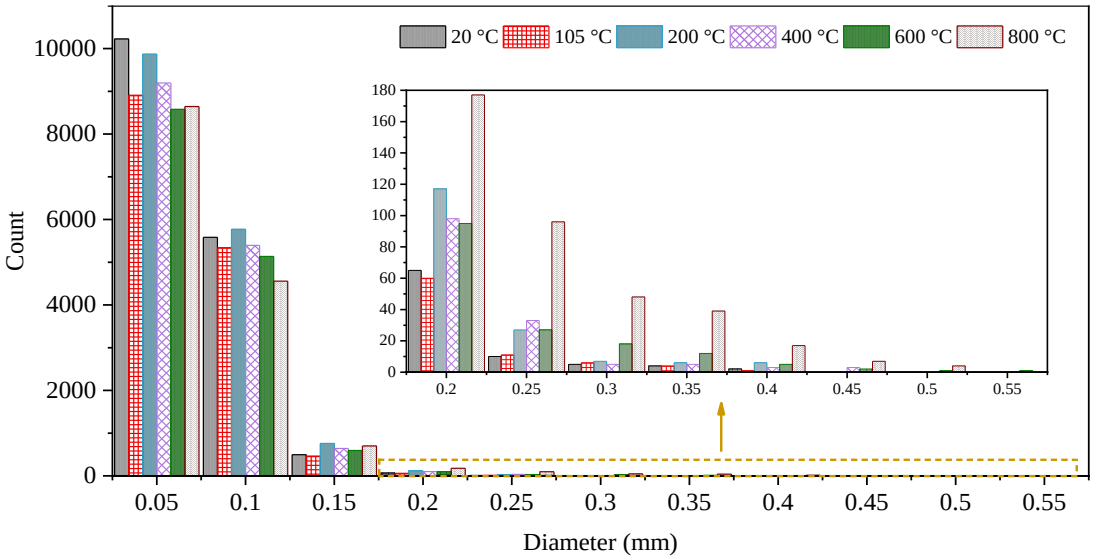

Figure 3.33. Pore size distribution of AAFS paste at elevated temperatures obtained from XCT imaging.

For quantitative analysis of porosity from XCT results, the single and inter-connected pores together with cracks were considered for the calculation of porosity in the tested AAFS specimen, which is shown in Figure 3.34. The porosity increased from 4.97% to 6.37% after 200 °C exposure, followed by an almost plateau until 600 °C. A significant jump from 6.88% to 11.47% appeared after 800 °C, indicating a critical microstructural change within AAFS paste, as displayed in the 3D visualisation in Figure 3.32(f).

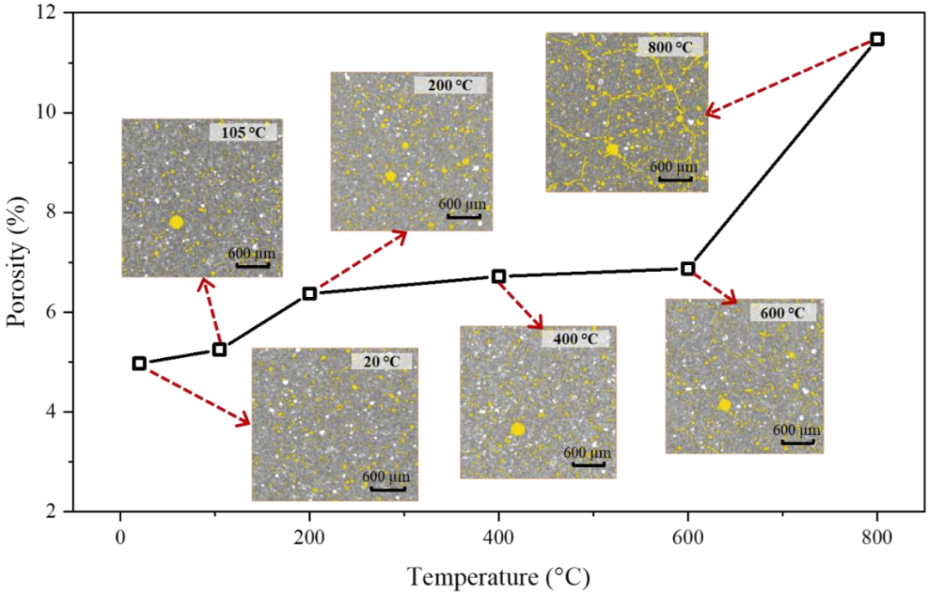

Figure 3.34. Porosity of AAFS paste at elevated temperatures obtained from XCT imaging.

3.8 Concluding remarks

In this chapter, the microstructural evolution in AAFS paste exposed to various temperatures (i.e. 20, 105, 200, 400, 600, and 800 °C) at multiple length scales covering solid gel particles, gel matrix and paste was systematically investigated using a series of advanced characterisation techniques including ^{29}Si NMR, XRD, FTIR, BSEM and MIP. Based on the obtained experimental results, the main conclusions can be drawn as follows:

- The nanostructure of solid gel particles in AAFS was highly sensitive to exposure temperature. At 20-200 °C, the bonding between Si and Al tetrahedra was promoted to form Q^2(1Al) with an over 10% rise in volume fraction. After 600 °C exposure, the proportion of Q^2(1Al) dropped rapidly, along with a jump from around 20% to 34% for Q^4(3Al), indicating the decomposition of C-A-S-H gel to form more cross-linked N-A-S-H gel. At 800 °C, N-A-S-H gel (≥ 40% in volume) dominated the nanostructure of AAFS, while the volume fractions of C-A-S-H and N-C-A-S-H gels reduced considerably to approximately 10% and 12%, respectively.
- The gel matrix in AAFS was composed of hybrid gels and gel pores (2-10 nm), which experienced refinement with a volume mitigation from about 60% to 35% after exposure to 200 °C. With the rise of exposure temperature from 200 to 600 °C, a continuous drop in gel porosity to around 5% took place, which can be attributed to the further reaction that could potentially fill the gel pores. After exposure to 800 °C, new crystalline phases including nepheline and gehlenite can be observed, which took up around 26.3% and 21.5% of the crystalline phases by volume, while the volume fraction of amorphous phase dropped by more than 46.1%, compared to that at ambient temperature.
- At the paste level, the crack development along with the formation of capillary (10-50 nm), medium (50-7500 nm) and large pores (> 7500 nm) occurred due to water evaporation and pore pressure accumulation in AAFS with the rising exposure temperature from 20 to 200 °C. At 600 °C, the pore pressure build-up and thermal stress led to further crack growth and medium pores dominated the pore structure. After exposure to 800 °C, viscous sintering took place, resulting in a more compact gel matrix with gel porosity of less than 5%, along with the decomposition of hybrid gels, while micro-cracks disappeared, attributing to the melting and potential self-healing effect of AAFS at 800 °C.

Chapter 4 Physical, Thermal and Mechanical Properties of AAFS Paste at Elevated Temperatures

4.1 Introduction

Based on Chapter 3, the multiscale microstructural characteristics of AAFS paste at elevated temperatures are comprehensively investigated. This chapter focuses on the understanding of the behaviour of AAFS paste at elevated temperatures ranging from 20 °C to up to 800 °C in terms of physical, thermal, micromechanical and mechanical properties as seen in Figure 4.1. The micromechanical properties with respect to local elastic modulus and hardness of AAFS paste are studied using atomic force microscopy (AFM) and nanoindentation. Thermogravimetric analysis (TGA) and dilatometry tests as well as compression and three-point bending tests are conducted to investigate the thermal and mechanical properties of AAFS paste. Moreover, the relationship between the macroscopic behaviour and microscopic characteristics is analysed in depth. Followed by Chapter 3, this chapter goes one step further and explored the link among microstructural features, micromechanical and mechanical properties in AAFS paste for the first time to gain insights into the underlying damage mechanisms of AAFS at elevated temperatures. Part of this chapter has been presented in the following manuscripts:

W. Tu, G. Fang, B. Dong, Y. Hu, M. Zhang, Behaviour of alkali-activated fly ash-slag paste at elevated temperatures: An experimental study, *Cement and Concrete Composites*, 147 (2024) 105438.

W. Tu, G. Fang, B. Dong, M. Zhang, Micromechanical analysis of alkali-activated fly ash-slag paste at elevated temperatures. *Cement and Concrete Research*, 153 (2024) 105735.

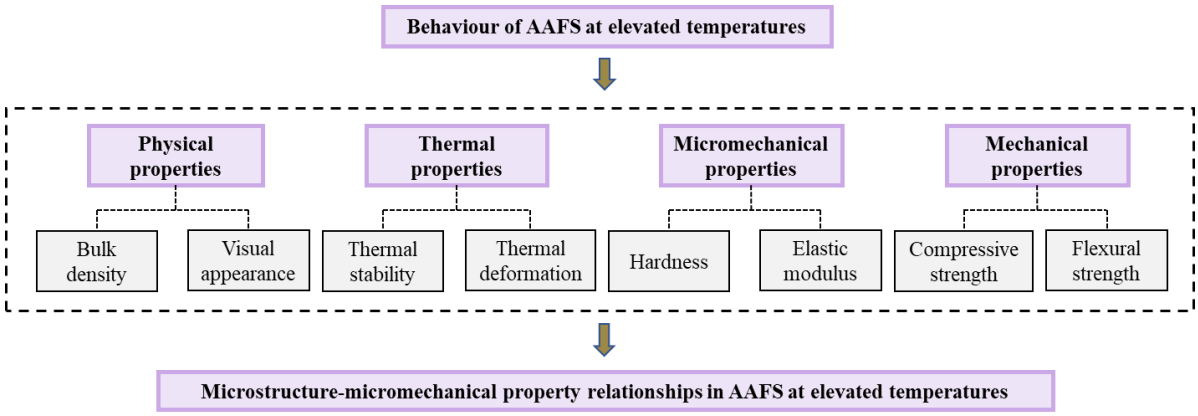

Figure 4.1. Outline of this chapter.

4.2 Test methods

4.2.1 Atomic force microscopy

The atomic force microscopy (AFM) test was conducted to measure the surface topography of the polished AAFS specimens via the AFM instrument (Bruker, Dimension ICON, USA) shown in Figure 4.2. The test was conducted with a peak force amplitude of 300 mV, scan rate of 1.0 Hz, engage setpoint of 0.85 V, and scanning size of 50 × 50 μm. This experimental work was conducted at the Institute for Advanced Study, Shenzhen University, China.

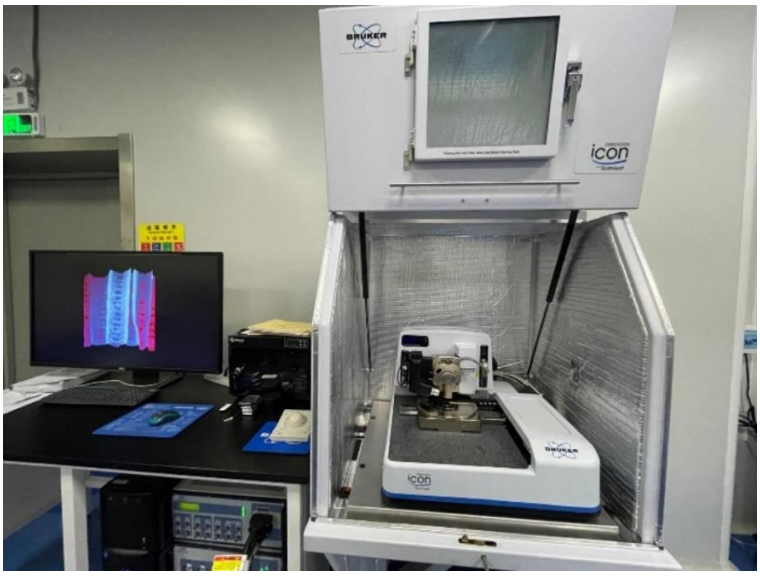

Figure 4.2. Instrument of AFM.

4.2.2 Thermogravimetric analysis

TGA (NETZSCH STA 490PC) was performed to understand the thermal behaviour of AAFS paste as seen in Figure 4.3. The powder samples (<0.074 mm) were taken from the crushed specimens (at room temperature) after compressive strength test. A constant heating rate of 10 °C/min from room temperature to 800 °C was employed for TGA. TGA results denote the weight loss of specimens as a function of temperature. The derivative thermogravimetry (DTG) curve can be determined from the first derivative of the TGA curve.

Figure 4.3. Instrument of thermogravimetry.

4.2.3 Dilatometry

The dilatometry test was conducted to monitor the thermal deformation of samples using the dilatometer NETZSCH DIL402C. A cylindrical sample with a diameter of 5 mm and length of 12 mm was tested under a constant heating rate of 10 °C/min from 20 to 800 °C.

4.2.4 Nanoindentation

The nanoindentation test was conducted to investigate the micromechanical properties of AAFS paste in terms of local elastic modulus and hardness [39]. Herein, the nanoindentation instrument with a Berkovich indenter tip (BRUKER, Hysitron TI 950, Germany) was used (see Figure 4.4), which had the load and displacement resolution of 1 nN and 0.04 nm, respectively. The loading curve of nanoindentation test includes three segments: 1) constant loading rate of

400 μN/s until the maximum load of 2 mN was achieved, 2) holding time of 2 s at the maximum load, and 3) unloading rate of 400 μN/s. The classical nanoindentation modes were applied in this study. 20 indentation tests were performed at different locations (i.e. unreacted particles and reaction products) of AAFS specimens in the classical mode. Figure 4.5 shows the examples of indentation locations in the paste at 20, 400 and 800 °C.

The elastic modulus is determined based on the initial slope of the elastic unloading curve. Firstly, the indentation modulus (M) and hardness (H) are obtained as follows:

$$M = \frac{1}{2}\left(\frac{dp}{dh}\sqrt{\frac{\pi}{A}}\right)|h = h_{max} \quad (4-1)$$

$$H = \frac{P_{max}}{A} \quad (4-2)$$

where p and p_{max} are the indentation load and the maximum indentation load, respectively. h is the indentation depth, h_{max} is the maximum indentation depth, and A is the projected area of the elastic contact [44].

The elastic modulus (E) is then calculated as follows:

$$E = (1-v^2) \times \left[\frac{1}{M} - \frac{\left(1-v_{tip}^2\right)}{E_{tip}}\right]^{-1} \quad (4-3)$$

where v is the Poisson's ratio of the sample. E_{tip} is the indenter tip and v_{tip} is the Poisson's ratio of the indenter tip, which are 1140 GPa and 0.07, respectively [44].

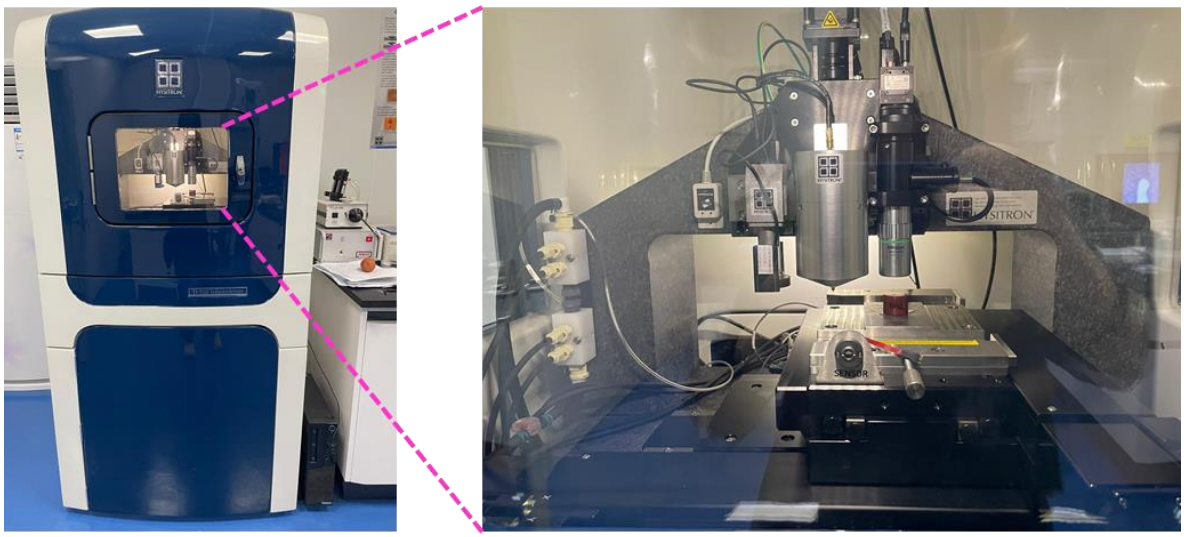

Figure 4.4. Instrument of nanoindentation.

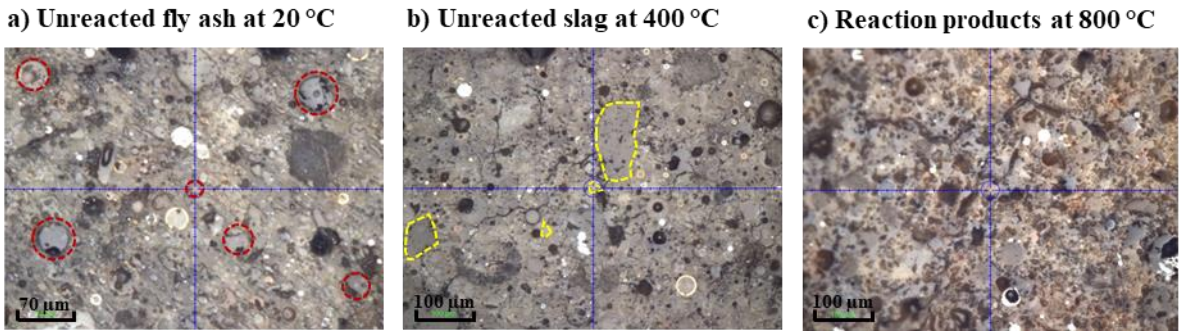

Figure 4.5. Examples of indentation locations in AAFS paste at different exposure temperatures.

4.2.5 Compressive strength test

The 40 mm cube specimens were prepared for the compressive strength test. The 28-d compressive strength of AAFS paste at various temperatures was tested using a universal testing machine with a constant loading rate of 0.3 kN/s in accordance to GB/T50081-2002 [481].

4.2.6 Three-point bending test

The three-point bending test was conducted to evaluate the flexural strength of AAFS paste as per the RILEM standard. The cuboid AAFS sample with 150 × 50 × 50 mm was prepared for this test. The loading rate was set as 0.01 mm/s. Figure 4.6 shows an example of the failure pattern of AAFS paste after three-point bending tests.

Figure 4.6. Failure pattern of AAFS paste after three point-bending tests.

4.3 Results and discussion

4.3.1 Bulk density

Figure 4.7 shows the bulk density of AAFS paste at elevated temperatures. In general, the bulk density of AAFS paste reduced with the rise of temperature up to 800 °C. From 20 to 200 °C, the bulk density declined dramatically from around 1.95 g/cm^3 to 1.62 g/cm^3, which can be attributed to the significant loss of moisture with looser matrix, as illustrated in the TGA results. After 200 °C, the gradient of bulk density reduction steadily slowed down, which can be ascribed to the combined effect of the formation of additional gel by further geopolymerisation and decomposition of remained binder gel [22]. At up to 800 °C, the bulk density stabilised at around 1.58 g/cm^3, owing to a balance between the sintering reaction that densified AAFS matrix and the recrystallisation of porous phases such as nepheline that resulted in a looser structure [56]. It was also confirmed that the consumption of unreacted fly ash particles due to sintering reaction could lead to the increase of bulk density in both AAF and AAFS paste with rich N-A-S-H gels [22]. Considering the mass changes shown in Figure 4.7, the mass loss increased from 0 to approximately 18% at 20-800 °C with a reversed tendency compared to that of bulk density.

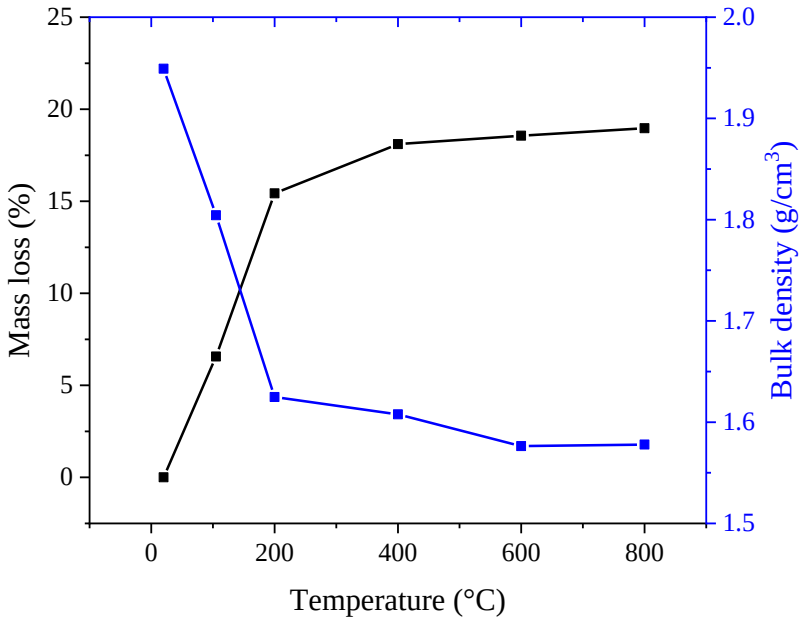

Figure 4.7. Mass loss and bulk density of AAFS paste at elevated temperatures.

4.3.2 Visual appearance

Surface roughness

To examine the micromechanical properties, the surface roughness was measured using AFM to investigate the surface conditions of specimens. Figure 4.8 displays the variations in surface topography of AAFS paste at elevated temperatures in both 2D and 3D AFM images. A relatively smooth texture is shown in the specimens after exposure to 20 to 600 °C, whereas an irregular porous surface can be observed in the specimen at 800 °C. This is consistent with the rough surface found in the BSEM image of AAFS paste after 800 °C exposure, which contains cavities and flaws in a porous structure. To characterise the surface roughness, two different amplitude parameters are used to quantify the topography of samples, including the average roughness R_a and root mean square R_q [482]. Table 4.1 summarises the roughness numbers of the specimens obtained from the AFM results. It is shown that R_a ranges from 13.0 to 102 nm with a mean value of 44.3 nm, while R_q ranges from 18.5 to 132 nm with a mean value of 59.3 nm.

These roughness values indicate the quality of the sample's surface preparation, which is crucial for accurate nanoindentation analysis, as indentations must occur on a flat surface [44]. Based on the surface roughness criteria concluded in the previous studies, the Rq values should be 3-5 times less than the indentation depth [44]. Given that the average indentation depth is approximately 180 nm, the maximum permissible Rq value is around 900 nm. The obtained Rq values are well below this threshold, which suggests the sample surfaces have been ground and polished effectively, thereby minimising the influence of surface roughness on the indentation results.

Table 4.1. Summary of surface roughness number in AAFS paste at elevated temperatures.

Temperature	20 °C		105 °C		200 °C		400 °C		600 °C		800 °C	
Roughness	R_a	R_q	R_a	R_q	R_a	R_q	R_a	R_q	R_a	R_q	R_a	R_q
Capture1	43	55.2	101	132	17.5	22.6	13.0	23.1	32.7	42.6	21.1	29.2
Capture2	62	84.4	91.1	116	55.4	67.8	13.8	18.5	36.7	46.6	23.4	33.1
Capture3	61.6	94.9	102	130	52.9	75.7	23.4	32.6	23.4	29.3	22.9	34.5

Roughness number (nm)

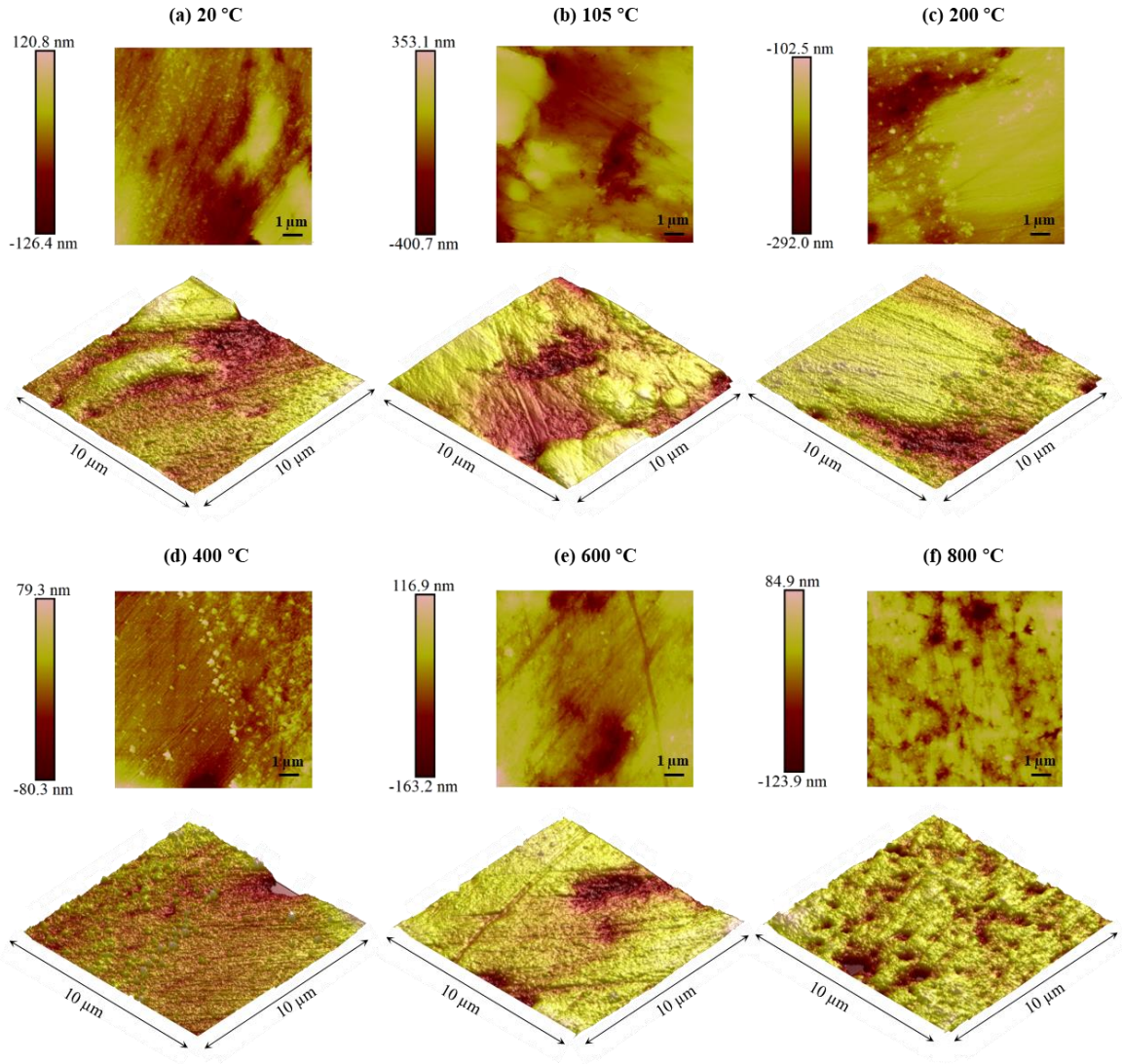

Figure 4.8. Surface topography of polished AAFS samples before and after high temperature exposure.

Surface appearance

Figure 4.9 displays the visual appearance of AAFS paste after exposure to different temperatures. Explosive spalling was not observed during heating process in all AAFS specimens. The unexposed specimen had no visible cracks. From 20 to 800 °C, the colour of specimen surface changed from dark brown to reddish brown, which can be ascribed to the oxidation of inherent iron compounds (Fe_2O_3) existing in fly ash-based alkali-activated system [22, 55, 346]. With the increase of temperature to up to 600 °C, AAFS matrix exhibited a smooth texture on surface without any visible cracks, whilst severe cracking can be observed

when the temperature reached 800 °C. This can be attributed to the rapid rise of thermal stress and drastic phase transformation at this stage, leading to the increase of sample dimensions with volumetric expansion as reported in the thermal deformation results [331, 483].

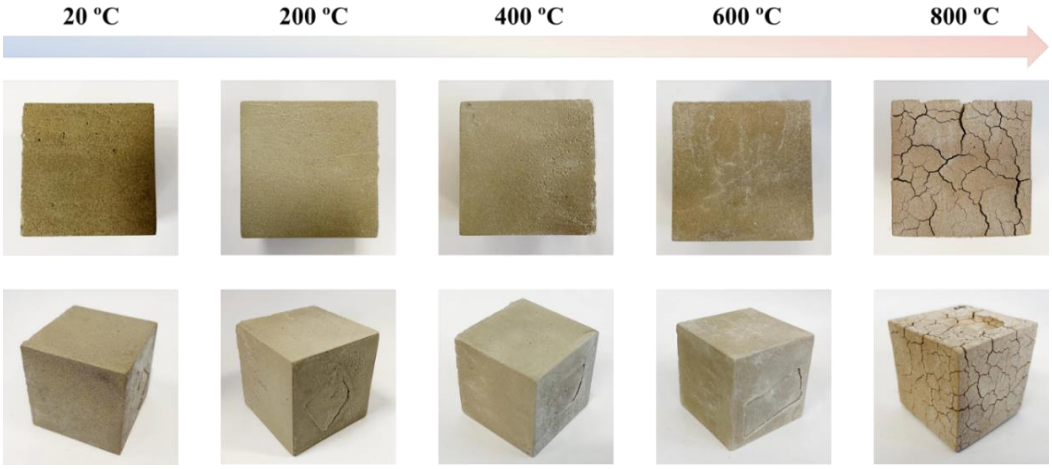

Figure 4.9. Surface topography of polished AAFS samples before and after high temperature exposure.

4.3.3 Thermal stability

TGA was performed to investigate the thermal stability of AAFS paste at elevated temperatures. Figure 4.10 presents the retained weight of AAFS paste before and after high temperature exposure, indicating that the higher exposure temperature can lead to less mass loss. Compared with ambient temperature, the retained weight went up by 3.26%, 3.79%, 7.53%, 10.6% and 10.5% when the temperature reached 105, 200, 400, 600 and 800 °C, respectively.

According to the derived results shown in Figure 4.11, the majority of the mass loss took place from 20 to around 250 °C with endothermic peaks, indicating the water evaporation process at early stage of heating. It was reported in the previous studies that the considerable mass loss up to 300 °C happened due to the loss of physically bound water and combined water in hybrid gels (i.e. N-A-S-H, C-A-S-H and N-(C)-A-S-H gels) and alkali-activated binders [335, 484, 485]. The fluctuation depicted between 300 and 400 °C can be ascribed to the further release of water. After 400 °C, the gradient of weight loss became relatively steady, implying that all moisture had evaporated from the matrix and pore pressure might not be the dominant reason to induce damage at higher temperatures (> 400 °C). It was also reported that within

500-700 °C, the rising exposure temperature had almost negligible effect on the final loss of AAFS paste [32, 36, 447].

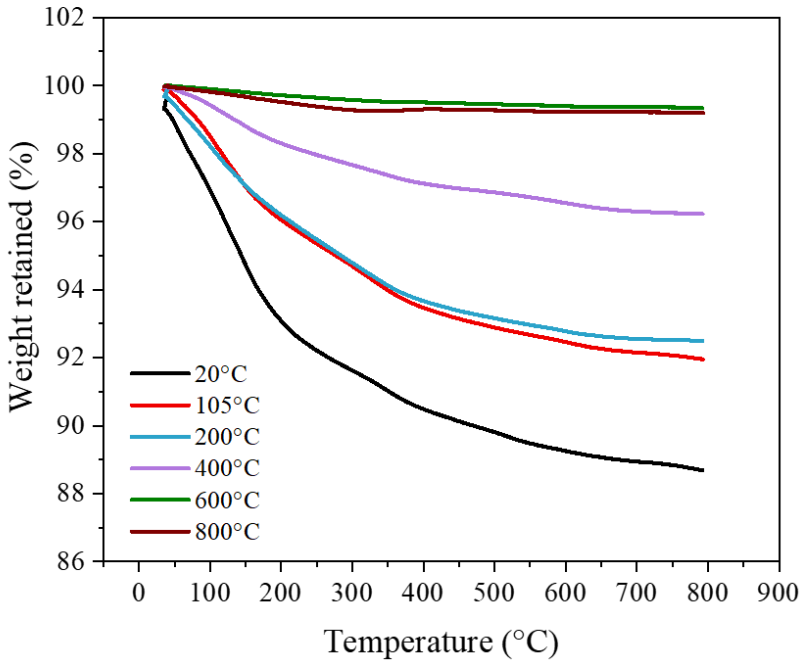

Figure 4.10. TGA results of AAFS paste at elevated temperatures.

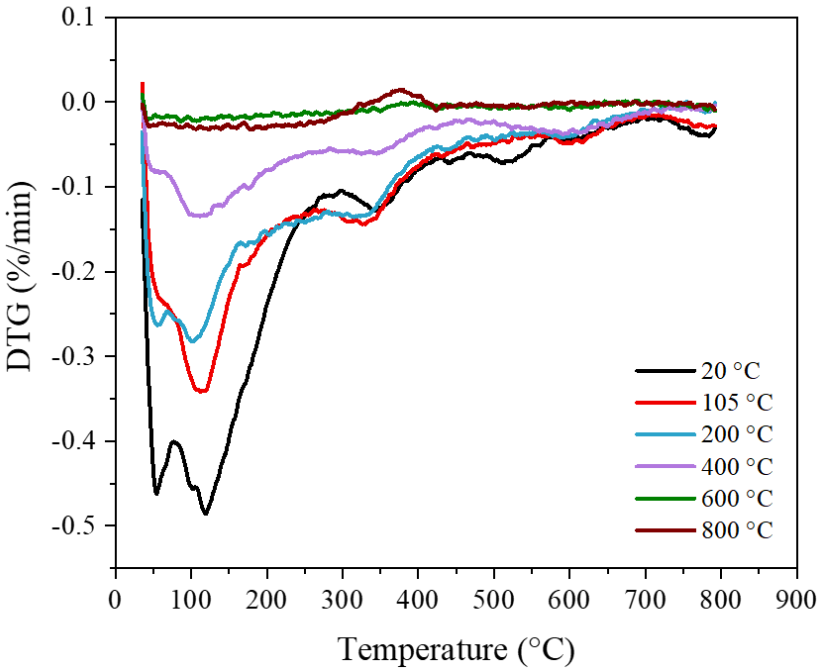

Figure 4.11. DTG results of AAFS paste at elevated temperatures.

4.3.4 Thermal deformation

The dilatometry test was conducted to monitor the thermal expansion or shrinkage of AAFS paste at elevated temperatures from 20 to 800 °C. The cylindrical AAFS sample was placed in the dilatometer, in which the changes of temperature and length were measured. The longitudinal strain was then determined based on the original length. Figure 4.12 presents the thermal deformation of AAFS paste at elevated temperatures. There was a little change of strain when the temperature increased from 20 to around 100 °C, followed by a continuous contraction in the specimen until up to 400 °C. This can be ascribed to a capillary shrinkage associated with the dehydration of AAFS matrix [53, 54, 341, 342]. A rapid growth of contraction can be observed from approximately 500 to 680 °C with a maximum strain of -5.47%, due to the consumption of fly ash particles and the collapse of nanostructures that led to the densification and therefore shrinkage of matrix [2, 22]. Afterwards, AAFS matrix started to experience a significant expansion until 3.12% at up to around 750 °C, which can be attributed to the formation of major cracks and cavities induced by phase transformation and thermal stress according to the BSEM results.

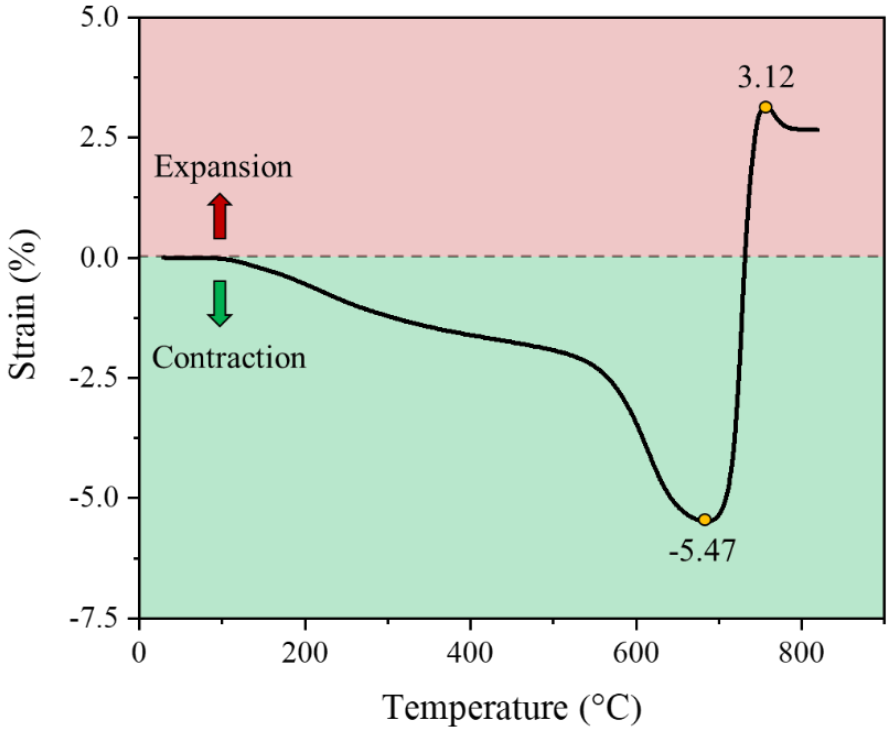

Figure 4.12. Thermal deformation of AAFS paste at elevated temperatures.

4.3.5 Hardness

Nanoindentation test was performed on the polished specimens to determine the micromechanical properties of different solid phases in AAFS paste at elevated temperatures. After experiencing the process of loading, constant holding and unloading, the indentation load and depth were tracked to determine the indentation modulus, hardness and elastic modulus of samples [84, 486]. The load-displacement curves of AAFS paste are shown in Figure 4.13. The average indentation depth in the specimen is around 160 nm, suggesting that the prepared sample is comparatively smooth to minimise the effect of surface topography on the indentation results in terms of the aforementioned mean roughness numbers of 44.3 and 59.3 nm for R_a and R_q, respectively. According to the curves, unreacted slag particles exhibit the lowest indentation depth of around 80-90 nm, while unreacted fly ash particles show a wider range varying from around 80 to 200 nm. The indentation depth of reaction products ranges from approximately 175 to 280 nm. Figure 4.14 demonstrates the relationship between elastic modulus and hardness of AAFS paste subjected to different temperatures. The hardness of reaction products varied around 0.59-0.73 GPa for N-A-S-H gels and 0.3-2.5 GPa for C-A-S-H gels, while the hardness of unreacted particles was typically reported to be around 6 GPa [84, 166, 198, 218, 223]. The overall hardness of AAFS paste at 20-800 °C ranges from around 0.6 to 14.5 GPa, which distinctly shows the micromechanical responses of different solid phases in the paste. Furthermore, the tendency of a higher hardness can also be denoted in the AAFS matrix when the temperature rises from 20 to 800 °C.

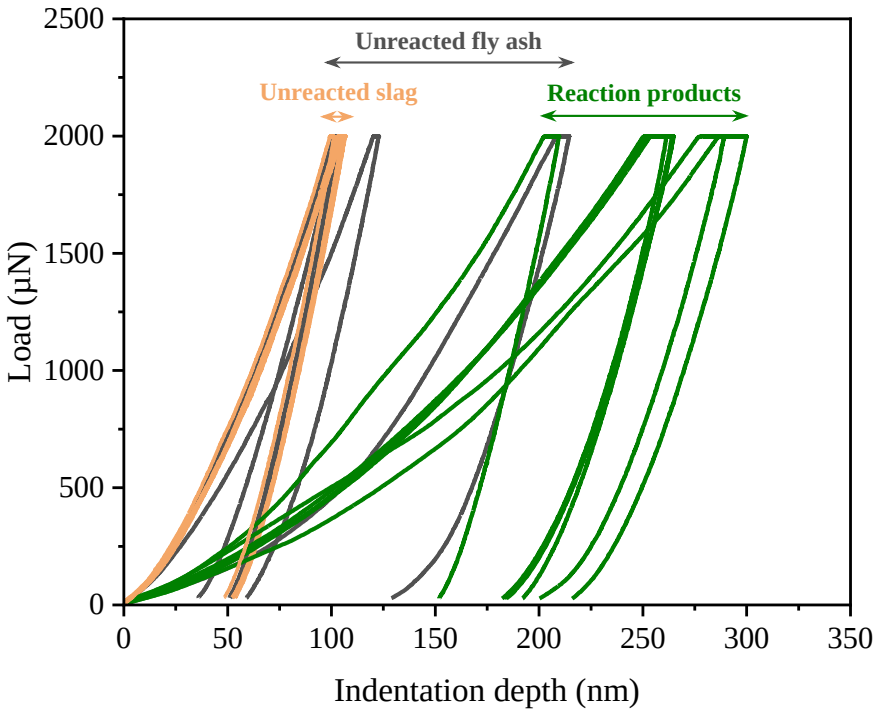

Figure 4.13. Load-displacement curves of different solid phases (i.e. unreacted fly ash, unreacted slag and reaction products) in AAFS paste at 20 ºC.

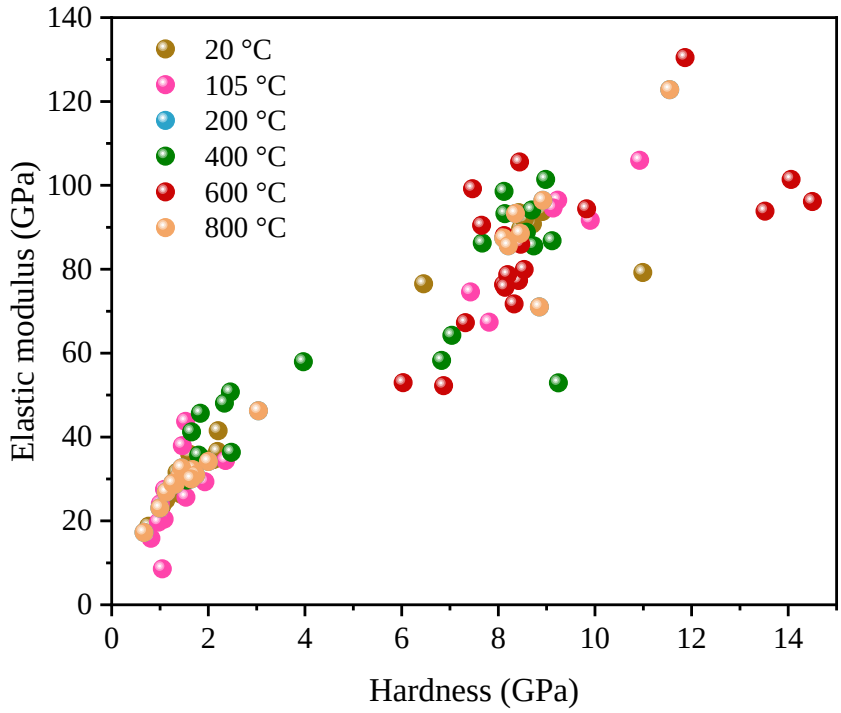

Figure 4.14. Elastic modulus and hardness of AAFS paste at elevated temperatures.

4.3.6 Elastic modulus

Figure 4.15 and Figure 4.16 show the elastic modulus of unreacted particles and reaction products in AAFS paste at elevated temperatures. As per the previous studies, the elastic modulus of unreacted fly ash was dependent on the mineral features, ranging from 30 to 140 GPa [212, 221, 222], while the elastic modulus of unreacted slag was in the range of approximately 46-70 GPa [167, 218]. As seen in Figure 4.15, the average elastic modulus of unreacted fly ash and slag particles at 20 ºC is 85.1 and 92.3, respectively. With the rising exposure temperature, the average elastic modulus of unreacted fly ash particles varies from around 78.4 to 90.0 GPa, whereas that of unreacted slag particles ranges from 88.6 to 104.2 GPa at up to 800 ºC. The discrepancies in the elastic modulus of unreacted particles can be associated with different factors. Regarding fly ash, the dissolution rate can be dependent on the heterogeneity of particles, as they contain both inert crystal phases and reactive amorphous phases with a random distribution [43, 165]. Unlike fly ash with a spherical shape, slag particles have a more irregular shape with relatively higher angularity, which also causes inhomogeneous dissolution of unreacted particles and therefore the variation of elastic modulus [84, 166]. Furthermore, the interaction between fly ash and slag particles can also make pronounced effects on the dissolution process and surrounding reaction products, resulting in the differences of their elastic moduli [43, 48, 162].

Regarding reaction products shown in Figure 4.16, the average elastic modulus of reaction products in AAFS paste tends to be relatively stable at around 27.0-33.9 GPa from 20 to 200 ºC. This suggests the stability of reaction products without significant phase decomposition and transformation at this stage, which is in good agreement with the previous research that the dominant damage mechanisms are further geopolymerisation and pore pressure build-up at up to 200 ºC [487]. Afterwards, there is a significant increase in the average elastic modulus by 50.3 GPa to 84.2 GPa from 200 to 600 ºC, followed by a sudden drop of 150.6% to 33.6 GPa at 800 ºC. It can be found that the phase transformation among different binder gels takes place. At 20 ºC, the elastic modulus of N-A-S-H and C-A-S-H gels was found to be about 4-20 GPa and 12-47 GPa, respectively [166, 212, 218, 221, 222]. Whereas, the hybrid N-C-A-S-H gels was reported to have an elastic modulus of 15.6 to 23.9 GPa [39]. Therefore, the significant decrease of average elastic modulus from 84.2 to 33.6 GPa at 600-800 ºC can be ascribed to the

decomposition of C-A-S-H gels and formation of new N-A-S-H gels, which is also notified from the SEM-EDS results. Since the classic nanoindentation is used to characterise the micromechanical properties of AAFS paste in this study, the future work can be focused on grid nanoindentation to capture features in ITZ, pore and cracks.

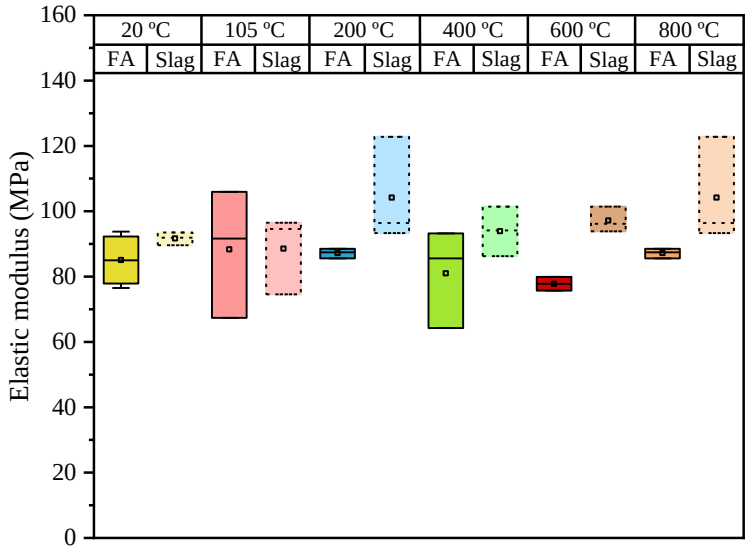

Figure 4.15. Statistical distribution of elastic modulus of unreacted particles in AAFS paste.

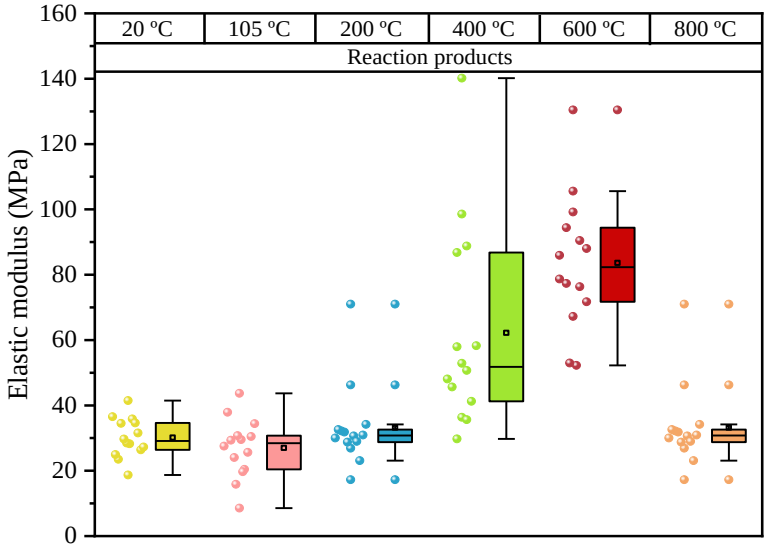

Figure 4.16. Statistical distribution of elastic modulus of reaction products in AAFS paste.

Overall, the elastic modulus of unreacted fly ash and slag particles is dependent on their mineral features, shape and local reactivity, while the decomposition and transformation of N-A-S-H, C-A-S-H and N-C-A-S-H gels can significantly affect the micromechanical responses

of reaction products in AAFS paste. With the increase of temperature, the simultaneous occurrence of decomposition of C-A-S-H gels (decreased by around 11.5%) and formation of N-A-S-H gels (increased by about 15.3%) in AAFS paste from 400 to 600 °C [34, 141, 459, 460], which agrees well with the EDS results showing the shift of spots from high-calcium to low-calcium zone.

4.3.7 Compressive strength

Mechanical performance of alkali-activated materials involves the contribution of micromechanical properties and microstructural features within a complex and heterogeneous structure, especially at elevated temperatures. Figure 4.17 demonstrates the compressive strength evolution of AAFS paste against elevated temperatures. The average compressive strength of AAFS paste at ambient temperature was 65.3 MPa. Compared with the initial state, the compressive strength was increased by 26.5 MPa after heating up to 105 °C, which continued to grow until 115.9 MPa after exposure to 200 °C. Strength gains in AAFS at 20-200 °C can be attributed to the further activation of unreacted fly ash particles by heat treatment that enhanced the strength in AAFS matrix [55, 394, 488]. After 200 °C, the specimen started to experience gradual strength loss with 87.5 MPa at 400 °C, followed by a significant reduction until 26.5 MPa after 600 °C exposure. Notably, an increase of compressive strength from 26.5 MPa to 32.1 MPa was detected with the rising temperature from 600 to 800 °C, attributing to the combined effect of viscous sintering and densification in AAFS matrix [2, 22, 49].

The relative strength with respect to the original compressive strength of AAFS at ambient temperature was calculated and presented in Figure 4.18, in comparison with those collected from literature on AAFS with various slag content ranging from 0 to 100%. The compressive strength of AAFS paste was enhanced with a strength gain by approximately 77.5% from ambient temperature to 200 °C exposure. This suggests the further geopolymerisation within AAFS matrix. Considering different slag content in AAFS at 200 °C, the strength gain for the paste with 0% slag (i.e. AAF) was around 60% [26], whereas the paste with 100% slag (i.e. AAS) exhibited negligible strength development at this stage. With the increase of slag content, the initial strength at ambient temperature could be boosted, owing to the activation of slag and the formation of C-A-S-H gels [320, 325, 368, 369]. Conversely, the strength loss after high temperature exposure could be more significant due to dehydration and decomposition of

calcite [38]. Therefore, fly ash-dominated AAFS was recognised to have better thermal performance than slag-dominated AAFS [2].

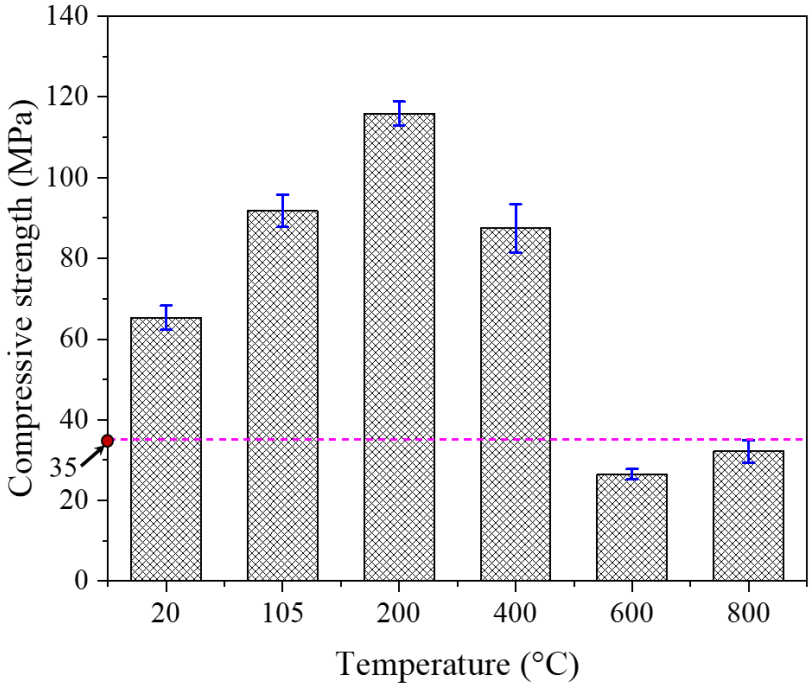

Figure 4.17. Compressive strength of AAFS paste at elevated temperatures.

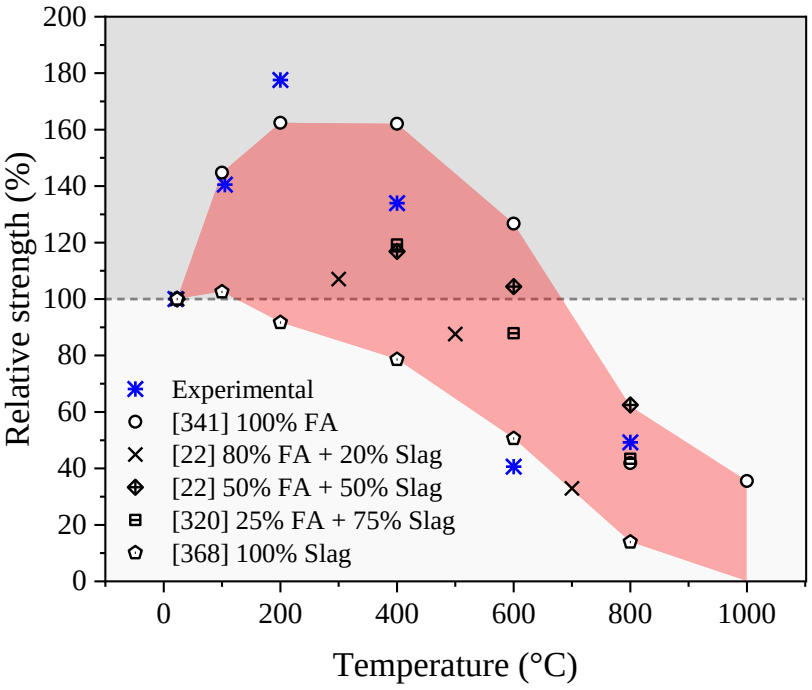

Figure 4.18. Relative strength ratio of AAFS paste at elevated temperatures.

It was noteworthy that a strength loss of around 40% took place in AAFS paste from 200 to 400 °C. As indicated in the BSEM results after exposure to 200 and 400 °C, the volume fraction of unreacted particles dropped from 35.12% to 14.74%, while the volume fraction of reaction products went up by almost 20% to 81.84%. This suggests that the consumption of unreacted particles could lead to the formation of reaction products that enhanced the retention strength of AAFS paste. Nevertheless, the strength reduction at this temperature level implied a combined effect of different factors. Further geopolymerisation could result in a strength gain, whereas dehydration, decomposition, pore pressure accumulation and crack development led to more severely deterioration that did not balance out with the simultaneous strength development [22, 34]. AAFS paste exhibited a more significant strength reduction (approximately 90%) after 600 °C exposure. At 800 °C, the residual strength went up to around 50% of the original value, mainly associated with the re-crystallisation and sintering effects [22, 52]. Beyond 800 °C, it was suggested that the incorporation of fine aggregates can lead to filling of open voids and thus a further rise in compressive strength by up to around 75% at 1000 °C [489, 490]. Figure 4.19 shows the failure patterns of AAFS paste after exposure to various temperatures. In comparison with a compact and smooth internal structure for AAFS paste at ambient temperature, a rougher texture can be observed from AAFS specimen after 800 °C exposure.

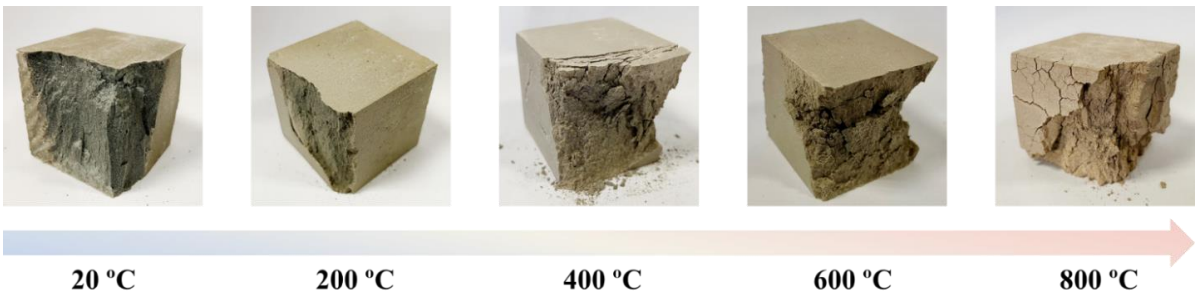

Figure 4.19. Failure modes of AAFS paste after high temperature exposure under uniaxial compression.

Based on the obtained results, the microstructure-micromechanical property relationships in AAFS paste at elevated temperatures are discussed in terms of phase type, volume fraction and micromechanical properties, as illustrated in Figure 4.20. According to the aforementioned phase assemblage from BSEM images, the evolution of volume fractions of different phases in AAFS paste were analysed. The corresponding microstructure-micromechanical property

relationships will be discussed in aspects of unreacted particles, reaction products, and pores and cracks in the paste.

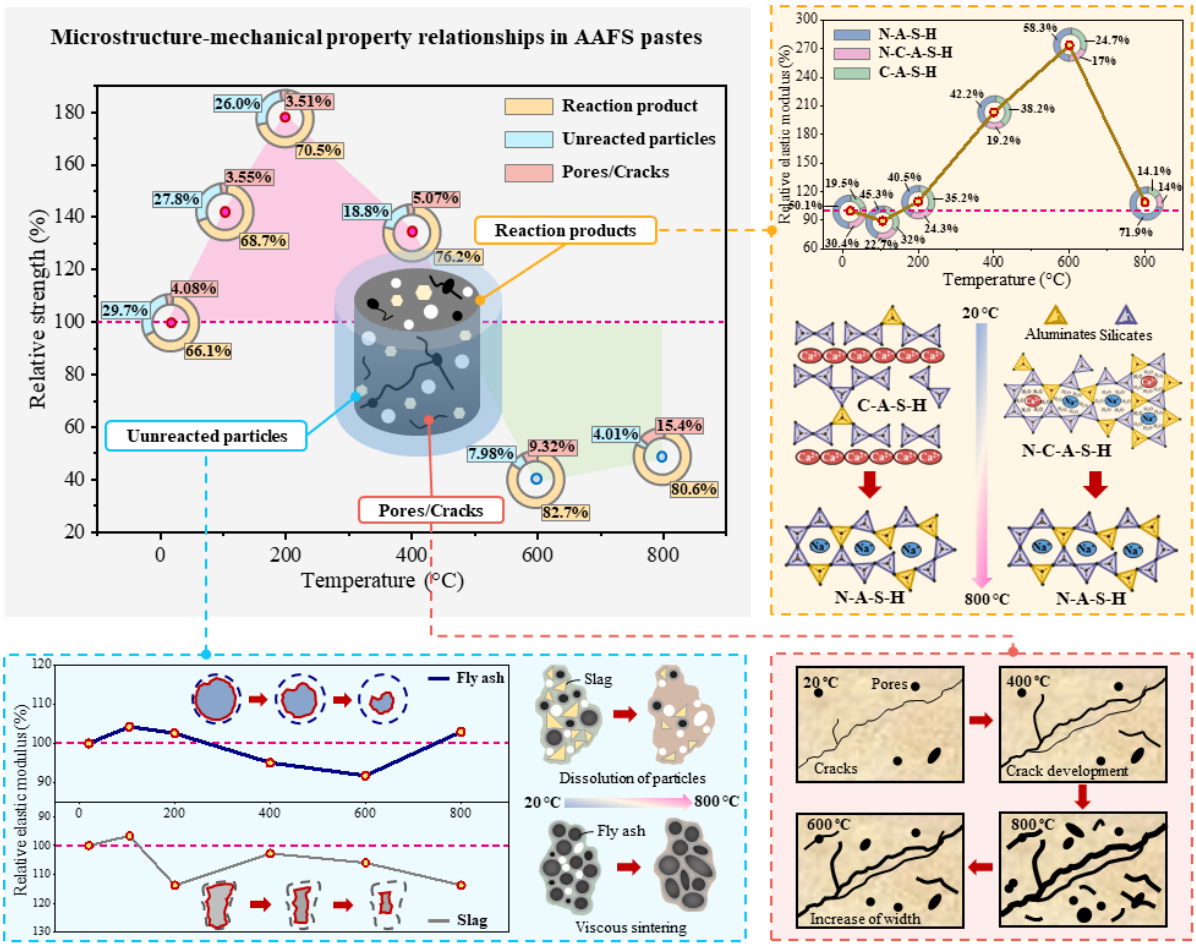

Figure 4.20. Schematic illustration of microstructure-micromechanical property relations in AAFS paste at elevated temperatures.

For unreacted fly ash and slag particles, a significant drop in the volume fraction takes place from 20 to 800 ºC, which can be attributed to the dissolution of unreacted particles and ongoing reaction to consume raw materials and thereby form different types of binder gels, depending on the local chemical environment [88, 126, 131, 132]. The relative elastic moduli of both fly ash and slag particles exhibit some fluctuations at approximately 90-115%. They would show less and less significant contribution to the overall strength as the temperature continuously went up to 800 ºC, as the remnant particles experience dissolution induced by high temperatures and viscous sintering at 800 ºC.

Conversely, there exists an increase in the volume fractions of reaction products in AAFS paste by up to 14.5% of the total volume from 20 to 800 ºC. The reaction products consist of crystalline and amorphous phases including N-A-S-H, N-C-A-S-H and C-A-S-H gels. During the alkaline activation of fly ash and slag in AAFS at 20 °C, different dissolved species can be rearranged and exchanged to form the binder gels [46, 85]. The reaction of aluminium is more rapid and unstable compared to that of silicon, due to a weaker bond in Al-O than Si-O [86]. From 400 to 600 °C, the EDS results report the shift of spots from high-Ca to low-Ca zone, indicating the decomposition of C-A-S-H gels. This is consistent with the previous findings with the simultaneous occurrence of decomposition of C-A-S-H gels (decreased by around 11.5%) and formation of N-A-S-H gels (increased by about 15.3%) in AAFS paste [34, 141, 459, 460]. Furthermore, compared to N-A-S-H gels in AAF paste, the hybrid N-C-A-S-H gels in AAFS paste exhibit a lower thermal stability, leading to phase decomposition after around 600 °C heating [2, 22]. After 800 °C, the phase transformation and recrystallisation in AAFS paste takes place [22, 385, 487]. The sudden drop of relative elastic modulus of reaction products by around 270% from 600 to 800 °C (Figure 4.20) indicates the transformation and rearrangement of different phases at this stage. Since the overall phase content of amorphous phases can experience a dramatic drop from around 84.1% to 36.0% of the total weight [141], the recrystallisation can occur in AAFS paste in terms of formation of nepheline (from N-A-S-H gels) and gehlenite (from C-A-S-H gels) [487].

Several pores and microcracks can be found in AAFS paste at 20 °C due to the heterogenous chemical distribution and pore structures within the matrix [84, 168]. Also, both the chemical shrinkage happened during the reaction process inside the specimen and drying shrinkage with loss of moisture through surfaces that contributes to the overall shrinkage that leads to the development of cracks in AAFS paste at 20 °C [6, 487]. With the rising temperature, new cracks start to initiate and develop. These cracks are mainly caused by migration of moisture as the pore pressure can be trapped in a dense structure with limited internal connectivity in the paste to release the excessive pressure [2, 26, 384, 393]. On the other hand, the consumption of unreacted particles and further reaction contribute to the formation of binder gels and filling of pores and voids. Therefore, there is a combined effect on the stability of the overall volume fraction of pores and cracks [385, 491]. After 400 °C, the connection between pores and multiple cracks forms an inter-connected network, which can locally release part of the pressure

and mitigate the damage induced by pore pressure build-up [4, 52, 385, 483]. Violent deterioration occurs in AAFS paste with the formation of thicker cracks and cavities after 600-800 °C, leading to a more porous structure that results in the significant strength loss of the paste.

In general, the mechanical performance of AAFS at elevated temperatures is highly associated with different damage mechanisms that existed in all three phases, along with changes of their volume fractions and local micromechanical responses.

4.3.8 Flexural strength

Figure 4.21 illustrates the evolution of flexural strength in AAFS. Overall, the residual flexural strength of AAFS paste reduced with the increase of exposure temperature. From ambient temperature to 200 °C, there was a drop of flexural strength from 3.4 to 1.9 MPa. This can be explained by the fact that water in the geopolymer structure can vaporise after the temperature exceeded 100 °C, leading to the formation of thermal cracks induced by pore pressure build-up in matrix with low permeability and thermal shrinkage [305, 376].

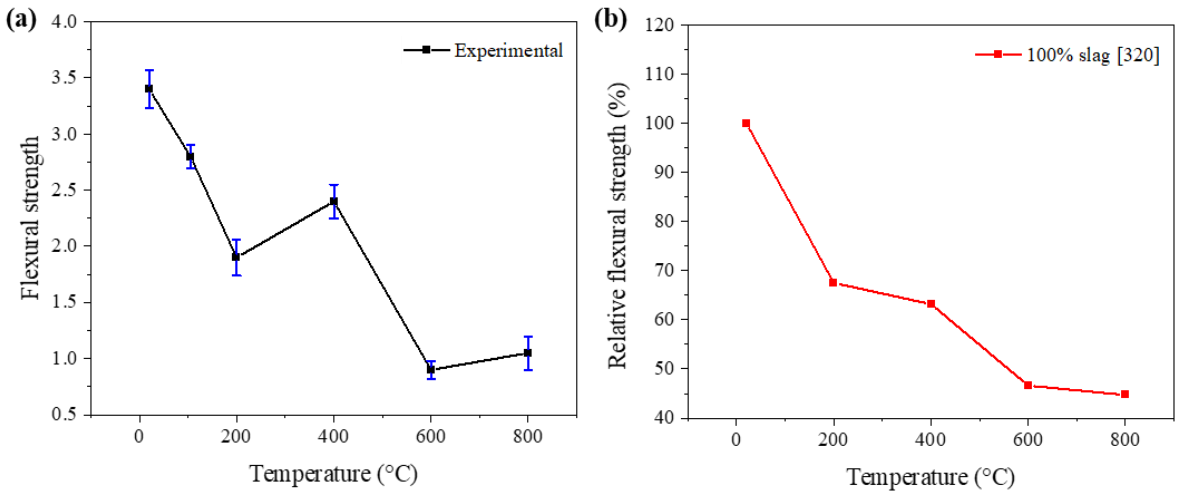

Figure 4.21. Flexural strength of AAFS paste at elevated temperatures regarding (a) this study and (b) 100% slag (adapted from [320]).

The specimen experienced a reduction of flexural strength by 47.4% from 200 to 600 °C with a fluctuation by 26.3% at 400 °C. Similar to the compressive strength results, the strength gains at this temperature level can be attributed to further geopolymerisation. It is worth noting

that there existed a slight increase of residual flexural strength by 4.4%, whereas a decline was reported at 600-800 °C in a previous study on sole slag based system [376], as shown in Figure 4.21. This can be ascribed to a combined result of volume, cavity structure, phase separation, recrystallisation and viscous sintering [376, 492].

4.4 Concluding remarks

In this chapter, the behaviour of AAFS paste exposed to elevated temperatures (i.e. 20, 105, 200, 400, 600, and 800 °C) in terms of physical, thermal, micromechanical and mechanical properties, and visual appearance was investigated using a series of advanced characterisation techniques. Based on the obtained experimental results, the main conclusions can be drawn as follows:

- From 20 to 200 °C, AAFS paste experienced a weight loss of up to 16.9% of the original weight and a compressive strength gain by up to 77.5% due to further geopolymerisation triggered by early stage of heating. However, pore pressure accumulation induced by moisture evaporation can lead to development of cracks and thereafter strength loss.
- At 200-600 °C, a noticeable reduction of residual strength of AAFS paste by almost 140% can be observed, mainly owing to phase decomposition and thermal gradient induced stresses. Moreover, there was a mitigation of residual flexural strength by 47.5% when the exposure temperature was increased to up to 600 °C.
- From 600 to 800 °C, AAFS paste exhibited visible macro-cracks on the surfaces with a change of colour from dark brown to reddish brown due to oxidation of inherent iron compounds. Viscous sintering and recrystallisation contributed to the increase of compressive and flexural strengths by 8.6% and 4.4%, respectively.
- Regarding micromechanical properties of AAFS paste, the overall hardness ranged from 0.6 to 14.5 GPa at 20-800 °C. The average elastic modulus of unreacted fly ash and slag particles varied between 78.4 GPa and 104.2 GPa at up to 800 °C, depending on their mineral features, shape and local reactivity. The elastic modulus of reaction products in AAFS paste was in the range of 27.0-84.2 GPa before and after high temperature exposure.

Chapter 5 Damage Mechanisms of AAFS Paste at Elevated Temperatures

5.1 Introduction

Based on the experimental results of microstructure and thermal and mechanical properties determined from previous chapters, the behaviour of AAFS paste at elevated temperatures has been systematically studied. This chapter further analyses the multiscale microstructural evolution of AAFS paste at elevated temperatures in terms of individual phase assemblage and pore structure characteristics, together with the proposed damage mechanisms corresponding to different levels: Level 0 - solid gel particles, Level I - gel matrix and Level II - AAFS paste. According to the variations of microstructural features of AAFS paste at elevated temperatures, the discussion can be made as per four different stages: (1) Stage 1: ambient temperature, Stage 2: 20-200 °C, Stage 3: 200-600 °C and Stage 4: 600-800 °C, as schematically illustrated in Figure 5.1.

5.2 Damage mechanisms

5.2.1 Stage 1: 20-200 ºC

At Level 0, the importance is attached to the nanostructure of solid gel particles including N-A-S-H, N-C-A-S-H and C-A-S-H particles. At 20 °C, Q^0 and Q^4(0Al) sites are associated with the unreacted precursors, which take up around 17.34% of the total volume. With the reaction of unreacted precursors, the aluminates and silicates are released as monomers after experiencing chemical attack and dissolution [63]. Level I refers to the gel matrix consisting of hybrid gels and gel pores (see Figure 5.1). At ambient temperature, the gel pores occupy around

60% of the total pore volume based on the MIP results, which indicates that the raw precursors have been significantly consumed to form reaction products, leaving a large number of gel pores in AAFS gel matrix [22]. This is consistent with the assemblage of different phases at Level 0. At level II, the focus is placed on paste, composed of unreacted fly ash and slag particles, reaction products and pores (i.e. capillary and larger pores with cracks and voids). A considerable amount of unreacted fly ash particles can be observed in the BSEM images, while some micro-cracks appear at this stage as well, due to shrinkage of AAFS matrix during the curing process. The capillary pores take up approximately 29% of the total porosity, whereas medium and larger pores play less crucial roles at this stage.

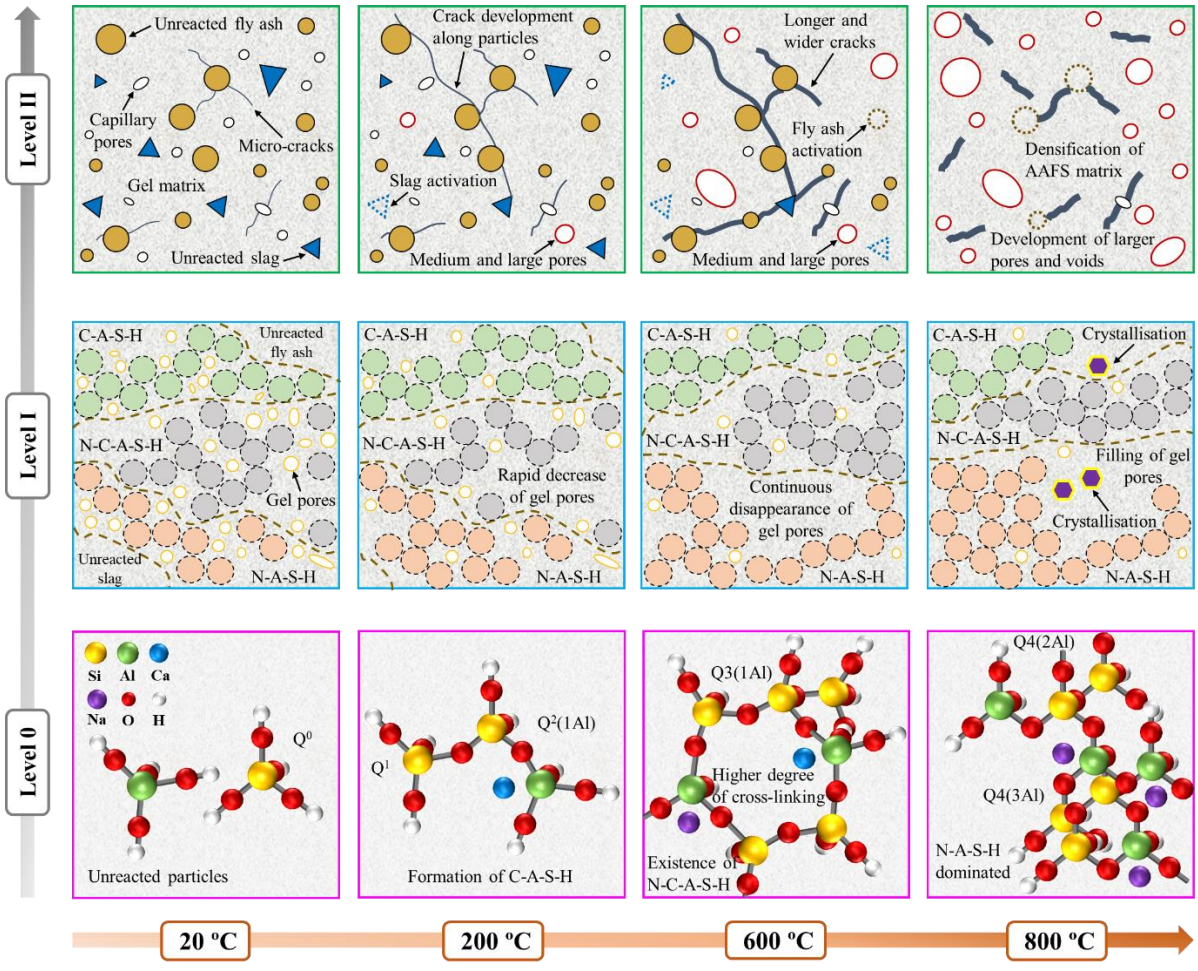

Figure 5.1. Schematic diagram of multiscale microstructural evolution of AAFS paste at elevated temperatures.

After 200 °C exposure, there is an obvious increase of Q^2(1Al) sites from 14.24% to 24.52%, ascribed to the formation of C-A-S-H, where Si and Al tetrahedra are bonded together with the presence of Ca^{2+} ions. This indicates the further promotion of slag activation from 20 to 200 °C. As per the ^{29}Si NMR test results, the temperature rise can generally cause the transformation of solid gel particles from lower degree of cross-linking to higher levels. Regarding gel matrix at Level I, there exhibits a rapid drop of gel pore volume fraction from about 65% to 35% due to the further reaction and the refinement of gel pores [55]. Meanwhile, new medium and large pores are generated at Level II, which can be attributed to the water evaporation and moisture transport. Crack development can be observed at this temperature due to the pore pressure-build up. The accumulation of vapour pressure in the pore structure can result in the initiation and propagation cracks, which develop along the weak transition zone between unreacted particles and reaction products [4].

Based on the microstructural features and mechanical performance, the damage mechanisms at this stage can be proposed. With the increase of exposure temperature, the release of free moisture is significantly promoted before 200 °C and in turn, moisture clog can be formed at the inner region, resulting in pore pressure accumulation and development of cracks [52]. Meanwhile, the heating favours further geopolymerisation in AAFS matrix by consuming free water to activate remaining precursors [22]. The newly formed gels, consumption of moisture and pore pressure build-up have a synergetic effect on the strength development in AAFS by up to 77.5% at 200 °C. Figure 5.2 illustrates the proposed damage mechanisms in AAFS paste.

5.2.2 Stage 2: 200-600 ºC

From 200 to 600 °C, an obvious mitigation of Q^2(1Al) by approximately 12.91% can be found. The signals associated with Q^3(1Al) sites at this stage indicate the existence of N-C-A-S-H, so that the main reaction products are composed of N-C-A-S-H and N-A-S-H structures where Si and Al tetrahedra can be bonded with a ring shape with Ca^{2+} and Na^+ ions [63]. As for gel matrix, the disappearance of calcite and C-S-H phase can be observed from the XRD and QXRD results, which is corresponding to the rapid decrease of Q^2(1Al) sites at Level 0. There is a continuous loss of gel pores at this temperature, implying further gel pore refinement with disordered gel structures. At Level II, the cracks become widened and lengthened compared to the previous stage. Medium pores dominate the inter-connected network, occupying about

56.2% of the total porosity. This can be ascribed to the collapse of gel and capillary pores to form larger ones, resulting in densification in the gel matrix at Level I with larger pores observed in the paste at Level II. Especially, pores with diameter of greater than 0.45 mm start to appear after 400 °C exposure, as observed in the XCT images.

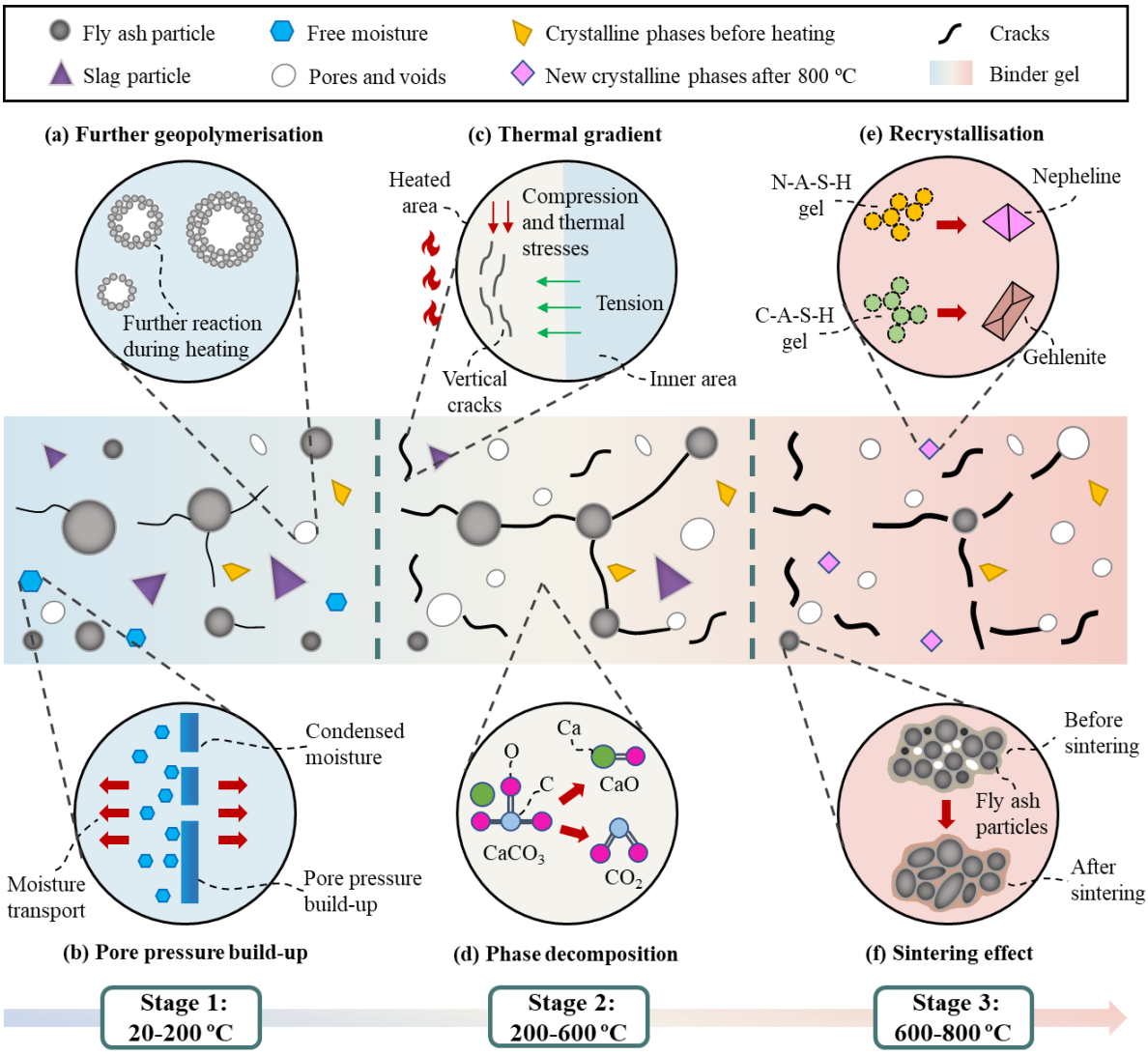

Figure 5.2. Proposed damage mechanisms of AAFS paste at elevated temperatures.

In terms of the damage mechanisms at Stage 2, both physically and chemically bonded moisture is fully evaporated. The AAFS matrix exhibits coalescence of microcracks within an inter-connected network. From 200 to 400 °C, the further geopolymerisation continues with a boost of reaction products by almost 20%, leading to the filling of voids and cracks. The porosity of AAFS is approximately remained the same at this stage, owing to a combined effect

of the growth in reaction products and the initiation of cracks. Other than pore pressure build-up, the damage in AAFS can be explained by two reasons: (1) phase decomposition with disappearance of calcite, and (2) thermal gradient induced stresses that promote the propagation and localisation of cracks, as illustrated in Figure 5.2. Consequently, AAFS paste deteriorates significantly with a strength loss of around 90%.

5.2.3 Stage 3: 600-800 ºC

After 800 °C, N-A-S-H with Q^4(3Al) dominates the reaction products, with the existence of Q^4(2Al) and Q^4(1Al) sites. Compared with Q^2(1Al) sites, Q^4(3Al) structure shows a higher degree of cross-linking, indicating the concentration of solid gel particles and the decomposition of C-A-S-H gels in AAFS after 800 °C exposure. This was also confirmed in the previous study on binder gels in AAFS at elevated temperatures that the increase of Q^4(nAl) sites revealed the dehydration of C-A-S-H gels at 800 °C, favouring the formation of more cross-linked N-A-S-H gel and new crystalline phases such as anorthite and nepheline (also indicated in the XRD results in this study) [56]. At Level 0, gel pores can barely be seen, with less than 5% of the total pore volume (i.e. an around 92.5% reduction from 20 to 800 °C) due to sintering effect. Crystallisation of nepheline and gehlenite happens at this stage, which respectively take up 26.3% and 21.5% of the whole crystalline phases. The formation of nepheline is associated with the highly cross-linked aluminosilicate, while monomeric Si can contribute to the presence of gehlenite [34].

Meanwhile, the amorphous phase drops significantly from more than 80% to 33.5% according to the QXRD results, which also explains the decomposition of hybrid gel while crystallisation happens. On the other hand, FTIR results show a tendency of the main band (assigned to the Si-O-T bonds) shifting from a position of lower to higher wavelength, which also suggests that N-A-S-H becomes the dominant reaction product in AAFS after 800 °C exposure. Both sintering and densification can enhance the compactness of gel matrix, whereas AAFS paste exhibits a more porous structure with flaws and voids due to the drastic matrix deterioration at Level I [22]. The disappearance of micro-cracks can be attributed to the melting and self-healing in AAFS at 800 °C. Overall, the main features about damage evolution in AAFS paste at elevated temperatures are summarised in Figure 5.3.

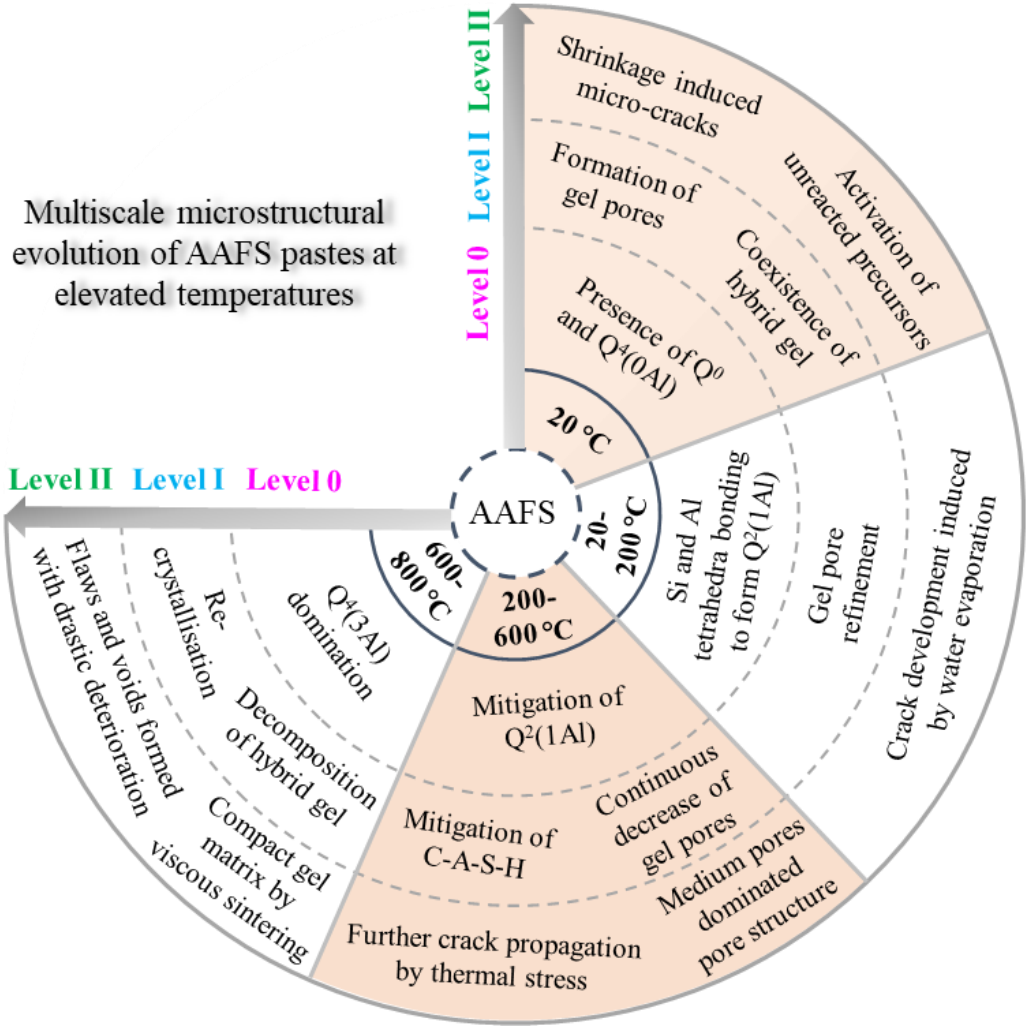

Figure 5.3. Multiscale microstructural evolution of AAFS paste at elevated temperatures.

To sum up the damage mechanisms at Stage 3, the rearrangement of AAFS matrix took place, along with the formation of large pores, cracks and cavities. Almost full consumption of unreacted particles and collapse of nano-pores led to the formation of larger pores with a drastic increase of porosity. Recrystallisation and viscous sintering play a dominant role at Level II [22, 52]. Recrystallisation refers to the phase transformation of N-A-S-H gels to form nepheline and the appearance of gehlenite associated with C-A-S-H gels. As a porous crystalline phase, nepheline has a negative impact on the compactness of paste and forms a more vulnerable gel skeleton. On the other hand, the viscous sintering can result in self-healing by filling micropores and densification of the paste, which diminishes the undesirable effects caused by crack

formation and phase changes. This contributes to a strength gain at 800 °C by about 10% of the original compressive strength.

5.3 Concluding remarks

In this chapter, the underlying damage mechanisms of AAFS paste at elevated temperatures were investigated based on different temperatures ranges from Stage 1 to 3. The multiscale microstructural characteristics were discussed, which provided fundamental understanding of this material with the identification of each damage mechanism in the matrix.

Chapter 6 Conclusions and Perspectives

6.1 Conclusions

This thesis systematically investigates the behaviour of alkali-activated fly ash-slag (AAFS) paste at elevated temperatures from 20 to 800 °C, focusing on multiscale microstructural characteristics, thermal and mechanical properties, and inherent damage mechanisms. The research delivers significant insights into high-temperature-induced damage evolution and extends the potential of this sustainable material for fire prevention and high-temperature-resistant applications. The main conclusions of this thesis can be drawn as follows:

(i) Multiscale microstructural characteristics of AAFS paste at elevated temperatures

- The nanostructure of solid gel particles was significantly altered with increasing temperature. At 20-200 °C, an enhancement in the bonding between Si and Al tetrahedra promoted the formation of Q_2(1Al), indicating a strengthening of the gel matrix. As temperatures rose beyond 200 °C, a sharp decline in Q_2(1Al) and a rise in Q_4(3Al) suggested a transition towards a more cross-linked N-A-S-H gel due to the decomposition of C-A-S-H gel.
- At the highest evaluated temperature of 800 °C, the nanostructure is dominated by N-A-S-H gel, with substantial reductions in C-A-S-H and N-C-A-S-H gels. Consequently, significant crystalline phases including nepheline and gehlenite emerge, indicating the existence of phase transformation at extreme temperatures.
- The volume fraction of unreacted particles in AAFS paste declined from around 30% to 5%, whereas that of pores and cracks went up from 2.3% to 10.3% as the temperature increased from 20 to 800 ºC. The gradual disappearance of unreacted fly ash and slag was observed, together with the initiation and propagation of cracks, cavities and flaws in a porous structure at up to 800 ºC.

(ii) Behaviour of AAFS paste at elevated temperatures

- The thermal performance of AAFS paste revealed that the majority of the mass loss took place from 20 to around 250 °C, whereas the rising exposure temperature had almost negligible effect on the final loss. There was a rapid growth of thermal contraction in the paste at 500 to 680 °C with a maximum strain of 5.47% due to matrix densification.
- From 20 to 200°C, AAFS paste exhibited a weight loss of up to 16.9% of its original weight and an increase in compressive strength by up to 77.5%, attributed to enhanced geopolymerisation induced by the initial phase of heating. There was a noticeable reduction of residual strength of AAFS paste by almost 140% at 200-600 °C, followed by a slight increase of residual strength (around 50% of the original value).
- Regarding micromechanical properties of AAFS paste, the overall hardness ranged from 0.6 to 14.5 GPa at 20-800 °C. The average elastic modulus of unreacted fly ash and slag particles varied between 78.4 GPa and 104.2 GPa at up to 800 °C, depending on their mineral features, shape and local reactivity. The elastic modulus of reaction products in AAFS paste was in the range of 27.0-84.2 GPa before and after high temperature exposure.

(iii) Damage mechanisms of AAFS paste at elevated temperatures

- The damage mechanisms of AAFS paste were identified based on different temperature ranges. At Stage 1 (20-200 °C), further geopolymerisation took place in AAFS matrix, which consumed unreacted precursors to produce new binder gels, thereby enhanced the mechanical properties within this temperature level. Meanwhile, the migration of free moisture triggered by elevated temperatures led to pore pressure build-up and crack initiation.
- At Stage 2 (200-600 °C), further crack propagation and development could be found in the paste, which was induced by thermal gradient and phase decomposition with disappearance of calcite.
- When it got to Stage 3 (600-800 °C), viscous sintering and recrystallisation were found as the dominant factors that led to a combined effect of matrix densification with self-healing of cracks and deterioration of AAFS internal structure.

6.2 Perspectives

Based on the experimental results of this thesis, the identified limitations and the recommendations for future research are outlined as follows:

- In this thesis, the behaviour of AAFS paste at elevated temperatures was investigated based on a fixed mix proportion, whereas the future research can focus on further modification of AAFS, including changes of slag content to study high-calcium based AAFS and replacement of alkaline activators to achieve higher sustainability with lower alkali.
- The behaviour of AAFS concrete at elevated temperatures can be further studied in the future, along with the strategies to make use of recycled materials to tailor this type of AAC. For example, the coarse and fine aggregates can be substituted by recycled aggregates from disposed Portland cement concrete.
- Based on the identified damage mechanisms, different damage mitigation approaches should be adopted to improve the high-temperature behaviour of AAFS like incorporation of fibres. For instance, the use of recycled tyre polymer fibres was proved to enhance the thermal-resistance of Portland cement by improving internal connectivity in the matrix after melting at elevated temperatures. The incorporation of recycled fibres and other additives in AAFS are worth investigating to mitigate thermal-induced damages in the future.
- The heating method applied in this research was based on a constant heating rate of 10 °C/min. However, the increase of temperature in a real fire situation was more rapid and inconsistent. Therefore, it is recommended to use the fire curve in the duration of heating to better simulate extreme scenarios and study the effect of heating rates on the behaviour of AAFS.
- In accordance with the experimental results of this thesis, the microstructural characteristics as well as physical, thermal and mechanical properties of can be used to develop the coupled thermal-mechanical models of AAFS for further numerical studies on this material.

List of Publications

- **W. Tu**, G. Fang, B. Dong, M. Zhang, Micromechanical analysis of alkali-activated fly ash-slag paste at elevated temperatures. *Cement and Concrete Composites*, 153 (2024) 105735.
- **W. Tu**, M. Zhang, Multiscale microstructure and micromechanical properties of alkali-activated concrete: A critical review. *Cement and Concrete Composites*, 152 (2024) 105664.
- **W. Tu**, G. Fang, B. Dong, Y. Hu, M. Zhang, Behaviour of alkali-activated fly ash-slag paste at elevated temperatures: An experimental study, *Cement and Concrete Composites*, 147 (2024) 105438.
- **W. Tu**, G. Fang, B. Dong, M. Zhang, Multiscale study of microstructural evolution in alkali-activated fly ash-slag paste at elevated temperatures, *Cement Concrete and Composites*, 143 (2023) 105258.
- **W. Tu**, M. Zhang, Behaviour of alkali-activated concrete at elevated temperatures: A critical review, *Cement and Concrete Composites*, 138 (2023) 104961.
- S. Naderi, **W. Tu**, M. Zhang, Meso-scale modelling of compressive fracture in concrete with irregularly shaped aggregates, *Cement and Concrete Research*, 140 (2021) 106317.
- M. Chen, Z. Sun, **W. Tu**, X. Yan, M. Zhang, Behaviour of recycled tyre polymer fibre reinforced concrete at elevated temperatures, *Cement and Concrete Composites*, 124 (2021) 104257.
- X. Fan, Z. Zhou, **W. Tu**, M. Zhang, Shear behaviour of inorganic polymer concrete beams reinforced with basalt FRP bars and stirrups, *Composite Structures*, 255 (2021) 112901.
- **W. Tu**, Y. Zhu, G. Fang, X. Wang, M. Zhang, Internal curing of alkali-activated fly ash-slag pastes using superabsorbent polymer, *Cement and Concrete Research*, 116 (2019) 179-190.
- G. Fang, W. Ho, **W. Tu**, M. Zhang, Workability and mechanical properties of alkali-activated fly ash-slag concrete cured at ambient temperature, *Construction and Building Materials*, 172 (2018) 476-487.

References

[1] A. Farzampour, Compressive behavior of concrete under environmental effects, Compressive Strength of Concrete (2019) 92-104.

[2] W.L. Tu, M.Z. Zhang, Behaviour of alkali-activated concrete at elevated temperatures: A critical review, Cement Concrete Comp 138 (2023) 104961.

[3] H.Y. Wu, X.S. Lin, A.N. Zhou, A review of mechanical properties of fibre reinforced concrete at elevated temperatures, Cement Concrete Res 135 (2020) 106117.

[4] Y. Li, P. Pimienta, N. Pinoteau, K.H. Tan, Effect of aggregate size and inclusion of polypropylene and steel fibers on explosive spalling and pore pressure in ultra-high-performance concrete (UHPC) at elevated temperature, Cement Concrete Comp 99 (2019) 62-71.

[5] M.K. Lahoti, K.H. Tan, E.H. Yang, A critical review of geopolymer properties for structural fire-resistance applications, Constr Build Mater 221 (2019) 514-526.

[6] W.L. Tu, Y. Zhu, G.H. Fang, X.G. Wang, M.Z. Zhang, Internal curing of alkali-activated fly ash-slag pastes using superabsorbent polymer, Cement Concrete Res 116 (2019) 179-190.

[7] Z.G. Shi, C.J. Shi, J. Zhang, S. Wan, Z.H. Zhang, Z.H. Ou, Alkali-silica reaction in waterglass-activated slag mortars incorporating fly ash and metakaolin, Cement Concrete Res 108 (2018) 10-19.

[8] J.L. Provis, Alkali-activated materials, Cement Concrete Res 114 (2018) 40-48.

[9] J.L. Provis, A. Palomo, C.J. Shi, Advances in understanding alkali-activated materials, Cement Concrete Res 78 (2015) 110-125.

[10] O.G. Rivera, W.R. Long, C.A. Weiss, R.D. Moser, B.A. Williams, K. Torres-Cancel, E.R. Gore, P.G. Allison, Effect of elevated temperature on alkali-activated geopolymeric binders compared to portland cement-based binders, Cement Concrete Res 90 (2016) 43-51.

[11] R.D. Moser, P.G. Allison, B.A. Williams, C.A. Weiss, A.D. Diaz, E.R. Gore, P.G. Malone, Improvement in the geopolymer-to-steel bond using a reactive vitreous enamel coating, Constr Build Mater 49 (2013) 62-69.

[12] G.H. Fang, W.K. Ho, W.L. Tu, M.Z. Zhang, Workability and mechanical properties of alkali-activated fly ash-slag concrete cured at ambient temperature, Constr Build Mater 172 (2018) 476-487.

[13] F. Colangelo, I. Farina, M. Travaglioni, C. Salzano, R. Cioffi, A. Petrillo, Eco-efficient industrial waste recycling for the manufacturing of fibre reinforced innovative geopolymer mortars: Integrated waste management and green product development through LCA, J Clean Prod 312 (2021) 127777.

[14] F. Xu, G.H. Gu, W. Zhang, H.M. Wang, X.M. Huang, J. Zhu, Pore structure analysis and properties evaluations of fly ash-based geopolymer foams by chemical foaming method, Ceram Int 44(16) (2018) 19989-19997.

[15] A. Hassan, M. Arif, M. Shariq, Use of geopolymer concrete for a cleaner and sustainable environment - A review of mechanical properties and microstructure, J Clean Prod 223 (2019) 704-728.

[16] J.H. Zhao, L.Y. Tong, B.E. Li, T.H. Chen, C.P. Wang, G.Q. Yang, Y. Zheng, Eco-friendly geopolymer materials: A review of performance improvement, potential application and sustainability assessment, J Clean Prod 307 (2021) 127085.

[17] D.L. Kong, J.G. Sanjayan, K. Sagoe-Crentsil, Comparative performance of geopolymers made with metakaolin and fly ash after exposure to elevated temperatures, Cement Concrete Res 37(12) (2007) 1583-1589.

[18] A. Hassan, M. Arif, M. Shariq, T. Alomayri, S. Pereira, Fire resistance characteristics of geopolymer concrete for environmental sustainability: a review of thermal, mechanical and microstructure properties, Environ Dev Sustain 9 (2022) 8975-9010.

[19] T. Luukkonen, Z. Abdollahnejad, J. Yliniemi, P. Kinnunen, M. Illikainen, One-part alkali-activated materials: A review, Cement Concrete Res 103 (2018) 21-34.

[20] T.W. Cheng, J.P. Chiu, Fire-resistant geopolymer produced by granulated blast furnace slag, Miner Eng 16(3) (2003) 205-210.

[21] A. Buchwald, M. Hohmann, C. Kaps, H. Bettzieche, J.T. Kuhnert, Stabilised foam clay material with high performance thermal insulation properties, Cfi-Ceram Forum Int 81(8) (2004) E39-E42.

[22] Y. Luo, S.H. Li, K.M. Klima, H.J.H. Brouwers, Q.L. Yu, Degradation mechanism of hybrid fly ash/slag based geopolymers exposed to elevated temperatures, Cement Concrete Res 151 (2022) 106649.

[23] Z. Pan, J.G. Sanjayan, B.V. Rangan, An investigation of the mechanisms for strength gain or loss of geopolymer mortar after exposure to elevated temperature, J Mater Sci 44(7) (2009) 1873-1880.

[24] Z. Pan, J.G. Sanjayan, F. Collins, Effect of transient creep on compressive strength of geopolymer concrete for elevated temperature exposure, Cement Concrete Res 56 (2014) 182-189.

[25] Z. Pan, Z. Tao, Y.F. Cao, R. Wuhrer, T. Murphy, Compressive strength and microstructure of alkali-activated fly ash/slag binders at high temperature, Cement Concrete Comp 86 (2018) 9-18.

[26] H.G. Zhang, L. Li, C. Yuan, Q.Y. Wang, P.K. Sarker, X.S. Shi, Deterioration of ambient-cured and heat-cured fly ash geopolymer concrete by high temperature exposure and prediction of its residual compressive strength, Constr Build Mater 262 (2020) 120924.

[27] D.L.Y. Kong, J.G. Sanjayan, Effect of elevated temperatures on geopolymer paste, mortar and concrete, Cement Concrete Res 40(2) (2010) 334-339.

[28] T. Alomayri, L. Vickers, F.U.A. Shaikh, I.M. Low, Mechanical properties of cotton fabric reinforced geopolymer composites at 200-1000 degrees C, J Adv Ceram 3(3) (2014) 184-193.

[29] G. Humur, A. Cevik, Mechanical characterization of lightweight engineered geopolymer composites exposed to elevated temperatures, Ceram Int 48(10) (2022) 13634-13650.

[30] X. Jiang, Y.Y. Zhang, R. Xiao, P. Polaczyk, M.M. Zhang, W. Hu, Y. Bai, B.S. Huang, A comparative study on geopolymers synthesized by different classes of fly ash after exposure to elevated temperatures, J Clean Prod 270 (2020) 122500.

[31] A. Hassan, M. Arif, M. Shariq, Mechanical Behaviour and Microstructural Investigation of Geopolymer Concrete After Exposure to Elevated Temperatures, Arab J Sci Eng 45(5) (2020) 3843-3861.

[32] F.L. Qu, W.G. Li, Z. Tao, A. Castel, K.J. Wang, High temperature resistance of fly ash/GGBFS-based geopolymer mortar with load-induced damage, Mater Struct 53(4) (2020) 1-21.

[33] A. Fernandez-Jimenez, J.Y. Pastor, A. Martin, A. Palomo, High-Temperature Resistance in Alkali-Activated Cement, J Am Ceram Soc 93(10) (2010) 3411-3417.

[34] S.M. Park, J.G. Jang, N.K. Lee, H.K. Lee, Physicochemical properties of binder gel in alkali-activated fly ash/slag exposed to high temperatures, Cement Concrete Res 89 (2016) 72-79.

[35] H.Y. Zhang, V. Kodur, B. Wu, L. Cao, S.L. Qi, Comparative Thermal and Mechanical Performance of Geopolymers derived from Metakaolin and Fly Ash, J Mater Civil Eng 28(2) (2016) 1-13.

[36] J.B. Sundararaj, P.R.K. Rajkumar, M. Sivasakthi, M. Jegan, Effect of mineral admixtures on mechanical and thermal properties of geopolymer mortar at elevated temperature, Innov Infrastruct So 7(6) (2022) 354.

[37] P. Duan, C.J. Yan, W. Zhou, W.J. Luo, C.H. Shen, An investigation of the microstructure and durability of a fluidized bed fly ash-metakaolin geopolymer after heat and acid exposure, Mater Design 74 (2015) 125-137.

[38] I.H. Aziz, M.M.A. Abdullah, C.Y. Heah, Y.M. Liew, Behaviour changes of ground granulated blast furnace slag geopolymers at high temperature, Adv Cem Res 32(10) (2020) 465-475.

[39] G.H. Fang, M.Z. Zhang, Multiscale micromechanical analysis of alkali-activated fly ash-slag paste, Cement Concrete Res 135 (2020) 105860.

[40] J.I.E. Garcia, K. Campos-Venegas, A. Gorokhovsky, A. Fernandez, Cementitious composites of pulverised fuel ash and blast furnace slag activated by sodium silicate: effect of Na2O concentration and modulus, Adv Appl Ceram 105(4) (2006) 201-208.

[41] X. Gao, Q.L. Yu, H.J.H. Brouwers, Reaction kinetics, gel character and strength of ambient temperature cured alkali activated slag-fly ash blends, Constr Build Mater 80 (2015) 105-115.

[42] A. Rafeet, R. Vinai, M. Soutsos, W. Sha, Effects of slag substitution on physical and mechanical properties of fly ash-based alkali activated binders (AABs), Cement Concrete Res 122 (2019) 118-135.

[43] G.H. Fang, Q. Wang, M.Z. Zhang, In-situ X-ray tomographic imaging of microstructure evolution of fly ash and slag particles in alkali-activated fly ash-slag paste, Compos Part B-Eng 224 (2021) 109221.

[44] G.H. Fang, Q. Wang, M.Z. Zhang, Micromechanical analysis of interfacial transition zone in alkali-activated fly ash-slag concrete, Cement Concrete Comp 119 (2021) 103990.

[45] G.H. Fang, M.Z. Zhang, The evolution of interfacial transition zone in alkali-activated fly ash-slag concrete, Cement Concrete Res 129 (2020) 105963.

[46] I. Ismail, S.A. Bernal, J.L. Provis, R.S. Nicolas, S. Hamdan, J.S.J. van Deventer, Modification of phase evolution in alkali-activated blast furnace slag by the incorporation of fly ash, Cement Concrete Comp 45 (2014) 125-135.

[47] X. Gao, Q.L. Yu, H.J.H. Brouwers, Apply Si-29, Al-27 MAS NMR and selective dissolution in identifying the reaction degree of alkali activated slag-fly ash composites, Ceram Int 43(15) (2017) 12408-12419.

[48] H.L. Ye, A. Radlinska, Fly ash-slag interaction during alkaline activation: Influence of activators on phase assemblage and microstructure formation, Constr Build Mater 122 (2016) 594-606.

[49] H.Q. Ma, C. Wu, Mechanical and microstructural properties of alkali-activated fly ash-slag material under sustained moderate temperature effect, Cement Concrete Comp 134 (2022) 104744.

[50] M. Saridemir, S. Celikten, Investigation of fire and chemical effects on the properties of alkali-activated lightweight concretes produced with basaltic pumice aggregate, Constr Build Mater 260 (2020) 119969.

[51] K. Yasaswini, A.V. Rao, Behaviour of geopolymer concrete at elevated temperature, Mater Today-Proc 33 (2020) 239-244.

[52] Y. Li, K.H. Tan, E.H. Yang, Synergistic effects of hybrid polypropylene and steel fibers on explosive spalling prevention of ultra-high performance concrete at elevated temperature, Cement Concrete Comp 96 (2019) 174-181.

[53] R. He, N. Dai, Z.J. Wang, Thermal and Mechanical Properties of Geopolymers Exposed to High Temperature: A Literature Review, Adv Civ Eng 2020 (2020) 1-17.

[54] M.M. Salahuddin, M. Norkhairunnisa, F. Mustapha, A review on thermophysical evaluation of alkali-activated geopolymers, Ceram Int 41(3) (2015) 4273-4281.

[55] C.L. Chan, M.Z. Zhang, Behaviour of strain hardening geopolymer composites at elevated temperatures, Cement Concrete Comp 132 (2022) 104634.

[56] N.K. Lee, K.T. Koh, G.H. An, G.S. Ryu, Influence of binder composition on the gel structure in alkali activated fly ash/slag pastes exposed to elevated temperatures, Ceram Int 43(2) (2017) 2471-2480.

[57] J.R. Ren, H.G. Chen, R.X. Dai, T. Sun, Behavior of combined fly ash/GBFS-based geopolymer concrete after exposed to elevated temperature, 2019 3rd International Workshop on Renewable Energy and Development (Iwred 2019) 267 (2019) 032056.

[58] W.G.V. Saavedra, R.M. de Gutierrez, Performance of geopolymer concrete composed of fly ash after exposure to elevated temperatures, Constr Build Mater 154 (2017) 229-235.

[59] J.R. Ren, H.G. Chen, T. Sun, H. Song, M.S. Wang, Flexural Behaviour of Combined FA/GGBFS Geopolymer Concrete Beams after Exposure to Elevated Temperatures, Adv Mater Sci Eng 2017 (2017) 6854043.

[60] W.B. Ren, J.Y. Xu, E.L. Bai, Strength and Ultrasonic Characteristics of Alkali-Activated Fly Ash-Slag Geopolymer Concrete after Exposure to Elevated Temperatures, J Mater Civil Eng 28(2) (2016) 04015124.

[61] W.D.A. Rickard, J. Temuujin, A. van Riessen, Thermal analysis of geopolymer pastes synthesised from five fly ashes of variable composition, J Non-Cryst Solids 358(15) (2012) 1830-1839.

[62] M. Lahoti, K.K. Wong, K.H. Tan, E.H. Yang, Effect of alkali cation type on strength endurance of fly ash geopolymers subject to high temperature exposure, Mater Design 154 (2018) 8-19.

[63] C.J. Shi, A.F. Jimenez, A. Palomo, New cements for the 21st century: The pursuit of an alternative to Portland cement, Cement Concrete Res 41(7) (2011) 750-763.

[64] J.L. Provis, S.A. Bernal, Geopolymers and Related Alkali-Activated Materials, Annu Rev Mater Res 44 (2014) 299-327.

[65] Y. Ma, G. Ye, The shrinkage of alkali activated fly ash, Cement Concrete Res 68 (2015) 75-82.

[66] C. Gunasekara, D.W. Law, S. Setunge, J.G. Sanjayan, Zeta potential, gel formation and compressive strength of low calcium fly ash geopolymers, Constr Build Mater 95 (2015) 592-599.

[67] P. Zhang, X.Y. Sun, F. Wang, J. Wang, Mechanical Properties and Durability of Geopolymer Recycled Aggregate Concrete: A Review, Polymers-Basel 15(3) (2023) 615.

[68] K. Korniejenko, P. Kejzlar, P. Louda, The Influence of the Material Structure on the Mechanical Properties of Geopolymer Composites Reinforced with Short Fibers Obtained with Additive Technologies, Int J Mol Sci 23(4) (2022) 2023.

[69] Z. Gao, P. Zhang, J.J. Guo, K.X. Wang, Bonding behavior of concrete matrix and alkali-activated mortar incorporating nano-SiO2 and polyvinyl alcohol fiber: Theoretical analysis and prediction model, Ceram Int 47(22) (2021) 31638-31649.

[70] M. Hanumananaik, K.V.L. Subramaniam, Shrinkage in low-calcium fly ash geopolymers for precast applications: Reaction product content and pore structure under drying conditions, J Build Eng 78 (2023) 107583.

[71] A. Fakhrabadi, A.J. Choobbasti, S.S. Kutanaei, Durability Evaluation of Clayey Sandy Soil Stabilized with Copper-Slag-Based Geopolymer Under Freezing-Thawing Cycles, Int J Pavement Res T (2023) 1-18.

[72] Z. Azimi, V. Toufigh, Influence of Blast Furnace Slag on Pore Structure and Transport Characteristics in Low-Calcium Fly-Ash-Based Geopolymer Concrete, Sustainability-Basel 15(18) (2023) 13348.

[73] F. Hong, S. Yu, D.S. Hou, Z.J. Li, H.W. Sun, P. Wang, M.H. Wang, Study on the mechanical properties, gelling products and alkalization process of alkali-activated metakaolin: From experiment to molecular dynamics simulation, J Build Eng 79 (2023) 107705.

[74] B. Zhang, H. Zhu, P. Feng, P. Zhang, A review on shrinkage-reducing methods and mechanisms of alkali-activated/geopolymer systems: Effects of chemical additives, J Build Eng 49 (2022) 104056.

[75] S.Y. Guo, Y.L. Wu, Z.Q. Jia, X.Q. Qi, W.R. Wang, Sodium-based activators in alkali-activated materials: Classification and comparison, J Build Eng 70 (2023) 106397.

[76] A. Erfanimanesh, M.K. Sharbatdar, Mechanical and microstructural characteristics of geopolymer paste, mortar, and concrete containing local zeolite and slag activated by sodium carbonate, J Build Eng 32 (2020) 101781.

[77] Y. Essam, N. El-Faramawy, W. Ramadan, M. Ramadan, From dangerous wastes to green construction materials, as thermally stable-radiation blocker, in presence of meso-porous magnesia and alumina, J Build Eng 66 (2023) 105896.

[78] Y.R. Wang, Y.B. Cao, Z.H. Zhang, P. Zhang, Y.W. Ma, A.G. Wang, H. Wang, Intrinsic sulfuric acid resistance of C-(N)-A-S-H and N-A-S-H gels produced by alkali-activation of synthetic calcium aluminosilicate precursors, Cement Concrete Res 165 (2023) 107068.

[79] I. Nikolic, L. Karanovic, I.J. Castvan, V. Radmilovic, S. Mentus, V. Radmilovic, Improved compressive strength of alkali activated slag upon heating, Mater Lett 133 (2014) 251-254.

[80] H.H. Chen, A. Nikvar-Hassani, S. Ormsby, D. Ramey, L.Y. Zhang, Mechanical and microstructural investigations on the low-reactive copper mine tailing-based geopolymer activated by phosphoric acid, Constr Build Mater 393 (2023) 132030.

[81] M. Hanumananaik, K.V.L. Subramaniam, Influence of Process Variables on Shrinkage in Low-Calcium Fly-Ash Geopolymers, J Mater Civil Eng 35(6) (2023) 04023143.

[82] C.H. Xue, V. Sirivivatnanon, A. Nezhad, Q.X. Zhao, Comparisons of alkali-activated binder concrete (ABC) with OPC concrete-A review, Cement Concrete Comp 135 (2023) 104851.

[83] C. Li, H.H. Sun, L.T. Li, A review: The comparison between alkali-activated slag (Si plus Ca) and metakaolin (Si plus Al) cements, Cement Concrete Res 40(9) (2010) 1341-1349.

[84] G. Fang, Multiscale Characterisation of Microstructure and Mechanical Properties of Alkali-Activated Fly Ash-Slag Concrete, UCL (University College London), 2021.

[85] Z.Q. Sun, A. Vollpracht, Isothermal calorimetry and in-situ XRD study of the NaOH activated fly ash, metakaolin and slag, Cement Concrete Res 103 (2018) 110-122.

[86] A. Palomo, P. Krivenko, I. Garcia-Lodeiro, E. Kavalerova, O. Maltseva, A. Fernandez-Jimeneza, A review on alkaline activation: new analytical perspectives, Mater Construcc 64(315) (2014) 22.

[87] N.K. Lee, H.K. Lee, Reactivity and reaction products of alkali-activated, fly ash/slag paste, Constr Build Mater 81 (2015) 303-312.

[88] I. Garcia-Lodeiro, A. Palomo, A. Fernandez-Jimenez, D.E. Macphee, Compatibility studies between N-A-S-H and C-A-S-H gels. Study in the ternary diagram Na2O-CaO-Al2O3-SiO2-H2O, Cement Concrete Res 41(9) (2011) 923-931.

[89] I. Garcia-Lodeiro, A. Fernandez-Jimenez, A. Palomo, Variation in hybrid cements over time. Alkaline activation of fly ash-portland cement blends, Cement Concrete Res 52 (2013) 112-122.

[90] H. Castillo, H. Collado, T. Droguett, M. Vesely, P. Garrido, S. Palma, State of the art of geopolymers: A review, E-Polymers 22(1) (2022) 108-124.

[91] Y.S. Wang, Y. Alrefaei, J.G. Dai, Silico-Aluminophosphate and Alkali-Aluminosilicate Geopolymers: A Comparative Review, Front Mater 6 (2019) 106.

[92] S. Qaidi, H.M. Najm, S.M. Abed, H.U. Ahmed, H. Al Dughaishi, J. Al Lawati, M.M. Sabri, F. Alkhatib, A. Milad, Fly Ash-Based Geopolymer Composites: A Review of the Compressive Strength and Microstructure Analysis, Materials 15(20) (2022) 7098.

[93] T. Yang, X. Yao, Z.H. Zhang, H. Wang, Mechanical property and structure of alkali-activated fly ash and slag blends, J Sustain Cem-Based 1(4) (2012) 167-178.

[94] A. Fernandez-Jimenez, A. Palomo, I. Sobrados, J. Sanz, The role played by the reactive alumina content in the alkaline activation of fly ashes, Micropor Mesopor Mat 91(1-3) (2006) 111-119.

[95] M. Criado, A. Fernandez-Jimenez, A. Palomo, Alkali activation of fly ash. Part III: Effect of curing conditions on reaction and its graphical description, Fuel 89(11) (2010) 3185-3192.

[96] F. Lolli, H. Manzano, J.L. Provis, M.C. Bignozzi, E. Masoero, Atomistic Simulations of Geopolymer Models: The Impact of Disorder on Structure and Mechanics, Acs Appl Mater Inter 10(26) (2018) 22809-22820.

[97] S. Le Roux, V. Petkov, ISAACS - interactive structure analysis of amorphous and crystalline systems, J Appl Crystallogr 43 (2010) 181-185.

[98] S.J. Louisnathan, R.J. Hill, G.V. Gibbs, Tetrahedral Bond Length Variations in Sulfates, Phys Chem Miner 1(1) (1977) 53-69.

[99] X.L. Yuan, A. Cormack, Si-O-Si bond angle and torsion angle distribution in vitreous silica and sodium silicate glasses, J Non-Cryst Solids 319(1-2) (2003) 31-43.

[100] M. Torres-Carrasco, F. Puertas, Alkaline activation of different aluminosilicates as an alternative to Portland cement: alkali activated cements or geopolymers, Rev Ing Constr 32(2) (2017) 5-12.

[101] V. Smilauer, P. Hlavacek, F. Skvara, R. Sulc, L. Kopecky, J. Nemecek, Micromechanical multiscale model for alkali activation of fly ash and metakaolin, J Mater Sci 46(20) (2011) 6545-6555.

[102] G.W. Scherer, Structure and properties of gels, Cement Concrete Res 29(8) (1999) 1149-1157.

[103] S.K. Nath, S. Kumar, Role of particle fineness on engineering properties and microstructure of fly ash derived geopolymer, Constr Build Mater 233 (2020) 117294.

[104] B. Aouan, S. Alehyen, M. Fadil, M. El Alouani, H. Saufi, M. Taibi, Characteristics, microstructures, and optimization of the geopolymer paste based on three aluminosilicate materials using a mixture design methodology, Constr Build Mater 384 (2023) 131475.

[105] M. El Alouani, S. Alehyen, H. El Hadki, H. Saufi, A. Elhalil, O.K. Kabbaj, M. Taibi, Synergetic influence between adsorption and photodegradation of Rhodamine B using synthesized fly ash based inorganic polymer, Surf Interfaces 24 (2021) 101136.

[106] S.Q. Ruan, S.K. Chen, Y.J. Zhang, J.X. Mao, D.M. Yan, Y. Liu, X.F. Liu, H. Hosono, Molecular-Level Hybridized Hydrophobic Geopolymer Ceramics for Corrosion Protection, Chem Mater (2023) 1735-1744.

[107] M.J.A. Qomi, F.J. Ulm, R.J.M. Pellenq, Evidence on the Dual Nature of Aluminum in the Calcium-Silicate-Hydrates Based on Atomistic Simulations, J Am Ceram Soc 95(3) (2012) 1128-1137.

[108] S.A. Hamid, The Crystal-Structure of the 11-a Natural Tobermorite Ca2.25[Si3O7.5(OH)1.5]]·1H2O, Z Kristallogr 154(3-4) (1981) 189-198.

[109] P. Faucon, J.M. Delaye, J. Virlet, J.F. Jacquinot, F. Adenot, Study of the structural properties of the C-S-H(I) by molecular dynamics simulation, Cement Concrete Res 27(10) (1997) 1581-1590.

[110] S. Merlino, E. Bonaccorsi, T. Armbruster, The real structure of tobermorite 11 angstrom: normal and anomalous forms, OD character and polytypic modifications, Eur J Mineral 13(3) (2001) 577-590.

[111] T. Mitsuda, H.F.W. Taylor, Normal and Anomalous Tobermorites, Mineral Mag 42(322) (1978) 229-235.

[112] H. Stade, D. Muller, On the Coordination of Al in Ill-Crystallized C-S-H Phases Formed by Hydration of Tricalcium Silicate and by Precipitation Reactions at Ambient-Temperature, Cement Concrete Res 17(4) (1987) 553-561.

[113] P. Faucon, A. Delagrave, J.C. Petit, C. Richet, J.M. Marchand, H. Zanni, Aluminum incorporation in calcium silicate hydrates (C-S-H) depending on their Ca/Si ratio, J Phys Chem B 103(37) (1999) 7796-7802.

[114] G.K. Sun, J.F. Young, R.J. Kirkpatrick, The role of Al in C-S-H: NMR, XRD, and compositional results for precipitated samples, Cement Concrete Res 36(1) (2006) 18-29.

[115] M.D. Andersen, H.J. Jakobsen, J. Skibsted, Incorporation of aluminum in the calcium silicate hydrate (C-S-H) of hydrated Portland cements: A high-field Al-27 and Si-29 MAS NMR Investigation, Inorg Chem 42(7) (2003) 2280-2287.

[116] A. Rawal, B.J. Smith, G.L. Athens, C.L. Edwards, L. Roberts, V. Gupta, B.F. Chmelka, Molecular Silicate and Aluminate Species in Anhydrous and Hydrated Cements, J Am Chem Soc 132(21) (2010) 7321-7337.

[117] M.D. Andersen, H.J. Jakobsen, J. Skibsted, A new aluminium-hydrate species in hydrated Portland cements characterized by Al-27 and Si-29 MAS NMR spectroscopy, Cement Concrete Res 36(1) (2006) 3-17.

[118] X. Pardal, I. Pochard, A. Nonat, Experimental study of Si-Al substitution in calcium-silicate-hydrate (C-S-H) prepared under equilibrium conditions, Cement Concrete Res 39(8) (2009) 637-643.

[119] I.G. Richardson, A.R. Brough, R. Brydson, G.W. Groves, C.M. Dobson, Location of Aluminum in Substituted Calcium Silicate Hydrate (C-S-H) Gels as Determined by Si-29 and Al-27 Nmr and Eels, J Am Ceram Soc 76(9) (1993) 2285-2288.

[120] J. Yang, D.S. Hou, Q.J. Ding, Structure, Dynamics, and Mechanical Properties of Cross-Linked Calcium Aluminosilicate Hydrate: A Molecular Dynamics Study, Acs Sustain Chem Eng 6(7) (2018) 9403-9417.

[121] J. Skibsted, M.D. Andersen, The Effect of Alkali Ions on the Incorporation of Aluminum in the Calcium Silicate Hydrate (C-S-H) Phase Resulting from Portland Cement Hydration Studied by Si-29 MAS NMR, J Am Ceram Soc 96(2) (2013) 651-656.

[122] A.A. Mohammed, H.U. Ahmed, A. Mosavi, Survey of Mechanical Properties of Geopolymer Concrete: A Comprehensive Review and Data Analysis, Materials 14(16) (2021) 4690.

[123] S.A. Bernal, J.L. Provis, B. Walkley, R.S. Nicolas, J.D. Gehman, D.G. Brice, A.R. Kilcullen, P. Duxson, J.S.J. van Deventer, Gel nanostructure in alkali-activated binders based on slag and fly ash, and effects of accelerated carbonation, Cement Concrete Res 53 (2013) 127-144.

[124] B. Walkley, R. San Nicolas, M.A. Sani, G.J. Rees, J.V. Hanna, J.S.J. van Deventer, J.L. Provis, Phase evolution of C-(N)-A-S-H/N-A-S-H gel blends investigated via alkali-activation of synthetic calcium aluminosilicate precursors, Cement Concrete Res 89 (2016) 120-135.

[125] P. Chindaprasirt, P. De Silva, K. Sagoe-Crentsil, S. Hanjitsuwan, Effect of SiO2 and Al2O3 on the setting and hardening of high calcium fly ash-based geopolymer systems, J Mater Sci 47(12) (2012) 4876-4883.

[126] I. Garcia-Lodeiro, A. Palomo, A. Fernández-Jiménez, An overview of the chemistry of alkali-activated cement-based binders, Handbook of alkali-activated cements, mortars and concretes (2015) 19-47.

[127] H.M. Jennings, A model for the microstructure of calcium silicate hydrate in cement paste, Cement Concrete Res 30(1) (2000) 101-116.

[128] P. Duxson, J.L. Provis, G.C. Lukey, S.W. Mallicoat, W.M. Kriven, J.S.J. van Deventer, Understanding the relationship between geopolymer composition, microstructure and mechanical properties, Colloid Surface A 269(1-3) (2005) 47-58.

[129] E. Kapeluszna, L. Kotwica, A. Rózycka, L. Golek, Incorporation of Al in C-A-S-H gels with various Ca/Si and Al/Si ratio: Microstructural and structural characteristics with DTA/TG, XRD, FTIR and TEM analysis, Constr Build Mater 155 (2017) 643-653.

[130] M.U. Kankia, L. Baloo, N. Danlami, N.A. Zawawi, A. Bello, S.I. Muhammad, Microstructural Analysis and Compressive Strength of Fly Ash and Petroleum Sludge Ash Geopolymer Mortar under High Temperatures, Sustainability-Basel 15(12) (2023) 9846.

[131] I. Zafar, K. Rashid, R. Hameed, K. Aslam, Correlating Reactivity of Fly Ash with Mechanical Strength of the Resultant Geopolymer, Arab J Sci Eng 47(10) (2022) 12469-12478.

[132] C. Kuenzel, N. Ranjbar, Dissolution mechanism of fly ash to quantify the reactive aluminosilicates in geopolymerisation, Resour Conserv Recy 150 (2019) 104421.

[133] A. Fernández-Jiménez, A. Palomo, M. Criado, Microstructure development of alkali-activated fly ash cement:: a descriptive model, Cement Concrete Res 35(6) (2005) 1204-1209.

[134] J.L. Provis, J.S.J. van Deventer, Geopolymerisation kinetics. 2. Reaction kinetic modelling, Chem Eng Sci 62(9) (2007) 2318-2329.

[135] J.J. Thomas, H.M. Jennings, A colloidal interpretation of chemical aging of the C-S-H gel and its effects on the properties of cement paste, Cement Concrete Res 36(1) (2006) 30-38.

[136] A. Hajimohammadi, J.S.J. van Deventer, Dissolution behaviour of source materials for synthesis of geopolymer binders: A kinetic approach, Int J Miner Process 153 (2016) 80-86.

[137] R.R. Lloyd, J.L. Provis, J.S.J. van Deventer, Microscopy and microanalysis of inorganic polymer cements. 1: remnant fly ash particles, J Mater Sci 44(2) (2009) 608-619.

[138] D.W. Zhang, X.M. Sun, H. Li, Relationship between macro-properties and amorphous gel of FA-based AAMs with different curing conditions after elevated temperature, Ceram Int 49(11) (2023) 17453-17467.

[139] M. Criado, A. Fernández-Jiménez, A. Palomo, I. Sobrados, J. Sanz, Effect of the Sio/NaO ratio on the alkali activation of fly ash. Part II: Si MAS-NMR Survey, Micropor Mesopor Mat 109(1-3) (2008) 525-534.

[140] A. Palomo, S. Alonso, A. Femandez-Jiménez, Alkaline activation of fly ashes:: NMR study of the reaction products, J Am Ceram Soc 87(6) (2004) 1141-1145.

[141] W.L. Tu, G.H. Fang, B.Q. Dong, M.Z. Zhang, Multiscale study of microstructural evolution in alkali-activated fly ash-slag paste at elevated temperatures, Cement Concrete Comp 143 (2023) 105258.

[142] M.R. Ahmad, M. Khan, A.G. Wang, Z.H. Zhang, J.G. Dai, Alkali-activated materials partially activated using flue gas residues: An insight into reaction products, Constr Build Mater 371 (2023) 130760.

[143] M. Jin, Y.F. Ma, W.W. Li, J.L. Huang, Y. Yan, H.Y. Zeng, C. Lu, J.P. Liu, Multi-scale investigation on composition-structure of C-(A)-S-H with different Al/Si ratios under attack of decalcification action, Cement Concrete Res 172 (2023) 107251.

[144] X. Liu, P. Feng, W. Li, G.Q. Geng, J.L. Huang, Y. Gao, S. Mu, J.X. Hong, Effects of pH on the nano/micro structure of calcium silicate hydrate (C-S-H) under sulfate attack, Cement Concrete Res 140 (2021) 106306.

[145] X. Liu, P. Feng, Y.X. Cai, X.H. Yu, Q. Liu, Carbonation behaviors of calcium silicate hydrate (C-S-H): Effects of aluminum, Constr Build Mater 325 (2022) 126825.

[146] V. Kanchanason, J. Plank, Role of pH on the structure, composition and morphology of C-S-H-PCE nanocomposites and their effect on early strength development of Portland cement, Cement Concrete Res 102 (2017) 90-98.

[147] E. L'Hôpital, B. Lothenbach, D.A. Kulik, K. Scrivener, Influence of calcium to silica ratio on aluminium uptake in calcium silicate hydrate, Cement Concrete Res 85 (2016) 111-121.

[148] A.K. Mohamed, P. Moutzouri, P. Berruyer, B.J. Walder, J. Siramanont, M. Harris, M. Negroni, S.C. Galmarini, S.C. Parker, K.L. Scrivener, L. Emsley, P. Bowen, The Atomic-Level Structure of Cementitious Calcium Aluminate Silicate Hydrate, J Am Chem Soc 142(25) (2020) 11060-11071.

[149] X. Pardal, F. Brunet, T. Charpentier, I. Pochard, A. Nonat, 27Al and 29Si Solid-State NMR Characterization of Calcium Aluminosilicate-Hydrate, Inorg Chem 51(3) (2012) 1827-1836.

[150] K.Y. Liao, A. Masuno, A. Taguchi, H. Moriwake, H. Inoue, T. Mizoguchi, Revealing Spatial Distribution of Al-Coordinated Species in a Phase-Separated Aluminosilicate Glass by STEM-EELS, J Phys Chem Lett 11(22) (2020) 9637-9642.

[151] E. L'Hopital, B. Lothenbach, G. Le Saout, D. Kulik, K. Scrivener, Incorporation of aluminium in calcium-silicate-hydrates, Cement Concrete Res 75 (2015) 91-103.

[152] E.T. Rodriguez, I.G. Richardson, L. Black, E. Boehm-Courjault, A. Nonat, J. Skibsted, Composition, silicate anion structure and morphology of calcium silicate hydrates (C-S-H) synthesised by silica-lime reaction and by controlled hydration of tricalcium silicate (C3S), Adv Appl Ceram 114(7) (2015) 362-371.

[153] Q. Zheng, J.Y. Jiang, X.L. Li, K.C. Bustillo, H.M. Zheng, TEM observation of calcium silicate hydrate nanostructure at high temperatures, Cement Concrete Res 149 (2021) 106579.

[154] F. Puertas, M. Palacios, H. Manzano, J.S. Dolado, A. Rico, J. Rodriguez, A model for the C-A-S-H gel formed in alkali-activated slag cements, J Eur Ceram Soc 31(12) (2011) 2043-2056.

[155] M. Vandamme, F.J. Ulm, Nanogranular origin of concrete creep, P Natl Acad Sci USA 106(26) (2009) 10552-10557.

[156] G. Constantinides, Invariant mechanical properties of calcium-silicate-hydrates (CHS) in cement-based materials: instrumented nanoindentation and microporomechanical modeling, Massachusetts Institute of Technology, 2006.

[157] A. Cuesta, I. Santacruz, A.G. De la Torre, M. Dapiaggi, J.D. Zea-Garcia, M.A.G. Aranda, Local structure and Ca/Si ratio in C-S-H gels from hydration of blends of tricalcium silicate and silica fume, Cement Concrete Res 143 (2021) 106405.

[158] J. Yang, Q.J. Ding, G.Z. Zhang, D.S. Hou, M.Y. Zhao, J.R. Cao, Effect of sulfate attack on the composition and micro-mechanical properties of C-A-S-H gel in cement-slag paste: A combined study of nanoindentation and SEM-EDS, Constr Build Mater 345 (2022) 128275.

[159] N. Marjanovic, M. Komljenovic, Z. Bascarevic, V. Nikolic, R. Petrovic, Physical-mechanical and microstructural properties of alkali-activated fly ash-blast furnace slag blends, Ceram Int 41(1) (2015) 1421-1435.

[160] P.T. Durdzinski, C.F. Dunant, M. Ben Haha, K.L. Scrivener, A new quantification method based on SEM-EDS to assess fly ash composition and study the reaction of its individual components in hydrating cement paste, Cement Concrete Res 73 (2015) 111-122.

[161] B.S. Gebregziabiher, R. Thomas, S. Peethamparan, Very early-age reaction kinetics and microstructural development in alkali-activated slag, Cement Concrete Comp 55 (2015) 91-102.

[162] S. Puligilla, P. Mondal, Role of slag in microstructural development and hardening of fly ash-slag geopolymer, Cement Concrete Res 43 (2013) 70-80.

[163] S. Bae, C. Meral, J.E. Oh, J. Moon, M. Kunz, P.J.M. Monteiro, Characterization of morphology and hydration products of high-volume fly ash paste by monochromatic scanning x-ray micro-diffraction (μ-SXRD), Cement Concrete Res 59 (2014) 155-164.

[164] T.H.Y. Nguyen, K. Tsuchiya, D. Atarashi, Microstructure and composition of fly ash and ground granulated blast furnace slag cement pastes in 42-month cured samples, Constr Build Mater 191 (2018) 114-124.

[165] R.T. Chancey, P. Stutzman, M.C.G. Juenger, D.W. Fowler, Comprehensive phase characterization of crystalline and amorphous phases of a Class F fly ash, Cement Concrete Res 40(1) (2010) 146-156.

[166] F. Puertas, M. Palacios, H. Manzano, J.S. Dolado, A. Rico, J. Rodríguez, A model for the C-A-S-H gel formed in alkali-activated slag cements, J Eur Ceram Soc 31(12) (2011) 2043-2056.

[167] Y. Luo, H.J.H. Brouwers, Q.L. Yu, Understanding the gel compatibility and thermal behavior of alkali activated Class F fly ash/ladle slag: The underlying role of Ca availability, Cement Concrete Res 170 (2023) 107198.

[168] I. García-Lodeiro, A. Fernández-Jiménez, A. Palomo, Variation in hybrid cements over time. Alkaline activation of fly ash-portland cement blends, Cement Concrete Res 52 (2013) 112-122.

[169] I. García-Lodeiro, A. Fernández-Jiménez, A. Palomo, D.E. Macphee, Effect of Calcium Additions on N-A-S-H Cementitious Gels, J Am Ceram Soc 93(7) (2010) 1934-1940.

[170] J.S.J. van Deventer, R.S. Nicolas, I. Ismail, S.A. Bernal, D.G. Brice, J.L. Provis, Microstructure and durability of alkali-activated materials as key parameters for standardization, J Sustain Cem-Based 4(2) (2015) 116-128.

[171] M.R. Ahmad, L.P. Qian, Y. Fang, A.G. Wang, J.G. Dai, A multiscale study on gel composition of hybrid alkali-activated materials partially utilizing air pollution control residue as an activator, Cement Concrete Comp 136 (2023) 104856.

[172] I. García-Lodeiro, O. Maltseva, A. Palomo, A. Fernández-Jiménez, Hybrid Alkaline Cements. Part I: Fundamentals, Rev Rom Mater 42(4) (2012) 330-335.

[173] A. Keulen, Q.L. Yu, S. Zhang, S. Grünewald, Effect of admixture on the pore structure refinement and enhanced performance of alkali-activated fly ash-slag concrete, Constr Build Mater 162 (2018) 27-36.

[174] S.K. Chen, S.Q. Ruan, Q. Zeng, Y. Liu, M.Z. Zhang, Y. Tian, D.M. Yan, Pore structure of geopolymer materials and its correlations to engineering properties: A review, Constr Build Mater 328 (2022) 127064.

[175] D.M. Yan, S.K. Chen, Q. Zeng, S.L. Xu, H.D. Li, Correlating the elastic properties of metakaolin-based geopolymer with its composition, Mater Design 95 (2016) 306-318.

[176] T. Yang, H.J. Zhu, Z.H. Zhang, Influence of fly ash on the pore structure and shrinkage characteristics of metakaolin-based geopolymer pastes and mortars, Constr Build Mater 153 (2017) 284-293.

[177] J.L. Provis, R.J. Myers, C.E. White, V. Rose, J.S.J. van Deventer, X-ray microtomography shows pore structure and tortuosity in alkali-activated binders, Cement Concrete Res 42(6) (2012) 855-864.

[178] Z.H. Zhang, J.L. Provis, A. Reid, H. Wang, Fly ash-based geopolymers: The relationship between composition, pore structure and efflorescence, Cement Concrete Res 64 (2014) 30-41.

[179] D. Ravikumar, S. Peethamparan, N. Neithalath, Structure and strength of NaOH activated concretes containing fly ash or GGBFS as the sole binder, Cement Concrete Comp 32(6) (2010) 399-410.

[180] Y. Luo, K.M. Klima, H.J.H. Brouwers, Q.L. Yu, Effects of ladle slag on Class F fly ash geopolymer: Reaction mechanism and high temperature behavior, Cement Concrete Comp 129 (2022) 104468.

[181] M. Nedeljkovic, K. Arbi, Y. Zuo, G. Ye, Microstructural and mineralogical analysis of alkali activated fly ash-slag pastes, Microdurability 2016: the International Rilem Conference on Microstructure Related Durability of Cementitious Composites, 2016.

[182] J.P. Ollivier, J.C. Maso, B. Bourdette, Interfacial Transition Zone in Concrete, Adv Cem Based Mater 2(1) (1995) 30-38.

[183] A. Bentur, M.G. Alexander, R.T. Comm, A review of the work of the RILEM TC 159-ETC: Engineering of the interfacial transition zone in cementitious composites, Mater Struct 33(226) (2000) 82-87.

[184] K.L. Scrivener, A.K. Crumbie, P. Laugesen, The interfacial transition zone (ITZ) between cement paste and aggregate in concrete, Interface Sci 12(4) (2004) 411-421.

[185] Z.Y. Luo, W.G. Li, K.J. Wang, A. Castel, S.P. Shah, Comparison on the properties of ITZs in fly ash-based geopolymer and Portland cement concretes with equivalent flowability, Cement Concrete Res 143 (2021) 106392.

[186] H.S. Wong, M. Zobel, N.R. Buenfeld, R.W. Zimmerman, Influence of the interfacial transition zone and microcracking on the diffusivity, permeability and sorptivity of cement-based materials after drying, Mag Concrete Res 61(8) (2009) 571-589.

[187] Z.Y. Luo, W.G. Li, K.J. Wang, S.P. Shah, D.C. Sheng, Nano/micromechanical characterisation and image analysis on the properties and heterogeneity of ITZs in geopolymer concrete, Cement Concrete Res 152 (2022) 106677.

[188] W.G. Li, Z.Y. Luo, Y.X. Gan, K.J. Wang, S.P. Shah, Nanoscratch on mechanical properties of interfacial transition zones (ITZs) in fly ash-based geopolymer composites, Compos Sci Technol 214 (2021) 109001.

[189] J.L. Provis, G.C. Lukey, J.S.J. van Deventer, Do geopolymers actually contain nanocrystalline zeolites? A reexamination of existing results, Chem Mater 17(12) (2005) 3075-3085.

[190] Z.Y. Luo, W.G. Li, Y.X. Gan, K. Mendu, S.P. Shah, Maximum likelihood estimation for nanoindentation on sodium aluminosilicate hydrate gel of geopolymer under different silica modulus and curing conditions, Compos Part B-Eng 198 (2020) 108185.

[191] F.J. Ulm, G. Constantinides, F.H. Heukamp, Is concrete a poromechanics material? - A multiscale investigation of poroelastic properties, Mater Struct 37(265) (2004) 43-58.

[192] J. Wongpa, K. Kiattikomol, C. Jaturapitakkul, P. Chindaprasirt, Compressive strength, modulus of elasticity, and water permeability of inorganic polymer concrete, Mater Design 31(10) (2010) 4748-4754.

[193] R. Sulc, T. Strnad, F. Skvara, P. Svoboda, Z. Bittnar, V. Smilauer, L. Kopecký, Concrete Based on Fly Ash Alumosilicate Polymers, Journal of Environmental Science and Engineering 5(6) (2011) 728-735.

[194] P. Duxson, A. Fernandez-Jimenez, J.L. Provis, G.C. Lukey, A. Palomo, J.S.J. van Deventer, Geopolymer technology: the current state of the art, J Mater Sci 42(9) (2007) 2917-2933.

[195] J.S.J. van Deventer, J.L. Provis, P. Duxson, G.C. Lukey, Reaction mechanisms in the geopolymeric conversion of inorganic waste to useful products, J Hazard Mater 139(3) (2007) 506-513.

[196] H. Manzano, J.S. Dolado, M. Griebel, J. Hamaekers, A molecular dynamics study of the aluminosilicate chains structure in Al-rich calcium silicate hydrated (C-S-H) gels, Phys Status Solidi A 205(6) (2008) 1324-1329.

[197] I.G. Richardson, G.W. Groves, The structure of the calcium silicate hydrate phases present in hardened pastes of white Portland cement blast-furnace slag blends, J Mater Sci 32(18) (1997) 4793-4802.

[198] Z.Y. Luo, W.G. Li, Y.X. Gan, K. Mendu, S.P. Shah, Applying grid nanoindentation and maximum likelihood estimation for N-A-S-H gel in geopolymer paste: Investigation and discussion, Cement Concrete Res 135 (2020) 106112.

[199] G.A. Lyngdoh, S. Nayak, N.M.A. Krishnan, S. Das, Fracture toughness of fly ash-based geopolymer gels: Evaluations using nanoindentation experiment and molecular dynamics simulation, Constr Build Mater 262 (2020) 120797.

[200] R.Z. Si, S.C. Guo, Q.L. Dai, J.Q. Wang, Atomic-structure, microstructure and mechanical properties of glass powder modified metakaolin-based geopolymer, Constr Build Mater 254 (2020) 119303.

[201] E. Kamseu, A.T. Akono, A. Nana, R.C. Kaze, C. Leonelli, Performance of geopolymer composites made with feldspathic solid solutions: Micromechanics and microstructure, Cement Concrete Comp 124 (2021) 104241.

[202] Z.Y. Luo, W.G. Li, Y.X. Gan, X.Z. He, A. Castel, D.C. Sheng, Nanoindentation on micromechanical properties and microstructure of geopolymer with nano-SiO and nano-TiO, Cement Concrete Comp 117 (2021) 103883.

[203] Z.Y. Luo, W.G. Li, P.R. Li, K.J. Wang, S.P. Shah, Investigation on effect of nanosilica dispersion on the properties and microstructures of fly ash-based geopolymer composite, Constr Build Mater 282 (2021) 122690.

[204] H. Alanazi, Y.R. Kim, J. Hu, D.N. Little, J.S. Jung, Multiscale Characterization of Fly Ash-Based Geopolymer and Type V Portland Cement Exposed to MgSO, J Mater Civil Eng 34(6) (2022) 04022095.

[205] P.S. Deb, M.N.N. Khan, P.K. Sarker, S. Barbhuiya, Nanomechanical characterization of ambient-cured fly ash geopolymers containing nanosilica, J Sustain Cem-Based 11(3) (2022) 164-174.

[206] M. Lizcano, H.S. Kim, S. Basu, M. Radovic, Mechanical properties of sodium and potassium activated metakaolin-based geopolymers, J Mater Sci 47(6) (2012) 2607-2616.

[207] M.R. Sadat, S. Bringuier, A. Asaduzzaman, K. Muralidharan, L. Zhang, A molecular dynamics study of the role of molecular water on the structure and mechanics of amorphous geopolymer binders, J Chem Phys 145(13) (2016) 134706.

[208] X.T. Xing, B.H. Wang, H. Liu, S.J. Luo, S.Z. Wang, J.X. Wei, W.T. Xu, Q.J. Yu, The mechanism of silane-grafted sodium polyacrylate on the toughening of slag-based geopolymer: an insight from macroscopic-microscopic mechanical properties, J Mater Sci 58(21) (2023) 8757-8778.

[209] J.E. Oh, P.J.M. Monteiro, S.S. Jun, S. Choi, S.M. Clark, The evolution of strength and crystalline phases for alkali-activated ground blast furnace slag and fly ash-based geopolymers, Cement Concrete Res 40(2) (2010) 189-196.

[210] X. Chen, G.R. Zhu, J. Wang, Q. Chen, Effect of polyacrylic resin on mechanical properties of granulated blast furnace slag based geopolymer, J Non-Cryst Solids 481 (2018) 4-9.

[211] B. Mast, S. Fransis, B. Vandoren, A. Cambriani, W. Schroeyers, Y. Pontikes, P. Samyn, S. Schreurs, Micromechanical and microstructural analysis of Fe-rich plasma slag-based inorganic polymers, Cement Concrete Comp 118 (2021) 103968.

[212] J. Nemecek, V. Smilauer, L. Kopecky, Nanoindentation characteristics of alkali-activated aluminosilicate materials, Cement Concrete Comp 33(2) (2011) 163-170.

[213] R.L. Cao, Z.J. Jia, S.Q. Zhang, C. Chen, Y.Y. Gao, Y.M. Zhang, Effect of low-calcium and high-magnesium ferronickel slag on the microstructure and micromechanical properties of alkali-activated blended ground granulated blast furnace slag, Constr Build Mater 406 (2023) 133421.

[214] Z.J. Jia, R.L. Cao, S.Q. Zhang, C. Chen, Y.M. Zhang, Insights into the microstructure and mechanical properties evolution of hydration products in cementitious materials incorporating GGBFS, J Sustain Cem-Based 12(4) (2023) 403-414.

[215] I.G. Richardson, S. Li, Composition and structure of an 18-year-old 5M KOH-activated ground granulated blast-furnace slag paste, Constr Build Mater 168 (2018) 404-411.

[216] A.R. Brough, A. Atkinson, Sodium silicate-based, alkali-activated slag mortars Part I. Strength, hydration and microstructure, Cement Concrete Res 32(6) (2002) 865-879.

[217] F. Puertas, A. Fernández-Jiménez, Mineralogical and microstructural characterisation of alkali-activated fly ash/slag pastes, Cement Concrete Comp 25(3) (2003) 287-292.

[218] R.J. Thomas, B.S. Gebregziabiher, A. Giffin, S. Peethamparan, Micromechanical properties of alkali-activated slag cement binders, Cement Concrete Comp 90 (2018) 241-256.

[219] Z.J. Jia, C. Chen, H.Y. Zhou, Y.M. Zhang, The characteristics and formation mechanism of the dark rim in alkali-activated slag, Cement Concrete Comp 112 (2020) 103682.

[220] U. Javed, F.U.A. Shaikh, P.K. Sarker, A comprehensive micro-nano investigative approach to study the development of aluminosilicate gel in binary blends of lithium slag geopolymer, Cement Concrete Comp 145 (2024) 105338.

[221] H. Lee, V. Vimonsatit, P. Chindaprasirt, Mechanical and micromechanical properties of alkali activated fly-ash cement based on nano-indentation, Constr Build Mater 107 (2016) 95-102.

[222] Y. Ma, G. Ye, J. Hu, Micro-mechanical properties of alkali-activated fly ash evaluated by nanoindentation, Constr Build Mater 147 (2017) 407-416.

[223] M. Nedeljkovic, B. Savija, Y.B. Zuo, M. Lukovic, G. Ye, Effect of natural carbonation on the pore structure and elastic modulus of the alkali-activated fly ash and slag pastes, Constr Build Mater 161 (2018) 687-704.

[224] X. Liu, S. Nair, K. Aughenbaugh, E. van Oort, Mud-to-cement conversion of non-aqueous drilling fluids using alkali-activated fly ash, Journal of Petroleum Science and Engineering 182 (2019) 106242.

[225] R.N. Thakur, S. Ghosh, Effect of mix composition on compressive strength and microstructure of fly ash based geopolymer composites, ARPN J. Eng. Appl. Sci 4(4) (2009) 68-74.

[226] M.N.S. Hadi, H.Q. Zhang, S. Parkinson, Optimum mix design of geopolymer pastes and concretes cured in ambient condition based on compressive strength, setting time and workability, J Build Eng 23 (2019) 301-313.

[227] X. Yao, T. Yang, Z.H. Zhang, Compressive strength development and shrinkage of alkali-activated fly ash-slag blends associated with efflorescence, Mater Struct 49(7) (2016) 2907-2918.

[228] M. Chi, Y. Liu, R. Huang, Mechanical and microstructural characterization of alkali-activated materials based on fly ash and slag, International Journal of Engineering and Technology 7(1) (2015) 59.

[229] X.W. Ouyang, Y.W. Ma, Z.Y. Liu, J.J. Liang, G. Ye, Effect of the Sodium Silicate Modulus and Slag Content on Fresh and Hardened Properties of Alkali-Activated Fly Ash/Slag, Minerals-Basel 10(1) (2020) 15.

[230] S.Q. Ruan, Y.L. Qiu, R.F. Gao, S.K. Chen, H. Qian, Y. Liu, D.M. Yan, Effect of organosilicone on the reaction process of functionalized geopolymers, J Build Eng 76 (2023) 107348.

[231] A.M. Rashad, Performance of autoclaved alkali-activated metakaolin pastes blended with micro-size particles derivative from dehydroxylation of kaolinite, Constr Build Mater 248 (2020) 118671.

[232] A.M. Rashad, A.S. Ouda, D.M. Sadek, Behavior of Alkali-Activated Metakaolin Pastes Blended with Quartz Powder Exposed to Seawater Attack, J Mater Civil Eng 30(8) (2018) 04018159.

[233] W. Zhang, X. Yao, T. Yang, C. Liu, Z.H. Zhang, Increasing mechanical strength and acid resistance of geopolymers by incorporating different siliceous materials, Constr Build Mater 175 (2018) 411-421.

[234] M. Ben Haha, B. Lothenbach, G. Le Saout, F. Winnefeld, Influence of slag chemistry on the hydration of alkali-activated blast-furnace slag - Part I: Effect of MgO, Cement Concrete Res 41(9) (2011) 955-963.

[235] M. Nili, A. Ehsani, Investigating the effect of the cement paste and transition zone on strength development of concrete containing nanosilica and silica fume, Mater Design 75 (2015) 174-183.

[236] P.G. Allison, C.A. Weiss, R.D. Moser, A.J. Diaz, O.G. Rivera, S.S. Holton, Nanoindentation and SEM/EDX characterization of the geopolymer-to-steel interfacial transition zone for a reactive porcelain enamel coating, Compos Part B-Eng 78 (2015) 131-137.

[237] M. Khedmati, Y.R. Kim, J.A. Turner, H. Alanazi, C. Nguyen, An integrated microstructural-nanomechanical-chemical approach to examine material-specific characteristics of cementitious interphase regions, Mater Charact 138 (2018) 154-164.

[238] M. Khedmati, Y.R. Kim, J.A. Turner, Investigation of the interphase between recycled aggregates and cementitious binding materials using integrated microstructural-nanomechanical-chemical characterization, Compos Part B-Eng 158 (2019) 218-229.

[239] H. Peng, C. Cui, C.S. Cai, Y. Liu, Z. Liu, Microstructure and microhardness property of the interface between a metakaolin/GGBFS-based geopolymer paste and granite aggregate, Constr Build Mater 221 (2019) 263-273.

[240] C. Shi, P. Xie, Interface between cement paste and quartz sand in alkali-activated slag mortars, Cement Concrete Res 28(6) (1998) 887-896.

[241] Y. Ding, J.G. Dai, C.J. Shi, Fracture properties of alkali-activated slag and ordinary Portland cement concrete and mortar, Constr Build Mater 165 (2018) 310-320.

[242] Z.Y. Luo, W.G. Li, K.J. Wang, S.P. Shah, Research progress in advanced nanomechanical characterization of cement-based materials, Cement Concrete Comp 94 (2018) 277-295.

[243] W.K.W. Lee, J.S.J. van Deventer, The interface between natural siliceous aggregates and geopolymers, Cement Concrete Res 34(2) (2004) 195-206.

[244] T. Ji, Q. Gao, W. Zheng, X. Lin, H.-C. Wu, Interfacial transition zone of alkali-activated slag concrete, Aci Mater J 114(3) (2017) 347.

[245] S.A. Bernal, R.M. de Gutiérrez, A.L. Pedraza, J.L. Provis, E.D. Rodriguez, S. Delvasto, Effect of binder content on the performance of alkali-activated slag concretes, Cement Concrete Res 41(1) (2011) 1-8.

[246] R.L. Cao, S.Q. Zhang, N. Banthia, Y.M. Zhang, Z.H. Zhang, Interpreting the early-age reaction process of alkali-activated slag by using combined embedded ultrasonic measurement, thermal analysis, XRD, FTIR and SEM, Compos Part B-Eng 186 (2020) 107840.

[247] S.K. Nath, S. Kumar, Reaction kinetics, microstructure and strength behavior of alkali activated silico-manganese (SiMn) slag - Fly ash blends, Constr Build Mater 147 (2017) 371-379.

[248] Y. Jin, D. Stephan, The unusual solidification process of alkali activated slag and its relationship with the glass structure of the slag, Cement Concrete Res 121 (2019) 1-10.

[249] L.J. Kong, Z.R. Fan, J.T. Lu, L.Y. Zhang, Microstructure evolution of interfacial transition zone between alkali-activated fly ash/slag matrix and aggregate, Mater Struct 55(7) (2022) 203.

[250] A.W. Pope, H.M. Jennings, The Influence of Mixing on the Microstructure of the Cement Paste Aggregate Interfacial Zone and on the Strength of Mortar, J Mater Sci 27(23) (1992) 6452-6462.

[251] R.S. Nicolas, J.L. Provis, The Interfacial Transition Zone in Alkali-Activated Slag Mortars, Front Mater 2 (2015) 70.

[252] J.A. Larbi, J.M.J.M. Bijen, Effects of Water-Cement Ratio, Quantity and Fineness of Sand on the Evolution of Lime in Set Portland-Cement Systems, Cement Concrete Res 20(5) (1990) 783-794.

[253] S.K. John, Y. Nadir, K. Girija, Effect of source materials, additives on the mechanical properties and durability of fly ash and fly ash-slag geopolymer mortar: A review, Constr Build Mater 280 (2021) 122443.

[254] A.S. Albidah, Effect of partial replacement of geopolymer binder materials on the fresh and mechanical properties: A review, Ceram Int 47(11) (2021) 14923-14943.

[255] P. Chindasiriphan, P. Nuaklong, S. Keawsawasvong, C. Thongchom, T. Jirawattanasomkul, P. Jongvivatsakul, W. Tangchirapat, S. Likitlersuang, Effect of superabsorbent polymer and polypropylene fiber on mechanical performances of alkali-activated high-calcium fly ash mortar under ambient and elevated temperatures, J Build Eng 71 (2023) 106509.

[256] L.J. Kong, Z.R. Fan, W.C. Ma, J.T. Lu, Y.Z. Liu, Effect of Curing Conditions on the Strength Development of Alkali-Activated Mortar, Crystals 11(12) (2021) 1455.

[257] H. Rashidian-Dezfouli, P.R. Rangaraju, V.S.K. Kothala, Influence of selected parameters on compressive strength of geopolymer produced from ground glass fiber, Constr Build Mater 162 (2018) 393-405.

[258] M.C. Chi, R. Huang, Binding mechanism and properties of alkali-activated fly ash/slag mortars, Constr Build Mater 40 (2013) 291-298.

[259] P. Nuaklong, K. Hamcumpai, S. Keawsawasvong, S. Pethrung, P. Jongvivatsakul, S. Tangaramvong, T. Pothisiri, S. Likitlersuang, Strength and post-fire performance of fiber-reinforced alkali-activated fly ash concrete containing granite industry waste, Constr Build Mater 392 (2023) 131984.

[260] G. Nagalia, Y. Park, A. Abolmaali, P. Aswath, Compressive strength and microstructural properties of fly ash–based geopolymer concrete, J Mater Civil Eng 28(12) (2016) 04016144.

[261] S.J. Chithambaram, S. Kumar, M.M. Prasad, D. Adak, Effect of parameters on the compressive strength of fly ash based geopolymer concrete, Struct Concrete 19(4) (2018) 1202-1209.

[262] A. Esparham, A.B. Moradikhou, Factors influencing compressive strength of fly ash-based geopolymer concrete, Amirkabir Journal of Civil Engineering 53(3) (2021) 21-31.

[263] A. Kalaiyarrasi, P. Partheeban, Influence of Si/Al ratio on the compressive strength of metakaolin based geopolymers, International Journal of Earth sciences and Engineering (2016) 87-91.

[264] M.C. Chi, Mechnical Strength and Durability of Alkali-Activated Fly Ash/Slag Concrete, J Mar Sci Tech-Taiw 24(5) (2016) 958-967.

[265] S. Divvala, Early strength properties of geopolymer concrete composites: An experimental study, Materials Today: Proceedings 47 (2021) 3770-3777.

[266] Y.R. Alharbi, A.A. Abadel, A.A. Salah, O.A. Mayhoub, M. Kohail, Engineering properties of alkali activated materials reactive powder concrete, Constr Build Mater 271 (2021) 121550.

[267] M.R. Bangi, T. Horiguchi, Pore pressure development in hybrid fibre-reinforced high strength concrete at elevated temperatures, Cement Concrete Res 41(11) (2011) 1150-1156.

[268] V. Kodur, W. Khaliq, Effect of Temperature on Thermal Properties of Different Types of High-Strength Concrete (vol 23, pg 793, 2011), J Mater Civil Eng 23(12) (2011) 1764-1764.

[269] ISO-834 Fire resistance tests-elements—elements of building construction., International Standard ISO 834 (1975).

[270] ASTM E119-16a Standard Test Methods for Fire Tests of Building Construction and Materials, ASTM International (2016).

[271] KSF 2257 Method of fire resistance test for elements of building construction Korean Industrial standard (2014).

[272] JIS A 1304 Method of fire resistance test for structural parts of buildings, Japanese Industrial Standard (1982).

[273] Subyakto, B. Subiyanto, T. Hata, S. Kawai, Evaluation of fire-retardant properties of edge-jointed lumber from tropical fast-growing woods using cone calorimetry and a standard fire test, J Wood Sci 49(3) (2003) 241-247.

[274] I.K. Kwon, Y.B. Kwon, Experimental Study on the Fire Resistance of Steel Columns Protected with Fire Boards, Int J Steel Struct 12(1) (2012) 25-35.

[275] S.H. Park, K.S. Chung, S.M. Choi, A study on failure prediction and design equation of concrete filled square steel tube columns under fire condition, Int J Steel Struct 7(3) (2007) 183-191.

[276] D.D. Yang, F.Q. Liu, S.S. Huang, H. Yang, ISO 834 standard fire test and mechanism analysis of square tubed-reinforced-concrete columns, J Constr Steel Res 175 (2020) 106316.

[277] M. Ozawa, H. Morimoto, Effects of various fibres on high-temperature spalling in high-performance concrete, Constr Build Mater 71 (2014) 83-92.

[278] Y.S. Heo, J.G. Sanjayan, C.G. Han, M.C. Han, Synergistic effect of combined fibers for spalling protection of concrete in fire, Cement Concrete Res 40(10) (2010) 1547-1554.

[279] N. Yermak, P. Pliya, A.L. Beaucour, A. Simon, A. Noumowe, Influence of steel and/or polypropylene fibres on the behaviour of concrete at high temperature: Spalling, transfer and mechanical properties, Constr Build Mater 132 (2017) 240-250.

[280] Y.N. Ding, C. Zhang, M.L. Cao, Y.L. Zhang, C. Azevedo, Influence of different fibers on the change of pore pressure of self-consolidating concrete exposed to fire, Constr Build Mater 113 (2016) 456-469.

[281] D.Y. Gao, D.M. Yan, X.Y. Li, Splitting strength of GGBFS concrete incorporating with steel fiber and polypropylene fiber after exposure to elevated temperatures, Fire Safety J 54 (2012) 67-73.

[282] P. Pliya, A.L. Beaucour, A. Noumowe, Contribution of cocktail of polypropylene and steel fibres in improving the behaviour of high strength concrete subjected to high temperature, Constr Build Mater 25(4) (2011) 1926-1934.

[283] W. Khaliq, V. Kodur, Thermal and mechanical properties of fiber reinforced high performance self-consolidating concrete at elevated temperatures, Cement Concrete Res 41(11) (2011) 1112-1122.

[284] C. Bing, J.Y. Liu, Residual strength of hybrid-fiber-reinforced high-strength concrete after exposure to high temperatures, Cement Concrete Res 34(6) (2004) 1065-1069.

[285] D. Zhang, A. Dasari, K.H. Tan, On the mechanism of prevention of explosive spalling in ultra-high performance concrete with polymer fibers, Cement Concrete Res 113 (2018) 169-177.

[286] M. Ezziane, L. Molez, R. Jauberthie, D. Rangeard, Heat exposure tests on various types of fibre mortar, Eur J Environ Civ En 15(5) (2011) 715-726.

[287] X.W. Liang, C.Q. Wu, Y.K. Yang, Z.X. Li, Experimental study on ultra-high performance concrete with high fire resistance under simultaneous effect of elevated temperature and impact loading, Cement Concrete Comp 98 (2019) 29-38.

[288] A.A. Deshpande, D. Kumar, R. Ranade, Influence of high temperatures on the residual mechanical properties of a hybrid fiber-reinforced strain-hardening cementitious composite, Constr Build Mater 208 (2019) 283-295.

[289] M.R. Bangi, T. Horiguchi, Effect of fibre type and geometry on maximum pore pressures in fibre-reinforced high strength concrete at elevated temperatures, Cement Concrete Res 42(2) (2012) 459-466.

[290] J. Novak, A. Kohoutkova, Mechanical properties of concrete composites subject to elevated temperature, Fire Safety J 95 (2018) 66-76.

[291] C.S. Poon, Z.H. Shui, L. Lam, Compressive behavior of fiber reinforced high-performance concrete subjected to elevated temperatures, Cement Concrete Res 34(12) (2004) 2215-2222.

[292] F. Aslani, B. Samali, Constitutive Relationships for Steel Fibre Reinforced Concrete at Elevated Temperatures, Fire Technol 50(5) (2014) 1249-1268.

[293] F. Aslani, B. Samali, High Strength Polypropylene Fibre Reinforcement Concrete at High Temperature, Fire Technol 50(5) (2014) 1229-1247.

[294] F.U.A. Shaikh, A. Hosan, Mechanical properties of steel fibre reinforced geopolymer concretes at elevated temperatures, Constr Build Mater 114 (2016) 15-28.

[295] A. Jameran, I.S. Ibrahim, S.H.S. Yazan, S.N.A.A. Rahim, Mechanical properties of steel-polypropylene fibre reinforced concrete under elevated temperature, Procedia Engineer 125 (2015) 818-824.

[296] P.S. Bhat, V. Chang, M. Li, Effect of elevated temperature on strain-hardening engineered cementitious composites, Constr Build Mater 69 (2014) 370-380.

[297] J. Kim, G.P. Lee, D.Y. Moon, Evaluation of mechanical properties of steel-fibre-reinforced concrete exposed to high temperatures by double-punch test, Constr Build Mater 79 (2015) 182-191.

[298] S. Sanchayan, S.J. Foster, High temperature behaviour of hybrid steel-PVA fibre reinforced reactive powder concrete, Mater Struct 49(3) (2016) 769-782.

[299] K. Watanabe, M.R. Bangi, T. Horiguchi, The effect of testing conditions (hot and residual) on fracture toughness of fiber reinforced high-strength concrete subjected to high temperatures, Cement Concrete Res 51 (2013) 6-13.

[300] X. Luo, W. Sun, S.Y.N. Chan, Effect of heating and cooling regimes on residual strength and microstructure of normal strength and high-performance concrete, Cement Concrete Res 30(3) (2000) 379-383.

[301] S.Q. Yang, T.C. Ling, C.S. Poon, High temperature performance of wet-mix and dry-mix mortars prepared with different contents and size gradings of glass aggregates: Hot test and cold test, Cement Concrete Comp 108 (2020) 103548.

[302] P. Bamonte, P.G. Gambarova, Thermal and Mechanical Properties at High Temperature of a Very High-Strength Durable Concrete, J Mater Civil Eng 22(6) (2010) 545-555.

[303] P. Bamonte, P.G. Gambarova, A study on the mechanical properties of self-compacting concrete at high temperature and after cooling, Mater Struct 45(9) (2012) 1375-1387.

[304] B. Zhang, N. Bicanic, Fracture energy of high-performance concrete at high temperatures up to 450 degrees C: the effects of heating temperatures and testing conditions (hot and cold), Mag Concrete Res 58(5) (2006) 277-288.

[305] O.A. Abdulkareem, A.M.M. Al Bakri, H. Kamarudin, I.K. Nizar, A.A. Saif, Effects of elevated temperatures on the thermal behavior and mechanical performance of fly ash geopolymer paste, mortar and lightweight concrete, Constr Build Mater 50 (2014) 377-387.

[306] S. Thokchom, K.K. Mandal, S. Ghosh, Effect of Si/Al Ratio on Performance of Fly Ash Geopolymers at Elevated Temperature, Arab J Sci Eng 37(4) (2012) 977-989.

[307] S.F. Dai, L. Zhao, S.P. Peng, C.L. Chou, X.B. Wang, Y. Zhang, D. Li, Y.Y. Sun, Abundances and distribution of minerals and elements in high-alumina coal fly ash from the Jungar Power Plant, Inner Mongolia, China, Int J Coal Geol 81(4) (2010) 320-332.

[308] H. Schneider, J. Schreuer, B. Hildmann, Structure and properties of mullite - A review, J Eur Ceram Soc 28(2) (2008) 329-344.

[309] N. Kawai, K.G. Nakamura, K. Kondo, High-pressure phase transition of mullite under shock compression, J Appl Phys 96(8) (2004) 4126-4130.

[310] T. Sato, M. Ishizuka, M. Shimada, Sintering and Characterization of Mullite Alumina Composites, Ceram Int 12(2) (1986) 61-65.

[311] C. Aksel, The effect of mullite on the mechanical properties and thermal shock behaviour of alumina-mullite refractory materials, Ceram Int 29(2) (2003) 183-188.

[312] A.M. Rashad, A.S. Ouda, An investigation on alkali-activated fly ash pastes modified with quartz powder subjected to elevated temperatures, Constr Build Mater 122 (2016) 417-425.

[313] T. Alomayri, F.U.A. Shaikh, I.M. Low, Thermal and mechanical properties of cotton fabric-reinforced geopolymer composites, J Mater Sci 48(19) (2013) 6746-6752.

[314] F. Shaikh, S. Haque, Effect of nano silica and fine silica sand on compressive strength of sodium and potassium activators synthesised fly ash geopolymer at elevated temperatures, Fire Mater 42(3) (2018) 324-335.

[315] F.U.A. Shaikh, V. Vimonsatit, Compressive strength of fly-ash-based geopolymer concrete at elevated temperatures, Fire Mater 39(2) (2015) 174-188.

[316] A.M.M. Al Bakri, H. Kamarudin, M. Bnhussain, A.R. Rafiza, Y. Zarina, Effect of Na2SiO3/NaOH Ratios and NaOH Molarities on Compressive Strength of Fly-Ash-Based Geopolymer, Aci Mater J 109(5) (2012) 503-508.

[317] A. Martin, J.Y. Pastor, A. Palomo, A.F. Jimenez, Mechanical behaviour at high temperature of alkali-activated aluminosilicates (geopolymers), Constr Build Mater 93 (2015) 1188-1196.

[318] P. Rovnanik, P. Bayer, P. Rovnanikova, Characterization of alkali activated slag paste after exposure to high temperatures, Constr Build Mater 47 (2013) 1479-1487.

[319] A.M. Rashad, Y. Bai, P.A.M. Basheer, N.C. Collier, N.B. Milestone, Chemical and mechanical stability of sodium sulfate activated slag after exposure to elevated temperature, Cement Concrete Res 42(2) (2012) 333-343.

[320] H.T. Turker, M. Balcikanli, I.H. Durmus, E. Ozbay, M. Erdemir, Microstructural alteration of alkali activated slag mortars depend on exposed high temperature level, Constr Build Mater 104 (2016) 169-180.

[321] M. Lahoti, K.K. Wong, E.H. Yang, K.H. Tan, Effects of Si/Al molar ratio on strength endurance and volume stability of metakaolin geopolymers subject to elevated temperature, Ceram Int 44(5) (2018) 5726-5734.

[322] W.D.A. Rickard, L. Vickers, A. van Riessen, Performance of fibre reinforced, low density metakaolin geopolymers under simulated fire conditions, Appl Clay Sci 73 (2013) 71-77.

[323] I. Niklioc, S. Markovic, I. Jankovic-Castvan, V.V. Radmilovic, L. Karanovic, B. Babic, V.R. Radmilovic, Modification of mechanical and thermal properties of fly ash-based geopolymer by the incorporation of steel slag, Mater Lett 176 (2016) 301-305.

[324] A. Fernandez-Jimenez, A. Palomo, J.Y. Pastor, A. Martin, New Cementitious Materials Based on Alkali-Activated Fly Ash: Performance at High Temperatures, J Am Ceram Soc 91(10) (2008) 3308-3314.

[325] L. Zuda, Z. Pavlik, P. Rovnanikova, P. Bayer, R. Cerny, Properties of alkali activated aluminosilicate material after thermal load, Int J Thermophys 27(4) (2006) 1250-1263.

[326] R.P. Williams, R.D. Hart, A. van Riessen, Quantification of the Extent of Reaction of Metakaolin-Based Geopolymers Using X-Ray Diffraction, Scanning Electron Microscopy, and Energy-Dispersive Spectroscopy, J Am Ceram Soc 94(8) (2011) 2663-2670.

[327] H. Cheng-Yong, L. Yun-Ming, M.M.A. Abdullah, K. Hussin, Thermal Resistance Variations of Fly Ash Geopolymers: Foaming Responses, Sci Rep-Uk 7 (2017) 45355.

[328] S. Celikten, M. Saridemir, I.O. Deneme, Mechanical and microstructural properties of alkali-activated slag and slag plus fly ash mortars exposed to high temperature, Constr Build Mater 217 (2019) 50-61.

[329] H.Y. Zhang, G.H. Qiu, V. Kodur, Z.S. Yuan, Spalling behavior of metakaolin-fly ash based geopolymer concrete under elevated temperature exposure, Cement Concrete Comp 106 (2020) 103483.

[330] Y.J. Zhang, S. Li, Y.C. Wang, D.L. Xu, Microstructural and strength evolutions of geopolymer composite reinforced by resin exposed to elevated temperature, J Non-Cryst Solids 358(3) (2012) 620-624.

[331] T. Bakharev, Thermal behaviour of geopolymers prepared using class F fly ash and elevated temperature curing, Cement Concrete Res 36(6) (2006) 1134-1147.

[332] F. Ameri, P. Shoaei, S.A. Zareei, B. Behforouz, Geopolymers vs. alkali-activated materials (AAMs): A comparative study on durability, microstructure, and resistance to elevated temperatures of lightweight mortars, Constr Build Mater 222 (2019) 49-63.

[333] P. Duan, C.J. Yan, W. Zhou, W.J. Luo, Thermal Behavior of Portland Cement and Fly Ash-Metakaolin-Based Geopolymer Cement Pastes, Arab J Sci Eng 40(8) (2015) 2261-2269.

[334] N.Y. Mostafa, Q. Mohsen, A. El-maghraby, Characterization of low-purity clays for geopolymer binder formulation, Int J Min Met Mater 21(6) (2014) 609-619.

[335] W.R. A.V. Riessen, J. Sanjayan, Geopolymers: Structure, Processing, Properties and Industrial Applications, Woodhead Publ Mater (2009) 1-454.

[336] W.D.A. Rickard, A. van Riessen, Performance of solid and cellular structured fly ash geopolymers exposed to a simulated fire, Cement Concrete Comp 48 (2014) 75-82.

[337] S.A. Bernal, J.L. Provis, Durability of Alkali- Activated Materials: Progress and Perspectives, J Am Ceram Soc 97(4) (2014) 997-1008.

[338] K. Dombrowski, A. Buchwald, M. Weil, The influence of calcium content on the structure and thermal performance of fly ash based geopolymers, J Mater Sci 42(9) (2007) 3033-3043.

[339] Z. Pan, J.G. Sanjayan, Stress-strain behaviour and abrupt loss of stiffness of geopolymer at elevated temperatures, Cement Concrete Comp 32(9) (2010) 657-664.

[340] Y.M. Gu, Y.H. Fang, D. You, Y.F. Gong, C.H. Zhu, Properties and microstructure of alkali-activated slag cement cured at below- and about-normal temperature, Constr Build Mater 79 (2015) 1-8.

[341] H. Rahier, B. VanMele, M. Biesemans, J. Wastiels, X. Wu, Low-temperature synthesized aluminosilicate glasses .1. Low-temperature reaction stoichiometry and structure of a model compound, J Mater Sci 31(1) (1996) 71-79.

[342] W.D.A. Rickard, A. van Riessen, P. Walls, Thermal Character of Geopolymers Synthesized from Class F Fly Ash Containing High Concentrations of Iron and alpha-Quartz, Int J Appl Ceram Tec 7(1) (2010) 81-88.

[343] M. Guerrieri, J. Sanjayan, F. Collins, Residual compressive behavior of alkali-activated concrete exposed to elevated temperatures, Fire Mater 33(1) (2009) 51-62.

[344] S. Sasui, G. Kim, J. Nam, A. van Riessen, M. Hadzima-Nyarko, G. Choe, D. Suh, W. Jinwuth, Effects of waste glass sand on the thermal behavior and strength of fly ash and GGBS based alkali activated mortar exposed to elevated temperature, Constr Build Mater 316 (2022) 125864.

[345] W.D.A. Rickard, G.J.G. Gluth, K. Pistol, In-situ thermo-mechanical testing of fly ash geopolymer concretes made with quartz and expanded clay aggregates, Cement Concrete Res 80 (2016) 33-43.

[346] W.D.A. Rickard, C.S. Kealley, A. van Riessen, Thermally Induced Microstructural Changes in Fly Ash Geopolymers: Experimental Results and Proposed Model, J Am Ceram Soc 98(3) (2015) 929-939.

[347] H.Y. Zhang, V. Kodur, B. Wu, L. Cao, F. Wang, Thermal behavior and mechanical properties of geopolymer mortar after exposure to elevated temperatures, Constr Build Mater 109 (2016) 17-24.

[348] D.L.Y. Kong, J.G. Sanjayan, Damage behavior of geopolymer composites exposed to elevated temperatures, Cement Concrete Comp 30(10) (2008) 986-991.

[349] M. Saridemir, S. Celikten, Investigation of fire and chemical effects on the properties of alkali-activated lightweight concretes produced with basaltic pumice aggregate, Constr Build Mater 260 (2020) 119969.

[350] O.A. Abdulkareem, M.M.A. Abdullah, K. Hussin, K.N. Ismail, M. Binhussain, Mechanical and Microstructural Evaluations of Lightweight Aggregate Geopolymer Concrete before and after Exposed to Elevated Temperatures, Materials 6(10) (2013) 4450-4461.

[351] L. Carabba, R. Moricone, G.E. Scarponi, A. Tugnoli, M.C. Bignozzi, Alkali activated lightweight mortars for passive fire protection: A preliminary study, Constr Build Mater 195 (2019) 75-84.

[352] I.J. Merchant, D.E. Macphee, H.W. Chandler, R.J. Henderson, Toughening cement-based materials through the control of interfacial bonding, Cement Concrete Res 31(12) (2001) 1873-1880.

[353] F. Shaikh, S. Haque, Behaviour of Carbon and Basalt Fibres Reinforced Fly Ash Geopolymer at Elevated Temperatures, Int J Concr Struct M 12(1) (2018) 1-12.

[354] S. Ishak, H.S. Lee, J.K. Singh, M.A.M. Ariffin, N.H.A.S. Lim, H.M. Yang, Performance of Fly Ash Geopolymer Concrete Incorporating Bamboo Ash at Elevated Temperature, Materials 12(20) (2019) 12.

[355] S.J. Chithambaram, S. Kumar, M.M. Prasad, Thermo-mechanical characteristics of geopolymer mortar, Constr Build Mater 213 (2019) 100-108.

[356] M. Kaya, M. Uysal, K. Yilmaz, C.D. Atis, Behaviour of Geopolymer Mortars after Exposure to Elevated Temperatures, Mater Sci-Medzg 24(4) (2018) 428-436.

[357] N. Ranjbar, M. Mehrali, U.J. Alengaram, H.S.C. Metselaar, M.Z. Jumaat, Compressive strength and microstructural analysis of fly ash/palm oil fuel ash based geopolymer mortar under elevated temperatures, Constr Build Mater 65 (2014) 114-121.

[358] S. Luhar, S. Chaudhary, I. Luhar, Thermal resistance of fly ash based rubberized geopolymer concrete, J Build Eng 19 (2018) 420-428.

[359] G. Mathew, B. Joseph, Flexural behaviour of geopolymer concrete beams exposed to elevated temperatures, J Build Eng 15 (2018) 311-317.

[360] F.U.A. Shaikh, Effect of cooling on the residual mechanical properties and cracking of plain and fibrous geopolymer concretes at elevated temperatures, Struct Concrete 20(5) (2019) 1583-1595.

[361] O.G. Zhang, L. Li, T. Long, P.K. Sarker, X.S. Shi, G.C. Cai, Q.Y. Wang, The Effect of Ordinary Portland Cement Substitution on the Thermal Stability of Geopolymer Concrete, Materials 12(16) (2019) 2501.

[362] P.K. Sarker, S. Kelly, Z.T. Yao, Effect of fire exposure on cracking, spalling and residual strength of fly ash geopolymer concrete, Mater Design 63 (2014) 584-592.

[363] L. Vickers, W.D.A. Rickard, A. van Riessen, Strategies to control the high temperature shrinkage of fly ash based geopolymers, Thermochim Acta 580 (2014) 20-27.

[364] O. Topal, M.B. Karakoc, A. Ozcan, Effects of elevated temperatures on the properties of ground granulated blast furnace slag (GGBFS) based geopolymer concretes containing recycled concrete aggregate, Eur J Environ Civ En (2021) 4847-4862.

[365] R. Manjunath, M.C. Narasimhan, K.M. Umesha, Studies on high performance alkali activated slag concrete mixes subjected to aggressive environments and sustained elevated temperatures, Constr Build Mater 229 (2019) 116887.

[366] S. Celikten, M. Saridemir, K. Akcaozoglu, Effect of calcined perlite content on elevated temperature behaviour of alkali activated slag mortars, J Build Eng 32 (2020) 101717.

[367] J.Y. Ye, W.S. Zhang, D. Shi, Effect of elevated temperature on the properties of geopolymer synthesized from calcined ore-dressing tailing of bauxite and ground-granulated blast furnace slag, Constr Build Mater 69 (2014) 41-48.

[368] H.M. Khater, Studying the effect of thermal and acid exposure on alkali activated slag Geopolymer, International Congress on Materials & Structural Stability 11 (2014) 1-9.

[369] A.M. Rashad, S.R. Zeedan, A.A. Hassan, Influence of the activator concentration of sodium silicate on the thermal properties of alkali-activated slag pastes, Constr Build Mater 102 (2016) 811-820.

[370] A. Albidah, A. Abadel, F. Alrshoudi, A. Altheeb, H. Abbas, Y. Al-Salloum, Bond strength between concrete substrate and metakaolin geopolymer repair mortars at ambient and elevated temperatures, J Mater Res Technol 9(5) (2020) 10732-10745.

[371] P. Behera, V. Baheti, J. Militky, P. Louda, Elevated temperature properties of basalt microfibril filled geopolymer composites, Constr Build Mater 163 (2018) 850-860.

[372] P. Behera, V. Baheti, J. Militky, S. Naeem, Microstructure and mechanical properties of carbon microfiber reinforced geopolymers at elevated temperatures, Constr Build Mater 160 (2018) 733-743.

[373] H.Y. Zhang, V. Kodur, B. Wu, L. Cao, S.L. Qi, Comparative Thermal and Mechanical Performance of Geopolymers derived from Metakaolin and Fly Ash, J Mater Civil Eng 28(2) (2016).

[374] D.L.Y. Kong, J.G. Sanjayan, K. Sagoe-Crentsil, Factors affecting the performance of metakaolin geopolymers exposed to elevated temperatures, J Mater Sci 43(3) (2008) 824-831.

[375] M. Guerrieri, J.G. Sanjayan, Behavior of combined fly ash/slag-based geopolymers when exposed to high temperatures, Fire Mater 34(4) (2010) 163-175.

[376] G. Kurklu, The effect of high temperature on the design of blast furnace slag and coarse fly ash-based geopolymer mortar, Compos Part B-Eng 92 (2016) 9-18.

[377] M.T. Junaid, A. Khennane, O. Kayali, Performance of fly ash based geopolymer concrete made using non-pelletized fly ash aggregates after exposure to high temperatures, Mater Struct 48(10) (2015) 3357-3365.

[378] K. Behfarnia, M. Shahbaz, The effect of elevated temperature on the residual tensile strength and physical properties of the alkali-activated slag concrete, J Build Eng 20 (2018) 442-454.

[379] K.D. Hertz, Concrete strength for fire safety design, Mag Concrete Res 57(8) (2005) 445-453.

[380] A. Noumowe, Mechanical properties and microstructure of high strength concrete containing polypropylene fibres exposed to temperatures up to 200 degrees C, Cement Concrete Res 35(11) (2005) 2192-2198.

[381] G.F. Peng, W.W. Yang, H. Zhao, Y.F. Liu, S.H. Bian, L.H. Zhao, Explosive spalling and residual mechanical properties of fiber-toughened high-performance concrete subjected to high temperatures, Cement Concrete Res 36(4) (2006) 723-727.

[382] S.L. Suhaendi, T. Horiguchi, Effect of short fibers on residual permeability and mechanical properties of hybrid fibre reinforced high strength concrete after heat exposition, Cement Concrete Res 36(9) (2006) 1672-1678.

[383] K.Y. Kim, T.S. Yun, K.P. Park, Evaluation of pore structures and cracking in cement paste exposed to elevated temperatures by X-ray computed tomography, Cement Concrete Res 50 (2013) 34-40.

[384] A. Behnood, M. Ghandehari, Comparison of compressive and splitting tensile strength of high-strength concrete with and without polypropylene fibers heated to high temperatures, Fire Safety J 44(8) (2009) 1015-1022.

[385] Y. Li, Material properties and explosive spalling of ultra-high performance concrete in fire. Thesis, (2018).

[386] Z. Bažant, G. Cusatis, Concrete creep at high temperature and its interaction with fracture: recent progress, Creep, shrinkage and durability of concrete and concrete structures, 2005.

[387] H.L. Zhang, C.T. Davie, A numerical investigation of the influence of pore pressures and thermally induced stresses for spalling of concrete exposed to elevated temperatures, Fire Safety J 59 (2013) 102-110.

[388] J. Zhao, J.J. Zheng, G.F. Peng, K. van Breugel, A meso-level investigation into the explosive spalling mechanism of high-performance concrete under fire exposure, Cement Concrete Res 65 (2014) 64-75.

[389] E.W. Klingsch, Explosive spalling of concrete in fire, IBK Bericht 356 (2014).

[390] R. Zhao, J.G. Sanjayan, Geopolymer and Portland cement concretes in simulated fire, Mag Concrete Res 63(3) (2011) 163-173.

[391] S.N. Abd Razak, N. Shafiq, L. Guillaumat, S.A. Farhan, V.K. Lohana, Fire-Exposed Fly-Ash-Based Geopolymer Concrete: Effects of Burning Temperature on Mechanical and Microstructural Properties, Materials 15(5) (2022) 1884.

[392] K. Traven, M. Cesnovar, S.D. Skapin, V. Ducman, High temperature resistant fly-ash and metakaolin-based alkali-activated foams, Ceram Int 47(17) (2021) 25105-25120.

[393] G.R. Consolazio, M. McVay, J. Rish III, Measurement and prediction of pore pressure in cement mortar subjected to elevated temperature, Proceedings of the International Workshop on Fire Performance of High-Strength Concrete, NIST, Gaithersburg, Maryland, (1997) 125-148.

[394] T. Bakharev, Geopolymeric materials prepared using Class F fly ash and elevated temperature curing, Cement Concrete Res 35(6) (2005) 1224-1232.

[395] K.M. Klima, K. Schollbach, H.J.H. Brouwers, Q.L. Yu, Thermal and fire resistance of Class F fly ash based geopolymers-A review, Constr Build Mater 323 (2022) 126529.

[396] K. Kupwade-Patil, F. Soto, A. Kunjumon, E.N. Allouche, D.S. Mainardi, Multi-scale modeling and experimental investigations of geopolymeric gels at elevated temperatures, Comput Struct 122 (2013) 164-177.

[397] T. Kovarik, D. Rieger, J. Kadlec, T. Krenek, L. Kullova, M. Pola, P. Belsky, P. France, J. Riha, Thermomechanical properties of particle-reinforced geopolymer composite with various aggregate gradation of fine ceramic filler, Constr Build Mater 143 (2017) 599-606.

[398] A. Behnood, H. Ziari, Effects of silica fume addition and water to cement ratio on the properties of high-strength concrete after exposure to high temperatures, Cement Concrete Comp 30(2) (2008) 106-112.

[399] J.H. Xie, Z. Zhang, Z.Y. Lu, M.W. Sun, Coupling effects of silica fume and steel-fiber on the compressive behaviour of recycled aggregate concrete after exposure to elevated temperature, Constr Build Mater 184 (2018) 752-764.

[400] B. Georgali, P.E. Tsakiridis, Microstructure of fire-damaged concrete. A case study, Cement Concrete Comp 27(2) (2005) 255-259.

[401] V.K.R. Kodur, M.A. Sultan, Effect of temperature on thermal properties of high-strength concrete, J Mater Civil Eng 15(2) (2003) 101-107.

[402] S.M.M. Alizadeh, A. Rezaeian, I. Rasoolan, B. Tahmouresi, Compressive stress-strain model and residual strength of self-compacting concrete containing recycled ceramic aggregate after exposure to fire, J Build Eng 38 (2021) 102206.

[403] Y.C. Guo, J.H. Zhang, G.M. Chen, Z.H. Xie, Compressive behaviour of concrete structures incorporating recycled concrete aggregates, rubber crumb and reinforced with steel fibre, subjected to elevated temperatures, J Clean Prod 72 (2014) 193-203.

[404] T.C. Ling, C.S. Poon, S.C. Kou, Influence of recycled glass content and curing conditions on the properties of self-compacting concrete after exposure to elevated temperatures, Cement Concrete Comp 34(2) (2012) 265-272.

[405] B. Arisoy, H.C. Wu, Material characteristics of high performance lightweight concrete reinforced with PVA, Constr Build Mater 22(4) (2008) 635-645.

[406] K. Schneider, A. Michel, M. Liebscher, L. Terreri, S. Hempel, V. Mechtcherine, Mineral-impregnated carbon fibre reinforcement for high temperature resistance of thin-walled concrete structures, Cement Concrete Comp 97 (2019) 68-77.

[407] A.B. Kizilkanat, N. Kabay, V. Akyuncu, S. Chowdhury, A.R. Akca, Mechanical properties and fracture behavior of basalt and glass fiber reinforced concrete: An experimental study, Constr Build Mater 100 (2015) 218-224.

[408] Z.G. Zhang, Q. Zhang, Matrix tailoring of Engineered Cementitious Composites (ECC) with non-oil-coated, low tensile strength PVA fiber, Constr Build Mater 161 (2018) 420-431.

[409] J.C. Liu, K.H. Tan, Mechanism of PVA fibers in mitigating explosive spalling of engineered cementitious composite at elevated temperature, Cement Concrete Comp 93 (2018) 235-245.

[410] M.M. Hilles, M.M. Ziara, Mechanical behavior of high strength concrete reinforced with glass fiber, Eng Sci Technol 22(3) (2019) 920-928.

[411] S. Liu, D.J. Zhu, Y.F. Ou, Y.M. Yao, C.J. Shi, Impact response of basalt textile reinforced concrete subjected to different velocities and temperatures, Constr Build Mater 175 (2018) 381-391.

[412] H.R. Pakravan, M. Latifi, M. Jamshidi, Hybrid short fiber reinforcement system in concrete: A review, Constr Build Mater 142 (2017) 280-294.

[413] Z. Wang, J.Z. Ju, J.S. Yang, Z. Ma, D. Liu, K.P. Cui, H.R. Yang, J.R. Chang, N.D. Huang, L.B. Li, The non-equilibrium phase diagrams of flow-induced crystallization and melting of polyethylene, Sci Rep-Uk 6 (2016) 32968.

[414] M. Kalaj, M.S. Denny, K.C. Bentz, J.M. Palomba, S.M. Cohen, Nylon-MOF Composites through Postsynthetic Polymerization, Angew Chem Int Edit 58(8) (2019) 2336-2340.

[415] N. Ranjbar, M.Z. Zhang, Fiber-reinforced geopolymer composites: A review, Cement Concrete Comp 107 (2020) 103498.

[416] J.D. Rios, C. Leiva, M.P. Ariza, S. Seitl, H. Cifuentes, Analysis of the tensile fracture properties of ultra-high-strength fiber-reinforced concrete with different types of steel fibers by X-ray tomography, Mater Design 165 (2019) 107582.

[417] W.Z. Zheng, B.F. Luo, Y. Wang, Compressive and tensile properties of reactive powder concrete with steel fibres at elevated temperatures, Constr Build Mater 41 (2013) 844-851.

[418] W.Z. Zheng, H.Y. Li, Y. Wang, Compressive stress-strain relationship of steel fiber-reinforced reactive powder concrete after exposure to elevated temperatures, Constr Build Mater 35 (2012) 931-940.

[419] W.Z. Zheng, B.F. Luo, Y. Wang, Stress-strain relationship of steel-fibre reinforced reactive powder concrete at elevated temperatures, Mater Struct 48(7) (2015) 2299-2314.

[420] F. Aslani, J. Kelin, Assessment and development of high-performance fibre-reinforced lightweight self-compacting concrete including recycled crumb rubber aggregates exposed to elevated temperatures, J Clean Prod 200 (2018) 1009-1025.

[421] O.E. Babalola, P.O. Awoyera, D.H. Le, L.M.B. Romero, A review of residual strength properties of normal and high strength concrete exposed to elevated temperatures: Impact of materials modification on behaviour of concrete composite, Constr Build Mater 296 (2021) 123448.

[422] L.H. Xu, L. Huang, Y. Chi, G.D. Mei, Tensile Behavior of Steel-Polypropylene Hybrid Fiber-Reinforced Concrete, Aci Mater J 113(2) (2016) 219-229.

[423] M. Kaya, Effect of Steel Fiber Additive on High Temperature Resistance in Geopolymer Mortars, Ijst-T Civ Eng 46(3) (2022) 1949-1967.

[424] Y.N. Chan, X. Luo, W. Sun, Compressive strength and pore structure of high-performance concrete after exposure to high temperature up to 800 degrees C, Cement Concrete Res 30(2) (2000) 247-251.

[425] K.K. Sideris, P. Manita, E. Chaniotakis, Performance of thermally damaged fibre reinforced concretes, Constr Build Mater 23(3) (2009) 1232-1239.

[426] Y.S. Heo, J.G. Sanjayan, C.G. Han, M.C. Han, Critical parameters of nylon and other fibres for spalling protection of high strength concrete in fire, Mater Struct 44(3) (2011) 599-610.

[427] C.G. Han, Y.S. Hwang, S.H. Yang, N. Gowripalan, Performance of spalling resistance of high performance concrete with polypropylene fiber contents and lateral confinement, Cement Concrete Res 35(9) (2005) 1747-1753.

[428] A.N.S.A.L. Qadi, K.N. Bin Mustapha, S. Naganathan, Q.N.S. Al-Kadi, Effect of polypropylene fibers on thermogravimetric properties of self-compacting concrete at elevated temperatures, Fire Mater 37(3) (2013) 177-186.

[429] W. Khaliq, V. Kodur, High Temperature Mechanical Properties of High-Strength Fly Ash Concrete with and without Fibers, Aci Mater J 109(6) (2012) 665-674.

[430] T. Drzymala, W. Jackiewicz-Rek, M. Tomaszewski, A. Kus, J. Galaj, R. Sukys, Effects of High Temperature on the Properties of High Performance Concrete (HPC), Modern Building Materials, Structures and Techniques 172 (2017) 256-263.

[431] W.Z. Zheng, H.Y. Li, Y. Wang, Compressive behaviour of hybrid fiber-reinforced reactive powder concrete after high temperature, Mater Design 41 (2012) 403-409.

[432] R. Serrano, A. Cobo, M.I. Prieto, M.D. Gonzalez, Analysis of fire resistance of concrete with polypropylene or steel fibers, Constr Build Mater 122 (2016) 302-309.

[433] V.M.D. Monteiro, L.R. Lima, F.D. Silva, On the mechanical behavior of polypropylene, steel and hybrid fiber reinforced self-consolidating concrete, Constr Build Mater 188 (2018) 280-291.

[434] J. Eidan, I. Rasoolan, A. Rezaeian, D. Poorveis, Residual mechanical properties of polypropylene fiber-reinforced concrete after heating, Constr Build Mater 198 (2019) 195-206.

[435] P.N. Hiremath, S.C. Yaragal, Performance evaluation of reactive powder concrete with polypropylene fibers at elevated temperatures, Constr Build Mater 169 (2018) 499-512.

[436] S. Guler, Z.F. Akbulut, Effect of high-temperature on the behavior of single and hybrid glass and basalt fiber added geopolymer cement mortars, J Build Eng 57 (2022).

[437] X. Jiang, R. Xiao, M.M. Zhang, W. Hu, Y. Bai, B.S. Huang, A laboratory investigation of steel to fly ash-based geopolymer paste bonding behavior after exposure to elevated temperatures, Constr Build Mater 254 (2020) 104809.

[438] M. Sivasakthi, R. Jeyalakshmi, N.P. Rajamane, R. Jose, Thermal and structural micro analysis of micro silica blended fly ash based geopolymer composites, J Non-Cryst Solids 499 (2018) 117-130.

[439] J.R.A. Goncalves, Y. Boluk, V. Bindiganavile, Crack growth resistance in fibre reinforced alkali-activated fly ash concrete exposed to extreme temperatures, Mater Struct 51(2) (2018) 1-10.

[440] M.T. Junaid, O. Kayali, A. Khennane, Response of alkali activated low calcium fly-ash based geopolymer concrete under compressive load at elevated temperatures, Mater Struct 50(1) (2017) 1-10.

[441] M.T. Junaid, A. Khennane, O. Kayali, A. Sadaoui, D. Picard, M. Fafard, Aspects of the deformational behaviour of alkali activated fly ash concrete at elevated temperatures, Cement Concrete Res 60 (2014) 24-29.

[442] M. Hanumananaik, M.S.K. Reddy, K.V.L. Subramaniam, High-Temperature Performance of Low-Calcium Fly Ash-Based Geopolymers, J Mater Civil Eng 34(5) (2022) 04022040

[443] S.N.A. Razak, N. Shafiq, E.H. Nikbakht, B.S. Mohammed, L. Guillaumat, S.A. Farhan, Fire performance of fly-ash-based geopolymer concrete: Effect of burning temperature on mechanical and microstructural properties, Mater Today-Proc 66 (2022) 2665-2669.

[444] A.N. Derinpinar, M.B. Karakoc, A. Ozcan, Performance of glass powder substituted slag based geopolymer concretes under high temperature, Constr Build Mater 331 (2022) 127318.

[445] K.M.L. Alventosa, B. Wild, C.E. White, The effects of calcium hydroxide and activator chemistry on alkali-activated metakaolin pastes exposed to high temperatures, Cement Concrete Res 154 (2022) 106742.

[446] H.M. Khater, M. Gharieb, Synergetic effect of nano-silica fume for enhancing physico-mechanical properties and thermal behavior of MK-geopolymer composites, Constr Build Mater 350 (2022) 128879.

[447] G.F. Huseien, A.R.M. Sam, J. Mirza, M.M. Tahir, M.A. Asaad, M. Ismail, K.W. Shah, Waste ceramic powder incorporated alkali activated mortars exposed to elevated Temperatures: Performance evaluation, Constr Build Mater 187 (2018) 307-317.

[448] C.L. Chan, M.Z. Zhang, Behaviour of strain hardening geopolymer composites at elevated temperatures, Cement Concrete Comp 132 (2022) 104634.

[449] H.Y. Zhang, V. Kodur, B. Wu, J. Yan, Z.S. Yuan, Effect of temperature on bond characteristics of geopolymer concrete, Constr Build Mater 163 (2018) 277-285.

[450] M.A. Salih, N. Farzadnia, R. Demirboga, A.A.A. Ali, Effect of elevated temperatures on mechanical and microstructural properties of alkali-activated mortar made up of POFA and GGBS, Constr Build Mater 328 (2022) 127041.

[451] H. Zhong, M.Z. Zhang, Effect of recycled tyre polymer fibre on engineering properties of sustainable strain hardening geopolymer composites, Cement Concrete Comp 122 (2021) 104167.

[452] A. Committee, Building code requirements for structural concrete (ACI 318-08) and commentary, American Concrete Institute, 2008.

[453] J.T. Xie, O. Kayali, Effect of superplasticiser on workability enhancement of Class F and Class C fly ash-based geopolymers, Constr Build Mater 122 (2016) 36-42.

[454] M. Chen, Z. Sun, W. Tu, X. Yan, M. Zhang, Behaviour of recycled tyre polymer fibre reinforced concrete at elevated temperatures, Cement and Concrete Composites (2021) 104257.

[455] G. Fang, H. Bahrami, M. Zhang, Mechanisms of autogenous shrinkage of alkali-activated fly ash-slag pastes cured at ambient temperature within 24 h, Constr Build Mater 171 (2018) 377-387.

[456] P.S. Singh, T. Bastow, M. Trigg, Structural studies of geopolymers by Si-29 and Al-21 MAS-NMR, J Mater Sci 40(15) (2005) 3951-3961.

[457] O. Burciaga-Diaz, J.I. Escalante-Garcia, Structure, Mechanisms of Reaction, and Strength of an Alkali-Activated Blast-Furnace Slag, J Am Ceram Soc 96(12) (2013) 3939-3948.

[458] D. Jeon, Y. Jun, Y. Jeong, J.E. Oh, Microstructural and strength improvements through the use of Na2CO3 in a cementless Ca(OH)(2)-activated Class F fly ash system, Cement Concrete Res 67 (2015) 215-225.

[459] O. Burciaga-Diaz, J.I. Escalante-Garcia, Comparative performance of alkali activated slag/metakaolin cement pastes exposed to high temperatures, Cement Concrete Comp 84 (2017) 157-166.

[460] L.P. Liu, H.N. Liu, Y. Xu, J.C. Xiang, Y. He, G.J. Zheng, Mechanical Properties and Microstructure of Alkali-Activated Slag Grouting Materials Exposed to Flowing NaHCO3 Solution, J Mater Civil Eng 34(12) (2022) 04022332.

[461] P. Florian, E. Veron, T.F.G. Green, J.R. Yates, D. Massiot, Elucidation of the Al/Si Ordering in Gehlenite Ca2Al2SiO7 by Combined Si-29 and Al-27 NMR Spectroscopy/Quantum Chemical Calculations, Chem Mater 24(21) (2012) 4068-4079.

[462] Z.J. Jia, C. Chen, J.J. Shi, Y.M. Zhang, Z.M. Sun, P.G. Zhang, The microstructural change of C-S-H at elevated temperature in Portland cement/GGBFS blended system, Cement Concrete Res 123 (2019) 105773

[463] X. Tian, F. Rao, C.X. Li, W. Ge, N.O. Lara, S.X. Song, L. Xia, Solidification of municipal solid waste incineration fly ash and immobilization of heavy metals using waste glass in alkaline activation system, Chemosphere 283 (2021) 131240.

[464] G.D. Huang, L. Yuan, Y.S. Ji, B.L. Liu, Z.S. Xu, Cooperative action and compatibility between Portland cement and MSWI bottom ash alkali-activated double gel system materials, Constr Build Mater 209 (2019) 445-453.

[465] A. Fernandez-Jimenez, A. Palomo, Mid-infrared spectroscopic studies of alkali-activated fly ash structure, Micropor Mesopor Mat 86(1-3) (2005) 207-214.

[466] S.Q. Ruan, S.K. Chen, X.Y. Zhu, Q. Zeng, Y. Liu, J.Y. Lai, D.M. Yan, Matrix wettability and mechanical properties of geopolymer cement-polydimethylsiloxane (PDMS) hybrids, Cement Concrete Comp 124 (2021) 104268.

[467] M. Cyr, R. Pouhet, Carbonation in the pore solution of metakaolin-based geopolymer, Cement Concrete Res 88 (2016) 227-235.

[468] S. Kumar, R. Kumar, T.C. Alex, A. Bandopadhyay, S.P. Mehrotra, Influence of reactivity of fly ash on geopolymerisation, Adv Appl Ceram 106(3) (2007) 120-127.

[469] P.Z. Wang, R. Trettin, V. Rudert, Effect of fineness and particle size distribution of granulated blast-furnace slag on the hydraulic reactivity in cement systems, Adv Cem Res 17(4) (2005) 161-166.

[470] I. Hager, M. Sitarz, K. Mróz, Fly-ash based geopolymer mortar for high-temperature application - Effect of slag addition, J Clean Prod 316 (2021) 128168.

[471] H. Liu, W. Jing, L.L. Qin, P. Duan, Z.H. Zhang, R. Guo, W.L. Li, Thermal stability of geopolymer modified by different silicon source materials prepared from solid wastes, Constr Build Mater 315 (2022) 125709.

[472] B. Kanagaraj, N. Anand, R.S. Raj, E. Lubloy, Behavioural studies on binary blended high strength self compacting geopolymer concrete exposed to standard fire temperature, Ain Shams Eng J 15(2) (2024) 102394.

[473] R.L. Burwell, Manual of Symbols and Terminology for Physicochemical Quantities and Units - Appendix 2 - Definitions, Terminology and Symbols in Colloid and Surface-Chemistry .2. Heterogeneous Catalysis, Pure Appl Chem 46(1) (1976) 71.

[474] L.M. Anovitz, D.R. Cole, Characterization and Analysis of Porosity and Pore Structures, Rev Mineral Geochem 80 (2015) 61.

[475] S. Diamond, Mercury porosimetry - An inappropriate method for the measurement of pore size distributions in cement-based materials, Cement Concrete Res 30(10) (2000) 1517-1525.

[476] H.Y. Ma, Mercury intrusion porosimetry in concrete technology: tips in measurement, pore structure parameter acquisition and application, J Porous Mat 21(2) (2014) 207-215.

[477] Y. Peng, G.R. Zhao, Y.X. Qi, Q. Zeng, In-situ assessment of the water-penetration resistance of polymer modified cement mortars by mu-XCT, SEM and EDS, Cement Concrete Comp 114 (2020) 103821.

[478] S.Q. Ruan, D.M. Yan, S.K. Chen, F.X. Jiang, W.W. Shi, Process and mechanisms of multi-stage water sorptivity in hydrophobic geopolymers incorporating polydimethylsiloxane, Cement Concrete Comp 128 (2022) 104460.

[479] S. Naderi, W.L. Tu, M.Z. Zhang, Meso-scale modelling of compressive fracture in concrete with irregularly shaped aggregates, Cement Concrete Res 140 (2021) 106317.

[480] S. Naderi, M.Z. Zhang, Meso-scale modelling of static and dynamic tensile fracture of concrete accounting for real-shape aggregates, Cement Concrete Comp 116 (2021) 103889.

[481] C. Code, Gb/T50081-2002 Test Method of Mechanical Properties on Ordinary Concrete, Standards Press of China: Beijing, China, 2003.

[482] P.M. Ashraf, S.N. Thomas, L. Edwin, Development of graphene-nanometre-sized cerium oxide-incorporated aluminium and its electrochemical evaluation, Appl Nanosci 6(2) (2016) 149-158.

[483] Y. Li, Y. Zhang, E.H. Yang, K.H. Tan, Effects of geometry and fraction of polypropylene fibers on permeability of ultra-high performance concrete after heat exposure, Cement Concrete Res 116 (2019) 168-178.

[484] E.D. Rodriguez, S.A. Bernal, J.L. Provis, J. Paya, J.M. Monzo, M.V. Borrachero, Effect of nanosilica-based activators on the performance of an alkali-activated fly ash binder, Cement Concrete Comp 35(1) (2013) 1-11.

[485] S.S. Choubi, C.M. Akgul, High temperature exposure of alkali-activated coal fly ashes, J Build Eng 59 (2022) 105081.

[486] C.L. Hu, Z.J. Li, A review on the mechanical properties of cement-based materials measured by nanoindentation, Constr Build Mater 90 (2015) 80-90.

[487] W.L. Tu, G.H. Fang, B.Q. Dong, Y.K. Hu, M.Z. Zhang, Behaviour of alkali-activated fly ash-slag paste at elevated temperatures: An experimental study, Cement Concrete Comp 147 (2024) 105438.

[488] H.Y. Zhang, V. Kodur, B. Wu, L. Cao, S.L. Qi, Comparative Thermal and Mechanical Performance of Geopolymers derived from Metakaolin and Fly Ash, J Mater Civil Eng 28(2) (2016) 04015092.

[489] A. Nana, R.C. Kaze, T.S. Alomayri, H.S. Assaedi, J.G.N. Deutou, J. Ngouné, H.K. Tchakouté, E. Kamseu, C. Leonelli, Innovative porous ceramic matrices from inorganic polymer composites (IPCs): Microstructure and mechanical properties, Constr Build Mater 273 (2021) 122032.

[490] R.B.E. Boum, F.M. Owono, C.R. Kaze, J.C.E. Essomba, B. Souleymanou, J.G.D. Nemaleu, M.J. Ntamak-Nida, Thermal behavior of acidic and alkali activated laterite based geopolymer: a comparative study, Geosystem Eng 25(5-6) (2022) 225-238.

[491] I. Abdulkadir, B.S. Mohammed, A.M. Al-Yacouby, E.L. Woen, T. Tafsirojjaman, Tailoring an engineered cementitious composite with enhanced mechanical performance at ambient and elevated temperatures using graphene oxide and crumb rubber, J Mater Res Technol 28 (2024) 4508-4530.

[492] Z.H. Zhang, J.L. Provis, A. Reid, H. Wang, Mechanical, thermal insulation, thermal resistance and acoustic absorption properties of geopolymer foam concrete, Cement Concrete Comp 62 (2015) 97-105.

Appendix A Sample Preparation

Preparation of SH (NaOH):

Firstly, the molecular weights of sodium, oxygen and hydrogen are listed as follows:

The molecular weight of sodium (Na) = 23 g/mol

The molecular weight of oxygen (O) = 16 g/mol

The molecular weight of hydrogen (H) = 1 g/mol

Therefore, the molecular weight of sodium hydroxide can be calculated as follows:

The molecular weight of sodium hydroxide (NaOH) = 23+16+1 = 40 g/mol

Which states that in the weight of 1 mol of NaOH is 40 g

Then, the mass of NaOH solid powder can be determined:

The mass required to prepare 10 M NaOH per litre solution

= Molecular weight of NaOH × 10 mol

= 40 g/mol × 10 mol

= 400 g

Hence,

For 1 litre of water, there should be 400 g NaOH to obtain 10 M solution.

Preparation of SS (Na_2SiO_3):

Firstly, the molecular weights of sodium, silicate and oxygen are listed as follows:

The molecular weight of sodium (Na) = 23 g/mol

The molecular weight of silicate (Si) = 28 g/mol

The molecular weight of oxygen (O) = 16 g/mol

Thus, the molecular weight of sodium oxide and silicon oxide can be determined:

The molecular weight of Sodium oxide (Na_2O) = 16 + 23 × 2 = 62 g/mol

The molecular weight of Silicon oxide (SiO_2) = 28 + 16 × 2 = 60 g/mol

Thus,

The total mass of Na_2O required for a M_s ratio of 2 can be calculated by:

$$M_s = 2 = \frac{\frac{m_{SiO_2}}{M_{SiO_2}}}{\frac{m_{Na_2O}}{M_{Na_2O}}} = \frac{\frac{31.10}{60}}{\frac{m_{Na_2O}}{62}} \quad \rightarrow \quad m_{Na_2O} = 16.068\ g$$

Since in the used SS solution, there are 8.5 g Na_2O per 100 g solution (as mentioned in Chapter 3),

Thus,

Additional water $m_{SiO_2} = 16.068 - 8.5 = 7.568\ g$

Since in the chemical reaction: $Na_2O + 2\ H_2O = 2NaOH + O_2 \quad ; \quad Na_2O \rightarrow 2NaOH$

Thus,

$$\frac{m_{Na_2O}}{M_{Na_2O}} = 2\frac{m_{NaOH}}{M_{NaOH}} \quad \rightarrow \quad \frac{7.568}{62} = \frac{m_{NaOH}}{2 * 40} \quad \rightarrow \quad m_{NaOH} = 9.77\frac{g}{100g}water$$